Title
Dynamic Soil-Structure Interaction of Instrumented Buildings and Test Structures

Author
Givens, Michael James

Publication Date
2013

Peer reviewed|Thesis/dissertation

UNIVERSITY OF CALIFORNIA
Los Angeles

Dynamic Soil-Structure Interaction of Instrumented Buildings and Test Structures

A dissertation submitted in partial satisfaction of the requirements for the degree of Doctor of Philosophy in
Civil Engineering

by

Michael James Givens
2013

ABSTRACT OF THE DISSERTATION

Dynamic Soil-Structure Interaction of

Instrumented Buildings and Test Structures

by

Michael James Givens

Doctor of Philosophy in Civil Engineering

University of California, Los Angeles, 2013

Professor Jonathan P. Stewart, Chair

The effects of soil-structure interaction (SSI) are investigated through careful interpretation of available data from instrumented buildings and recently performed forced vibration experiments on instrumented buildings and test structures. Conventional engineering practice typically ignores soil-structure interaction (SSI) during evaluation of the seismic demand on buildings based on the perception that consideration of SSI will reduce demands on structures and ignoring SSI effects will cause seismic demands to be conservatively biased. I show that it is not always conservative to ignore SSI effects. Analysis of field performance data is undertaken to provide deeper insights into SSI phenomena ranging from kinematic effects on foundation ground

motions to mobilized foundation stiffness and damping across a wide range of frequencies and loading levels. These data are interpreted to evaluate strengths and limitations of engineering analysis procedures for SSI.

Foundation damping incorporates the combined effects of energy loss due to waves propagating away from the vibrating foundation in translational and rotational modes (radiation damping), as well as hysteretic action in the soil (material damping). Previous foundation damping models were developed for rigid circular foundations on homogenous halfspace and were often expressed using confusing or incomplete functions. Starting from first principles, we derive fundamental expressions for foundation damping in which foundation impedance components representing radiation damping and the soil hysteretic damping ratio appear as variables, providing maximum flexibility to the analyst. We utilize these general expressions with impedance solutions for rectangular-footprint foundations to: (1) compare predicted foundation damping levels with those from field case histories and (2) develop new foundation damping relationships for application in the building code (NEHRP Provisions).

Ground motions at the foundation levels of structures differ from those in the free-field as a result of inertial and kinematic interaction effects. Inertial interaction effects tend to produce narrow-banded ground motion modification near the fundamental period of the soil-structure system, whereas kinematic effects are relatively broad-banded but most significant at high frequencies. Kinematic interaction effects can be predicted using relatively costly finite element analyses with incoherent input or simplified models. The simplified models are semi-empirical in nature and derived from California data. These simplified models are the basis for seismic design guidelines used in the western United States, such as ASCE-41 and NIST (2012). We compile

some available data from building and ground instrumentation arrays in Japan for comparison to these two sets of models. We demonstrate that the model predictions for the sites under consideration are very similar to each other for modest foundation sizes (equivalent radii under about 50 m). However, the data show that both approaches overestimate the transfer function ordinates relative to those from a subset of the Japanese buildings having pile foundations. The misfit occurs at frequencies higher than the first-mode resonant frequency and appears to result from pile effects on kinematic interaction that are not accounted for in current models.

A complete model of a soil-foundation-structure system for use in response history analysis requires modification of input motions relative to those in the free-field to account for kinematic interaction effects, foundation springs and dashpots to represent foundation-soil impedance, and a structural model. The recently completed NIST (2012) report developed consistent guidelines for evaluation of kinematic interaction effects and foundation impedance for realistic conditions. We implement those procedures in seismic response history analyses for two instrumented buildings in California, one a 13-story concrete-moment frame building with two levels of basement and the other a 10-story concrete shear wall core building without embedment. We develop three-dimensional baseline models (MB) of the building and foundation systems (including SSI components) that are calibrated to reproduce observed responses from recorded earthquakes. SSI components considered in the MB model include horizontal and vertical springs and dashpots that represent the horizontal translation and rotational impedance, kinematic ground motion variations from embedment and base slab averaging, and ground motion variations over the embedment depth of basements. We then remove selected components of the MB models one at a time to evaluate their impact on engineering demand

parameters (EDPs) such as inter-story drifts, story shear distributions, and floor accelerations. We find that a "bathtub" model that retains all features of the MB approach except for depth-variable motions provides for generally good above-ground superstructure responses, but biased demand assessments in subterranean levels. Other common approaches using a fixed-based representation can produce poor results.

To expand the data inventory of response histories to evaluate SSI, we performed forced vibration testing of a well-instrumented steel and reinforced concrete structure that has removable bracing. The testing was performed at three sites with varying soil conditions. I describe testing at one of the sites located in Garner Valley, California. During testing at this site an adjacent structure and local concrete slab were also instrumented in addition to the test structure. I describe the testing setup, schemes, instrumentation, and data processing techniques. The data are analyzed to evaluate the stiffness and damping associated with the foundation-soil interaction, revealing linear-elastic behavior at low forcing levels characterized by smaller stiffnesses and both lower and higher damping than is predicted by classical models. Nonlinear behavior at stronger shaking levels includes pronounced reductions of stiffness and changes in damping. Interestingly, kinematic interaction effects observed on an adjacent slab excited principally by surface waves were of a similar character to expectations from analytical models for body wave excitation from earthquakes. If verified, these results could lead to site- and foundation-specific test methods for evaluating kinematic interaction effects.

The dissertation of Michael James Givens is approved:

Scott Brandenberg

Ertugrul Taciroglu

An Yin

George Mylonakis

Jonathan P. Stewart, Committee Chair

University of California, Los Angeles

2013

To My Loving Family
With them everything is better

TABLE OF CONTENTS

PAGE

FIGURES

PAGE

TABLES

PAGE

SYMBOLS

LATIN SYMBOLS

A	footing area, m^2 (ft^2)
a_o	dimensionless frequency for rectangular footings, $\omega B/V_s$
a_0^r	dimensionless frequency for circular footings, $\omega r/V_s$
B	foundation half-width (small plan dimension), m (ft)
B_e^A	half-dimension of an equivalent square footing matching the area of the actual footing, m (ft)
B_e^I	half-dimension of an equivalent square footing matching the moment of inertia of the actual footing, m (ft)
c_j	dashpot coefficient for translation along the *j*-axis, kN-sec/m (kipf-sec/ft)
c_{jj}	dashpot coefficient for rotation about the *j*-axis, kN-m/rad (kipf-ft/rad)
c_s	structural dashpot coefficient, kN-sec/m (kipf-sec/ft)
c_z^i	dashpot intensity, kN-sec/m^3 (kipf-sec/ft^3)
C	dashpot matrix, , kN-sec/m^3 (kipf-sec/ft^3)
C_s	seismic coefficient
$\tilde{C}_s$	seismic coefficient read from the design spectrum at elongated period $\tilde{T}$
D	embedment depth, m (ft)
D_L	internal node spacing, m (ft)
d_w	height of effective side wall contact of embedded foundation, m (ft)
E_f	foundation Young's modulus, kPa (ksi)
E_s	Young's modulus of the soil, kPa (ksi)
F	force, kN (lbf)
f_L	limiting frequency (Hz)
f_1	first-mode frequency from parametric system identification (Hz)
G	soil shear modulus, kPa (ksi)
G_0	maximum soil shear modulus (at small strains), kPa (ksi)
h	height of the center of mass for the first-mode shape, m (ft)
h_f	height of foundation, m (ft)

H Horizontal force

H_u kinematic transfer function

I_i area moment of inertia of soil-foundation contact, m^4 (ft^4); *i* denotes the axis about which the surface is taken

I_f mass moment of inertia about the foundation, m^4 (ft^4)

j index denoting modes of translation displacement or rotation

J_t polar moment of inertia of soil-foundation contact surface, m^4 (ft^4)

k spring stiffness, translation, kN/m (lbf/ft), and rotation, kN-m/rad (lbf-ft/rad)

k_j spring stiffness, translation, along the *j*-axis, N/m (psi)

k_s structural stiffness (structural compliance), cm (in)

K stiffness matrix, Mg (lbs)

K_j foundation static stiffness for mode *j*, translation, N/m (lbf/ft), and rotation, N-m/rad (lbf-ft /rad)

k_j^* complex-valued impedance function for mode *j*, translation, N/m (lbf/ft), and rotation, N-m/rad (lbf-ft/rad)

k_{jj} spring stiffness, rotation, about the *j*-axis, kN-m/rad (lbf-ft/rad)

k_z^i stiffness intensity (coefficient of subgrade reaction), kN/m^3 (lbf/ft^3)

L foundation half-length, m (ft)

L_{end} end region length of foundation with increase stiffness, m (ft)

m mass, Mg (lbs)

M mass matrix, Mg (lbs)

m_f mass of foundation, Mg (lbs)

m_s mass of superstructure, Mg (lbs)

n, n_s, n_x, n_{yy} exponents related with foundation damping

R_c dashpot intensities scalar (Equation 2-21 in NIST report)

R_e end length ratio

R_k spring stiffness intensities scalar (Equation 2-21 in NIST report)

r foundation radius, m (ft)

rr rotational mode about axis of a circular foundation

S_a, $S_{a\text{-}FIM}$ spectral acceleration, fixed base, and with FIM effects, respectively, m/s^2, (ft/s^2), g

S_a^e equivalent spectral acceleration, m/sec^2 (ft/sec^2), g

$\tilde{S}_a$ spectral acceleration for a flexible-base structure, m/sec^2, (ft/sec^2), g

S_d, S_d^e spectral displacement and equivalent spectral displacement, m (ft)

T undamped natural vibration period, sec

$\tilde{T}$ flexible-base period, sec

t_f foundation thickness, m (ft)

T_i fixed-base period for a case history (Sections 2.6.2 and 6.6), sec;

$\hat{\tilde{T}}_i$ flexible-base period for a modeled prediction (Sections 2.6.2 and 6.6), sec

T_p predominant period of ground motion, sec

T_x, T_{yy} fictitious vibration periods, calculated as if the only source of the vibration was translation or rotation, sec

$\overline{T}_x$, $\overline{T}_{yy}$ complex-valued fictitious vibration periods, calculated as if the only source of the vibration was translation or rotation, sec

$\tilde{T}/T$ period lengthening ratio due to SSI

$\tilde{T}_i/T_i$ period lengthening ratio from case history data (Sections 2.6.2 and 6.6)

$\hat{\tilde{T}}_i/T_i$ period lengthening ratio predicted from model (Sections 2.6.2 and 6.6)

u_f measured foundation horizontal deflection, cm (in)

u_{FIM} foundation input motion, acceleration, m/sec^2, velocity, m/sec or displacement, m

u_g free-field ground motion, acceleration, m/sec^2, velocity, m/sec or displacement, m

u_s deflection amount of structural mass associated with the structural compliance, cm (in)

$\ddot{U}, \dot{U}, \& \ U$ horizontal and rotational accelerations, velocity and displacements, respectively, of each degree of freedom

V_{app} apparent wave propagation velocity, m/sec (ft/sec)

V base shear force, kN (lbf)

V_s shear wave velocity over a representative depth, m/sec (ft/sec); used generally in report for either measured or averaged result

$V_{s,d}$ time-averaged shear wave velocity over the embedment depth (D) of the foundation

V_{s0} time-averaged shear wave velocity in free-field, over depth interval z_p, m/sec (ft/sec)

$V_{s,f}$ overburden-corrected shear wave velocity under footing, m/sec (ft/sec)

z_p depth interval, m (ft)

GREEK SYMBOLS

α_j dynamic (frequency) stiffness modifier for surface foundation for mode *j*

β_f foundation damping ratio

$\beta_{f,i}$ foundation damping ratio for a case history (Sections 2.6.2 and 6.6)

$\hat{\beta}_{f,i}$ foundation damping ratio for a modeled prediction (Sections 2.6.2 and 6.6)

β_i fixed base structural damping ratio

β_j dynamic damping ratio for mode *j*

β_0 flexible-base system damping ratio

β_{rj} radiation damping ratio for mode *j*

β_s soil hysteretic damping ratio

β_1 corresponding first-mode damping ratio from parametric system identification

γ shear strain

γ_m soil-structure mass ratio = $m/\rho hA$; typical range of 0.1 to 0.2 for flexible to stiff structures, respectively, based on Veletsos (1977)

Δ deflection, m (ft)

$\tilde{\Delta}$ total deflection with respect to free-field at the top of a SDOF structure, cm (in)

$\Delta\sigma_v$ increment of vertical stress at depth *z* from the structural weight, kPa (ksi)

η_j, η_{jj} embedment correction factor for rigid footing spring constants for mode *j*

θ rotation deflection amount in a SDOF structure due to base moment (rad)

θ_f measured foundation rotation (rad)

κ_a dimensionless parameter accounting for effects of incoherence from wave passage and stochastic processes, as well as Fourier amplitude variability

ν soil Poisson's ratio

ν_f foundation Poisson's ratio

ρ_s soil mass density, Mg/m^3 (lbs/ft^3)

σ_m' effective confining stress, kPa (ksi)

σ'_{v0} effective stress from the self-weight of the soil, kPa (ksi)

ω undamped natural vibration frequency (rad/sec)

ACKNOWLEDGMENTS

I would like to express my great appreciation and gratitude to my advisor Jonathan P. Stewart for his guidance and support during my research. He was instrumental in shaping my doctoral program and providing me the opportunities to get a well-rounded breath of knowledge of soil-structure interaction. Thank you for selecting me to carry out these tasks and in turn helping me become a better engineer. Our almost weekly meetings discussing research and various related topics were invaluable to me.

Thank you to my committee members Scott Brandenberg, An Yin, Ertugrul Taciroglu, and George Mylonakis for their valuable input into this document. I appreciate the time you have spent reading, discussing and critiquing my work. I am honored to have had my work reviewed by such well-accomplished people. A special thanks to George Mylonakis for his countless hours of collaboration with me.

Support for my work to produce Chapter 4 was provided by the NEHRP Consultants Joint Venture, a partnership of the Applied Technology Council and Consortium of Universities for Research in Earthquake Engineering, through Contract SB134107CQ0019, Earthquake Structural and Engineering Research, issued by the National Institute of Standards and Technology (NIST).

Support for my work to produce Chapters 5 and 6 was provided by the National Science Foundation under Grant No. CMMI-0618804 through the George E. Brown Jr. Network for Earthquake Engineering Simulations (NEES), PI: Dr. Jack Moehle.

This research could have not been possible without the love and support of my family and friends. My wife Debbie has been my biggest supporter and confidante during my studies. The satisfaction that she brings to my life makes me better at everything.

VITA

2003-2005	Engineering Technician / Geologist-in-Training Geo-Environmental, Inc. Irvine, California
2006	B.S., Geology California State University, Long Beach
2006-2009	Staff Geologist Geo-Environmental, Inc. Irvine, California
2010	M.S., Civil Engineering University of California, Los Angeles
2010-2011	Project Graduate Student Consortium of Universities for Research in Earthquake Engineering (CUREE) Richmond, California
2011-2013	Graduate Research Student Department of Civil and Environmental Engineering University of California, Los Angeles
2013	Teaching Assistant Department of Civil and Environmental Engineering University of California, Los Angeles *Awarded: UCLA ASCE "TA of the Year 2012-2013"*

PUBLICATIONS

Givens, M.J., Haselton, C., Mazzoni, S., and Stewart, J.P., 2012. Assessment of Soil-Structure Interaction Modeling Strategies for Response History Analysis of Buildings, *Proc. 15th World Conf. on Eqk. Engrg*, September 24-28, Lisbon Congress Center, Lisbon.

Givens, M.J., Mikami, A., Kashima, T., and Stewart, J.P, 2012. Kinematic Soil-Structure Interaction Effects from Building and Free-Field Seismic Arrays in Japan, *Proc. 8th Inter. Conf. on Urban Eqk. Engrg & 4th Asia Conf on Eqk. Engrg/*, March 6-8, Tokyo Institute of Technology, Tokyo.

National Institute of Standards and Technology, (NIST), 2012. Soil-Structure Interaction for Building Structures, *Report NIST/GCR 12-917-21*, presented by NEHRP Consultants Joint Venture, J.P. Stewart (project director), September; *Working Group Member.*

1 INTRODUCTION

1.1 Soil-Structure Interaction in Engineering Practice

In this Ph.D. research, I seek to perform analysis of field performance data to provide deeper insights into SSI phenomena ranging from kinematic effects on foundation ground motions to mobilized foundation stiffness and damping across a wide range of frequencies and loading levels. These data are interpreted to evaluate strengths and limitations of engineering analysis procedures for SSI. The profession seeks to provide accurate evaluations of facility performance in response to seismic excitation. This includes formal consideration of uncertainties in the representations of seismic demand and the engineering evaluation of response to that demand. For that reason, a seismic response analysis operates most effectively when the model of the structural system in question is as realistic as is reasonable possible. Currently, however, conventional design practice typically ignores SSI based on the perception that the SSI components would provide beneficial effects to the structure during seismic events. It is assumed that the increase in flexibility of the structure due to SSI would decrease the demand on the structure. Conventional engineering practice is not performance-based, but is based on certain prescriptive requirements for demand specification and structural detailing that is intended to achieve a single performance goal – collapse prevention.

What is problematic about this approach is that, because it is assumed that SSI effects reduce the demands on structures, ignoring SSI effects is considered the equivalent of erring conservatively. In reality, it is not always conservative to ignore SSI effects, as will be described in Chapter 2 of this research. Moreover, because conventional design practice seeks to evaluate accurately the expected building response and its dispersion, deliberately erring an analysis result (conservatively or not) is counter-productive. I will argue that comprehensive design analysis should consider SSI, and indeed there is strong evidence that the profession is moving in this direction at an increasing rate.

1.2 Alternative Frameworks for SSI Analysis

SSI can be incorporated into seismic response analysis using direct or substructure approaches. The direct approach represents the SSI system globally as a continuum during the analysis. Figure 1-1 depicts the direct approach using a finite element method where the conventional analysis is expanded beyond just detailed modeling of the structure and foundation elements to include the foundation-soil interface elements, soil elements, and the seismic incident wave interactions. The direct approach of modeling the entire SSI system in one step can be computationally costly.

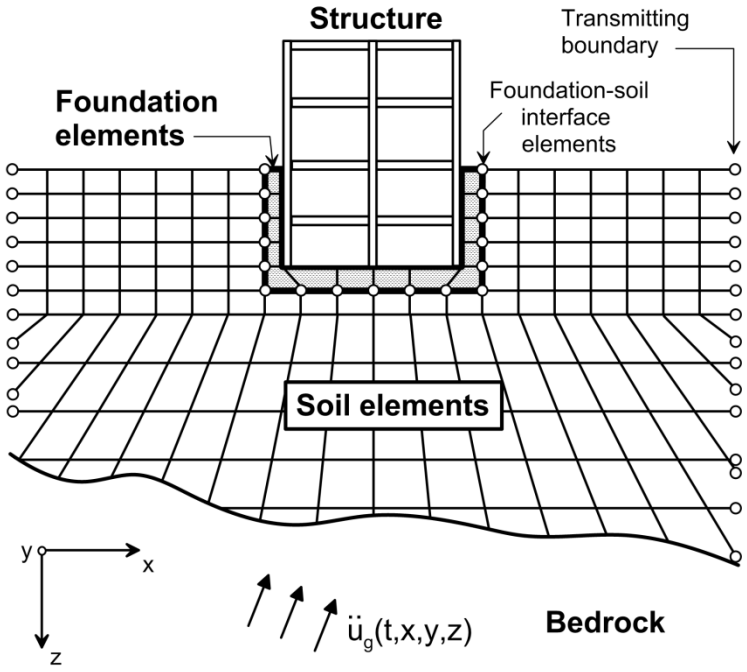

Figure 1-1 Schematic illustration of direct approach to analysis of the soil-structure interaction (SSI) problem using continuum modeling (NIST, 2012).

The substructure approach breaks up the SSI system into several parts (to simplify the analysis) as shown in Figure 1-2. The substructure approach is described below:

a) *Complete System*: The complete soil-foundation-structure system is excited by an incident wave field represented by a free-field ground motion (u_g). Motion u_g refers to ground motion that would occur in the absence of a foundation at the site.

b) *Kinematic Interaction*: A non-embedded rigid foundation excited by vertically propagating seismic incident waves would theoretically experience the motion u_g. However, in reality, incident waves are incoherent and do not propagate vertically. Kinematic interaction refers to the deviation of the foundation motion from the u_g as a result of the foundation's geometry and embedment in the absence of the building and foundation inertial responses (which is considered in Section c below). Kinematic

interaction results from base slab averaging, wave scattering and embedment effects. As a result, the substructure approach uses the modified motion termed a Foundation Input Motion (FIM) for analysis.

c) *Foundation-Soil Flexibility and Damping*: The seismic loading at the foundation level introduces an inertial response into the building which in turn produces base moment, shear, and torsion. These demands produce foundation displacements and rotations that result in a redistribution of forces within the building relative to a fixed-base case (no SSI), altering the building's inertial response. This process is known as inertial interaction and is captured in the substructure approach by using frequency-dependent soil springs and dashpots. Classical solutions for impedance functions (Section 2.2) were developed for the rigid foundation case represented in Figure 1-2 by $\bar{k}_x$ and $\bar{k}_{yy}$ for translation and rocking, respectively. These springs and dashpots can be applied in a simple manner for a rigid foundation (Figure 1-2c.i) or dispersed in a series of springs and dashpots for flexible foundations (Figure 1-2c.ii).

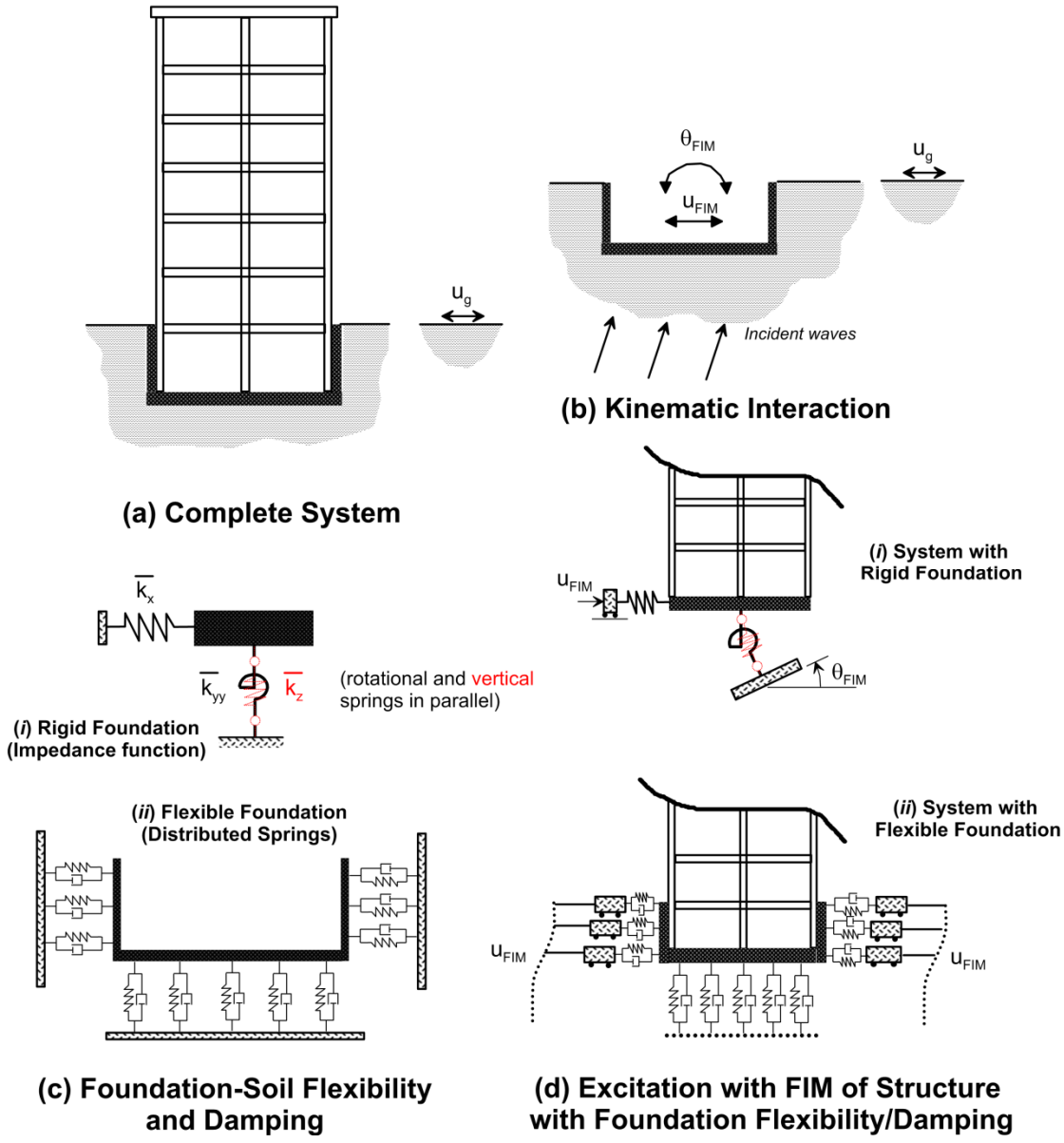

Figure 1-2 **Schematic illustration of substructure approach to analysis of soil-foundation-structure interaction (SFSI) problem using either (i) rigid foundation or (ii) flexible foundation assumption (NIST, 2012).**

d) *Excitation with FIM of Structure with Foundation Flexibility/Damping*: Response history analysis is performed through superposition of the inertial interaction and kinematic interaction effects. The system is excited by the FIM at the end of the

springs, rather than using the u_g. As opposed to the rigid foundation case (Figure 1-2d.i) where springs are excited by a single u_{FIM} and θ_{FIM}, the flexible embedded foundation case (Figure 1-2d.ii) requires multi-support excitation. The multi-support excitation results from site response effects to the u_{FIM} and is commonly determined by a simple equivalent linear ground response analysis.

The substructure approach represents the SSI problem in a simplistic manner. It entails evaluating the SSI effects as two separate components before performing the seismic response analysis. First, the soil elements are represented with frequency-dependent springs and dashpots. Second, the seismic incident wave motion is introduced as a FIM. This approach allows for the two components (representing inertial interaction and kinematic interaction, respectively) to be applied in structural analysis computer software to perform relatively realistic response history analyses of buildings (as compared to fixed-base analysis). The substructure approach does not account for soil nonlinearities introduced by the inertial response (i.e., the spring deflection), which may affect the incoherent demand distribution and impedance. Nonlinearity can be incorporated in an approximate way through the site response (often called primary nonlinearities).

1.3 Research Motivations and Organization

I was a working group member for a National Institute of Standards and Technology (NIST) Task Order 69221 entitled "Improved Procedures for Characterizing and Modeling Soil-Structure Interaction for Performance-Based Seismic Engineering." The task order resulted in the NIST/GCR 12-917-21 report, entitled "Soil-Structure

Interaction for Building Structures," referred to in this document as "NIST report." The NIST report provides a detailed description of analysis methods reflecting the current state of SSI knowledge. My contributions to the NIST report included assistance to the Project Director in SSI literature review and development of publication quality figures presenting SSI concepts, becoming the first user of the NIST report to develop soil springs and dashpots and variable ground motions inputs (FIM and u_g) for problem focused studies (PFS) outlined in the NIST report, evaluation of EDPs that resulted from the PFS, and implementation of review comment changes produced from practitioners and researches at a NIST workshop after a 90% completion of the NIST report.

The SSI system behavior is often represented by period lengthening and damping of a single-degree-of-freedom (SDOF) system, which is used in the design provisions (e.g., FEMA-440, 2005). Whereas the period lengthening effect is relatively straightforward, there is little consistency in the literature on foundation damping. Currently, design provisions such as ASCE-7 (2010) present graphical correlations of period lengthening versus foundation damping that are based on rigid, circular foundations on homogenous soils. There is a need to understand the reasons for the different foundation damping models and then to provide more representative models that account for rectangular shaped foundations. Guidance on how to account for the effects of flexible foundations and heterogeneous soils in the analysis of foundation damping is also needed.

Starting from first principles, we derive fundamental expressions for foundation damping in which foundation impedance components representing radiation damping and

the soil hysteretic damping ratio appear as variables, providing maximum flexibility to the analyst. We utilize these general expressions with impedance solutions for rectangular-footprint foundations to: (1) compare predicted foundation damping levels with those from field case histories and (2) develop new foundation damping relationships for application in the building code (NEHRP Provisions).

Kinematic interaction effects are commonly expressed as transfer functions to represent the foundation to free-field motions. Simplified models for these transfer functions have been distilled from the literature and presented in the NIST report (2012) and ASCE-41. As a result, these models have become widely used, though they have recently been questioned by some researchers. The critiques have argued that the models have predicted unconservative results compared to recorded seismic arrays and therefore should be used 'with caution.' The simplified models were developed from western United States sites with foundation base dimensions of B_e^A=15-40 m (where B_e^A is the square root of the foundation area divided by 4). Data from Japan has recently become available for comparative studies to the existing models. Chapter 3 presents a comparison of the aforementioned models to Japanese data and presents conclusions as to the validity of those models for use in the substructure approach to SSI analysis. Some issues related to kinematical modeling of foundations with heavy pile foundations are identified.

During the development of the NIST (2012) report, an internal baseline knowledge report was completed presenting the state of knowledge for SSI modeling, including proposed procedures for substructure modeling. Problem focused studies (PFS) were undertaken to apply the procedures. A primary goal of the PFS was to shed light on

the relative significance of different elements of the modeling process in the predictions of structural Engineering Demand Parameters (EDPs). PFS of two buildings were completed as part of the NIST report. In an effort to evaluate the effects of SSI components on the dynamic structural response, the PFS included multiple modeling schemes of varying complexity to evaluate the relative significance of various modeling details on the computed EDPs.

I was tasked with developing the soil springs/dashpots and input ground motions for the PFS. The development of the springs/dashpots required a background review of construction drawings and reports containing local geotechnical boring logs and seismic surveys at or close to the sites modeled. Following the review, I was faced with several difficulties including appropriate selection of shear modulus for stiffness values in the presence of embedded structures, how to deal with hybrid foundation systems that have both shallow and deep components, evaluation of the flexibility of the foundation, determination of increased stiffness values at the edges of the foundation, and soil damping modeling. Additionally, the input ground responses were modeled as both the u_g and u_{FIM}. The issue for the PFS was reversed from typical practice in that the u_{FIM} was known and the u_g was back-calculated. During the development of the multi-excitation motions, I encountered phasing issues from the site response analysis (performed with DeepSoil computer software) compared to the original FIM. The PFS are discussed in detail in Chapter 4.

Chapter 5 describes the forced vibration testing of a steel and reinforced concrete structure that was performed to evaluate soil-structure interaction (SSI) systems. Testing

was performed at multiple George E. Brown, Jr. Network for Earthquake Engineering Simulations (NEES) sites. This work has been completed as part of a multi-institutional National Science Foundation (NSF) grand challenge (NSF 06-504 Program) project called, "Mitigation of Collapse Risk in Vulnerable Concrete Buildings." This project has been documented on the Network for Earthquake Engineering Simulations Research (NEESR) website, known as NEEShub, as project NEES-2008-0637. The SSI test series consisted of three test sites with varying degress of base flexibility: University of California, Los Angeles Laboratory (LAB), Wildlife Liquefaction Array (WLA), and Garner Valley Downhole Array (GVDA). The LAB represents an effectively fixed-base condition with structural columns attached to the existing laboratory strong-floor. The WLA site, with a soft clay layer overlying loose, liquefiable sands, and the GVDA site, with firm lake-bed alluvium material, represent flexible base conditions having variable levels of soil stiffness. The three sites were chosen to represent a range of SSI effects based on the foundation conditions with practically no SSI effect expected at the LAB to moderate effects at the GVDA site to a strong SSI influence at the WLA. Chapter 5 presents the details of the experiment performed at the GVDA site, which was my principal contribution to the NEES testing sequence.

Chapter 6 presents an evaluation of SSI effects from forced vibration testing at the GVDA site. As will be shown, a limited number of full-scale field tests have been performed to specifically to evaluate SSI effects for comparison to the existing models. Many full-scale forced vibration tests have been performed; however, when evaluation of SSI effects is not the motivation of the work the responses needed to properly identify

SSI effects are commonly missing. The evaluation of SSI effects on buildings requires the horizontal accelerometers at the free-field, foundation, and roof and two vertical accelerometers on the foundation to evaluate rocking response (Stewart and Fenves, 1998). The structure that was forced with shakers at GVDA was well-instrumented along with a concrete slab and adjacent structure. Chapter 6 presents analysis and interpretations of SSI effects that were ascertained from the field testing at GVDA.

Chapter 7 reviews the scope of the research undertaken in my doctoral studies. I then summarize the principle findings and recommendations of the technical work described in Chapters 2-6. Finally, I provide recommendations for future work based on lessons learned during this research.

2 FOUNDATION DAMPING

2.1 Introduction

The contribution of foundation damping to the overall damping of a soil-foundation-structure system was introduced in the 1970s in seminal studies by Bielak, Veletsos and colleagues. The work was predicated on the need to evaluate the effects of soil-structure interaction (SSI) on the seismic response of nuclear power plants. Based on that need, alternative sets of equations were developed to predict foundation damping of a rigid circular foundation resting on a uniform elastic halfspace. Due in part to the convenience of its application in the specification of seismic demands using response spectrum (force-based) or pushover (displacement-based) methods of analysis, foundation damping has more recently appeared in several seismic design guidelines for building structures (e.g., ASCE-7; ASCE-41). In this chapter, we investigate the alternate assumptions used to derive foundation damping equations. Moreover, considering most foundations are neither circular nor situated on uniform elastic soils, we reevaluate the foundation damping equations to consider various site-specific conditions such as a rectangular footprint, embedment and non-uniform soil conditions.

2.2 Applications of Foundation Damping

In this section, we review the application of foundation damping in force-based and displacement-based methods of analyzing seismic demands in structures.

2.2.1 Foundation Damping in Force-Based Methods

Force-based methods of analysis for seismic demand take the seismic base shear force as the product of pseudo spectral acceleration (PSA) at the first-mode period (normalized by *g*) and the building weight. Within this context, the effect of inertial SSI on the base shear for a building structure is illustrated in Figure 2-1. The PSA for a flexible-based structure $(\tilde{S}_a)$ is obtained by entering the spectrum drawn for flexible-base damping ratio β_0 at the corresponding flexible base period $\tilde{T}$. As indicated in Figure 2-1, both the damping ratio and period are modified from the fixed-base case in which inertial SSI effects are ignored; period is elongated from T (fixed-base) to $\tilde{T}$, while damping β_0 can decrease or increase from the fixed-base value, β_i, although damping increase is more common. For the common case of buildings with relatively long periods on the descending portion of the spectrum, using $\tilde{S}_a$ in lieu of S_a typically reduces base shear demand, whereas in relatively short-period structures SSI can increase the base shear. These modifications of base shear are related to the slope of the spectrum: base shear tends to increase when the slope is positive and decrease when the slope is negative.

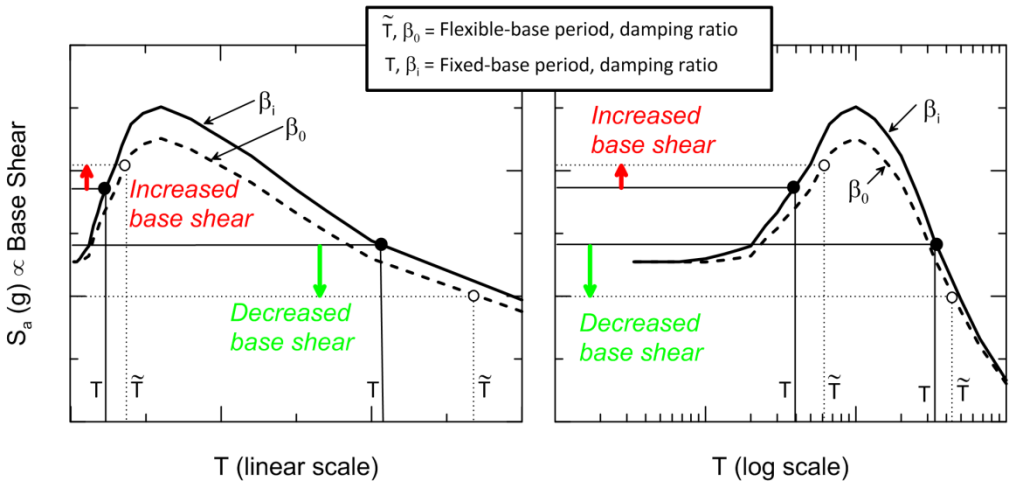

Figure 2-1 **Illustration of effects of period lengthening and change of damping on fundamental mode spectral acceleration from which base shear is evaluated. (NIST, 2012)**

Since the effects of SSI on base shear is related to its impact on fundamental-mode period and damping ratio, simplified procedures have been developed to predict both of these quantities (Veletsos 1977, Stewart et al 2003). Figure 2-2 shows a single-degree-of-freedom (SDOF) oscillator that is useful to visualize the link between foundation compliance and period lengthening. Figure 2-2(a) depicts the fixed-base system having height h and period $T = 2\pi\sqrt{m/k}$, which neglects SSI. Figure 2-2(b) depicts the deformable nature of the soil-foundation system using translational and rotational springs, which enable the base of the structure to displace horizontally and rotate in response to base shear and moment, respectively.

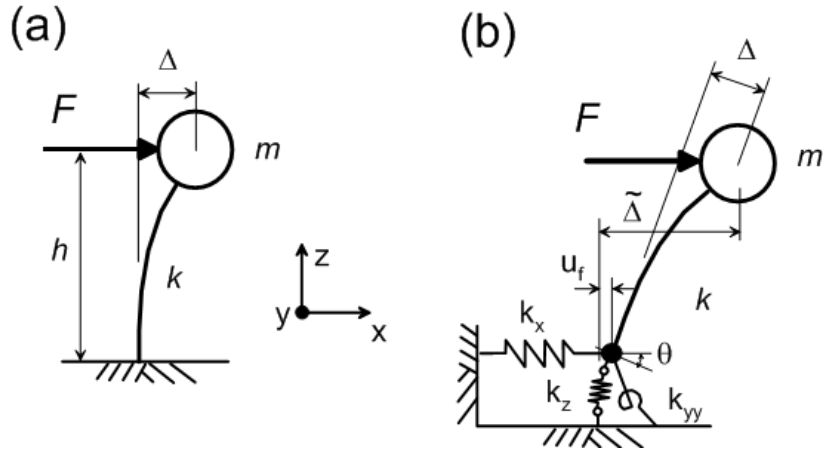

Figure 2-2 **Schematic illustration of deflections caused by force applied to (a) fixed-base structure and (b) structure with horizontal and rotational compliance. (NIST, 2012)**

The springs in Figure 2-2(b) are the real component of complex numbers. Spring k_x represents the horizontal spring stiffness and k_{yy} represents the rotational stiffness against foundation rocking in the *x*-*z* plane. For simplicity, throughout this chapter equations will be adapted to these subscript notations in which horizontal translation is along the *y*-axis (*y*) and rotation is about the *x*-axis (*xx*). The period of the flexible-base structure can be readily computed from the approximate formula (Veletsos and Meek, 1974):

$$\frac{\tilde{T}}{T} = \sqrt{1 + \frac{k}{k_x} + \frac{kh^2}{k_{yy}}} \tag{2-1}$$

where $\tilde{T}/T$ is referred to as the period lengthening ratio.

Foundation damping represents the second necessary component of the SSI modeling to modify the base shear, as depicted in Figure 2-1. As discussed further in

Section 2.2, foundation damping β_f can be related to fixed-base damping β_i and flexible-base damping β_0 as:

$$\beta_f = \beta_o - \frac{1}{\left(\tilde{T}/T\right)^n}\beta_i \tag{2-2}$$

where n is an exponent related to details of the foundation damping derivation, as described in Section 2.2. In practice, β_f is computed using procedures in Section 2.2, and then combined with the β_i term in Eq. (2-2) to compute β_0.

2.2.2 Foundation Damping in Displacement-Based Methods

In displacement-based methods, the system performance is represented by a lateral force-displacement relationship calculated using pushover analyses. As illustrated in Figure 2-3, pushover analyses involve application of static lateral loads distributed over the height of the structure and calculation of the resulting displacements from a model of the SSI system. The cumulative lateral load (resultant H in Figure 2-3) is related to a reference displacement Δ from the nonlinear pushover curve. A point on this diagram defines a damage state in the building, since the deformation of all of the structural components is assumed to be related to the reference displacement. For some applications, the pushover curve is modified to an acceleration-displacement response spectrum (ADRS) by converting H to an equivalent spectral acceleration and by converting Δ to an equivalent spectral displacement (e.g, Chopra and Goel, 1999; Powell, 2006).

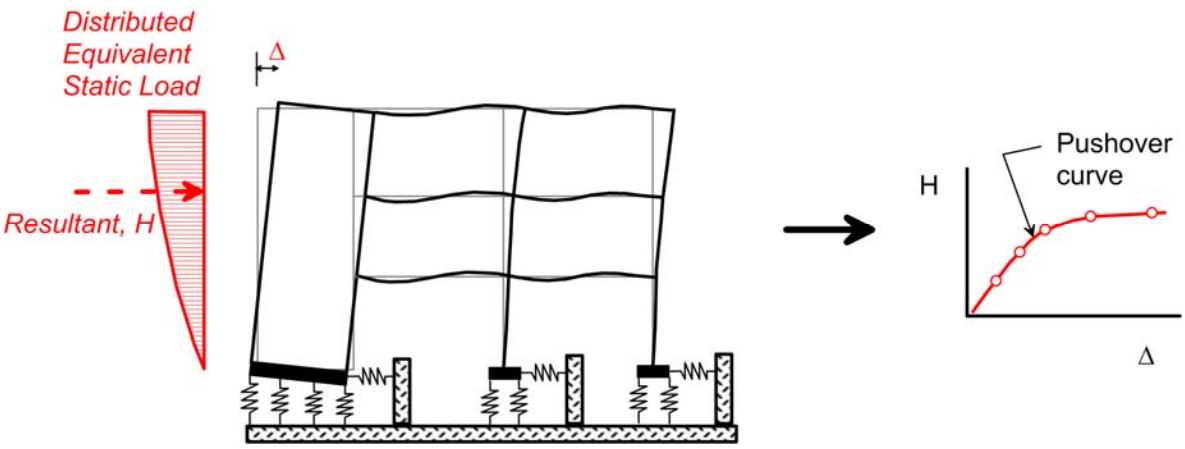

Figure 2-3 Schematic illustration of analysis to develop pushover curve (NIST, 2012)

The expected seismic structural performance is assessed by combining the capacity diagram with an Acceleration-Displacement Response Spectra (ADRS) as illustrated in Figure 2-4. The ADRS represents the seismic demand, and consists of a plot of elastic spectral acceleration (S_a) vs. spectral displacement (S_d). The free-field demand spectrum is reduced twice, first for kinematic interaction effects (Chapter 3), then for the effects of inelastic deformation of the structure and potential damping increase from β_i to β_0. The reduced ADRS is compared to the capacity diagram. The capacity and demand spectra meet at the performance point, which represents the expected structural performance given the seismic demand.

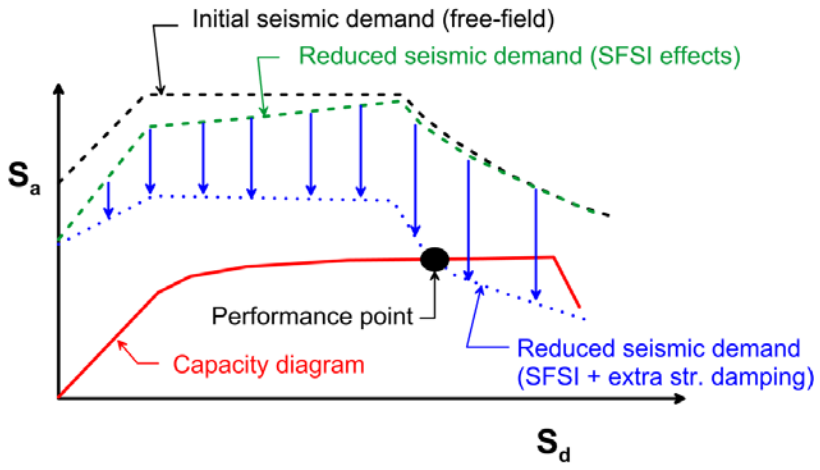

Figure 2-4 **Schematic illustration of SFSI effects on displacement-based method of evaluating nonlinear structural performance.**

SSI enters displacement-based analysis procedures through three components: (1) springs used in pushover analysis; (2) reduction of free-field design spectrum for kinematic interaction; and (3) reduction of design spectrum for SSI system damping ratios β_0 greater than β_i. Hence, the role of foundation damping is similar to force-based methods, in that it is used to scale the response spectrum representing the seismic demand. Procedures similar to these appear in ATC-40, FEMA-440, and ASCE-41 (ATC, 1996; FEMA, 2005; ASCE, 2007, respectively).

2.3 General Solution for Foundation Damping

Most seismic design guidelines utilize the analogy of a replacement oscillator with period $\tilde{T}$ and an adjusted flexible-base damping ratio β_0 in the analysis of seismic demand (e.g., base shear). In the previous section, it was shown how the analysis of foundation damping is integral to evaluating β_0.

Whereas the analysis of period lengthening is relatively straightforward, formulating an analytical solution for foundation damping is more complex, as it requires assessing the relative contributions of hysteretic and radiation damping in multiple modes of foundation vibration. Analytical models for foundation damping of circular foundations have been presented, among others, by Veletsos and Nair (1975), Bielak (1971, 1975, 1976), Roesset (1980), Wolf (1985), and Maravas et al. (2007). These foundation damping models are discussed in the remainder of this section.

2.3.1 Impedance Solutions for Shallow Foundations

The complex-valued impedance functions ($\bar{k}_j$) of a general foundation system in vibration mode j can be expressed as function of the frequency-dependent foundation stiffness (k_j) and dashpot coefficient (c_j) as:

$$\bar{k}_j = k_j + i\omega c_j \tag{2-3}$$

where ω=cyclic frequency (rad/s) and j subscript denotes either the translational (x) or rotational (yy) vibration mode. For circular foundations, translation is often indicated with subscript r and rotation as θ_r.

The real part of the complex-valued springs are denoted k_j (no overbar) and represent ordinary springs. The imaginary part (c_j) accounts for the phase difference (lag) between excitation and response in a harmonically excited damped system, and can be interpreted as viscous damper (c_j). An alternative form for Eq. 2-3 is

$$\bar{k}_j = k_j\left(1 + 2i\beta_j\right) \tag{2-4}$$

where

$$\beta_j = \frac{\omega c_j}{2k_j} \text{ (defined for } k_j > 0) \tag{2-5}$$

An advantage of using β_j over c_j is that at resonance of the SSI system the former can be interpreted as a percentage of critical damping in the classical sense (Clough and Penzien, 1993). The stiffness coefficient (k_j) is a function of the soil shear modulus (G), Poisson's ratio (ν), dynamic stiffness modifier (α_j) and foundation dimension:

$$k_j = K_j \cdot \alpha_j \tag{2-6a}$$

$$\text{Circular foundation: } K_j = Gr^m f(\nu) \quad \alpha_j = f(a_0^r, \nu) \tag{2-6b}$$

$$\text{Rectangular foundation: } K_j = GB^m f\left(B/L, \nu\right) \quad \alpha_j = f(a_0, B/L) \tag{2-6c}$$

$$\text{Circular foundation: } a_0^r = \frac{\omega r}{V_s} \tag{2-7a}$$

$$\text{Rectangular foundation: } a_0 = \frac{\omega B}{V_s} \tag{2-7b}$$

where K_j is the static foundation stiffness at zero frequency for mode j, a_0^r and a_0 are dimensionless frequency parameters, exponent m is 1 for translation (x or r) and 3 for rotation (yy or θ_r), and B and L are foundation plan half-dimensions, as indicated in Figure 2-5. The aforementioned equations are described for circular and rectangular foundations.

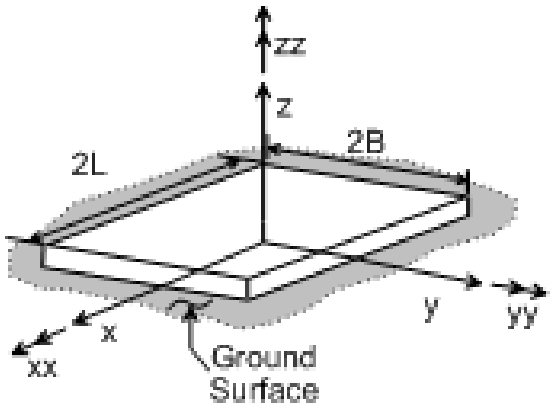

Figure 2-5 Sketch showing the geometry adapted for the rectangular foundation $(L \geq B)$.

Solutions for circular foundation impedance terms in Eq. (2-3) to (2-7) were derived by Luco and Westmann (1971) and Veletsos and Wei (1971) for the condition of rigid circular discs resting on elastic halfspace. The solutions were formulated from numerical analysis of the mixed boundary value problem (i.e., without assuming a particular distribution of tractions or displacement at the soil-footing interface). They worked independently and produced similar results.

Veletsos and Verbic (1973) presented simplified approximate solutions for impedance functions involving circular rigid foundations resting on an elastic or viscoelastic halfspace. Figure 2-6 shows those approximate solutions relative to the elastic solutions for α_j and β_j by Veletsos and Wei (1971) (for Poisson's ratios of 0.45 and 0.33). Results similar to those shown in Figure 2-6 were obtained by Luco (1976), who solved the circular foundation impedance problem for a viscoelastic halfspace, which extends his previous (1971) results for an elastic halfspace. The Veletsos and Verbic (1973) solutions are convenient in that they present closed-form equations that

can directly account for dynamic effects in the impedance functions including soil damping.

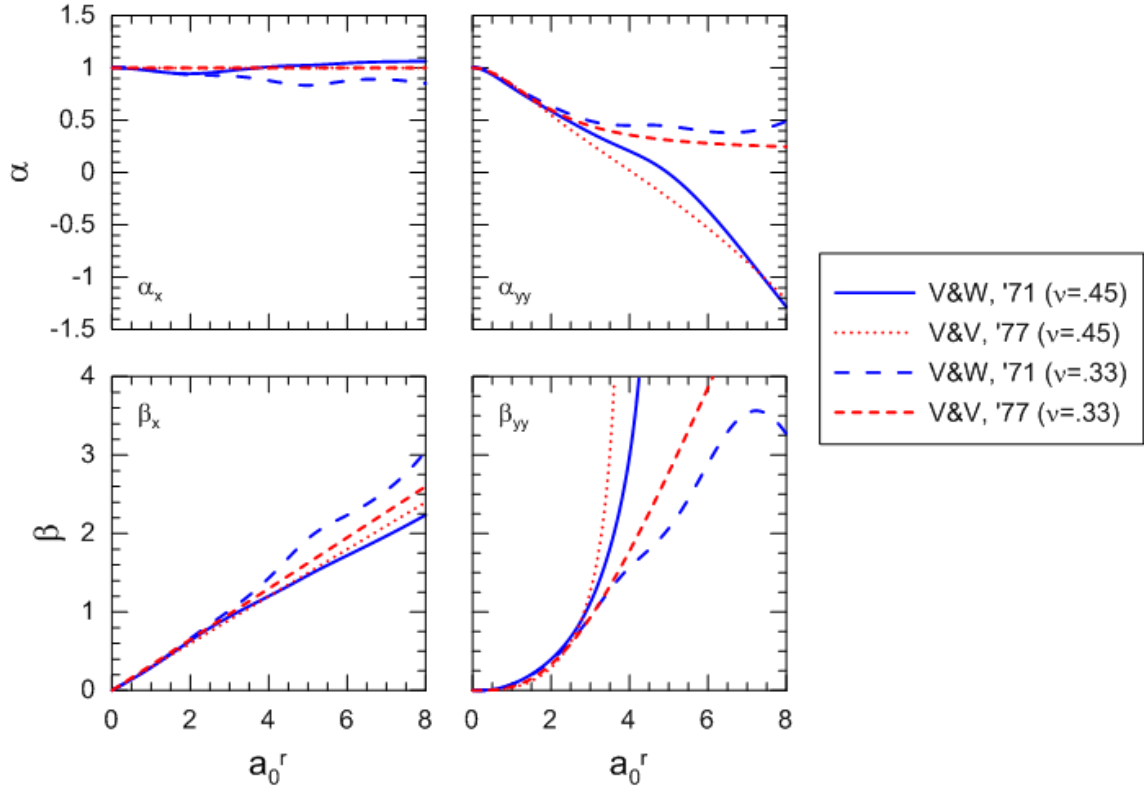

Figure 2-6 **Shows the comparison of the dynamic stiffness modifiers and radiation damping ratios as determined by the numerical data (Veletsos and Wei 1971) and the approximate method (Veletsos and Verbic 1973). Conditions for plots are a rigid, massless, circular disc supported on an elastic homogeneous isotropic halfspace with hysteretic soil damping β_s = 0. ν = 0.45 for a nearly saturated clay and ν = 0.33 for sand.**

The numerical solution and approximate solution trends in Figure 2-6 match fairly well for both soil types from a_0^r = 0 – 2. This is a practical range of analysis, since most foundation excited by an earthquake will have the frequency range of interest fall below

$a_0^r = 2$. Solutions for rectangular foundations are presented subsequently in Section 2.5 as part of our proposed model for foundation damping.

2.3.2 Considerations on the Use of Viscous Structural Damping

As shown in Figure 2-2, structural damping is represented here with damping ratio β_i. The damping ratio is an expression of the decay of oscillations in a system and several models for damping exist. Damping is often taken as either viscous (linearly frequency-dependent) or hysteretic (frequency-independent).

If a viscous damping ratio is assumed, then a modification must be made to the equations in which it appears. A viscous damping ratio for a vibrating system with natural frequency ω_n is defined as (e.g., Chopra, 2011):

$$\beta_i^{vis} = \frac{c_i^{vis}}{2\omega_n m} \tag{2-8}$$

where β_i^{vis} = viscous damping ratio, c_i^{vis} is the viscous dashpot coefficient, and other variables are as given above. The complex-valued structural stiffness can be expressed as follows:

$$\overline{k} = k + i\omega c_i^{vis} = k\left(1 + 2i\frac{\omega c_i^{vis}}{2k}\right) \tag{2-9}$$

From structural dynamics, the undamped natural vibration frequency, ω_n, and period, T, of the structure are given by Clough and Penzien (1993) as:

$$\omega_n = \sqrt{\frac{k}{m}}, \quad T = \frac{2\pi}{\omega_n} = 2\pi\sqrt{\frac{m}{k}} \tag{2-10}$$

Substituting Eq. (2-8) into Eq. (2-9) and recognizing the ω_n definition in Eq. (2-10) provides an expression for the complex-valued structural stiffness with a viscous damping ratio:

$$\bar{k} = k\left(1 + 2i\frac{\omega}{\omega_n}\beta_i^{vis}\right) \tag{2-11}$$

Recall that ω in this expression is the excitation frequency. Recognizing that $\bar{k} = k\left(1 + 2i\beta_i\right)$ and comparing to Eq. (2-11), we see that the general damping ratio β_i can be related to its viscous counterpart as follows:

$$\beta_i = \frac{\omega}{\omega_n}\beta_i^{vis} \tag{2-12a}$$

At resonance, the excitation frequency ω is equivalent to the system frequency, $\tilde{\omega}$, and the above expression can be expressed as:

$$\beta_i = \frac{\tilde{\omega}}{\omega_n}\beta_i^{vis} = \frac{1}{\tilde{T}/T}\beta_i^{vis} \tag{2-12b}$$

Hence, the use of a viscous damping ratio introduces a dependence on period lengthening into the imaginary part of the structural stiffness.

2.3.3 Foundation Damping Derivations

Foundation damping as a distinct component of the damping of a structural system was introduced as part of Bielak's (1971, 1973) derivation of the replacement SDOF system and was later refined by Veletsos and Nair (1975), Roesset (1980) and others. According to this approach, the overall damping of the soil-foundation-structure systems (β_o) can be partitioned into components associated with soil-foundation interaction (including hysteretic and radiation damping), β_f, and damping within the structural system, β_i, by re-arranging Eq. (2-2) as follows:

$$\beta_o = \beta_f + \frac{1}{\left(\widetilde{T}/T\right)^n}\beta_i \tag{2-13}$$

Equation 2-13 appears in many seismic design guidelines with n = 3. As shown in the previous section, the exponent n is dependent on the type of damping (i.e., viscous or general, including hysteretic). Historical precedent and system identification studies often dictate values of β_i in the range of 2-5% in structural design practice for buildings responding in the elastic range (FEMA 440, 2005). Since β_i can be established from such guidelines and period lengthening analysis is relatively straightforward as described in Section 2.2.1, the most challenging aspect of deriving the system damping β_0 is the evaluation of foundation damping β_f.

We consider the SDOF replacement oscillator shown in Figure 2-2(b). The total deflection ($\widetilde{\Delta}$) of a flexible-base oscillator mass (m) at height (h) from the application of a horizontal force (F) results from horizontal deflection of the structural spring and rigid

body displacement of the structural mass from horizontal foundation displacement (u_f) and base rotation (θ).

$$\tilde{\Delta} = \frac{F}{k} + u_f + \theta \cdot h$$
$$\tilde{\Delta} = \frac{F}{k} + \frac{F}{k_x} + \left(\frac{F \cdot h}{k_{yy}} \right) h \tag{2-14}$$

Considering that the replacement oscillator has deflection $\tilde{\Delta}$ in response to force F, the stiffness of the replacement oscillator $\tilde{k}$ can be taken as the ratio of $\tilde{\Delta}$ to F, which leads directly to the period lengthening expression given in Eq. (2-1).

The formulation of the damping component of the equivalent oscillator requires consideration of the imaginary part. Damping results from the phase difference between the real and imaginary parts. We present two derivations for foundation damping. Both begin by dividing the right and left sides of Eq. (2-14) by force F, recognizing that $\tilde{\Delta}/F$ is equivalent to an effective flexible stiffness of the replacement oscillator $\tilde{k}$, and generalizing each term for dynamic loading through the introduction of complex-valued stiffness terms (indicated by an overbar), as follows:

$$\frac{1}{\bar{\tilde{k}}} = \frac{1}{\bar{k}} + \frac{1}{\bar{k}_x} + \frac{h^2}{\bar{k}_{yy}} \tag{2-15a}$$

We present two ways to proceed from Eq. (2-15a) to derive expressions for foundation damping. The first approach (Section 2.3.3.1), which is similar in some respects to prior work by Bielak (1971) and Maravas et al. (2007), separates Eq. (2-15a) into its real and complex parts, then operates exclusively on the imaginary part to evaluate the effective damping of the replacement oscillator. The foundation damping is then readily derived

from the system damping. The second approach (Section 2.3.3.2), which is similar in some respect to prior work by Veletsos and Nair (1975), retains both the real and complex parts of Eq. (2-15a) in the evaluation of expressions for the dynamic properties of the replacement oscillator. The resulting expressions for foundation damping retain complex-valued terms, which are not present in the first approach. Differences between foundation damping predictions derived from the two approaches are presented in Section 2.3.3.3.

2.3.3.1 Derivation from Imaginary Component

The first approach proceeds from (Eq. 2-15a) by expanding each complex stiffness term according to Eq. (2-4):

$$\frac{1}{\tilde{k}\left(1+2i\beta_0\right)} = \frac{1}{k\left(1+2i\beta_i\right)} + \frac{1}{k_x\left(1+2i\beta_x\right)} + \frac{h^2}{k_{yy}\left(1+2i\beta_{yy}\right)} \tag{2-15b}$$

Note that hysteretic soil damping effects are not considered at this stage, but are introduced subsequently. Multiplying and dividing each term by its complex conjugate, neglecting the higher-order damping term (i.e., $\beta^2 \approx 0$), and multiplying both sides by k, we obtain:

$$\frac{k}{\tilde{k}}\left(1-2i\beta_0\right) = \left(1-2i\beta_i\right) + \frac{k}{k_x}\left(1-2i\beta_x\right) + \frac{kh^2}{k_{yy}}\left(1-2i\beta_{yy}\right) \tag{2-16}$$

The equality in Eq. (2-16) requires that both the real and imaginary parts of the expressions on the right and lefts sides of the equal sign be equivalent. Accordingly, we consider the equivalence of the imaginary parts exclusively as follows:

$$\beta_0 = \frac{\tilde{k}}{k}\beta_i + \frac{\tilde{k}}{k_x}\beta_x + \frac{\tilde{k}h^2}{k_{yy}}\beta_{yy} \tag{2-17a}$$

$$\beta_0 = \frac{\tilde{k}}{k}\beta_i + \frac{\tilde{k}}{k}\left(\frac{k}{k_x}\beta_x + \frac{kh^2}{k_{yy}}\beta_{yy}\right) \tag{2-17b}$$

Eq. (2-17b) is convenient in the sense that the flexible-base system damping components are proportional to the stiffness ratio for flexible-base and fixed-base oscillators ($\tilde{k}/k$), which can be related to the period lengthening (Eq. 2-1) when foundation mass is ignored. Using the definitions in Eq. (2-10), period lengthening can be recovered from the stiffness ratio as follows:

$$\frac{\tilde{k}}{k} = \frac{\tilde{k}}{m}\cdot\frac{m}{k} = \frac{\tilde{\omega}^2}{\omega^2} = \frac{\tilde{\omega}^2}{2\pi}\cdot\frac{2\pi}{\omega^2} = \frac{1}{\left(\tilde{T}/T\right)^2} \tag{2-18}$$

Using Eq. (2-18), the flexible-base system damping in Eq. (2-17b) can now be presented as a function of period lengthening:

$$\beta_0 = \frac{1}{\left(\tilde{T}/T\right)^2}\beta_i + \frac{1}{\left(\tilde{T}/T\right)^2}\left(\frac{k}{k_x}\beta_x + \frac{kh^2}{k_{yy}}\beta_{yy}\right) \tag{2-19}$$

To further simplify, we introduce the following fictitious vibration periods, calculated as if the only source of the vibration was foundation translation or rotation, as follows:

$$T_x = 2\pi\sqrt{\frac{m}{k_x}} \quad T_{yy} = 2\pi\sqrt{\frac{mh^2}{k_{yy}}} \tag{2-20}$$

Using Eq. (2-20) and recalling $T = 2\pi\sqrt{m/k}$, term $k/k_x = \left(T_x/T\right)^2$ and $kh^2/k_{yy} = \left(T_{yy}/T\right)^2$. With these substitutions, Eq. (2-19) becomes:

$$\beta_0 = \frac{1}{\left(\tilde{T}/T\right)^2}\beta_i + \frac{1}{\left(\tilde{T}/T_x\right)^2}\beta_x + \frac{1}{\left(\tilde{T}/T_{yy}\right)^2}\beta_{yy} \tag{2-21}$$

Eq. (2-19) and (2-21) have been developed based on the general impedance functions (Eq. 2-3) that considers the damping terms to be non-viscous. Frequency-independent (i.e., hysteretic) soil damping (β_s) can be included in the system by simply adding it to the translational and rotational damping terms (Rosset, 1980, and Wolf, 1985). When this is applied to the damping formulation in Eq. (2-19), we obtain:

$$\beta_0 = \frac{1}{\left(\tilde{T}/T\right)^2}\left[\beta_i + \frac{k}{k_x}\left(\beta_x + \beta_s\right) + \frac{kh^2}{k_{yy}}\left(\beta_{yy} + \beta_s\right)\right] \tag{2-22a}$$

Rearranging Eq. (2-22a) based on the damping terms gives:

$$\beta_0 = \frac{1}{\left(\tilde{T}/T\right)^2}\left[\beta_i + \frac{k}{k_x}\beta_x + \frac{kh^2}{k_{yy}}\beta_{yy} + \left(\frac{k}{k_x} + \frac{kh^2}{k_{yy}}\right)\beta_s\right] \tag{2-22b}$$

The soil damping dependent terms can be further reduced using the real parts of Eq. (2-15a):

$$\frac{1}{\tilde{k}} = \frac{1}{k} + \frac{1}{k_x} + \frac{h^2}{k_{yy}} \tag{2-23a}$$

Factoring out the structural stiffness from the right-side produces:

$$\frac{1}{\tilde{k}} = \frac{1}{k}\left(1 + \frac{k}{k_x} + \frac{kh^2}{k_{yy}}\right) \tag{2-23b}$$

Eq. (2-23b) can be re-written to isolate the terms associated with the soil damping that appear in Eq. (2-22b):

$$\frac{k}{\tilde{k}} - 1 = \frac{k}{k_x} + \frac{kh^2}{k_{yy}} \tag{2-23c}$$

Using the relation between $\tilde{k}/k$ and period lengthening given in Eq. (2-18) and the soil damping dependent terms identified on the right side of Eq. (2-23c), we re-write Eq. (2-22b) as:

$$\beta_0 = \frac{1}{\left(\tilde{T}/T\right)^2} \cdot \left[\beta_i + \frac{k}{k_x}\beta_x + \frac{kh^2}{k_{yy}}\beta_{yy} + \left(\left(\tilde{T}/T\right)^2 - 1\right)\beta_s \right] \tag{2-24a}$$

Recognition of the steps taken from Equations 2-19 through 2-21 produces the following expression for flexible-base system damping:

$$\beta_0 = \frac{1}{\left(\tilde{T}/T\right)^2}\beta_i + \left[1 - \frac{1}{\left(\tilde{T}/T\right)^2}\right]\beta_s + \frac{1}{\left(\tilde{T}/T_x\right)^2}\beta_x + \frac{1}{\left(\tilde{T}/T_{yy}\right)^2}\beta_{yy} \tag{2-24b}$$

The foundation damping then becomes:

$$\beta_f = \left[1 - \frac{1}{\left(\tilde{T}/T\right)^2}\right]\beta_s + \frac{1}{\left(\tilde{T}/T_x\right)^2}\beta_x + \frac{1}{\left(\tilde{T}/T_{yy}\right)^2}\beta_{yy} \tag{2-25}$$

This is the same expression given for general application in a pending national guideline developed in the course of this research (NIST, 2012). The advantage of the last expression over earlier formulations in the literature lies in the nature of the dimensionless multipliers of damping terms, which can be interpreted as weight factors. Indeed neglecting the additional contributions of radiation damping, the sum of the two factors multiplying β_i and β_s terms is unity.

2.3.3.2 Derivation from Complex-Valued Impedance Expressions

Our second derivation of foundation damping retains the complex-valued form of (Eq. 2-15a), but also utilizes the principal described in the prior section that both the real and imaginary parts of the expression must hold. Specifically, this derivation utilizes the equality of the real-valued terms as shown previously in Eq. (2-23). Minor re-arrangement of the real term (Eq. 2-23) and the complex form (Eq. 2-15a) gives:

$$\frac{1}{\tilde{k}} - \frac{1}{k} = \frac{1}{k_x} + \frac{h^2}{k_{yy}} \tag{2-26a}$$

$$\frac{1}{\bar{\tilde{k}}} - \frac{1}{\bar{k}} = \frac{1}{\bar{k}_x} + \frac{h^2}{\bar{k}_{yy}} \tag{2-26b}$$

The left-side of Eq. (2-26b) can be expanded to include the real and imaginary terms (per Eq. 2-4), and then multiplied by the complex conjugate, to produce:

$$\frac{1}{\bar{\tilde{k}}} - \frac{1}{\bar{k}} = \frac{1-2i\beta_0}{\tilde{k}} - \frac{1-2i\beta_i}{k} \tag{2-27}$$

Eq. (2-27) is re-written by isolating the complex terms on the right side and using the relations in Eq. (2-26) as:

$$-2i\left(\frac{\beta_0}{\tilde{k}} - \frac{\beta_i}{k}\right) = \left(\frac{1}{\bar{k}_x} - \frac{1}{k_x}\right) + \left(\frac{1}{\bar{k}_{yy}} - \frac{1}{k_{yy}}\right)h^2 \tag{2-28a}$$

Reducing the right side of Eq. (2-28a) for common denominators provides:

$$\left(\frac{1}{\bar{k}_x} - \frac{1}{k_x}\right) + \left(\frac{1}{\bar{k}_{yy}} - \frac{1}{k_{yy}}\right)h^2 = \left(\frac{k_x - \bar{k}_x}{\bar{k}_x k_x}\right) + \left(\frac{k_{yy} - \bar{k}_{yy}}{\bar{k}_{yy} k_{yy}}\right)h^2 \tag{2-28b}$$

The right side of Eq. (2-28b) can be re-written by expanding the complex-valued impedance terms in the numerator to include their real and complex parts per Eq. (2-4) as:

$$\left(\frac{k_x-\bar{k}_x}{\bar{k}_x k_x}\right)+\left(\frac{k_{yy}-\bar{k}_{yy}}{\bar{k}_{yy}k_{yy}}\right)h^2 = \left(\frac{k_x-k_x\left(1+2i\beta_x\right)}{\bar{k}_x k_x}\right)+\left(\frac{k_{yy}-k_{yy}\left(1+2i\beta_{yy}\right)}{\bar{k}_{yy}k_{yy}}\right)h^2 = \frac{-2i\beta_x}{\bar{k}_x}+\frac{-2i\beta_{yy}h^2}{\bar{k}_{yy}} \tag{2-28c}$$

Equating the left side of Eq. (2-28a) to the right side of Eq. (2-28c) produces:

$$-2i\left(\frac{\beta_0}{\tilde{k}}-\frac{\beta_i}{k}\right)=-2i\left(\frac{\beta_x}{\bar{k}_x}+\frac{\beta_{yy}h^2}{\bar{k}_{yy}}\right) \tag{2-29a}$$

Dividing through by -2i, multiplying through by $\tilde{k}$, and moving the β_i term to the right side produces:

$$\beta_0=\frac{\tilde{k}}{k}\beta_i+\frac{\tilde{k}}{\bar{k}_x}\beta_x+\frac{\tilde{k}h^2}{\bar{k}_{yy}}\beta_{yy}=\frac{\tilde{k}}{k}\beta_i+\frac{\tilde{k}}{k}\left(\frac{k}{\bar{k}_x}\beta_x+\frac{kh^2}{\bar{k}_{yy}}\beta_{yy}\right) \tag{2-29b}$$

Recalling the relationship between $\tilde{k}/k$ and $\left(\tilde{T}/T\right)^2$ in Eq. (2-18), we obtain:

$$\beta_0=\frac{1}{\left(\tilde{T}/T\right)^2}\beta_i+\frac{1}{\left(\tilde{T}/T\right)^2}\left(\frac{k}{\bar{k}_x}\beta_x+\frac{kh^2}{\bar{k}_{yy}}\beta_{yy}\right) \tag{2-30}$$

Eq. (2-30) matches Eq. (2-19) with the exception that the horizontal and rotational impedance terms within the brackets have gone from real-valued to complex-valued. As with the first derivation, we introduce hysteretic soil damping at this stage:

$$\beta_0=\frac{1}{\left(\tilde{T}/T\right)^2}\beta_i+\frac{1}{\left(\tilde{T}/T\right)^2}\left(\frac{k}{\bar{k}_x}\left(\beta_x+\beta_s\right)+\frac{kh^2}{\bar{k}_{yy}}\left(\beta_{yy}+\beta_s\right)\right) \tag{2-31}$$

It should be noted that the impedance functions as written in Eqs. 2-3 and 2-4 do not include soil hysteretic damping. As we have shown, the soil damping effect can be accounted for by adding β_s to the respective radiation damping ratios β_x and β_{yy}. This addition should also be performed within the imaginary term of the complex-valued impedance functions as follows:

$$\bar{k}_j = k_j\left[1 + 2i\left(\beta_j + \beta_s\right)\right] \tag{2-32}$$

As with the first derivation, we introduce fictitious vibration periods, which are now complex-valued:

$$\bar{T}_x = 2\pi\sqrt{\frac{m}{\bar{k}_x}} \quad \bar{T}_{yy} = 2\pi\sqrt{\frac{m}{\bar{k}_{yy}}} \tag{2-33}$$

Using Eq. (2-33) and recalling $T = 2\pi\sqrt{m/k}$, term $k/\bar{k}_x = \left(\bar{T}_x/T\right)^2$ and $kh^2/\bar{k}_{yy} = \left(\bar{T}_{yy}/T\right)^2$. With these substitutions, Eq. (2-30) (the case without hysteretic soil damping) becomes:

$$\beta_0 = \frac{1}{\left(\tilde{T}/T\right)^2}\beta_i + \frac{1}{\left(\tilde{T}/\bar{T}_x\right)^2}\beta_x + \frac{1}{\left(\tilde{T}/\bar{T}_{yy}\right)^2}\beta_{yy} \tag{2-34a}$$

Likewise, Eq. (2-31) (the case with hysteretic soil damping) becomes:

$$\beta_0 = \frac{1}{\left(\tilde{T}/T\right)^2}\beta_i + \frac{1}{\left(\tilde{T}/\bar{T}_x\right)^2}\left(\beta_x + \beta_s\right) + \frac{1}{\left(\tilde{T}/\bar{T}_{yy}\right)^2}\left(\beta_{yy} + \beta_s\right) \tag{2-34b}$$

A general expression for foundation damping can then be written as:

$$\beta_f = \frac{1}{\left(\tilde{T}/\bar{T}_x\right)^2}\left(\beta_x + \beta_s\right) + \frac{1}{\left(\tilde{T}/\bar{T}_{yy}\right)^2}\left(\beta_{yy} + \beta_s\right) \tag{2-35}$$

The solution of foundation damping is complex-valued; the amplitude of the complex number is usually taken for application (Veletsos and Nair, 1975).

2.3.3.3 Comparison of Alternate Solutions for Foundation Damping

On theoretical grounds, there is no clear benefit of one of the aforementioned foundation damping solutions over the other. The two expressions for foundation damping are given in Eqs. (2-25) and (2-35). A practical benefit of the first solution is that it is expressed entirely in terms of real-valued variables, whereas the second includes complex variables that produce a complex-valued foundation damping that is relatively difficult to understand.

In Figure 2-7, we plot foundation damping derived from the two solutions against the ratio $\left(h/(V_s T)\right)$, which is often called the wave parameter (Veletsos, 1977). The wave parameter can be thought of as a structure-to-soil stiffness ratio because $\left(h/T\right)$ represents the stiffness of a structure's lateral force resisting system in velocity units whereas soil shear wave velocity V_s is related to the soil shear stiffness. In Figure 2-7, foundation damping solutions are given for circular foundations and various structure height aspect ratios (*h/r*). Translation modes of foundation vibration dominate for small height aspect ratios (< 1), and rocking dominates for larger height aspect ratios (> 2). Veletsos and Wei (1971) impedance functions were used for the two sets of solutions shown in Figure 2-7.

Figure 2-7 shows foundation damping results for the cases of radiation damping only (Figure 2-7a; β_s=0) and combined radiation and hysteretic soil damping (Figure 2-

7b; β_s=0.1). The solution from the first approach (derived from the imaginary component) produces higher damping, particularly for small height aspect ratios. Otherwise, the solutions show well-known patterns of behavior, in particular:

- As $h/(V_sT)$ increases, the significance of inertial SSI increases, causing increased foundation damping;
- As h/r increases, rotational modes of foundation vibration become more dominant, which reduces foundation damping because foundation rotation produces less radiation damping than foundation translation;
- The effects of hysteretic soil damping scale with the significance of inertial SSI, as measured for example by $h/(V_sT)$. For low $h/(V_sT)$, hysteretic damping has little effect (zero at $h/(V_sT) = 0$), whereas at high $h/(V_sT)$ the foundation damping is nearly the sum of foundation damping from radiation damping and β_s.

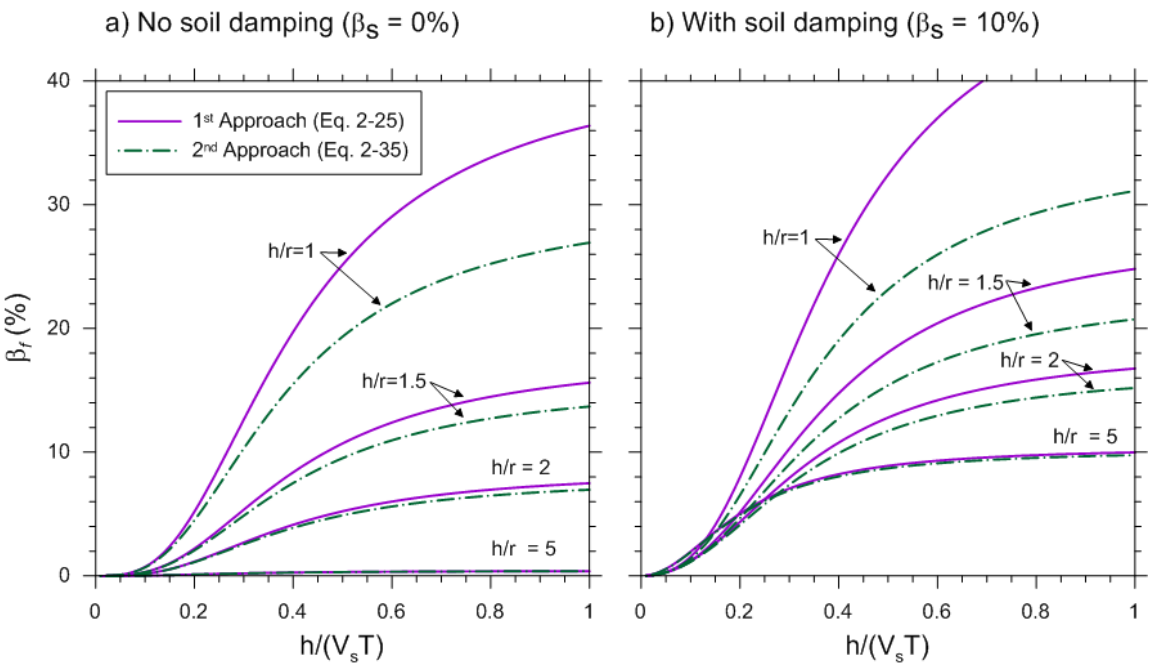

Figure 2-7 **Comparison of foundation damping solutions based on the two approaches from Section 2.3.3, plotted against structure-to-soil stiffness ratio ($h/(V_sT)$). Conditions for the plots are a rigid, massless, circular disc supported on an homogeneous isotropic halfspace with hysteretic soil damping a) β_s = 0% and b) β_s = 10%. ν = 0.33. Impedance functions from Veletsos and Wei (1971) used to derive the foundation damping.**

2.4 Comparison to Foundation Damping Solutions in Literature

2.4.1 Bielak (1971) Solution

Bielak's (1971) derived an expression for foundation damping by identifying the dynamic properties of a replacement fixed-based oscillator to match those of the flexible-base oscillator shown in Figure 2-2(b). In the derivation, the foundation mass and mass moment of inertia were taken as negligible (as above), the structural damping was considered to be viscous, the foundation was assumed circular with a radius *r*, and the

higher-order damping terms were neglected. The viscous damping assumption for the structure was made for the sake of computational efficiency.

Bielak's derivation is similar to the approach presented in Section 2.3.3.1 in which the damping is derived by equating the imaginary parts of the stiffness terms in the replacement oscillator and flexible-base system. As such, the Bielak derivation mirrors that in Section 2.3.3.1 up to Eq. (2-19). However Bielak makes the specific assumption of viscous structural damping, which requires modification of the structural damping ratio as given in Eq. (2-12). With the substitution of β_i^{vis} for β_i in Eq. (2-19), we obtain:

$$\beta_0 = \frac{1}{\left(\tilde{T}/T\right)^3}\beta_i^{vis} + \frac{1}{\left(\tilde{T}/T\right)^2}\left(\frac{k}{k_x}\beta_x + \frac{kh^2}{k_{yy}}\beta_{yy}\right) \tag{2-36}$$

Eq. (2-36) matches Eq. (3.66c) in Bielak (1971), except the nomenclature has been adapted to be consistent with this work and periods instead of frequencies have been used. The foundation damping (β_f) is then taken from the damping components unrelated to structural damping as follows:

$$\beta_f = \frac{1}{\left(\tilde{T}/T\right)^2}\left(\frac{k}{k_x}\beta_x + \frac{kh^2}{k_{yy}}\beta_{yy}\right) \tag{2-37}$$

System damping solutions incorporating viscous structural damping (Eq. 2-36) are used in current force-based seismic provisions (e.g., BSSC, 2009). To the extent that actual structural damping is not purely viscous, the expression in Eq. (2-36) can be considered as an approximation to the true flexible-base system damping (Eq. 2-24b or 2-

34b). If the exponent n on the period lengthening terms is taken as 2 instead of 3, the more general expressions given in Section 2.3.3 are recovered.

2.4.2 Veletsos and Nair (1975) Solution

Veletsos and Nair (1975) derived an expression for foundation damping by equating amplitudes of responses between the real parts of the flexible-base system and those of the replacement oscillator. Their derivation utilized the full complex form of stiffness terms in equating the stiffness of the replacement oscillator to that of the flexible-base oscillator, which is similar to the second approach described in Section 2.3.3.2 above. Assumptions similar to those of Bielak (1971) were made regarding the properties of the replacement oscillator (i.e., viscous damping, negligible foundation mass, etc.). The Veletsos and Nair damping terms can be derived using a process matching that in Section 2.3.3.2 with the exception of two deviations.

The first deviation is that Veletsos and Nair (1975) used viscous structural damping. As in the prior section, in the equation of system damping (e.g. Eq. 2-36), this converts to 3 the exponent on the period lengthening applied to structural damping.

The second deviation concerns the incorporation of hysteretic soil damping into the solution. The simple addition of β_s to radiation damping terms applied in Section 2.3.3 represents an approximate solution to mathematically complex problem of how these damping terms interact. For example, an integral equation approach to this problem is presented by Apsel and Luco (1987) (their result is a numerical solution, not a closed-form equation). Veletsos and Nair (1975) use an approximate solution to this problem by Veletsos and Verbic (1973) (the approximation is in the fitting of the dynamic impedance

coefficients for the case of zero soil damping with simple closed for expressions, along with an assumption of real-valued Poisson's ratio). In the Veletsos and Verbic solution, the soil damping appears as a term in a series of equations used to derive dynamic modifiers in the general equations for foundation impedance (α_j and β_j in Eq. 2-6 and 2-4, respectively).

These two deviations have little impact on the damping solution given in Section 2.3.3.2, and the derived system damping, given below, is very similar to that in Eq. (2-30):

$$\beta_0 = \frac{1}{\left(\widetilde{T}/T\right)^3}\beta_i^{vis} + \frac{1}{\left(\widetilde{T}/T\right)^2}\left(\frac{k}{\bar{k}_x}\beta_x + \frac{kh^2}{\bar{k}_{yy}}\beta_{yy}\right) \tag{2-38}$$

The only differences between Eq. (2-38) and Eq. (2-30) are in the structural damping terms (due to the use of viscous damping) and in the form of impedance function terms $\bar{k}_x$ and $\bar{k}_{yy}$. Note that Eq. (2-38) is used with or without soil damping; the effect of including soil damping is confined to its effect on the impedance.

In Figure 2-8 we show the effect of the different approaches for incorporating hysteretic soil damping β_s into the solution. As a baseline case, we show the predicted foundation damping for $\beta_s = 0.1$ using the second approach given in Section 2.3.3.2 (Eq. 2-35). For the baseline calculation, radiation damping terms were computed using the closed form expressions given in Veletsos and Verbic (1973) for the elastic medium (i.e., radiation damping only, or $\beta_s = 0$), and hysteretic damping was added to radiation damping ratios as described in Section 2.3.3. We also show the foundation damping

obtained using Eq. (2-38) with the Veletsos and Verbic (1973) solution for impedance terms on a visco-elastic medium. Similar results are found in Figure 2-8 for both approaches of accounting for soil damping. The results slightly diverge as $h/(V_s T)$ increases, with the exception of the largest height aspect ratio shown $(h/r = 5)$.

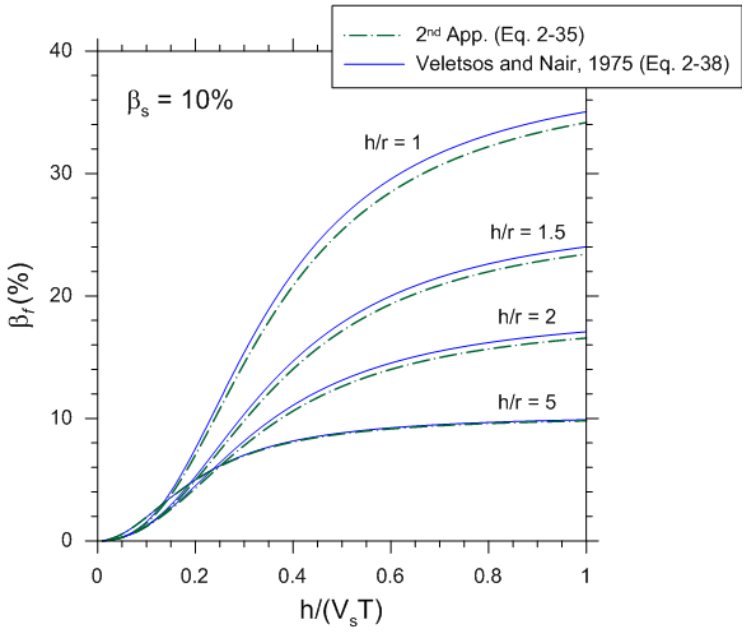

Figure 2-8 **Comparison of foundation damping models (Eq. 2-35 and Eq. 2-38) accounting for soil damping (β_s = 10%) differently, plotted against structure-to-soil stiffness ratio ($h/(V_S T)$). Conditions for the plot are a rigid, massless, circular disc supported on an elastic homogeneous isotropic halfspace with hysteretic soil damping β_s = 10 %. ν = 0.33. Impedance functions from Veletsos and Verbic (1973) were used to derive the foundation damping. Eq. 2-35 used Veletsos and Verbic (1973) elastic impedance solution with additive soil damping, whereas Eq. 2-38 uses an alternative impedance solution in which soil damping for a visco-elastic medium is incorporated into the solution.**

2.4.3 Roesset (1980) and Wolf (1985) Solutions

Roesset's (1980) presented a foundation damping solution in which the imaginary component of the replacement oscillator stiffness is matched to that of the flexible-base system. He also used a general (non-viscous) damping formulation for the structural stiffness and similar assumptions to other investigators, so the derivation matches that given in Section 2.3.3.1. Using our nomenclature, Roesset expressed the foundation damping as:

$$\beta_f = \left[1 - \frac{1}{\left(\widetilde{T}/T\right)^2}\beta_s\right] + \frac{1}{\left(\widetilde{T}/T\right)^2}\left(\frac{k}{k_x}\beta_x + \frac{kh^2}{k_{yy}}\beta_{yy}\right) \tag{2-39}$$

The derivation of Wolf (1985) matches that of Roesset (1980), except that the fictitious vibration periods given in Section 2.3.3.1 ($T_x = 2\pi\sqrt{m/k_x}$ and $T_{yy} = 2\pi\sqrt{mh^2/k_{yy}}$) are introduced to re-write the foundation damping in the form given in Eq. (2-25).

2.4.4 Maravas et al. (2007) Solution

Recognizing the previous solutions as approximate, Maravas et al. (2007) developed an exact solution for foundation damping of rigid circular foundations. The derivation begins by using the complex-valued impedance functions of the replacement oscillator represented by Eq. (2-15). Multiplying each term by the complex-conjugate, without ignoring the higher-order damping terms results in:

$$\frac{\left(1-2i\beta_0\right)}{\tilde{k}\left(1+4\beta_0^2\right)}=\frac{\left(1-2i\beta_i\right)}{k\left(1+4\beta_i^2\right)}+\frac{\left(1-2i\beta_x\right)}{k_x\left(1+4\beta_x^2\right)}+\frac{h^2\left(1-2i\beta_{yy}\right)}{k_{yy}\left(1+4\beta_{yy}^2\right)} \tag{2-40}$$

Eq. (2-40) can be separated into real and imaginary parts as follows:

$$\frac{1}{\tilde{k}\left(1+4\beta_0^2\right)}=\frac{1}{k\left(1+4\beta_i^2\right)}+\frac{1}{k_x\left(1+4\beta_x^2\right)}+\frac{h^2}{k_{yy}\left(1+4\beta_{yy}^2\right)} \tag{2-41a}$$

$$\frac{\beta_0}{\tilde{k}\left(1+4\beta_0^2\right)}=\frac{\beta_i}{k\left(1+4\beta_i^2\right)}+\frac{\beta_x}{k_x\left(1+4\beta_x^2\right)}+\frac{h^2\beta_{yy}}{k_{yy}\left(1+4\beta_{yy}^2\right)} \tag{2-41b}$$

Recognizing that the term $\tilde{k}\left(1+4\beta_0^2\right)$ exists in both the real and imaginary part of the solution, the foundation damping can be established by first rearranging the real part (Eq. 2-41a) as

$$\tilde{k}\left(1+4\beta_0^2\right)=\frac{1}{\frac{1}{k\left(1+4\beta_i^2\right)}+\frac{1}{k_x\left(1+4\beta_x^2\right)}+\frac{h^2}{k_{yy}\left(1+4\beta_{yy}^2\right)}} \tag{2-42a}$$

Secondly, both sides of the imaginary part (Eq. 2-41b) are multiplied by $\tilde{k}\left(1+4\beta_0^2\right)$ to get an expression for the flexible-base system damping:

$$\beta_0=\tilde{k}\left(1+4\beta_0^2\right)\cdot\left[\frac{\beta_i}{k\left(1+4\beta_i^2\right)}+\frac{\beta_x}{k_x\left(1+4\beta_x^2\right)}+\frac{h^2\beta_{yy}}{k_{yy}\left(1+4\beta_{yy}^2\right)}\right] \tag{2-42b}$$

The flexible-base system damping is then formulated by inserting the right side of Eq. (2-42a) into Eq. (2-42b) and multiplying the numerator and denominator by *k*:

$$\beta_0 = \frac{\dfrac{\beta_i}{\left(1+4\beta_i^2\right)} + \dfrac{k}{k_x}\dfrac{\beta_x}{\left(1+4\beta_x^2\right)} + \dfrac{kh^2}{k_{yy}}\dfrac{\beta_{yy}}{\left(1+4\beta_{yy}^2\right)}}{\dfrac{1}{\left(1+4\beta_i^2\right)} + \dfrac{k}{k_x}\dfrac{1}{\left(1+4\beta_x^2\right)} + \dfrac{kh^2}{k_{yy}}\dfrac{1}{\left(1+4\beta_{yy}^2\right)}} \tag{2-44}$$

It should be noted that soil hysteretic damping β_s can be directly added into the radiation damping terms β_x and β_{yy} in Eq. (2-43). Foundation damping can be determined from the Maravas et al. (2007) system damping (Eq. 2-43) from a back-calculation of Eq. (2-13) with n=2.

The exact solution for the period lengthening can be established as a function of the system damping (Eq. 2-42) based on a re-expression of the real part of the derivation (Eq. 2-41a) as:

$$\frac{\widetilde{T}}{T} = \sqrt{\frac{\left(1+4\beta_i^2\right)}{\left(1+4\beta_0^2\right)} \cdot \left[1 + \frac{k}{k_x}\frac{\left(1+4\beta_i^2\right)}{\left(1+4\beta_x^2\right)} + \frac{kh^2}{k_{yy}}\frac{\left(1+4\beta_i^2\right)}{\left(1+4\beta_{yy}^2\right)}\right]^{-1}} \tag{2-44}$$

Figure 2-9 shows the aforementioned foundation damping model and the two approaches discussed in Section 2.3.3 compared to the structure-to-soil stiffness ratio $\left(h/V_sT\right)$. The cases of radiation damping only (Figure 2-9a; β_s=0) and combined radiation and hysteretic soil damping (Figure 2-9b; β_s=0.1) are shown for rigid circular foundations. Figure 2-9 uses Veletsos and Wei (1971) impedance functions for an elastic halfspace, with the soil damping being added to the radiation damping terms. At small structure-to-soil ratios $\left(h/V_sT \le 0.3\right)$ the exact solution of Maravas et al. (2007) tends to match Eq. (2-35). As the ratio increases $\left(h/V_sT > 0.3\right)$ for the small height aspect ratios

$(h/r < 2)$ the damping trend follows Eq. (2-25) and yields more foundation damping than Eq. (2-35).

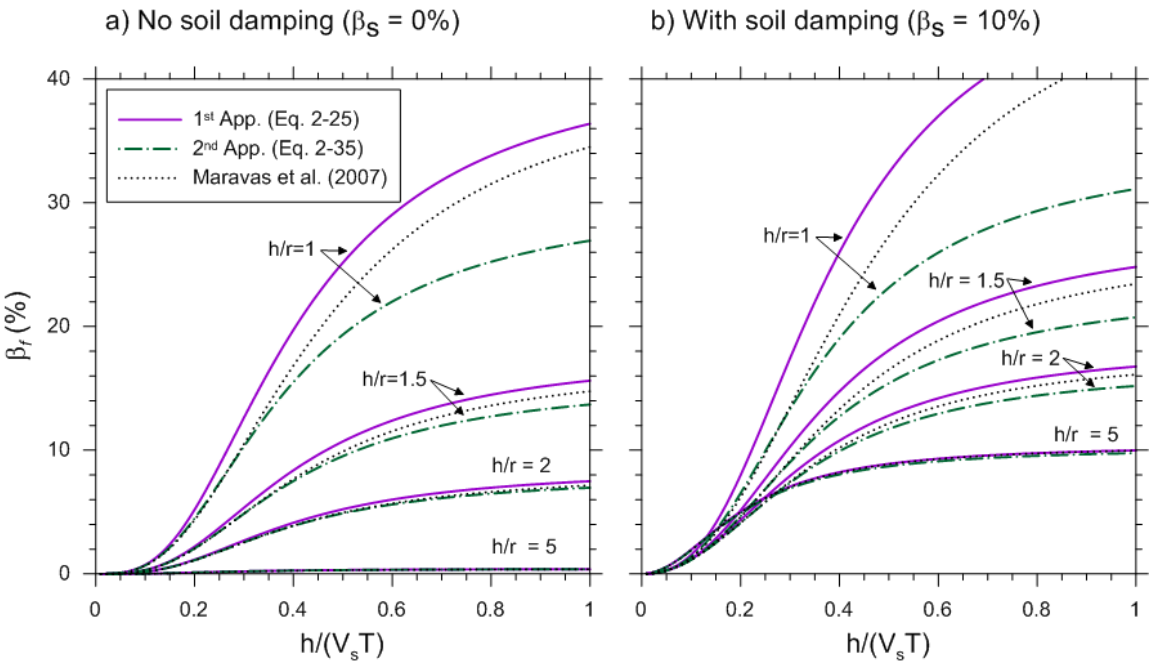

Figure 2-9 **Comparison of the foundation damping models for the two proposed formulations and the exact solution of Maravas et al. (2007). All results shown in the figure are based on the Veletsos and Wei (1971) impedance model for a rigid, massless, circular disc supported on an elastic homogeneous isotropic halfspace with ν = 0.33 and a) β_s = 0% and b) β_s = 10%.**

2.4.5 Relating Foundation Damping to Period Lengthening

Because both period lengthening and foundation damping are related to similar impedance terms, Veletsos (1977) proposed to simplify the analysis of foundation damping to a relationship between $\tilde{T}/T$ and β_f. This simplified approach has been retained in more recent seismic guidelines (e.g., ASCE 7, 2006 & 2010, FEMA 450, 2003 and FEMA P-750, 2009) with the solution always derived for the case of circular foundations using the Veletsos and Nair (1975) foundation damping equations with the

Veletsos and Verbic (1973) approximate impedance functions. In the most recent provisions (ASCE 7-10, 2010 and FEMA P-750, 2009), the Veletsos and Nair (1975) solution (Eq. 24 of their paper) was implemented with a programming bug in which an a_0 term was taken at the fixed-base frequency instead of the flexible-base frequency, which caused the foundation damping to be underestimated for large values of $h/(V_s T)$ or $\tilde{T}/T$. This has been corrected in the present formulation.

The seismic provisions include the effects of soil hysteretic damping and strain-reduction by relating it to the peak short period design spectral response acceleration parameter, S_{DS}. S_{DS} is the peak spectral response acceleration value used for earthquake design loads. The S_{DS} parameter is based on site conditions and the maximum considered earthquake (MCE) ground motion. S_{DS} is roughly proportional to the expected strain demands and hence damping in the underlying foundation soils. Recognition of this relationship led to its use in seismic provisions for modification of a buildings system damping to include the approximate effects of hysteretic soil damping.

Figure 2-10 shows the graphical solutions provided in previous (Figure 2-10a) and current (Figure 2-10b) seismic guidelines. The graphical solutions present unique solutions for specific height aspect ratios and S_{DS} relationships using a Poisson's ratio of 0.33. Linear interpretation is recommended for determination of values between height aspect ratios and S_{DS} values. To error conservatively, seismic provisions limit the amount of overall damping for analysis to not be less than 5% and not greater than 20%. Comparing the previous provisions (Figure 2-10a) to current provisions (Figure 2-10b) shows reduced foundation damping for low aspect ratio structures in the current

provisions. New relationships for foundation damping are recommended in a subsequent section of this chapter.

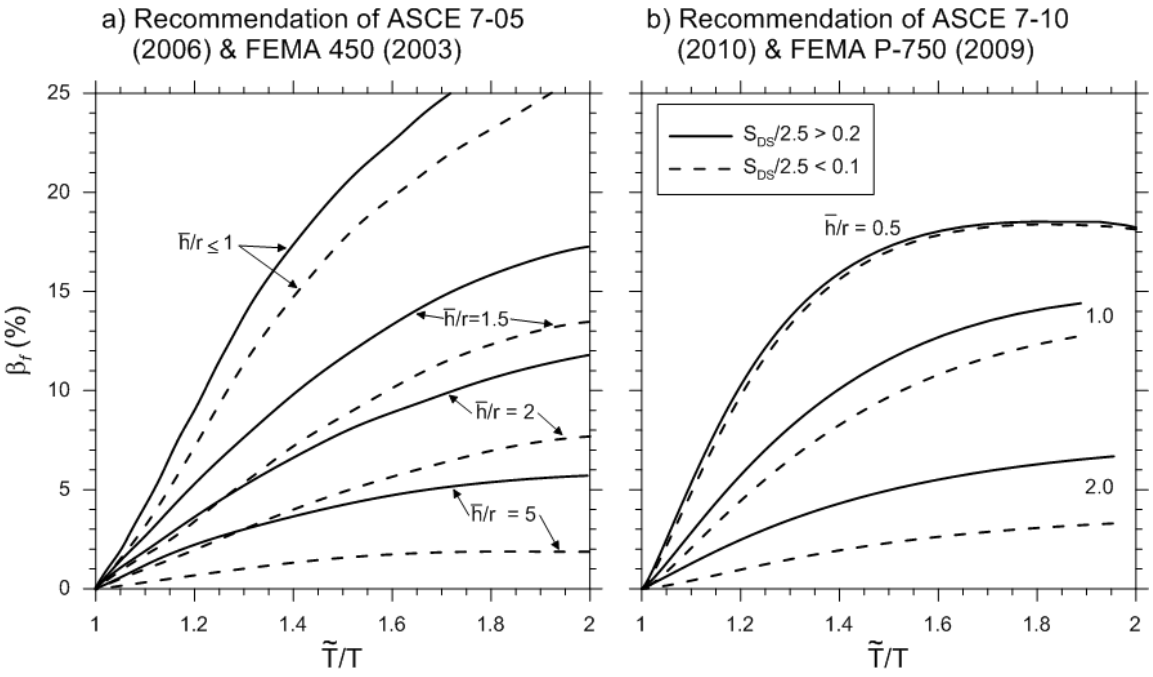

Figure 2-10 **Foundation damping as a function of period lengthening from a) ASCE 7-05, 2006 and FEMA 450, 2003 and b) ASCE 7-10, 2010 and FEMA P-750, 2009. Foundation damping computed using Veletsos and Verbic (1973) impedance functions for rigid circular foundation. ν = 0.33 and *D* = 0 for plots.**

2.5 Solutions for Damping of Rectangular Foundations

In this section, we apply the general solutions for foundation damping derived in Section 2.3 to foundations having a rectangular geometry in plan view. Specifically, we apply the foundation damping in Eqs. (2-25) and (2-35), which includes terms β_x and β_{yy} for radiation damping from foundation translation and rotation. The geometric shape of the foundation enters the foundation damping formulation through those terms as given in

Table 2-1a from the formulation of Pais and Kausel (1988), as adapted by NIST (2012). If the foundation is embedded, the corresponding impedance terms are given in Table 2-1b. While the circular foundation geometry has been prevalent in prior foundation damping solutions, it is not representative of the geometry of most building structures. The present extension to rectangular geometries is therefore motivated in large part by a practical need to update design guidelines and codes for a more representative, while still simplified, representation of foundation geometry.

Table 2-1a Equations for Radiation Damping Ratios & Corresponding Terms for Surface Foundations (Pais and Kausel, 1988)

Translation along x-axis

$$\beta_x = \left[\frac{4(L/B)}{K_x/GB}\right]\left[\frac{a_0}{2\alpha_x}\right]$$

$$K_x = \frac{GB}{2-\nu}\left[6.8\left(\frac{L}{B}\right)^{0.65} + 2.4\right]$$

$$\alpha_x = 1$$

Translation along y-axis

$$\beta_y = \left[\frac{4(L/B)}{K_y/GB}\right]\left[\frac{a_0}{2\alpha_y}\right]$$

$$K_y = \frac{GB}{2-\nu}\left[6.8\left(\frac{L}{B}\right)^{0.65} + 0.8\left(\frac{L}{B}\right) + 1.6\right]$$

$$\alpha_y = 1$$

Rocking about the x-axis

$$\beta_{xx} = \left[\frac{(4\psi/3)(L/B)a_0^2}{\left(\frac{K_{xx}}{GB^3}\right)\left[\left(2.2 - \frac{0.4}{(L/B)^3}\right) + a_0^2\right]}\right]\left[\frac{a_0}{2\alpha_{xx}}\right]$$

$$K_{xx} = \frac{GB^3}{1-\nu}\left[3.2\left(\frac{L}{B}\right) + 0.8\right]$$

$$\alpha_{xx} = 1.0 - \left[\frac{\left(0.55 + 0.01\sqrt{L/B - 1}\right)a_0^2}{\left(2.4 - \frac{0.4}{(L/B)^3}\right) + a_0^2}\right]$$

Rocking about the y-axis

$$\beta_{yy} = \left[\frac{(4\psi/3)(L/B)^3 a_0^2}{\left(\frac{K_{yy}}{GB^3}\right)\left[\left(\frac{1.8}{1 + 1.75(L/B - 1)}\right) + a_0^2\right]}\right]\left[\frac{a_0}{2\alpha_{yy}}\right]$$

$$K_{yy} = \frac{GB^3}{1-\nu}\left[3.73\left(\frac{L}{B}\right)^{2.4} + 0.27\right]$$

$$\alpha_{yy} = 1.0 - \left[\frac{0.55a_0^2}{\left(0.6 - \frac{1.4}{(L/B)^3}\right) + a_0^2}\right]$$

where $\psi = \left(\sqrt{2(1-\nu)/(1-2\nu)}\right) \leq 2.5$, L = half-length and B = half-width (see Figure 2-5)

Table 2-1b Equations for Radiation Damping Ratios & Corresponding Terms for Embedded Foundations (Pais and Kausel, 1988)

Translation along x-axis

$$\beta_x = \left[\frac{4\left[L/B + (D/B)(\psi + L/B)\right]}{(K_x\eta_x)/GB}\right]\left[\frac{a_0}{2\alpha_x}\right]$$

$$\eta_x = \left[1.0 + \left(0.33 + \frac{1.34}{1 + L/B}\right)\left(\frac{D}{B}\right)^{0.8}\right]$$

Translation along y-axis

$$\beta_y = \left[\frac{4\left[L/B + (D/B)(1 + \psi \cdot L/B)\right]}{(K_y\eta_y)/GB}\right]\left[\frac{a_0}{2\alpha_y}\right]$$

$$\eta_y = \left[1.0 + \left(0.33 + \frac{1.34}{1 + L/B}\right)\left(\frac{D}{B}\right)^{0.8}\right]$$

Rocking about the x-axis

$$\beta_{xx} = \left[\frac{(4/3)\left[\left(\frac{D}{B}\right) + \left(\frac{D}{B}\right)^3 + \psi\left(\frac{D}{B}\right)^3\left(\frac{L}{B}\right) + 3\left(\frac{D}{B}\right)\left(\frac{L}{B}\right) + \psi\left(\frac{L}{B}\right)\right]a_0^2}{\left(\frac{K_{xx}\eta_{xx}}{GB^3}\right)\left[\left(\frac{1.8}{1 + 1.75(L/B - 1)}\right) + a_0^2\right]} + \frac{\left(\frac{4}{3}\right)\left(\psi \cdot \frac{L}{B} + 1\right)\left(\frac{D}{B}\right)^3}{\left(\frac{K_{xx}\eta_{xx}}{GB^3}\right)}\right]\left[\frac{a_0}{2\alpha_{xx}}\right]$$

$$\eta_{xx} = \left[1.0 + \frac{D}{B} + \left(\frac{1.6}{0.35 + L/B}\right)\left(\frac{D}{B}\right)^2\right]$$

Rocking about the x-axis

$$\beta_{yy} = \left[\frac{(4/3)\left[\left(\frac{L}{B}\right)^3\left(\frac{D}{B}\right) + \psi\left(\frac{D}{B}\right)^3\left(\frac{L}{B}\right) + \left(\frac{D}{B}\right)^3 + 3\left(\frac{D}{B}\right)\left(\frac{L}{B}\right)^2 + \psi\left(\frac{L}{B}\right)^3\right]a_0^2}{\left(\frac{K_{yy}\eta_{yy}}{GB^3}\right)\left[\left(\frac{1.8}{1 + 1.75(L/B - 1)}\right) + a_0^2\right]} + \frac{\left(\frac{4}{3}\right)\left(\frac{L}{B} + \psi\right)\left(\frac{D}{B}\right)^3}{\left(\frac{K_{yy}\eta_{yy}}{GB^3}\right)}\right]\left[\frac{a_0}{2\alpha_{yy}}\right]$$

$$\eta_{yy} = \left[1.0 + \frac{D}{B} + \left(\frac{1.6}{0.35 + (L/B)^4}\right)\left(\frac{D}{B}\right)^2\right]$$

where $\psi = \left(\sqrt{2(1-\nu)/(1-2\nu)}\right) \le 2.5$, D = embedment, L = half-length and B = half-width (see Figure 2-5)

Figure 2-11 shows foundation damping computed using the above impedance solutions for square foundations along with solutions based on the impedance of circular foundations (Veletsos and Wei, 1971). In both cases, foundation damping is computed with Eqs. (2-25) and (2-35). Foundation damping is very sensitive to height aspect ratio, so it is important that *h/B* and *h/r* for these plots reflect similar foundation conditions. For low aspect ratios where foundation damping is dominated by the translational mode, this is accomplished by selecting *h/B* and *h/r* to represent common foundation areas:

$$\frac{h}{B} = \frac{h}{r} \cdot \sqrt{\frac{4}{\pi}} \tag{2-45a}$$

At larger height aspect ratios $(h/r \,\&\, h/B > 2)$, foundation damping is controlled by the rocking mode, so we match the moment of inertia rather than foundation contact area as follows:

$$\frac{h}{B} = \frac{h}{r} \cdot \sqrt[4]{\frac{12}{3\pi}} \tag{2-45b}$$

Figure 2-11 shows good agreement between the circular and square impedance functions when equivalent foundation properties are accounted for as done using Eq. (2-45).

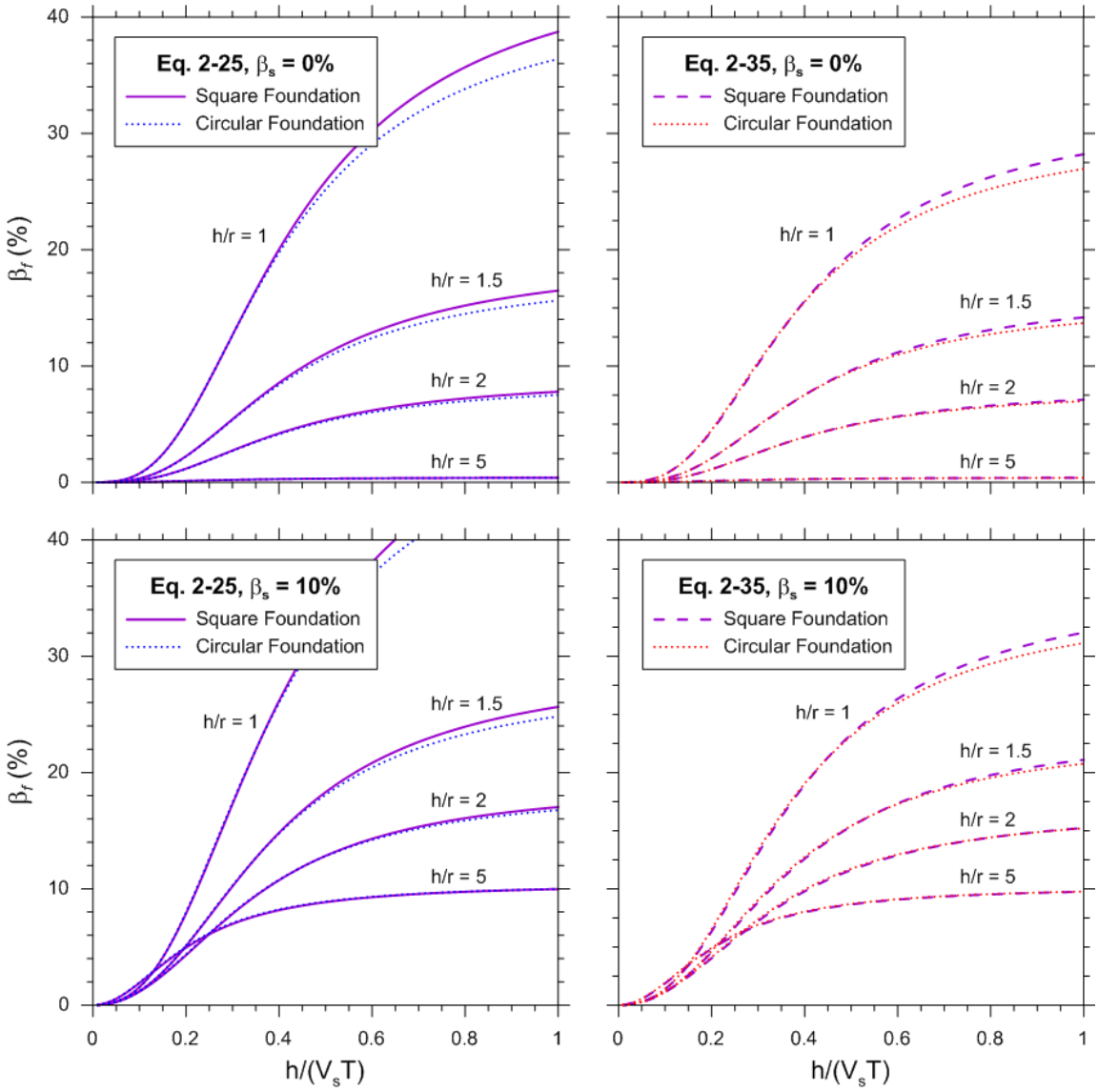

Figure 2-11 **Foundation damping as a function of $h/(V_sT)$ using Eqs. 2-25 and 2-35. Top plots show contributions from radiation damping only (β_s = 0) for circular and square foundations. Bottom plots include soil hysteretic damping (β_s = 0.1). ν = 0.33 and *D* = 0 for plots. Veletsos and Wei (1971) impedance functions were used for the circular case. The *h/B* input for the Pais and Kausel (1988) impedance functions for the square case was modified to represent equivalent areas per Eq. (2-45) and are denoted by the equivalent *h/r* input.**

Figures 2-12 and 2-13 show the relationship between period lengthening and foundation damping using the impedance functions for rectangular foundations in Table 2.1. These are candidate relationships for replacing the $\tilde{T}/T$ vs β_f plots used in current seismic guidelines (e.g., ASCE 7, 2010 and FEMA P-750, 2009: See Figure 2-10 and Section 2.4.5). The rectangular foundation case introduces an additional design parameter, the foundation aspect ratio (L/B) that introduces a dependency on the shaking direction.

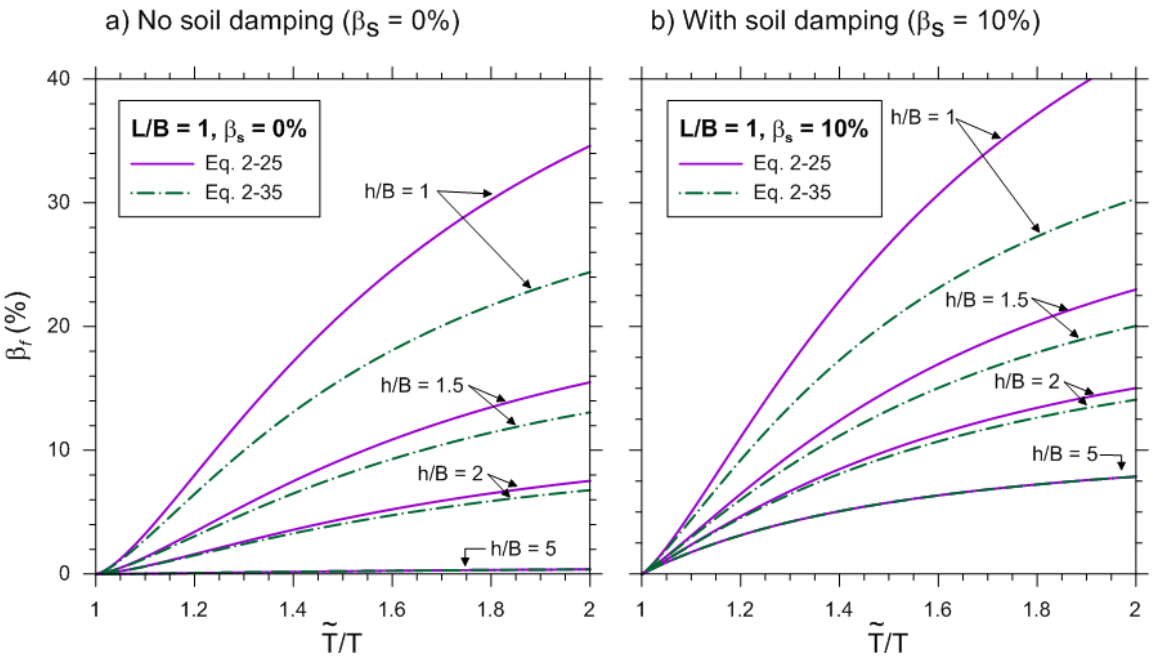

Figure 2-12 **Foundation damping as a function of period lengthening using Eqs. (2-25) and (2-35). Foundation damping computed for square foundations using a) only radiation damping terms (β_s = 0) and b) soil hysteretic damping (β_s = 0.1). *L/B* = 1, ν = 0.33 and *D* = 0 used for plots.**

Figure 2-12 shows a comparison of the two approaches (Eqs. 2-25 and 2-35) discussed in Section 2.3.3 for square foundations $(L/B = 1)$ with different height aspect

ratios (h/B). Cases of radiation damping only (Figure 2-12a; β_s=0) and combined radiation and hysteretic soil damping (Figure 2-12b; β_s=0.1) are shown. Both the translational and rotational terms are affected by the introduction of imaginary terms in Eq. (2-35) (relative to the terms in Eq. 2-25) by amounts ranging from 0-10% for the translational term and 0-16% for the rotational term. These differences have negligible influence at high height aspect ratios (e.g., $h/B \geq 2$), but substantial influence as the height aspect ratio is reduced. In all cases, Eq. (2-25) results in more foundation damping than does Eq. (2-35).

Figure 2-13 shows the effect of different foundation aspect ratios ($L = B$, $L/B = 2$, and $L/B = 4$). The solutions have been calculated for height aspect ratios of $h/B = 1$ and $h/B = 2$. The effects of changes in foundation aspect ratio (*L/B*) and height aspect ratio (*h/B*) can be summarized as follows:

- For $L/B > 1$, shaking in the long direction (*x*-direction) produces higher foundation damping than does shaking in the short (*y*) direction. This occurs because rocking will be less pronounced for shaking in the long direction, in turn causing foundation translation to dominate, which produces more foundation damping.
- Eq. (2-25) has more sensitivity to L/B than does Eq. (2-35). For example, a structure with $h/B = 1$ has a foundation damping differential between $L = B$ and $L/B = 2$ of about 4% using Eq. (2-25) and 1% using Eq. (2-35).

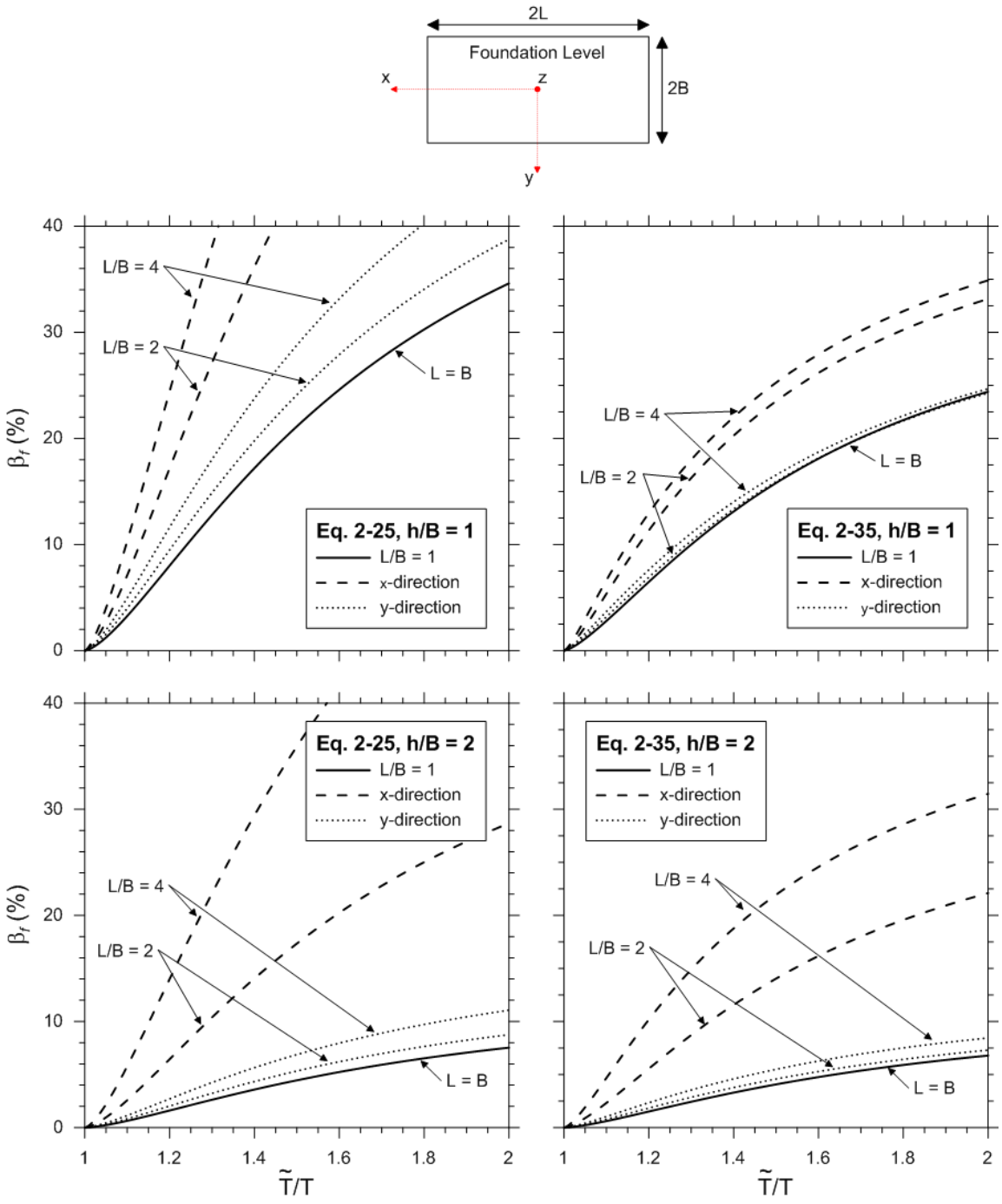

Figure 2-13 **Foundation damping as a function of foundation aspect ratios (*L/B*) and period lengthening using Eqs. (2-25) and (2-35). Top plots show foundation damping for *h/B*= 1; bottom plots are for *h/B* = 2. β_s = 0, ν = 0.33 and *D* = 0 for plots.**

2.6 Evaluation of Foundation Damping Solutions

For practical use, we recommend the use of closed form equations (such as Eq. 2-25 or 2-35) over design charts such as those shown in Figures 2-10, 2-12 and 2-13. We consider both Eq. (2-25) and Eq. (2-35) to be theoretically correct, yet they produce differences in foundation damping that can be significant. We turn to available empirical data from Stewart et al. (1999a,b), Tileylioglu et al. (2011) and recently performed forced vibration testing to guide the selection of a single solution for foundation damping. Since empirical data applies for realistic conditions that do not match those in idealized solutions for foundation impedance, we begin by describing how effects such as soil nonhomogeneity and nonlinearity are considered in the analysis of foundation damping. We then apply both damping formulations to the buildings for which damping is known from prior system identification work, to facilitate selection of the solution producing the best fit to the data.

2.6.1 Idealized Solutions Adapted for Realistic Conditions

The foundation damping solutions given in Eqs. (2-25) and (2-35) are fully general, but their typical application will be with solutions for foundation impedance that apply for rigid foundations of either circular or rectangular geometries resting on a homogenous half-space. This section summarizes procedures for adapting those solutions for conditions involving non-uniform soil profiles and nonlinear soil behavior. Both of these considerations affect the shear modulus that should be used with the impedance models (Table 2-1).

Non-uniform soil stiffnesses can be addressed by selecting an effective average velocity across a depth interval extending from the base of the foundation to a depth of z_p below the foundation depth. The effective velocity profile is established by computing the ratio of z_p to the travel time (tt) for shear waves to travel over the depth interval of z_p to the base of the foundation. The effective velocity profile is z_p /tt. The depth interval has been related to the foundation area and moment of inertia as shown below (NIST, 2012):

$$Horizontal(x\,\&\,y):\quad z_p = B_e^A,\quad B_e^A = \sqrt{A/4} = \sqrt{BL} \tag{2-46a}$$

$$\begin{aligned} Rocking(xx\,\&\,yy):\quad z_p \approx B_e^i,\ \ xx: B_e^I &= \sqrt[4]{0.75 I_x} = \sqrt[4]{B^3 L}, \\ yy: B_e^I &= \sqrt[4]{0.75 I_y} = \sqrt[4]{B L^3} \end{aligned} \tag{2-46b}$$

where A is the foundation-soil contact area and I_x and I_y are the foundation moment of inertia about the x and y axis, respectively. It should be noted that Eq. (2-46) has been reduced for the most common foundation geometry (rectangular, with half-width B and half-length L dimensions). Eq. 2-46 can easily be adapted for circular foundations of radius r with the following relations:

$$Horizontal(x\,\&\,y):\quad z_p = B_e^A,\quad B_e^A = \sqrt{A/4} = \frac{r}{2}\sqrt{\pi} \tag{2-47a}$$

$$Rocking(rr):\quad z_p = B_e^I,\quad B_e^I = \sqrt[4]{0.75 I_{rr}} = \frac{r}{4}\sqrt[4]{3\pi} \tag{2-47b}$$

where subscript rr refers to the rotational mode. Shear modulus reduction factors for different site categories and ground motion levels are provided in design guidelines (such as IBC 2012, NIST 2012 (Table 4-1), and FEMA P-750) as shown in Table 2-2. However, the preferred method is to complete a site-specific equivalent-linear ground

response analysis. Shear modulus reduction factors from such analyses or from Table 2-2 can be used to adjust the shear modulus in the static stiffness equations in Table 2-1.

Table 2-2 Values of Shear Modulus Reduction for Various Site Classes and Shaking Amplitudes

Site Class	Site Class Soil $V_{s,30}$ (m/s)	Value of Vs/Vs_0			Value of G/G_0		
		PGA			PGA		
		≤ 0.1	0.4	≥ 0.8	≤ 0.1	0.4	≥ 0.8
A	$V_s > 1500$	1.00	1.00	1.00	1.00	1.00	1.00
B	$1500 > V_s > 760$	1.00	0.97	0.95	1.00	0.95	0.90
C	$760 > V_s > 360$	0.97	0.87	0.77	0.95	0.75	0.60
D	$360 > V_s > 180$	0.95	0.71	0.32	0.90	0.50	0.10
E	$180 > V_s$	0.77	0.22	*	0.60	0.05	*
F	*	*	*	*	*	*	*

Note: Use straight line interpolation for intermediate values of PGA
* = should be evaluated from site-specific analysis

2.6.2 Comparison to Recorded Data

This section investigates how well Eqs. (2-25) and (2-35) predict the levels of foundation damping observed empirically from field tests and case histories. Foundation damping is not measured directly from field performance data; rather system identification analyses are performed to evaluate fixed- and flexible-base properties of structures, from which foundation damping is computed using Eq. (2-2).

System identification refers to the process of mathematically evaluating the unknown properties (i.e., period and damping characteristics) of a dynamic system. Non-parametric and parametric methods exist for evaluating the fixed-base and flexible-base period and damping ratios. Non-parametric studies consist of simply examining ratios of output/input motions in the frequency domain (e.g., Ljung, 1987; Pandit, 1991; Mikami et al., 2008). Parametric system identification requires regression analyses in which the

properties of a parametric model of the system are evaluated for a given output/input pair of motions (e.g., Stewart and Fenves, 1998). Whether parametric or non-parametric analyses are to be performed, a crucial element of system identification for SSI purposes is the selection of appropriate input-output motions to evaluate fixed-base and flexible-base properties of the structure.

Parametric system identification of several buildings shaken by earthquakes with varying degrees of SSI effects was performed by Stewart et al. (1999b) to evaluate their first mode period and damping ratio for the fixed-base (T, β_i) and flexible-base ($\tilde{T}, \beta_0$) conditions. Based on the identified fixed-base and flexible-base damping ratios, Eq. (2-2) is used to back-calculate the foundation damping ratio of the system. Similar analyses were performed by Tileylioglu et al. (2011) using forced vibration and earthquake loading of a field test structure in Garner Valley, CA (referred to as 'Dr. Evil' in Chapter 5). To expand the data inventory, additional data sets from forced vibration testing of a field test structure (referred to as 'Mini-Me' in Chapter 5) have been analyzed using parametric system identification procedures. Mini-Me was cyclically loaded with varying degrees of force and structural stiffness at two sites (as discussed in Chapter 5) and the response history data from both sites have been evaluated for the fixed-base and flexible base periods and damping ratios.

To place the value of these forced vibration tests in context, Figure 2-14 shows histograms of the available data set with respect to $h/(V_sT)$ and h/B. The data derived from earthquake shaking of instrumented buildings (Stewart et al., 1999b) is dominated by low values of the wave parameter $\left(h/\left(V_sT\right) \le 0.1\right)$ for which inertial SSI effects are

small. The forced vibration tests (Tileylioglu et al., 2011; this study) occupy a range of $h/(V_s T) = 0.1\text{-}0.5$ with an average value of approximately 0.27. Height aspect ratios (*h/B*) range from about 0-6 in the instrumented structures data set and 2-3 in the forced vibration test data set.

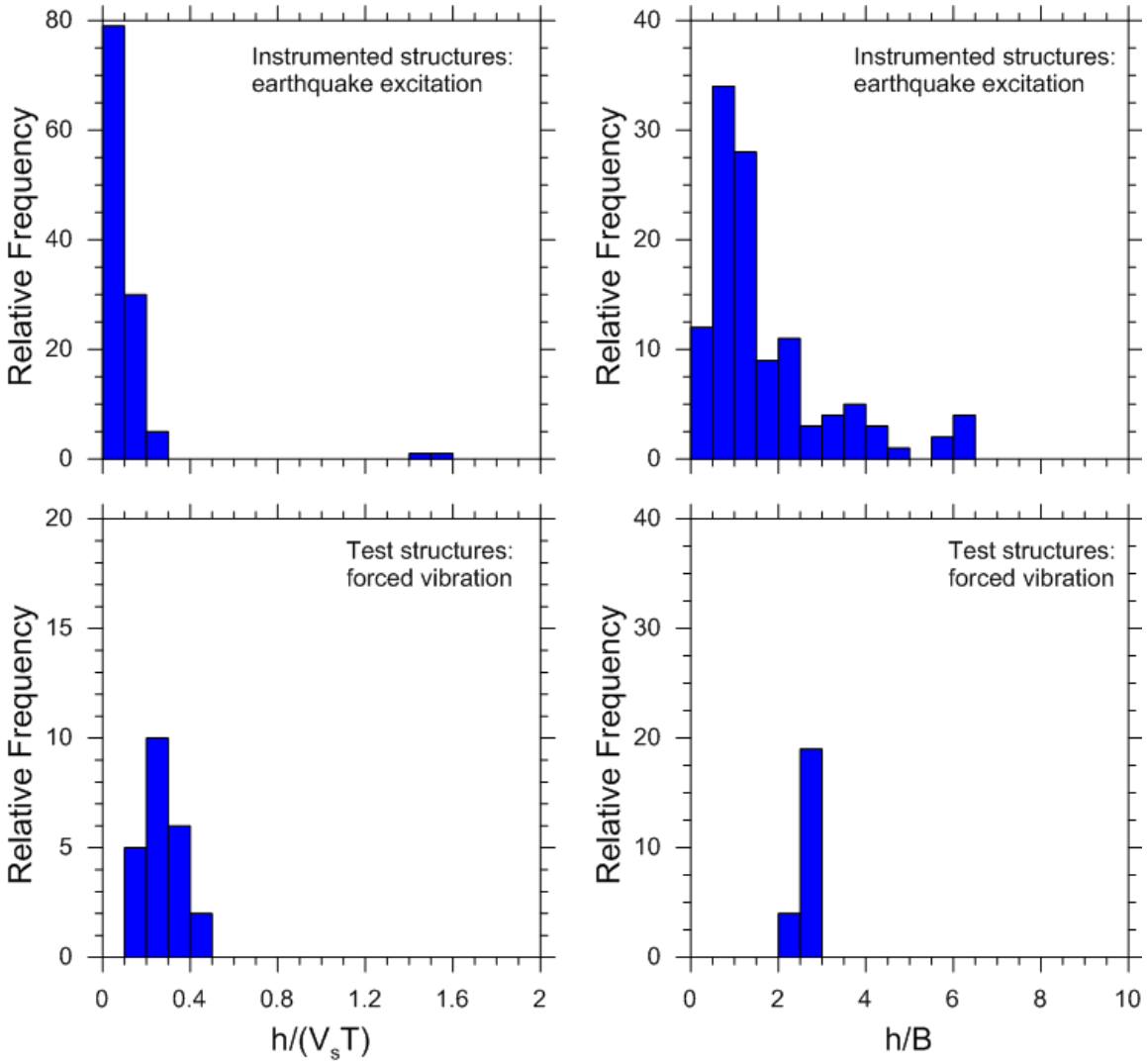

Figure 2-14 **Histograms of $h/(V_sT)$ and h/B in data sets used to evaluate SSI effects from instrumented structures. Top row corresponds to instrumented structures shaken by earthquakes and analyzed by Stewart et al. (1999b); bottom row corresponds to forced vibration tests results from this study and Tileylioglu et al., (2011).**

Table 2-3 presents critical attributes of the first data set, including meta data [earthquake sources, lateral force resisting systems, foundation condition (i.e., whether on piles, rock, soil, etc.], calculated period lengthening and foundation damping from first-mode periods and damping ratios evaluated from parametric system identification, and predicted period lengthening and damping based on Eqs. (2-25) and (2-35). All of these results are as given in Stewart et al. (1999b), with the exception of foundation damping (re-computed using Eq. 2-2 with n=2) and model predictions.

Table 2-4 summarizes attributes of the second data set associated with test structures used for forced vibration testing (this study and Tileylioglu et al., 2011). We list applicable metadata [test structure, site, source of shaking (earthquake or forced vibration), type of shaker], period lengthening and foundation damping identified from first-mode vibration properties established from system identification (details in Section 6.6, and period lengthening and foundation damping from the models presented earlier in this chapter (period lengthening from Eq. 2-1; damping from Eqs. 2-25 and 2-35).

We denote the foundation damping observed from data analysis as $\beta_{f,i}$, with subscript i serving as an index for the case history under consideration. The corresponding foundation damping from the model is denoted $\hat{\beta}_{f,i}$, and the residual (data minus model) is $\beta_{f,i} - \hat{\beta}_{f,i}$. Residuals are plotted against the wave parameter for both data sets in Figures 2-15 and 2-16 (using Eq. 2-25 and 2-35 for $\hat{\beta}_{f,i}$, respectively). With regard to period lengthening, T_i denotes fixed-base period for case history i, $\tilde{T}_i/T_i$ is

period lengthening from data, $\hat{\tilde{T}}_i / T_i$ is predicted period lengthening, which is identical for both approaches, and the residual is $\left(\tilde{T}_i - \hat{\tilde{T}}_i\right) / T_i$.

Period lengthening residuals, shown in both figures, generally range between -0.2 and 0.2. Binned means for ranges of $h/(V_s T)$ = 0-0.05, 0.05-0.1, 0.1-0.2, 0.2-0.3, and > 0.3 show a tendency of Eq. (2-1) with Table 2.1 impedance functions to underpredict the case studies' period lengthening as $h/(V_s T)$ increases. Generally the confidence intervals on the binned means encompass zero, indicating that the misfits are not statistically significant. Note that the under-prediction of period lengthening corresponds to computed impedances that are too stiff. Similar misfits have been observed for impedance functions inferred from field testing, as described in Chapter 6.

Foundation damping residuals in Figures 2-15 and 2-16 mostly fall within a range of -5% to 5%. There are a number of significant outliers, particularly in the case of Figure 2-15, including site A17 from the Stewart et al. (1999b) data set. The residuals are more nearly centered at zero and have fewer outliers in Figure 2-16. The differences between Figures 2-15 and 2-16 are principally between $h/(V_s T) > 0.1$, where SSI effects are most significant. The sites within that range of the wave parameter show a tendency for Eq. (2-25) to overpredict damping. For site A46, which is at the upper end of the $h/(V_s T)$ range (1.54), Eq. (2-25) overpredicts foundation damping, while Eq. (2-35) underpredicts.

These results do not necessarily indicate that the formulation in Eq. (2-35) is 'correct' and Eq. (2-25) is 'incorrect,' because there are likely compensating errors related to the impedance functions. In particular, halfspace models for impedance tend to

over-predict translational radiation damping and under-predict rotational radiation damping (Tileylioglu et al., 2011 and this study). If impedance functions were developed that removed these sources of bias in the predicted radiation damping, we could very well find that Eq. (2-25) is unbiased and (2-35) is biased. All that can be said at present is that given the limitations of halfspace-based impedance functions, Eq. (2-35) provides a better fit to the available empirical data than does Eq. (2-25).

Table 2-3 Attributes of data set for instrumented structures with earthquake recordings (Stewart et al., 1999b) showing period lengthening and foundation damping from system identification and models.

Site #[a]	EQK[a]	Lateral Force Resistance[b]	Piles[b]	D>0[a]	Rock/Soil[b]	Confidence[d]	h/(V$_s$T)[a]	Traverse (y-direction)						h/(V$_s$T)[a]	Longitudinal (x-direction)					
								System ID		Eq. 2-25		Eq. 2-35			System ID		Eq. 2-25		Eq. 2-35	
								$\tilde{T}/T^a$	$\beta_{f,i}{}^c$	$\tilde{\tilde{T}}_i/T_i$	$\hat{\beta}_{f,i}$	$\tilde{\tilde{T}}_i/T_i$	$\hat{\beta}_{f,i}$		$\tilde{T}/T^a$	$\beta_{f,i}{}^c$	$\tilde{\tilde{T}}_i/T_i$	$\hat{\beta}_{f,i}$	$\tilde{\tilde{T}}_i/T_i$	$\hat{\beta}_{f,i}$
A1	PT	SW	N	N	S	A	0.29	1.57	13.1	1.39	21.4	1.39	13.8	0.2	1.09	8.2	1.14	14.7	1.14	9.1
A2	PT	SW	N	N	S	L	0.08	1.04	10.0	1.06	8.6	1.06	4.7	0.1	1.08	24.0	1.09	15.7	1.09	7.3
	PTA						0.08	1.05	3.6	1.06	8.6	1.06	4.7	0.1	1.03	9.0	1.09	15.7	1.09	7.3
A4	LP	CF	Y	N	S	A	0.2	1.02	5.9	1.19	2.9	1.19	2.8	0.18	1.00	6.9	1.15	2.2	1.15	2.2
A5	LP	DWF	Y	N	R	A	0.03	1.04	0.6	1.01	0.0	1.01	0.0	0.04	1.03	0.0	1.00	0.0	1.00	0.0
A7	LP	SW	N	N	S	A	0.08	1.03	9.0	1.04	3.4	1.04	2.4							
A8	LP	SW	Y	N	R	A	0.09	1.16	3.2	1.04	2.0	1.04	1.7	0.06	1.00	1.9	1.03	1.6	1.03	1.4
A9	CGA	DWF	N	Y	S	L	0.09	1.00	3.0	1.02	1.0	1.02	0.8							
A10	LP	DWF	N	Y	S	A	0.16	1.06	5.7	1.11	11.4	1.11	6.5	0.16	1.03	13.1	1.08	11.3	1.08	6.2
A11	LP	SF	N	N	R	A	0.02	1.00	0.0	1.00	0.0	1.00	0.0	0.02	1.00	0.0	1.00	0.0	1.00	0.0
A12	IMP	DWF	Y	N	S	A	0.23	1.47	5.2	1.23	9.4	1.23	7.4	0.09	1.00	0.0	1.03	1.0	1.03	0.9
A13	LD	DWF	Y	Y	S	A	0.12	1.05	3.5	1.05	2.2	1.05	1.7	0.13	1.03	0.6	1.04	2.5	1.04	1.9
A14	WT	SW	Y	N	S	A	0.14	1.00	1.0	1.10	6.8	1.10	4.9							
A15	NR	SF	Y	N	S	A	0.06	1.06	3.3	1.02	0.9	1.02	0.8	0.06	1.02	0.0	1.02	1.0	1.02	0.9
A16	NR	SF	N	N	S	L	0.18	1.28	0.0	1.15	0.8	1.15	0.8	0.2	1.34	1.3	1.18	1.0	1.18	1.0
A17	NR	SW	N	N	R	A	0.14	1.17	10.8	1.18	34.6	1.18	13.2	0.12	1.09	5.4	1.14	24.5	1.14	10.3
A18	WT	SF	Y	N	S	A								0.08	1.00	0.0	1.02	0.4	1.02	0.4
A20	NR	SW	Y	Y	R	A	0.17	1.13	0.0	1.09	3.2	1.09	2.6	0.16	1.05	0.8	1.08	2.7	1.08	2.2
A21	SM	BI	N	N	R	L	0.03	1.01	0.0	1.01	0.2	1.01	0.2	0.03	1.00	3.8	1.01	0.2	1.01	0.2
	LD						0.02	1.00	0.0	1.00	0.1	1.00	0.1	0.02	1.00	0.0	1.00	0.1	1.00	0.1
	NR						0.02	1.00	0.0	1.00	0.1	1.00	0.1	0.03	1	0.0	1.01	0.2	1.01	0.2
A23	NR	SF	N	Y	S	L	0.11	1.08	0.0	1.04	0.6	1.04	0.6							
A24	NR	SW	Y	N	S	A	0.09	1.04	1.0	1.07	8.5	1.07	4.8	0.23	1.60	3.6	1.25	12.4	1.25	8.8
A25	LD	BI	N	N	R	A	0.05	1.00	0.0	1.01	0.2	1.01	0.2	0.05	1.00	0.0	1.01	0.2	1.01	0.2
	NR						0.05	1.00	0.0	1.01	0.3	1.01	0.3	0.05	1.01	0.0	1.01	0.3	1.01	0.3
A26	NR	DWF	N	Y	S	L	0.19	1.04	0.0	1.12	3.0	1.12	2.7	0.11	1.00	0.0	1.03	0.7	1.03	0.6
A27	LD	SF	N	N	R	A	0.05	1.00	0.9	1.01	0.1	1.01	0.1	0.05	1.00	0.3	1.01	0.1	1.01	0.1
	NR						0.05	1.00	5.7	1.01	0.1	1.01	0.1	0.05	1.00	6.8	1.01	0.1	1.01	0.1
A29	WT	CF	Y	N	S	L	0.06	1.01	3.8	1.02	0.2	1.02	0.2							
	NR						0.05	1.02	3.5	1.02	0.2	1.02	0.2	0.15	1.06	0.4	1.04	1.1	1.04	1.0
A30	NR	SF	Y	Y	S	A	0.09	1.08	1.3	1.04	3.2	1.04	2.3							
A31	LD	SW	N	N	S	A	0.13	1.19	2.7	1.10	0.9	1.10	0.8							
	NR						0.13	1.16	0.0	1.10	1.0	1.10	1.0	0.14	1.14	0.5	1.06	1.2	1.06	1.1
A32	WT	SF	Y	Y	S	A								0.06	1.00	1.1	1.01	0.4	1.01	0.4
A33	WT	SF	Y	Y	S	A	0.07	1.00	0.2	1.02	1.1	1.02	0.9	0.07	1.00	0.5	1.02	1.1	1.02	0.9
	NR						0.06	1.00	1.4	1.02	0.7	1.02	0.6	0.07	1.00	1.2	1.02	1.0	1.02	0.8
A34	NR	SW	N	N	S	A	0.12	1.66	9.8	1.09	6.7	1.09	4.5	0.09	1.22	9.1	1.04	4.0	1.04	2.9

*Table continued on next page.

Site #[a]	EQK[a]	Lateral Force Resistance[b]	Piles[b]	D>0[a]	Rock/Soil[b]	Confidence[d]	h/(V$_s$T)[a]	Traverse (y-direction)						h/(V$_s$T)[a]	Longitudinal (x-direction)					
								System ID		Eq. 2-25		Eq. 2-35			System ID		Eq. 2-25		Eq. 2-35	
								$\tilde{T}/T^a$	$\beta_{f,i}{}^c$	$\hat{\tilde{T}}_i/T_i$	$\hat{\beta}_{f,i}$	$\hat{\tilde{T}}_i/T_i$	$\hat{\beta}_{f,i}$		$\tilde{T}/T^a$	$\beta_{f,i}{}^c$	$\hat{\tilde{T}}_i/T_i$	$\hat{\beta}_{f,i}$	$\hat{\tilde{T}}_i/T_i$	$\hat{\beta}_{f,i}$
A35	WT	CF	N	Y	S	A	0.09	1.02	3.4	1.03	2.5	1.03	1.8	0.09	1.02	0.0	1.03	2.5	1.03	1.8
	UP						0.06	1.01	4.4	1.03	1.9	1.03	1.4	0.06	1	0.0	1.03	1.9	1.03	1.4
A36	LD	CF	N	Y	S	L	0.04	1.17	0.0	1.01	0.1	1.01	0.1	0.05	1.39	4.9	1.01	0.1	1.01	0.1
A37	RD	BI	N	Y	S	A	0.06	1.03	0.8	1.03	1.6	1.03	1.2	0.06	1.00	1.4	1.02	1.6	1.02	1.3
	WT						0.06	1.02	0.0	1.03	1.6	1.03	1.3	0.07	1.01	2.4	1.02	1.1	1.02	0.9
	UP						0.07	1.00	0.0	1.02	1.2	1.02	1.0	0.07	1.00	0.0	1.02	1.2	1.02	1.0
	LD						0.06	1.01	0.0	1.02	0.8	1.02	0.7	0.06	1.02	0.5	1.01	0.8	1.01	0.6
	NR						0.07	1.02	0.0	1.02	1.1	1.02	0.9	0.06	1.02	0.0	1.01	0.7	1.01	0.6
A38	LD	SF	N	N	S	L	0.06	1.07	0.0	1.02	1.3	1.02	1.1	0.06	1.03	0.0	1.02	1.4	1.02	1.1
A39	NR	SW	N	Y	S	L	0.06	1.00	3.9	1.01	0.6	1.01	0.5	0.08	1.00	1.3	1.02	1.4	1.02	1.1
A40	LD	SF	Y	N	S	A	0.04	1.00	0.0	1.01	0.1	1.01	0.1	0.04	1.00	1.4	1.01	0.1	1.01	0.1
A41	NR	SF	Y	N	S	A	0.07	1.01	0.0	1.03	2.1	1.03	1.6	0.04	1.02	0.7	1.01	0.4	1.01	0.4
A42	NR	SF	N	N	R	L	0.04	1.02	4.6	1.02	0.0	1.02	0.0	0.04	1.00	3.1	1.01	0.0	1.01	0.0
A43	LD	BI	Y	Y	S	A	0.07	1.02	0.0	1.02	0.4	1.02	0.4	0.06	1.04	0.0	1.02	0.6	1.02	0.5
	NR						0.06	1.03	0.0	1.02	0.7	1.02	0.6	0.09	1.03	0.9	1.02	0.9	1.02	0.8
A44	WT	SW	N	N	S	A	0.16	1.10	0.9	1.12	10.9	1.12	7.4	0.17	1.17	3.2	1.14	12.4	1.14	8.2
	NR						0.15	1.04	1.0	1.11	10.6	1.11	6.9	0.21	1.29	12.9	1.20	22.7	1.20	12.8
A45	NR	SW	Y	N	S	A	0.15	1.34	0.8	1.12	1.7	1.12	1.5							
A46	LO7		N	Y	S	A	1.45	4.14	30.4	3.20	33.3	3.20	25.1	1.54	4.01	30.8	3.36	33.6	3.36	25.1
B1	LP	SW	N	N	S	A	0.17	1.06	0.0	1.04	0.5	1.04	0.5							
B2	LP	SW	N	N	S	A	0.07	1.13	3.6	1.02	0.4	1.02	0.4							
B3	LP	SF	Y	Y	S	A	0.17	1.03	0.0	1.19	1.4	1.19	1.4							
B4	LP	SF	N	Y	S	A														
B5	LP	SW	Y	N	S	A	0.27	1.64	0.0	1.35	7.6	1.35	6.2							
B6	LP	SF	N	Y	S	A	0.07	1.01	0.0	1.02	0.2	1.02	0.2	0.07	1.01	0.6	1.02	0.2	1.02	0.2
B7	LP	DWF	Y	N	R	A	0.1	1.17	0.0	1.05	0.3	1.05	0.3							
B9	NR	SF	N	N	S	A														
B10	NR	DWF	N	Y	S	A	0.08	1.00	2.5	1.03	0.4	1.03	0.4	0.1	1.03	0.0	1.03	0.6	1.03	0.6
B11	LD	SW	Y	N	R	A	0.09	1.13	1.4	1.12	0.3	1.12	0.3							
	NR						0.09	1.17	2.1	1.12	0.4	1.12	0.4							
B12	NR	DWF	N	Y	R	A	0.12	1.06	1.3	1.05	0.3	1.05	0.3							
B13	NR	SF	N	Y	R	A	0.06	1.02	0.0	1.02	0.1	1.02	0.1							
B14	NR	SW	N	N	S	A	0.12	1.14	2.2	1.15	1.3	1.15	1.2							

*EQK: CGA: Colinga Aftershock, IMP: Imperical Valley, LD: Landers, LO7: Lotung Event 7, NR:Northridge, PTA: Petolia Aftershock, PT: Petrolia SM: Sierra Madre, UP: Upland, WT: Whittier

*Lateral force resisting system: BI=Base Isolation, CF=Concrete frame, DWF=dual wall/frame system, SF=steel frame, SW=shaer wall, masonry or conc.

[a]Data from Stewart et al. 1999; [b]Data from Stewart and Stewart 1997, [c]Derived from Stewart et al. 1999 data, [d]A=acceptable confidence & L=low confidence in Stewart et al. '99 results

Table 2-4 Attributes of data set for field test structures subject to forced vibration testing and earthquake shaking, including period lengthening and foundation damping from system identification and models.

Structure & Site[a]	Data Source[b]	Structure Condition	Direction of Shaking	Shake Source[c]	h/B[d]	L/B	β_s[e]	h/(V_sT)	Observed Data		Predicted Data			
									System ID		Eq. 2-25		Eq. 2-35	
									$\tilde{T}/T$[a]	$\beta_{f,i}$[c]	$\hat{\tilde{T}}_i/T_i$	$\hat{\beta}_{f,i}$	$\hat{\tilde{T}}_i/T_i$	$\hat{\beta}_{f,i}$
DE @ GVDA	TEA (2011)	Unbraced	NA	EQ M_L = 4.2	2.15	1.00	1.20	0.15	1.15	0.9	1.12	0.8	1.12	0.8
	TEA (2011)	Unbraced	NA	EQ M_w = 5.4			1.20	0.15	1.15	3.4	1.12	0.8	1.12	0.8
	TEA (2011)	Unbraced	NA	LM			1.20	0.14	1.09	0.4	1.10	0.7	1.10	0.7
	TEA (2011)	Braced	NA	LM			1.20	0.28	1.29	0.0	1.38	3.0	1.38	2.8
MM @ GVDA	Exp. 3.3.1a	Unbraced	X	AA	2.68	2.00	1.20	0.17	1.13	2.4	1.10	1.5	1.10	1.4
	Exp. 3.4.9b	Unbraced	X	MME-10%			9.80	0.26	1.28	4.3	1.22	7.1	1.22	6.2
	Exp. 3.4.13a	Unbraced	X	MME-50%			13.70	0.29	1.25	6.4	1.27	10.2	1.27	8.6
	Exp. 3.4.15a	Unbraced	X	MME-100%				Error in test						
	Exp. 3.3.5a	Unbraced	Y	AA			1.20	0.17	1.31	2.4	1.19	1.2	1.19	1.1
	Exp. 3.4.3a	Unbraced	Y	MME-10%			7.00	0.23	1.61	8.2	1.33	4.5	1.33	4.3
	Exp. 3.4.17a	Unbraced	Y	MME-50%			12.10	0.27	1.76	8.7	1.43	8.2	1.43	7.5
	Exp. 3.4.19a	Unbraced	Y	MME-100%			12.90	0.26	1.78	11.1	1.41	8.3	1.41	7.6
	Exp. 3.1.1a	Braced	X	AA			1.20	0.24	1.12	0.8	1.19	3.5	1.19	3.2
	Exp. 3.2.6a	Braced	X	MME-10%			9.00	0.33	1.33	10.0	1.34	10.5	1.34	9.1
	Exp. 3.2.12a	Braced	X	MME-50%			13.90	0.45	1.63	9.1	1.59	19.5	1.59	15.8
	Exp. 3.2.14	Braced	X	MME-100%			14.90	0.31	1.12	13.5	1.31	11.9	1.31	9.9
	Exp. 3.1.6a	Braced	Y	AA			1.20	0.22	1.38	2.5	1.30	1.9	1.30	1.8
	Exp. 3.2.1a	Braced	Y	MME-10%			7.10	0.31	1.65	5.3	1.55	6.6	1.55	6.1
	Exp. 3.2.11	Braced	Y	MME-50%			12.40	0.27	1.63	7.8	1.43	8.4	1.43	7.7
	Exp. 3.2.15	Braced	Y	MME-100%			12.40	0.34	2.27	14.8	1.64	10.6	1.64	9.6
MM @ WLA	Exp. 2.1.9a	Unbraced	X	AA	2.68	2.00	2.00	0.33	1.44	8.8	1.3	7.1	1.30	6.4
	Exp. 2.1.7a	Unbraced	Y	AA			2.00	0.29	1.53	6.0	1.42	3.3	1.42	3.0
	Exp. 2.1.17a	Braced	X	AA			2.00	0.41	1.53	11.8	1.45	10.6	1.45	9.4
	Exp. 2.1.15a	Braced	Y	AA			2.00	0.39	1.81	6.7	1.69	4.8	1.69	4.4

[a]GVDA - Garner Valley Downhole Array Site; WLA - Wildlife Liquefaction Array Site; DE - Dr. Evil Structure; MM - Mini-Me Structure (See Chap. 5)

[b]TEA = Tileylioglu et al (2011); Data with "Exp" names were compiled as part of a UCLA field testing series, information can be found at https://nees.org/warehouse/project/637/ and Chapter 5.

[c]AA = Atom Ant shaker; MME-#% = Mighty Mouse shaker with #% eccentricity force; LM - Linear mass shaker, similar to AA

[d]Center of mass height of the roof slab.

[e]Based on Menq (2003) model using 65% of approximated strain values (fondation velocity per soil shear wave veolicty) at flexible-base frequency, Note: $V_s/V_{s0} = (G_s/G_{s0})^{1/2}$ and WLA site approximated $\beta_s = 0.2$

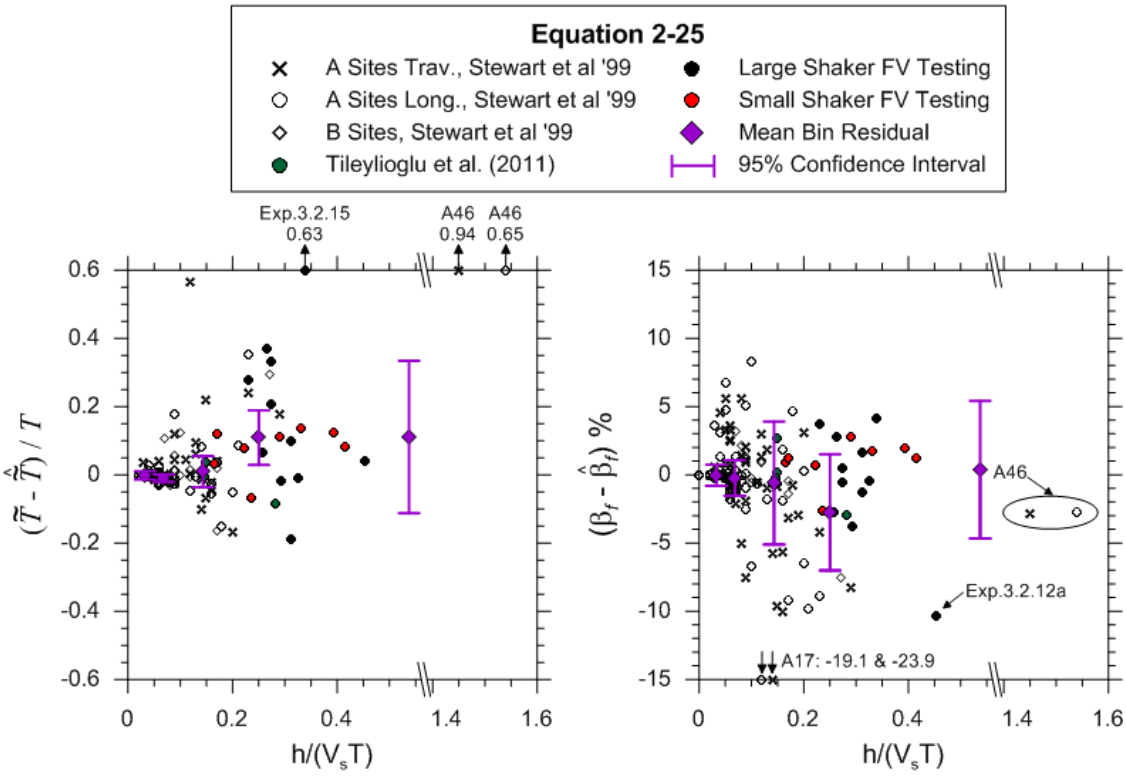

Figure 2-15 **Period lengthening and foundation damping residuals from combined data sets. Foundation damping residuals from model in Eq. (2-25).**

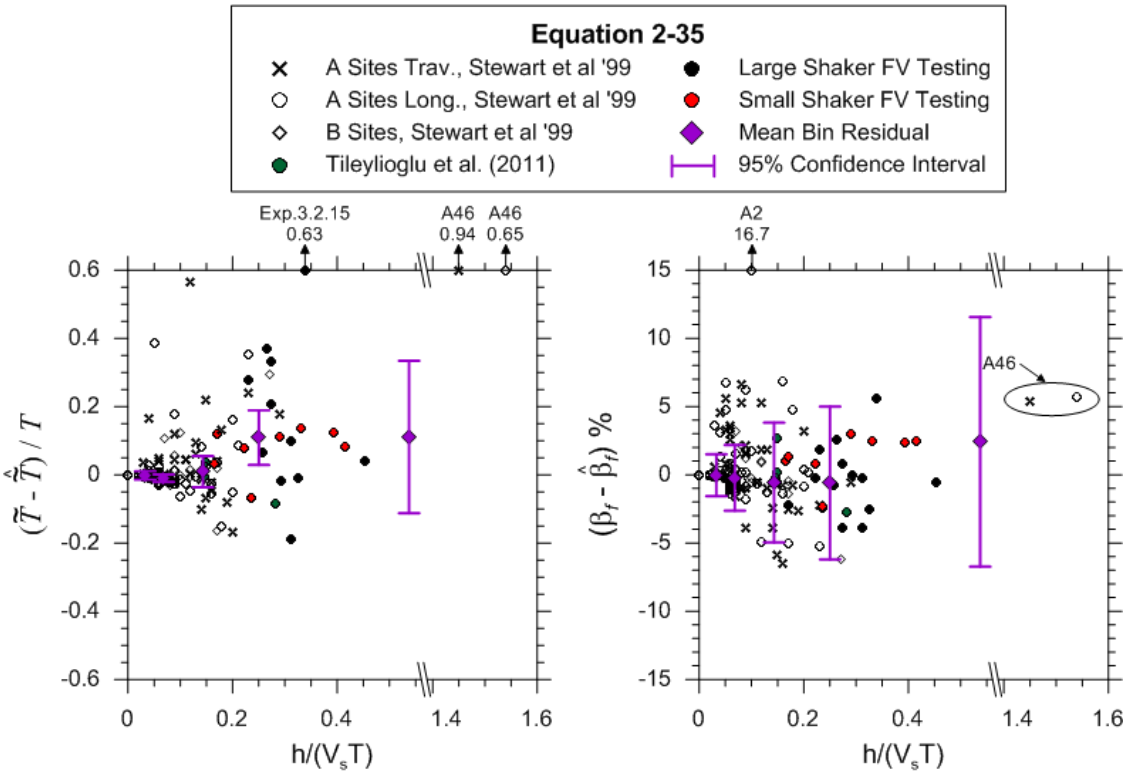

Figure 2-16 Period lengthening and foundation damping residuals from combined data sets. Foundation damping residuals from model in Eq. (2-35).

2.7 Conclusions and Recommendations

Closed-form solutions to determine the period lengthening and foundation damping have been presented. Eqs. (2-25) and (2-35) are both general expressions for foundation damping that can incorporate the Pais and Kausel (1988) closed-form impedance function solutions (Table 2-1) for either surface or embedded rectangular shaped foundations. Both models allow for a direct calculation of the foundation damping of rectangular foundations and obviate the use of traditional models for circular footings. The models can be adapted to accommodate site-specific soil nonhomogeneity and design-levels of shear strain using approximate methods from the literature (NIST, 2012).

While either solution (Eqs. 2-25 and 2-35) is a valid formulation of foundation damping on a conceptual level, the levels of damping from Eq. (2-25) are higher than those from Eq. (2-35) for foundations of modest height aspect ratios. The lower damping from Eq. (2-35) is generally more consistent with field case histories either re-analyzed or presented for the first time in this chapter. Because of known biases in radiation damping formulations for translation and rocking used in the foundation damping equations, it cannot be concluded on the basis of these comparisons that one equation is fundamentally better than the other. However, given the limitations of current radiation damping models for halfspace representations of the foundation medium, Eq. (2-35) appears to be the preferred formulation at the present time.

3 KINEMATIC SOIL-STRUCTURE INTERACTION EFFECTS FROM BUILDING AND FREE-FIELD SEISMIC ARRAYS IN JAPAN

This Chapter presents work that was completed in collaboration with our Japanese colleagues for a joint conference proceeding of the 9th International Conference on Urban Earthquake Engineering and 4th Asia Conference on Earthquake Engineering that will be held at the Tokyo Institute of Technology in Tokyo Japan on March 6-8, 2012. The coauthors of this work include Atsushi Mikami of the University of Tokushima in Japan, Toshihide Kashima of the International Institute of Seismology and Earthquake Engineering, Building Research Institute in Japan and Jonathan P. Stewart of the University of California, Los Angeles.

3.1 Introduction

Foundation-level and free-field seismic ground motions are identical only for vertically propagating incident waves and non-embedded foundations. In reality, incident waves are neither vertically propagating nor coherent, which gives rise to spatially variable ground

motions even on sites with relatively uniform site conditions. In the presence of such incident wave fields, motions on foundations will be reduced in amplitude relative to free-field motions, an effect termed *base slab averaging*. Base slab averaging is one type of *kinematic soil-structure interaction* effect. Other kinematic effects result from foundation embedment below the ground surface (e.g., buildings with basements) and the presence of pile foundations.

The spatial variability of seismic ground motions in the free-field (i.e., away from building foundations), has been examined by a number of investigators (e.g., Abrahamson, 1991; Zerva and Zervas, 2002) who have derived empirical functions that express the variability of phase angle in terms of a coherency function. Those functions were derived largely using dense array records from Lotung, Taiwan, although they have since been validated and adjusted using data from other arrays (Ancheta et al., 2011). Recently, Abrahamson's ground motion coherency model was implemented into the Computer Program SASSI (a System for Analysis of Soil-Structure Interaction; Ostadan, 2005). SASSI computes the relative motion of the foundation to the free-field (input motion) in terms of a transfer function expressing the frequency-dependent ratio of foundation motion amplitude to free-field motion amplitude. The result is one solution to the kinematic interaction problem, including base slab averaging.

Another approach that has been utilized to predict foundation/free-field transfer functions from base slab averaging is based on a theoretical solution by Veletsos and co-workers (1989, 1997) coupled with empirical calibration of an incoherence parameter by Kim and Stewart (2003). This approach is inherently calibrated for California sites, but

the degree to which its application is appropriate for building types not represented in the database and regions other than California remains unknown. This approach has been implemented for engineering application, in combination with a simple transfer function for embedment effects, in two design standards: ASCE-41 (2013) and NIST (2012).

In this chapter, we apply the above two models for predicting transfer functions to a subset of the available data from Japan for several particularly interesting structures. Both models are applied under the assumption of vertically propagating, incoherent incident wave fields, with the implicit understanding that bias could result from this assumption under some circumstances. The predicted transfer functions are compared to each other and to transfer functions derived from the data.

3.2 Structural-Ground Arrays in Japan

As part of an ongoing project, we compiled a list of instrumented structures in Japan with neighboring ground stations, which can be used for the evaluation of foundation/free-field ground motion variations of the type described in the Introduction. This list of structures is given in Table 3-1.

Table 3-1 List of currently compiled instrumented structure and ground arrays in Japan.

Location	Array owner	Lat/Long	Station code	Two base vertical sensors (Y/N)	# Stories above ground	# Basement levels	Foundation type	Instrumented stories	Site condition	# Earthquakes recorded
Sendai, Miyagi	Tohoku Institute of Technology	38º14'44"N, 140º51'12"E	J1	no	4	0	pile	GL,4,FF		100
Hachinohe, Aomori	Hachinone National College of Tech.	40º29'32"N, 141º26'57"E	J5	no		0	pile	GL,FF		
Toda Corp., Tsukuba?	Toda Corporation	36º06'37"N, 140º04'36"E	J6		6	0	pile	GL,6,FF		13
Tokushima Univ.	The University of Tokushima	34º04'39"N, 134º33'46"E	J7	no	6	0	pile	GL,6,FF	sand	2
Nihon Univ. Bldg. #14	Nihon University	35º43'31"N, 140º03'28"E			5	1	pile	GL,4,RF,FF		many
Nagoya Univ.	Nagoya University	35º09'20"N, 136º58'01"E								
	Hachinohe Institute of Technology	40º28'44"N, 141º33'36"E								
		35º00'45"N, 135º46'06"E			7	1		B1,7,4,FF		
	Nikken Sekkei	35º41'59"N, 139º45'04"E								
	Shimizu Corporation	35º39'46"N, 139º47'52"E								
	Kanagawa University	35º29'07"N, 139º37'13"E			8	2		B2,B1,3,6,8		
NPS										
NPS Kashiwazaki	Tokyo Electric Power Company	37º25'17"N, 138º35'44"E								
NPS Fukushima	Tokyo Electric Power Company	37º25'14"N, 141º01'59"E								
NPS Onagawa	Tohoku Electric Power Company	38º24'04"N, 141º29'59"E								
BRI										
Takamatsu, Kagawa	BRI	34º20'20"N, 134º02'48"E	J2, TKM	no	8	1	pile?	B1,RF,FF	sand	23
Fukuoka, Fukuoka	BRI	33º35'16"N, 130º25'27"E	J3	no	10	1	pile	B1,10,FF	sand	14
Nagoya, Aichi	BRI	35º10'51"N, 136º54'11"E	J4, FKO	no	12	2	pile	B2,GL,12	sand	55
Miyako	BRI	39º38'29"N, 141º57'25"E	MYK		7	0		GL,7,FF		224
Hachinohe	BRI	40º30'42"N, 141º29'20"E	HCN2		10	1		B1, GL,10,FF		467
Yachiyo	BRI	35º43'20"N, 140º05'59"E	YCY		6	1		B1,GL,7		23
Nippon Inst. Tech.	BRI	36º01'38"N, 139º42'41"E	NIT		6	1		GL,6,FF		327
Misato City Hall	BRI	35º49'48"N, 139º52'20"E	MST	no	7	1		GL,7,FF		14
Funabashi	BRI	35º42'26"N, 140º00'20"E	FNB		8	0		GL,8,FF		37
Chiba	BRI	35º36'24"N, 140º07'22"E	CHB		8	1		B1,GL,8		23
Toda City Hall	BRI	35º49'03"N, 139º40'40"E	TDS		8	1		B1,GL,8		27
The National Museum of Western Art	BRI	35º42'55"N, 139º46'32"E	NMW		3	1		B1,GL,4,FF		264
Univ. of Tokyo, Bldg.11	BRI	35º42'49"N, 139º45'34"E	UTK		9	0		GL,7,FF		49
Marine Sci. and Tech.	BRI	35º37'42"N, 139º44'53"E	TUF		7	0		GL,7,FF		37
College of MLIT	BRI	35º43'08"N, 139º28'53"E	KDI		3	0		GL,3,FF		69
Yamanashi Pref. Hall	BRI	35º39'50"N, 138º34'06"E	YMN		8	1		B1,GL,8,FF		15
Kushiro	BRI	42º59'11"N, 144º22'40"E	KGC		9	1		B1,GL,9,FF		253
Olumpic	BRI	35º40'36"N, 139º41'39"E	YYG		4	1		B1,GL,4		16
	BRI	36º07'58"N, 140º04'34"E	NCTD		7	0		GL,8,FF		2
	BRI	35º40'42"N, 139º44'39"E	NDLM		5	4		GL,17		48
	BRI	35º40'44"N, 139º44'38"E	NDLA		4	8		B8,B4,GL,4		37
	BRI	35º40'41"N, 139º44'42"E	NDLG							242
	BRI	36º07'55"N, 140º04'24"E	ANX		8	1		B1,GL,2,5,8,FF, ground array		1142

B# = Basement floor level #, BRI = Building Research Institute, FF = Free-field, GL = Ground level, Ground array = sensors at depth in soil, NPS = Nuclear power station, and RF = Roof level

The Building Research Institute (BRI) in Japan owns most of the structural-ground arrays and distributes seismic data at the web site: http://smo.kenken.go.jp/. Most of the BRI instrumented buildings range from 3 to 10 stories in height above ground. Foundation types are not provided on the site. Base rocking cannot be directly estimated for most of these buildings since BRI sensor array configurations typically have only one vertical accelerometer at its lowest level.

The Electric Power Company in Japan is another major owner of structural-ground arrays from in nuclear power stations. When released for public use, the data is distributed by the Japan Association for Earthquake Engineering (JAEE) at their web site: http://www.jaee.gr.jp/stack/sta05.html.

From the list in Table 3-1, we select three buildings for consideration in this manuscript: Nagoya office building (hereafter referred to as 'Nagoya'), Onagawa nuclear power plant ('Onagawa'), and Sendai university building ('Sendai').

The Sendai site consists of a four story building above ground and contains nine accelerometers (including three free-field), as shown in Figure 3-1. Lateral loads are resisted by reinforced concrete frames and shear walls in the longitudinal and transverse directions, respectively. The foundation consists of end-bearing concrete piles connected by grade beams. Figure 3-1 shows the underlying soil stratigraphy and geophysical data that were determined from boring operations which included suspension logging at the site (OYO Corporation, 2007). The Sendai site was investigated previously by Mikami et al. (2006) using data from the 2003 Off Miyagi earthquake. This data is considered again here along with recordings from the recent 2011 Tohoku earthquake, which produced

much stronger ground motions. The site peak ground acceleration (PGA) for the Off Miyagi and Tohoku earthquakes are 0.232g and 0.813g, respectively. The purpose for selecting this site was to examine possible differences in the kinematic response for the variable strengths of shaking.

The Onagawa site consists of a five story reactor above ground with two sub-terranean levels (embedment of 16 m) and contains 22 accelerometers (including three free-field), as shown in Figure 3-2. The foundation consists of a 3.5 m thick concrete slab with dimensions of 55.3 by 51.8 m. Figure 3-2 shows the underlying soil lithology and geotechnical data. The Onagawa structure was selected because it has the only available array that enables evaluation of base rocking. The site is investigated for the 2011 Tohoku earthquake that had a PGA of 0.533g at the site.

The Nagoya site consists of a 10 story building above ground with two basement levels (embedment of 12.83 m) and contains 9 accelerometers (including three free-field), as shown in Figure 3-3. The foundation consists of a 2.53 m thick concrete slab with dimensions of 79.6 by 23.2 m overlying reinforced concrete piles. Figure 3-3 shows the underlying soil lithology and geotechnical data that were determined from boring operations which included suspension logging 440 m west of the site (CRBOMLIT, 2003). The Nagoya structure was selected because it has a large footprint area, which is of interest because its dimensions are near the limit of the calibration range for the Kim and Stewart (2003) semi-empirical model. The site was investigated for the 2004 Off Kii Pensinsula earthquake that had a PGA of 0.014g. To our knowledge, neither the Onagawa nor the Nagoya structures have been examined in prior studies.

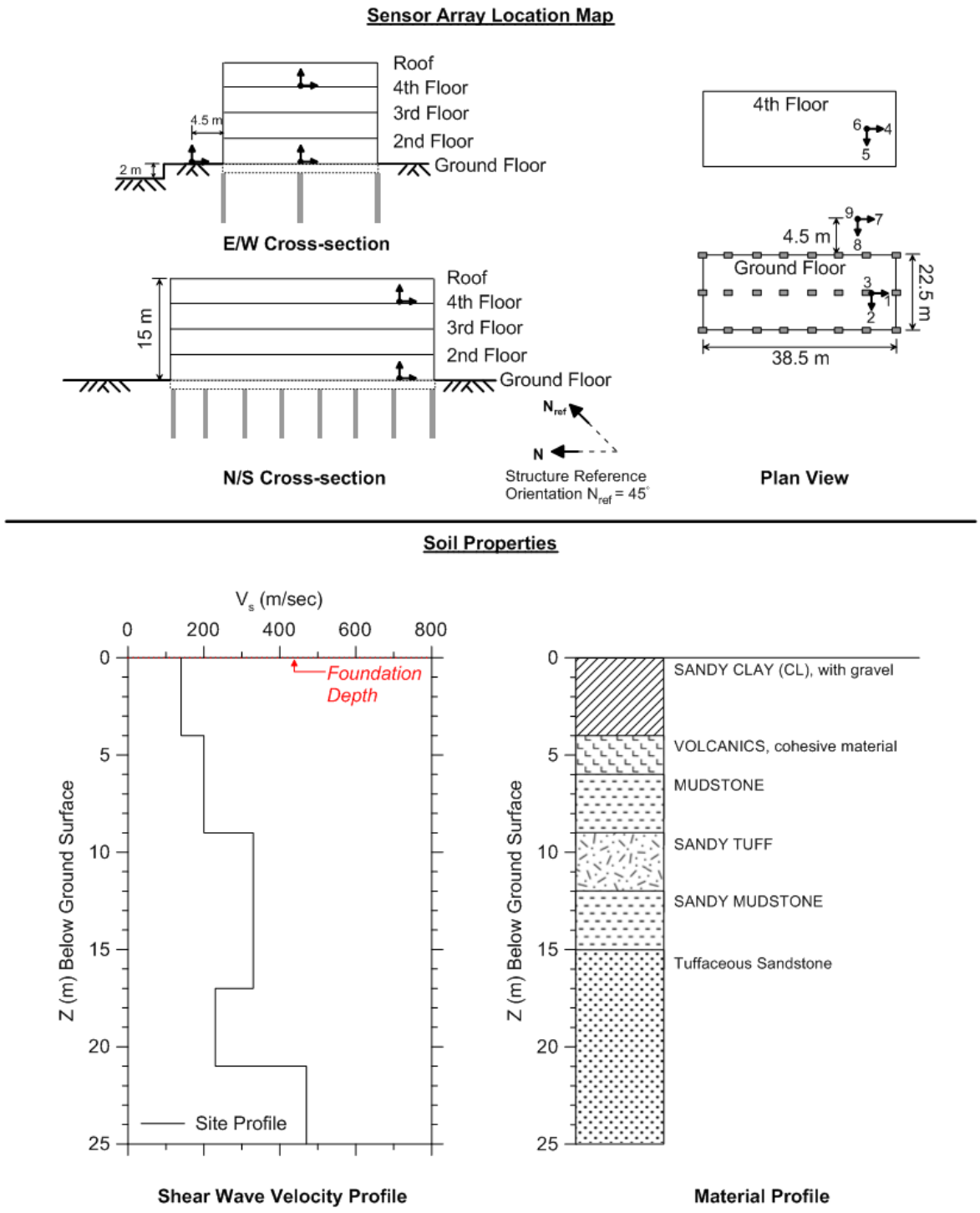

Figure 3-1. **Building layout and site conditions at Sendai University site (J1). Data source: OYO Corporation, 2007.**

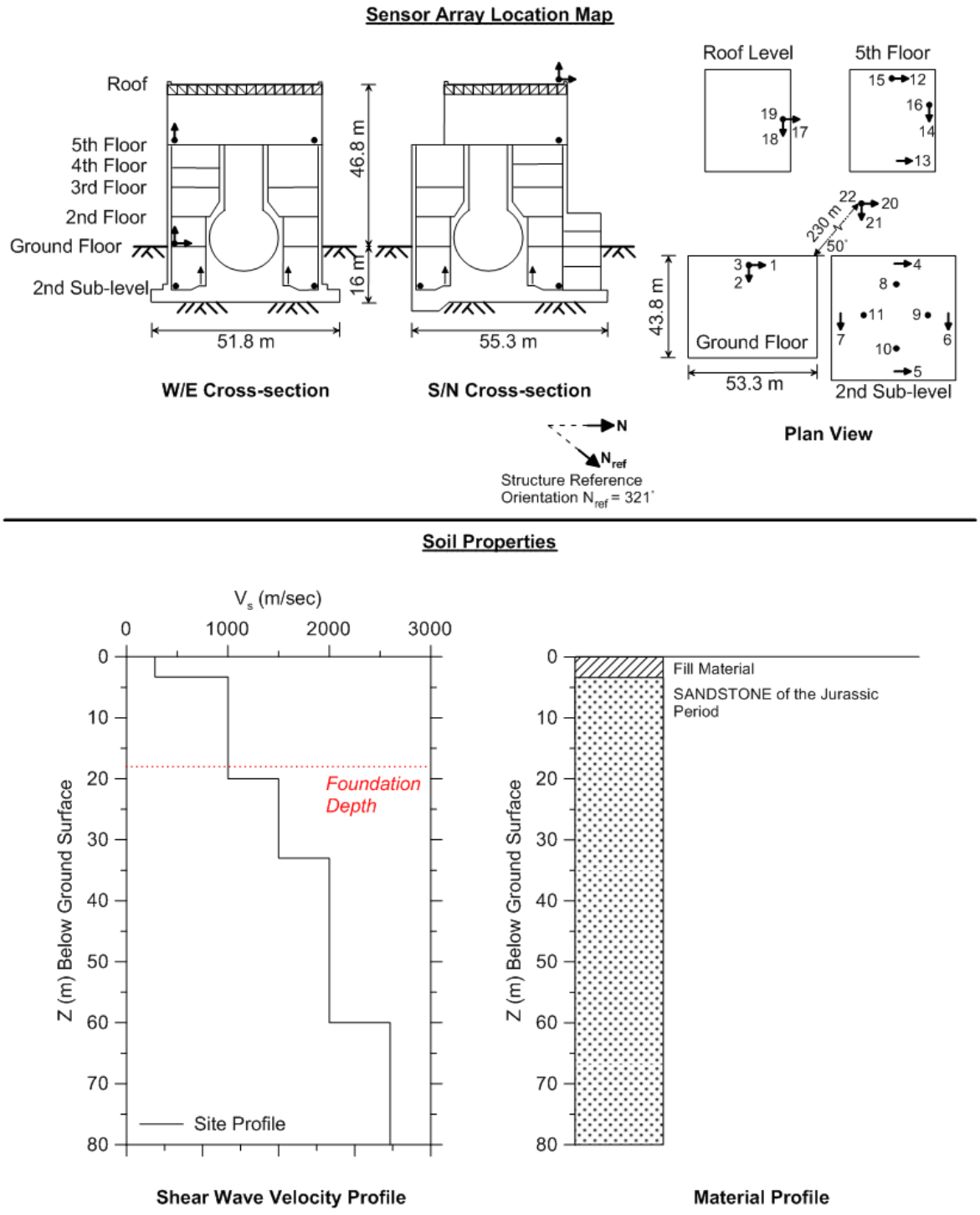

Figure 3-2. **Building layout and site conditions at Onagawa Nuclear Power Plant, Reactor 1. Data sources: Tohoku Electric Power Company, 2009 and 2011.**

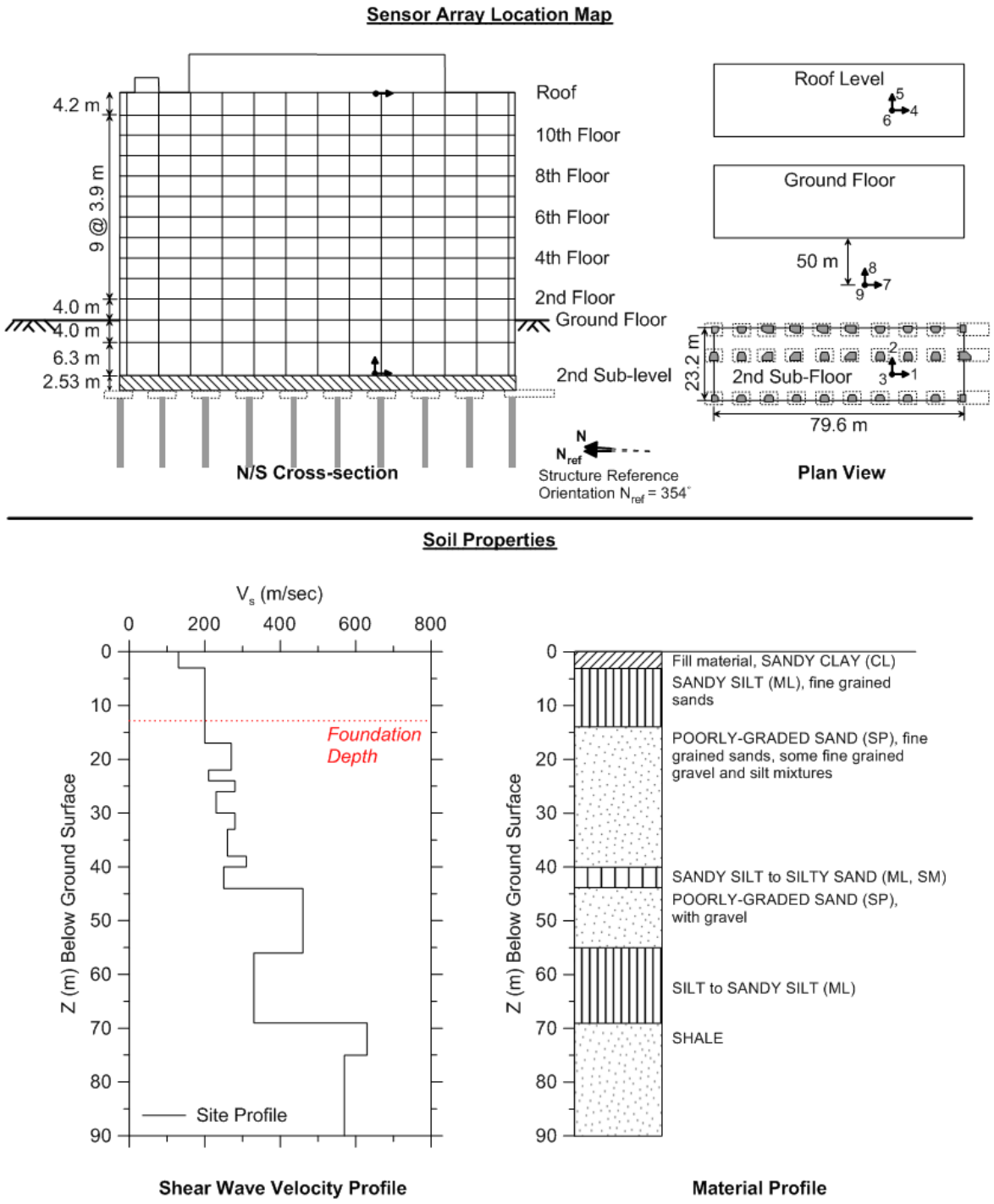

Figure 3-3. **Building layout and site conditions at Nagoya Office Building (J4). Data sources: CRBOMLIT, 2003 and 2005.**

3.3 Models for Prediction of Foundation to Free-Field Transfer Functions

3.3.1 Spatial Coherency Model Implemented in SASSI

The spatial variation of phase of strong ground motion is quantified by coherency. Using recordings from dense arrays in Lotung, Taiwan Abrahamson (1991) derived empirical functions that describe coherency as a function of separation distance and frequency. Coherency is unity at zero frequency and reduces strongly with increasing frequency and relatively weakly with increasing distance. Coherency less than unity results both from deterministic phase lag and relatively random (stochastic) wave scattering effects. Abrahamson (1991) present a model for *lagged coherency*, which represents the stochastic component only (wave passage removed). The model is considered applicable to frequencies greater than 1 Hz and for separation distances of 6 to 85 meters (Abrahamson, 1991). That coherency model has been implemented into SASSI by Ostadan (2005) and ACS-SASSI by Ghiocel (2006).

SASSI was originally developed at the University of California, Berkeley (Lysmer et al., 1981, 1999). SASSI utilizes the substructuring approach in which the linear SSI problem is divided into sub problems based on the principle of superposition; thus the analysis is performed using linear material properties. Soil is assumed to consist of horizontal layers overlying either a rigid base or an elastic half-space. The structure and foundation are modeled by finite elements. Foundations are modeled as rigid, massless slabs to exclude inertial effects. Piles are modeled as hollow elements using representative stiffness of prestressed high-strength concrete.

3.3.2 Semi-Empirical Approach

Veletsos and co-workers (1989, 1997) developed useful models for theoretical base slab averaging that combine an analytical representation of the spatial variation of ground motion with rigorous treatment of foundation-soil contact.

Kim and Stewart (2003) calibrated Veletsos' analysis procedure against observed foundation/free-field ground motion variations as quantified by frequency dependent transfer functions. Two types of transfer functions can be obtained from well instrumented structures as follows:

$$H_u(\omega) = \frac{u_f}{u_g} \qquad H_\theta = \frac{\theta L}{u_g} \tag{3-1}$$

where u_f denotes foundation translation, u_g ground motion translation in the same direction, θ denotes kinematic rotation about an axis normal to the direction of u_f and u_g, and L is the foundation half dimension in the same direction as u_f and u_g. The Kim and Stewart calibration considered the horizontal translation transfer function only (H_u), and resulted in apparent κ values (denoted κ_a) for each structure/data set combination. Those κ_a values reflect not only incoherence effects, but necessarily also include average foundation flexibility and wave inclination effects for the calibration data set.

The data set considered by Kim and Stewart (2003) consisted of buildings with mat, footing and grade beam, and grade beam and friction pile foundations, generally with base dimensions in the range of B_e^A=15-40 m (where B_e^A is the square root of foundation area divided by four). Although the Veletsos models strictly apply to rigid foundations, the semi-empirical model applies to the more realistic foundation conditions

present in the calibration data set, which consist principally of shallow foundations that are inter-connected (i.e., continuous mats or footings interconnected with grade beams). Errors could occur when the model is applied to conditions beyond the calibration data set. In particular, the effects of incoherence in the Veletsos models is taken as proportional to wavelength, thus implying strong scaling with frequency and distance. As mentioned previously, array data indicates the distance scaling is much weaker than the frequency scaling (Abrahamson et al., 1991; Ancheta et al., 2011), so the model would be expected to over-predict the effects of incoherence (under-predict H_u) for very large foundations (opposite for small foundations). Even within the parameter space of the calibration data set, it should be recognized that the empirical model fits the data set in an average sense but would not be expected to match any particular observation. Example applications showing fits to data are given in subsequently in the paper.

Two of the three buildings considered in this research have foundation embedment (Nagoya and Onagawa). We utilize a model originally presented by Kausel et al. (1978) in combination with the Kim and Stewart model for these buildings. As presented by NIST (2012), the model is given as follows:

$$H_u = \cos\left(\frac{D\omega}{V_{s,d}}\right), \quad \frac{D\omega}{V_{s,d}} < 1.1 \tag{3-2a}$$

$$H_u = 0.45, \quad \frac{D\omega}{V_{s,d}} > 1.1 \tag{3-2b}$$

$$H_\theta(\omega) = 0.26\left(1 - \cos\left(\frac{D\omega}{V_{s,d}}\right)\right), \quad \frac{D\omega}{V_{s,d}} < \frac{\pi}{2} \tag{3-3a}$$

$$H_\theta(\omega) = 0.26, \quad \frac{D\omega}{V_{s,d}} > \frac{\pi}{2} \tag{3-3b}$$

where D = embedment depth and $V_{s,d}$ is a time-averaged shear wave velocity over the embedment depth of the foundation.

3.4 Evaluation and Comparison of Transfer Functions

3.4.1 Transfer Function Calculation from Data

Transfer functions are evaluated from the recordings using procedures described in Mikami et al. (2008). In particular, frequency domain smoothing is applied to spectral density functions for the 'input' (denominator in Eq. 3-1, denoted y) and 'output' (numerator in Eq. 3-1, denoted x) as follows:

$$\left|H(\omega)\right| = \sqrt{\frac{S_{xx}}{S_{yy}}} \tag{3-4}$$

where S_{xx} and S_{yy} are auto-spectral density functions for the input and output, respectively. The smoothing is applied using a 7-point Hamming window, which provides an equivalent frequency bandwidth of B_e = 0.207 Hz. In addition, the coherence (square of coherency) of the data is calculated as:

$$\gamma^2(\omega) = \frac{\left|S_{xy}(\omega)\right|^2}{S_{xx}(\omega)S_{yy}(\omega)} \tag{3-5}$$

where S_{xy} is the cross spectral density function. The coherence is used the judge the effects of noise in the data. Frequency ranges in the transfer function that are dominated by noise will have low coherence. The average coherence of pairs of white noise signals for our frequency bandwidth is 0.25^{2} 0.04 (Mikami et al., 2008).

3.4.2 Application of Models

The models describes in Section 3 are applied to the conditions at the three building sites. Equivalent linear shear wave velocity profiles were developed using deconvolution analysis with the free-field ground motions and velocity profiles shown in Figures 3-1 to 3-3. Nonlinear properties were developed based on the soil conditions using the modulus reduction and damping models from Menq (2003) for sands and Darendeli (2001) for other soil and weathered rock materials

The properties developed through the above process are the direct input for the SASSI analysis, which is a linear analysis with no iteration on strain-dependent soil properties. The model for embedment used a time-averaged version of these velocities over the embedment depth for use in Eqs. (3-2) and (3-3). The Kim and Stewart model also uses a shear wave velocity for the evaluation of the κ_a parameter, which is time-averaged over the depth range zero to D+B_e^A.

3.4.3 Results for Subject Buildings

Figures 3-4 to 3-8 show predicted transfer functions from the SASSI and NIST models along with transfer function and coherence ordinates for each site considered. The dots show transfer function ordinates with high coherence.

The predicted transfer function ordinates are similar from the SASSI and NIST models for each considered structure. Further research is needed to evaluate the range of foundation conditions where this similarity holds.

Figures 3-4 and 3-5 present results for the Sendai site for the two earthquakes. The transfer and coherence functions from the two sets of earthquake recordings are

remarkably similar for the two events. For frequencies less than about 8 Hz where the data have high coherence and hence relatively little effects of noise, the transfer functions are nearly identical. The transfer functions from data fall below those from the two models to a significant degree for frequencies beyond 2.5 Hz. This occurs despite the slower velocities produced by the larger shear strains in the Tohoku earthquake.

In Figures 3-4 and 3-5 at frequencies above about 9 Hz, the coherence is low, being near the range of 0.2-0.3 that is associated with pure noise for the level of smoothing used in the calculations. Some peculiar transfer function ordinates are observed in this range, including transfer function ordinates above unity, but those results are not considered reliable due to the strong effects of noise. Investigation of piles with incoherent inputs is beyond the ability of SASSI. The Sendai building was modeled with piles for the coherent case, however, excluded for the incoherent case.

Figures 3-6 and 3-7 presents horizontal and rotational transfer functions from the Onagawa site. The two models produce similar transfer functions for the horizontal direction. The SASSI model produces higher rotational transfer functions than NIST, which is likely due to stiffer materials below the foundation that are accounted for in the SASSI model. The horizontal transfer functions (Figure 3-6) from these models over-predict those from data for frequencies under about 7 Hz, where the coherence is sufficiently high for the results to be meaningful. The rotational transfer functions (Figure 3-7) begin at zero, gradually rise up to about 15 Hz, but have a pronounced peak at about 3 Hz which is likely due to base rocking from inertial interaction. The NIST model matches the data reasonably well whereas the SASSI model under-predicts.

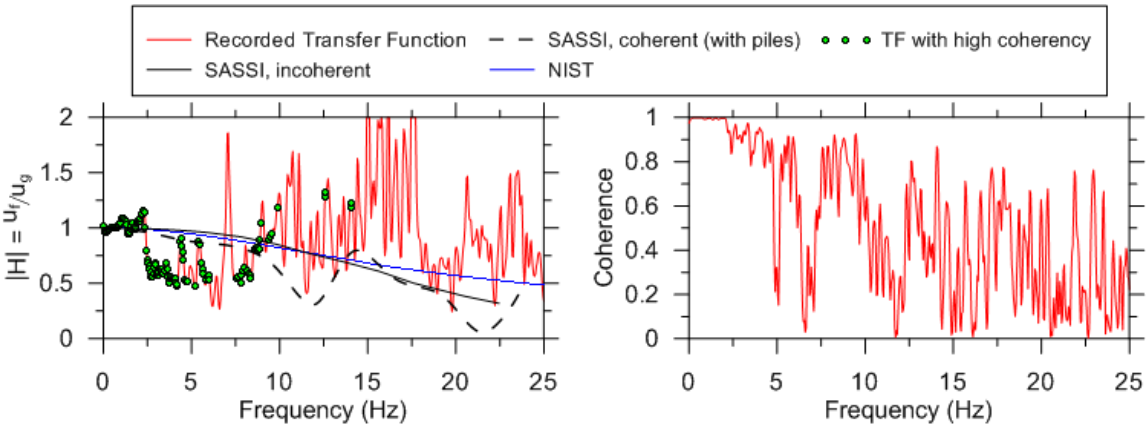

Figure 3-4 **Sendai site horizontal transfer functions and coherence for the 2003 Off Miyagi earthquake.**

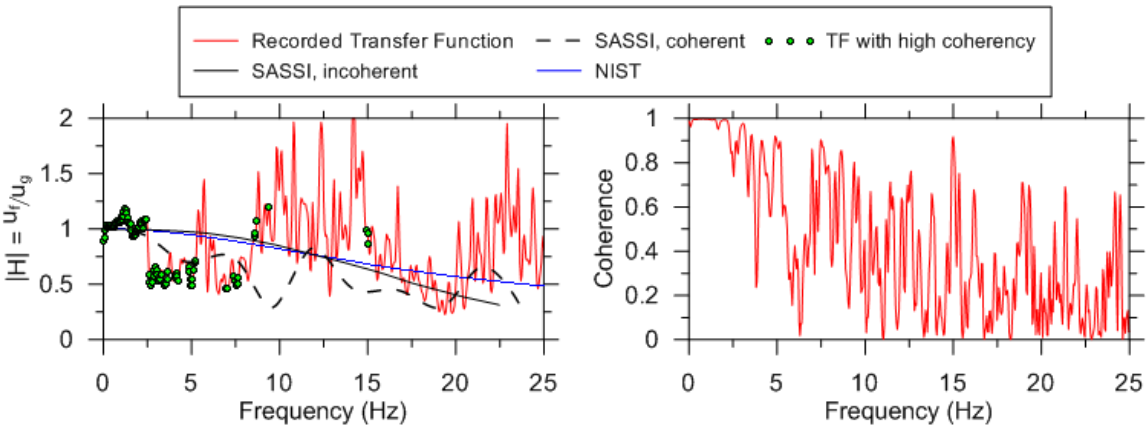

Figure 3-5 **Sendai site horizontal transfer functions and coherence for the 2011 Tohoku earthquake.**

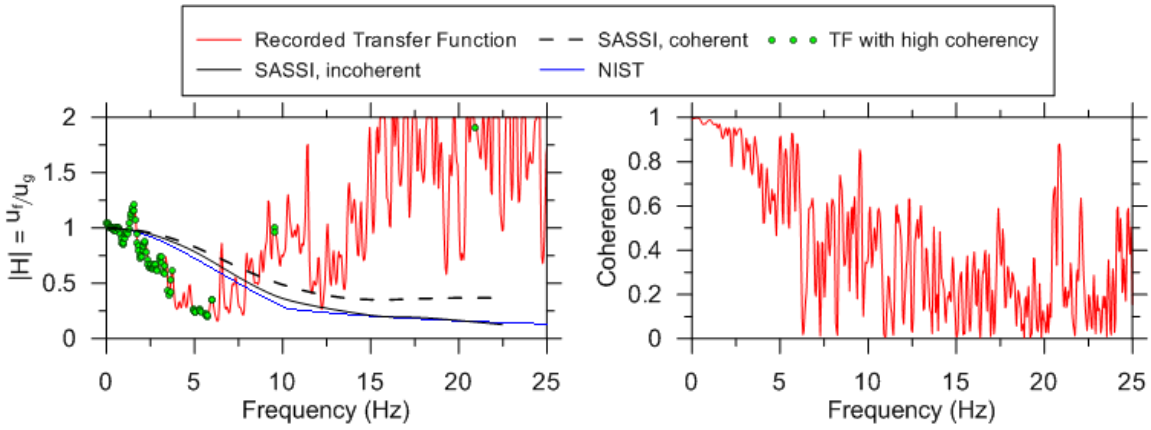

Figure 3-6 **Onagawa site horizontal transfer functions and coherence for the 2011 Tohoku earthquake.**

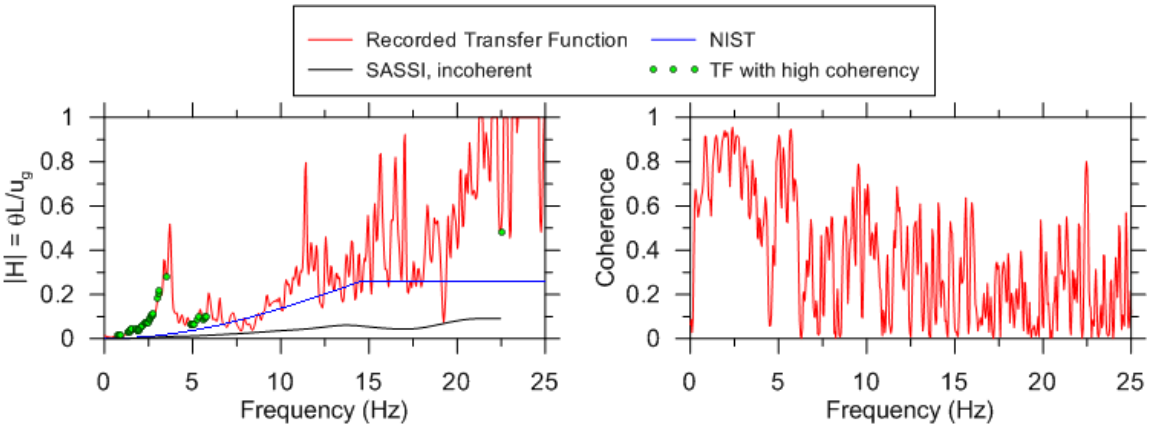

Figure 3-7 **Onagawa site rocking transfer functions and coherence for the 2011 Tohoku earthquake.**

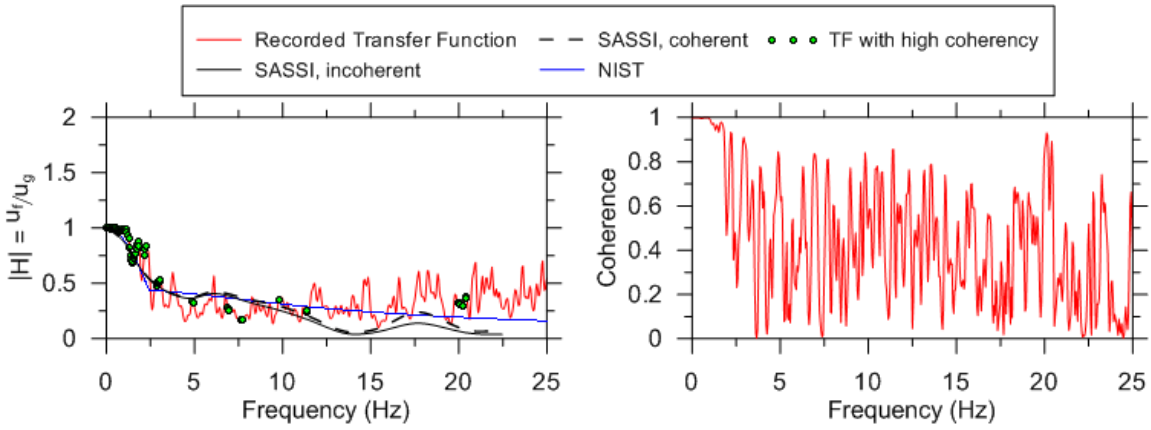

Figure 3-8 **Nagoya site horizontal transfer functions and coherence for the 2004 Off Kii Peninsula earthquake.**

Figure 3-8 presents horizontal transfer functions for the Nagoya site, which is of special interest because of the large embedment and the relatively large foundation horizontal dimensions, which are near the limit of the calibration range in the Kim and Stewart study. The data from this site are a relatively high quality as indicated by high coherence over a wide frequency range. The data are quite consistent with the model, and the low transfer function ordinates (indicating substantial reductions of foundation motions relative to free-field motions) are dominated by embedment effects.

3.5 Interpretation and Conclusions

It has become increasingly common in recent years for structural engineers to take advantage of kinematic interaction effects to reduce foundation level ground motions relative to those specified in the free-field. The guidelines that appear in NIST (2012) and other documents account for the effects of base slab averaging and embedment. The base slab averaging model is semi-empirical, being based on a theoretical formulation calibrated for use in California.

We examine data from several sites in Japan to investigate the effectiveness of the NIST procedures, both relative to the data and relative to predictions from the finite element code SASSI. For all three sites, predictions of horizontal transfer functions from the SASSI code and the NIST procedures are similar over the frequency range of principal interest (up to about 10 Hz). For horizontal motions, the model-based transfer functions were too large (hence conservative) for the Sendai and Onagawa sites. For kinematic base rocking, the model-based predications are accurate from the NIST model but too low from the SASSI model, when compared to data. The model predictions are fairly accurate relative to data at the Nagoya site, which is dominated by embedment effects.

An interesting aspect of the data from the Sendai site is that it has experienced numerous earthquakes of varying shaking amplitudes. Two earthquakes producing moderate and very strong shaking are considered here, with remarkably similar results, suggesting a lack of significant nonlinear effects on the kinematic ground motion reductions for this site. Whether this finding is repeatable and transferable to other sites requires further investigation.

Based on this work, we find generally satisfactory performance of the simplified models for kinematic interaction presented in NIST (2012) using these data from Japan.

4 ASSESSMENT OF ALTERNATIVE SSI MODELING STRATEGIES

4.1 Introduction

The analysis of building seismic response can utilize various approaches for modeling soil-structure interaction (SSI) at the base of the building, including ignoring SSI effects altogether. While some of these approaches are relatively simple, others require significant effort to capture the linear or nonlinear SSI. What is not clear is whether more complex and time-consuming approaches produce substantially different or more accurate results than simpler approaches. This issue is examined while also demonstrating the application of analysis tools presented in a recent guidelines document (NIST, 2012) referred to here as the "NIST report." The NIST recommendations for kinematic effects have been previously discussed in Chapter 3. The analysis tools are applied in the context of substructure analysis of the SSI problem, which requires assumptions of equivalent-linear soil behaviour.

The approach taken in this work is to identify suitable instrumented buildings that have recorded earthquakes, develop complete SSI models for substructure-based analysis of seismic response (referred to as a baseline model), roughly calibrate the structural

elements of the baseline model to approximately match recordings, and then remove components of the baseline model for additional analyses to evaluate the impact of those components. This process is used to identify the critical components of an SSI model for use in response history analysis, and develop recommendations based on those results as well as prior results in the literature. Prior studies have taken a similar approach, but utilized conventional structural software packages (ETABS and SAP) on different buildings (Tileylioglu et al., 2010; Naeim et al., 2008) with slightly different SSI analysis procedures.

4.2 Similar Studies in the Literature

Naeim et al. (2008) and Tileylioglu et al. (2010) utilized conventional structural engineering software packages (ETABS and SAP) to perform response history analysis including elements to capture SSI. The analyses were performed for two buildings (54- and 6-story buildings in Los Angeles) with embedded foundations that had recorded earthquake motions, although only the 54-story building results have been published. The analyses were carried out initially with the model components show in Figure 4-1, where kinematic base rocking was applied to the base of vertical foundation springs in addition to depth-variable ground motions, which double-counts the effects of kinematic rotation. Fortunately, those kinematic rocking effects were minor for the investigated structures and hence do not affect significantly the findings.

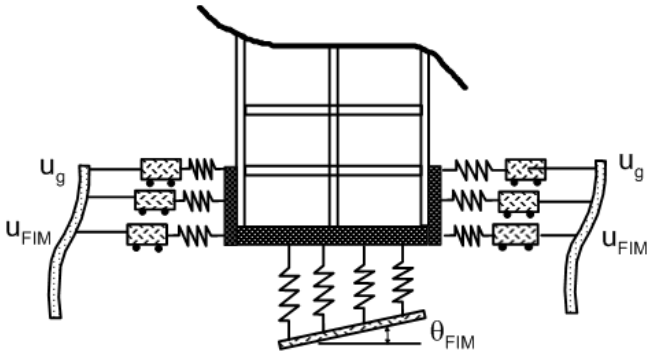

Figure 4-1 **Schematic illustration of simulation used in Naeim et al. (2008) and Tileylioglu et al. (2010).**

The springs were elastic without a compression capacity limit and zero tension capacity. Kinematic effects were evaluated for embedded foundations in a manner similar to that described in Chapter 3 of the NIST report (with exception of kinematic base rocking, which was applied in this work but is not recommended in Chapter 3 of the NIST report except for rigid foundations for which a single horizontal input motion is provided). Difficulties were encountered implementing multi-support excitation in the computer programs, and the results that were obtained were considered reliable for displacements but not for forces. Nonetheless, good matches to observed responses with the model were obtained.

Elements of the model depicted in Figure 4-1 were then stripped from the structural models to investigate their impact on the computed response. Factors found to not significantly influence the results include consideration of multi-support excitation along basement walls and application of the zero-tension condition on foundation springs. Consideration of kinematic interaction effects was significant for the distribution of inter-

story drifts, particularly below the ground line. Consideration of foundation springs was important for the building vibration periods and drift distributions.

Two approximations commonly used in practice were shown to provide poor results: (1) fixing the structure at ground line with input consisting of free-field translation (Model 1 in present study, as described in following section) and (2) fixing the structure at the base level, applying free-field motions as input at the base level, and using horizontal foundation springs along basement walls with their end condition fixed to the free-field ground motion (Model 3 in present study). Fixing the structure at the foundation level (i.e., not ignoring the below ground portion of the structure) and applying free-field translations provided better results. A procedure was used in which kinematic base rocking was applied to a rigid element connected to the foundation springs (termed Model 2b by Naeim et al., 2008). That approach provided an excellent match to MB results.

4.3 Model Types

4.3.1 Baseline Model (MB)

Similar to Naeim et al. (2008) and Tileylioglu et al. (2010) work, analyses of the subject structures began by developing three-dimensional models of the buildings and foundation systems, which are referred to as "baseline models" (MBs). MBs are not intended to be the most accurate models that could be developed (e.g., a direct SSI analysis in a finite element platform could potentially provide improved results), but instead represent the implementation of procedures given in the NIST report. As shown in Figure 4-2, MBs incorporate SSI in the vertical and horizontal directions, including rocking, with a series

of springs and dashpots representing site soil properties. Seismic demands imposed on MBs include base translation as well as kinematic loading of basement walls (simulated by displacement histories applied to the ends of horizontal springs attached to basement walls). Using those seismic demands, MBs are calibrated to match the response interpreted from recorded motions.

Figure 4-2 depicts the MB model, which is implemented using a substructure approach. The springs and dashpots in the figure represent the frequency-dependent foundation impedance for horizontal, vertical, and rocking modes of vibration. The motion u_{FIM} in Figure 4-2 represents the Foundation Input Motion, which is modified from the free-field motion (u_g) for the effects of kinematic interaction.

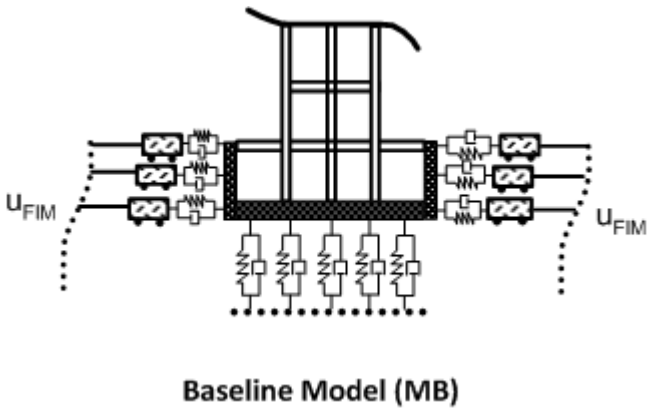

Figure 4-2 Schematic illustration of baseline model considered in simulations.

4.3.2 Simplified and Alternative Models

Once the MBs successfully match the recorded data, components of the seismic demand and soil-foundation interaction elements are replaced, one or more at a time, to match modeling approaches used in practice. The goal of simulations with these simpler models is to assess the changes induced by each simplification on computed engineering demand

parameters (EDPs). As illustrated in Figure 4-3, four simplified models were considered, as follow:

Model 1: Model the above-ground portion of the structure as fixed at the ground surface and exclude subterranean and foundation components. Excite the base of the structure with free-field ground motion u_g. (Flexible structure, rigid basement and soil)

Model 2: Model above-ground and subterranean portions of structure but use no horizontal foundation springs along basement walls and fix the base of the structure against translation or rocking. Excite base of structure with free-field ground motion u_g. (Flexible structure and basement, rigid soil)

Model 3: Subterranean levels are modeled and horizontal and vertical soil springs are included. Horizontal spring at base slab receives input motion (u_g) but horizontal springs at higher elevations are fixed at end with no input. Vertical springs are supported on a fixed base. Applications of Model 3 in engineering practice have been predominantly for pushover analysis, although its use here is for response history analysis, which is expected to demonstrate poor performance.

Model 4 (bathtub): Subterranean levels are supported by horizontal and vertical soil springs that are fixed at their ends to a rigid "bathtub." The bathtub is excited with the horizontal foundation input motion (u_{FIM}) or free-field motion (u_g). (Flexible structure, basement and soil)

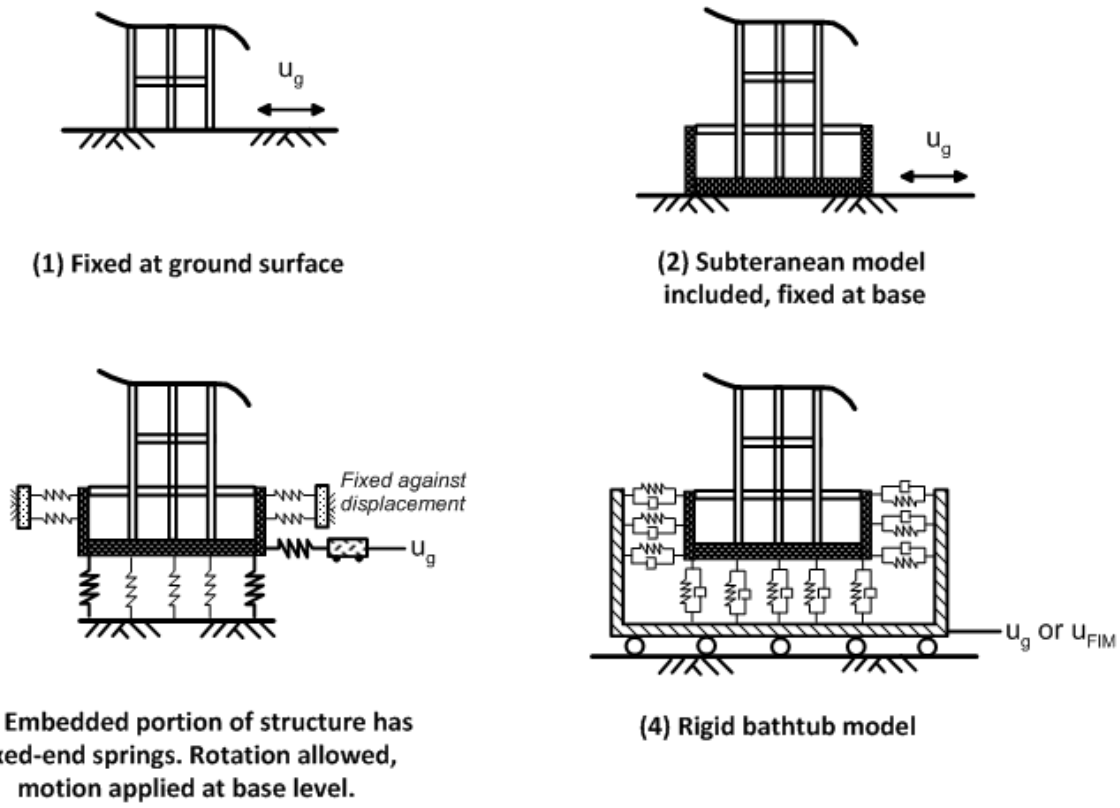

Figure 4-3 Schematic illustration of simplified models 1 to 4 considered in simulations.

These simplified approaches were chosen based on consultations between the ATC/NIST project team and structural and geotechnical engineering practitioners. The purpose of those consultations was to document the state-of-practice in SSI analysis. The outcome of that process is described in the NIST report. Referring to Figure 4-3, Models 1 and 2 are used most often, followed by Model 3. Model 4, which was introduced by Naeim et al. (2008) and was evaluated in the present work, has only very recently begun to see applications in practice.

The only differences between Model 4 and MB pertain to the manner in which seismic demand is specified. The implementation of Model 4 with u_{FIM} is identical to MB

except that the effects of kinematic loading of basement walls associated with depth-variable displacement histories applied to the ends of horizontal foundation springs is neglected. The implementation of Model 4 with u_g takes this a step further by neglecting kinematic interaction altogether by replacing the recorded motions at the base of the building by equivalent free-field motions applied uniformly to the end of all horizontal foundation springs. Input motions are generally specified in the engineering software as accelerations. An exception is the multi-support excitation runs applied for the MB, in which ground motions are specified as displacement histories that are obtained through integration.

Table 4-1 Summary of the Properties of the MB and the Simplified Models Considered

	Model Variations						
Parameters	No. 1	No. 2	No. 3	No. 4 (Bathtub)	MB	MB.1	MB.2
Structural Foundation Elements	N/A	Flexible	Flexible	Flexible	Flexible	Rigid	Flexible
Input Motion	u_g	u_g	u_g	4a: u_{FIM} 4b: u_g	u_{FIM}	u_{FIM}	u_{FIM}
Depth-variable ground motion	No	No	No	No	Yes	Yes	Yes
Spring tension	N/A	N/A	Allowed	Allowed	Allowed	Allowed	Not Allowed

As shown in Table 4-1, variations on the MB (denoted MB.1 and MB.2) are considered as follows:

1. The embedded portion of the building is assumed to be rigid (MB.1). The specification of seismic demand is not modified. The objective here is to specifically investigate the effects of flexibility in structural elements below ground line.

2. Change the manner in which soil flexibility is modeled (MB.2). Specifically, springs are not allowed to develop tension (removal of no-tension interface elements) to provide insight into the effects of nonlinearities in the foundation springs. More sophisticated nonlinear springs were not considered because this effect proved to be minor at the levels of demand imposed by the recorded ground motions.

As shown in Table 4-1, all modeling schemes but MB.2 allow tension in soil springs. The rationale for this approach is that actual basement wall-soil contact prior to earthquake shaking is characterized by a compressive normal stress that would fall in the range of at rest to active earth pressures, whereas the springs have an initial condition of zero force. Earthquake shaking will impose alternating cycles of increased and decreased pressure relative to the initial state, which is well represented by a spring that can develop tension provided the level of deformation does not lead to gap formation. Given the modest demand levels imposed on the Sherman Oaks and Walnut Creek buildings, this was anticipated to be a reasonable assumption, which was tested with Model MB.2 for the Sherman Oaks building.

4.4 Buildings Considered

Only buildings with seismic instrumentation and available earthquake recordings in California were considered. Desirable attributes of a building in this selection process were as follows: (1) embedded foundations, so that kinematic effects associated with embedment and depth-variable ground motions could be evaluated; (2) two vertical sensors to record rocking at the foundation level; (3) relatively regular structural configurations, so that the results obtained are not peculiar to an atypical building type;

and (4) structural configurations and site conditions that would tend to be conducive to significant inertial SSI effects. No single building met all of these criteria. The buildings that were selected are a 13-story building with two-levels of basement in Sherman Oaks, California and a 10-story building without embedment in Walnut Creek, California, shown in Figure 4-4. The Sherman Oaks building is a reinforced concrete moment frame structure that was shaken strongly by the 1994 Northridge earthquake and weakly by several other more distant events. The building is founded on grade beams and friction pile foundations supported by alluvial sediments. The Walnut Creek building is a reinforced concrete dual-system structure with perimeter moment frames and a central core of shear walls. The shear walls are founded on a mat foundation with shallow embedment, resting on weathered shale bedrock. The Sherman Oaks building satisfies the criteria (1) and (3) above, while the Walnut Creek building satisfies (2), (3), and (4).

Figure 4-4 **Photographs of the example applications: 13-story Sherman Oaks building (left) and the 10-story Walnut Creek (right). Photographs obtained from CESMD.**

A parameter that is often used to identify conditions where inertial SSI effects are likely to significantly affect structural response is $h/(V_sT)$, where h is approximately 2/3 of the building height (distance from base of foundation to centroid of first mode shape), V_s is the time-averaged strain-compatible shear wave velocity of the foundation soil over a representative depth, and T is the fixed-base first mode period for the structure. The ratio $h/(V_sT)$ effectively represents a ratio of structure to soil stiffness, and inertial SSI becomes more significant as this parameter increases, typically being important for values of approximately 0.05 to 0.1 or greater (e.g., Veletsos, 1977; Stewart et al., 1999). The $h/(V_sT)$ parameter for each case study is discussed in the following subsections.

4.5 Sherman Oaks Building

The building has 13 stories above the ground surface and a two-level basement. The building is 50 m (164 ft) tall from the ground surface to the roof, with approximately 6.2 m (20.5 ft) of embedment. The height of the first floor is 7.0 m (23 ft), while all other floors above are 3.6 m (11.75 ft). The 1st and 2nd subterranean levels are 3.5 m (11.5 ft) and 2.7 m (9 ft) tall, respectively. The lateral loads are carried by moment-resisting concrete frames that extend from the roof to the foundation, supplemented by perimeter concrete walls at the subterranean levels. Vertical loads are carried by 11.4 cm (4.5 in) concrete slabs supported by the concrete beams and columns in the moment frames. The building was designed in 1964 and was later seismically rehabilitated with friction dampers following the 1994 Northridge Earthquake.

The ratio of structure to soil stiffness for this building is $h/(V_sT) = 0.07$, using building height, soil shear wave velocity, and period values given in subsequent sections.

Because this ratio is < 0.1, strong inertial SSI effects in the form of period lengthening and foundation damping are not expected. The building was nonetheless analyzed because of the other attributes mentioned in Section 4.4 (common building type, regular configuration, embedded foundation, multiple recordings) and the potential for significant kinematic interaction effects on higher mode responses. Moreover, we sought to investigate whether a building for which traditional first-mode SSI metrics indicate no significant effect (i.e., period lengthening near unity, foundation damping near zero), could in fact exhibit potentially significant impacts of SSI on the vertical distribution of EDPs used in structural design (e.g., inter-story drifts, story shears, etc.).

4.5.1 Site Description

Figure 4-5 shows a plan view of the site. The ground surface elevation is approximately 216 m (709 ft) above mean sea level (AMSL). Geotechnical reports with boring and geophysical logs for adjacent properties were obtained from MACTEC Engineering and Consulting Inc. The reports contained 11 borings at a property south of the site and 36 borings at another property northwest of the site. Boring depths ranged from 15 to 38 m (50 to 125 ft). The borings indicate relatively consistent soil conditions, consisting of alluvial deposits composed of silt, with sand and clay overlying shale bedrock at depths ranging from 21-27 m (70 to 90 ft). Figure 4-6 shows our interpretation of the soil layering at the site based on the borehole data.

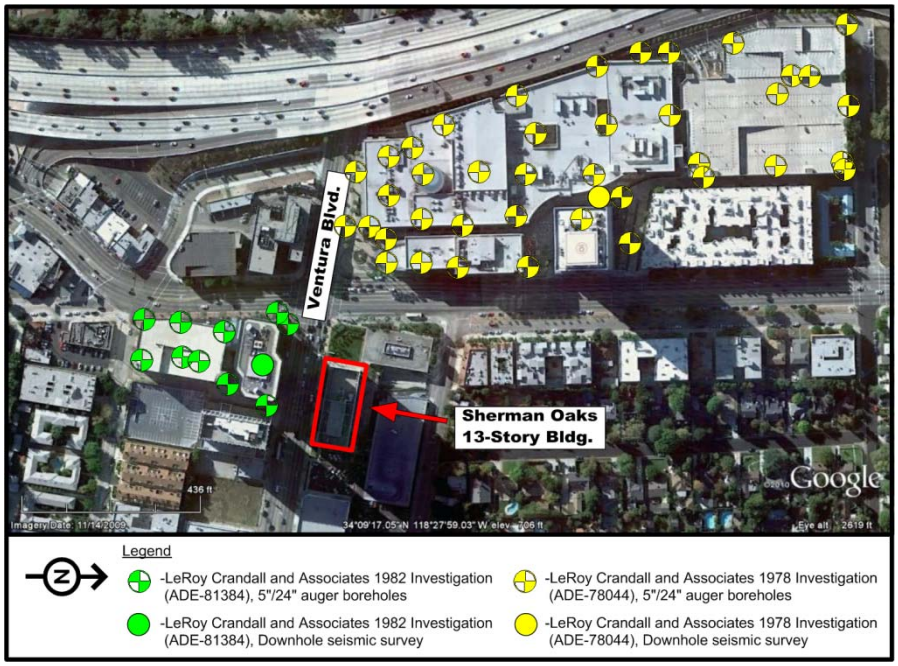

Figure 4-5 **Plan view of Sherman Oaks building site showing locations of borehole and geophysical logs used for site characterization**

The geophysical data at the two neighboring sites was developed from downhole seismic surveys; results from both are shown in Figure 4-6. Also shown is the profile utilized for subsequent analysis, which gives weight to the conditions revealed by the borings south of the site due to their relative proximity. Based on the MACTEC reports, average moist unit weight is approximately 20 kN/m^3 (124 lb/ft^3). The water table was measured at adjacent sites at an approximate depth of 12 m (40 ft) below the ground surface.

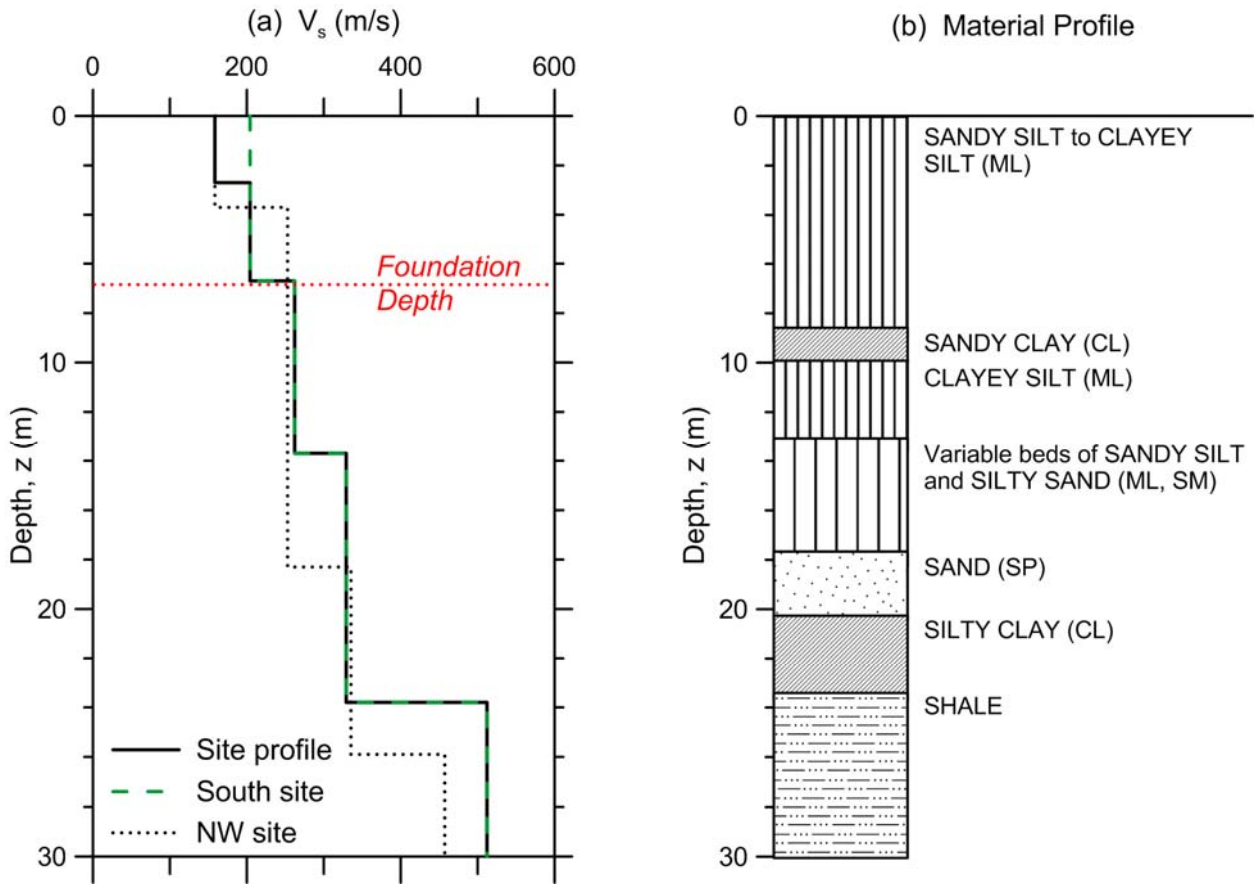

Figure 4-6 **Subsurface characteristics based on adjacent site exploration at sites south and northwest (NW) of the local intersection of the Sherman Oaks building: a) shear wave velocity profile and b) material profile. 1 ft = 0.3048 m**

To estimate strength properties of the foundation soils, drained direct shear test results from samples retrieved at the south and NW properties were utilized. In the shallow soils where most of the foundation-soil load transfer will occur, the soil is unsaturated so drained shear strengths are used. For the range of surcharge pressures appropriate for the soil profile across the pile depth of 16.2 m (53.1 ft) below ground surface, the soil Mohr Coulomb strength parameters inferred from the available data in the MACTEC reports are c' = 20.1 kN/m^2 (419.8 psf) and $\phi' = 30°$ for 0 to 6.1 m (0 to 20 ft) and c' = 12.9 kN/m^2 (269.4 psf) and $\phi' = 38°$ for 6.1 to 16.8 m (20 to 55.1 ft).

4.5.2 Ground Motion Recordings

The Sherman Oaks building is designated as CSMIP Station No. 24322. It contains 15 accelerometers at the locations shown in Figure 4-7 and has been instrumented since 1977. The accelerometers are located on 5 levels: the 2nd subterranean, ground surface, 2nd, 8th and roof levels. Note that there is only one vertical sensor at the foundation level, so base rocking effects cannot be measured. There is also no free-field ground instrument in the vicinity of the site. The foundation and structural conditions illustrated in Figure 4-7 are described in the next section.

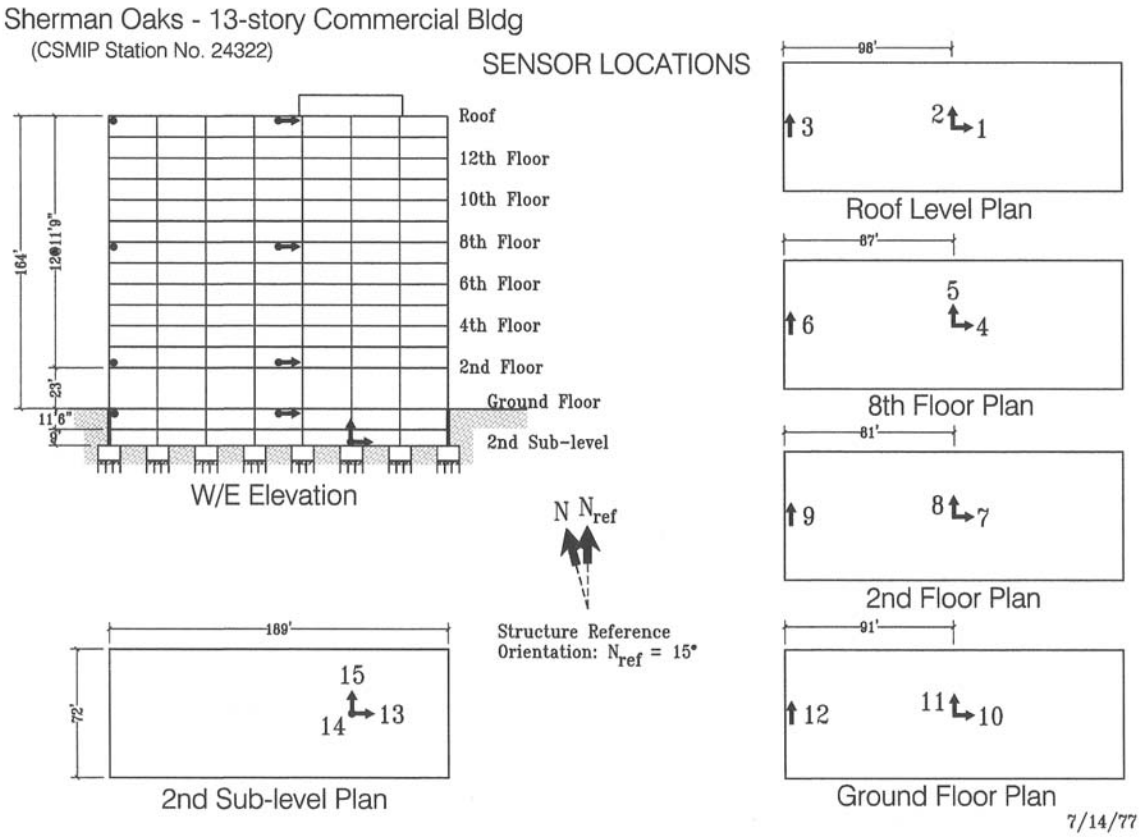

Figure 4-7 CSMIP Station No. 24322: Sherman Oaks 13-Story commercial building, cross-sectional view and sensor location sketch

The Center for Engineering Strong Motion Data (CESMD) has cataloged and reviewed six sets of recorded motions at this building since 1977. The recorded earthquake events and peak accelerations for the 2nd subterranean level, ground floor and roof are presented in Table 4-2. Note that the accelerations follow an unusual pattern in which the largest motions are at the ground floor (foundation and roof motions being smaller).

The horizontal translations recorded at the base of the 2nd subterranean level of the building were used as the foundation input motions (u_{FIM}). The u_{FIM} is the modified u_g response due to base slab averaging and embedment effects as discussed in Chapter 3. Typically in practice, u_g is known and the u_{FIM} would be calculated for structural analysis from transfer functions. In this case, u_{FIM} was measured and u_g was back-calculated by removing the base slab averaging and embedment effects. Figure 4-8 shows the u_{FIM} and u_g response spectra for the Northridge earthquake. The identified periods shown in Figure 4-8 were calculated as horizontal transfer functions of the power spectral density functions of the foundation recording and roof recording from the Northridge earthquake.

Table 4-2 Summary of Recorded Earthquake Events and Peak Accelerations (g) at Three Levels

Earthquake	2nd Subterranean			Ground Floor			Roof		
	NS	EW	V	NS	EW	V	NS	EW	V
1987 Whittier	0.100	0.148	0.038	0.250	0.169	----	0.140	0.140	----
1992 Landers	0.039	0.031	0.012	0.045	0.035	----	0.085	0.095	----
1994 Northridge	0.453	0.227	0.181	0.886	0.392	----	0.467	0.257	----
2007 Chatsworth	0.015	0.022	------	0.045	0.058	----	0.025	0.036	----
2008 Chino Hills	0.049	0.037	0.010	0.073	0.045	----	0.082	0.067	----
2010 Calexico	0.004	0.004	0.003	0.004	0.005	----	0.049	0.022	----

*NS, EW, and V = north-south, east-west, and vertical, respectively.

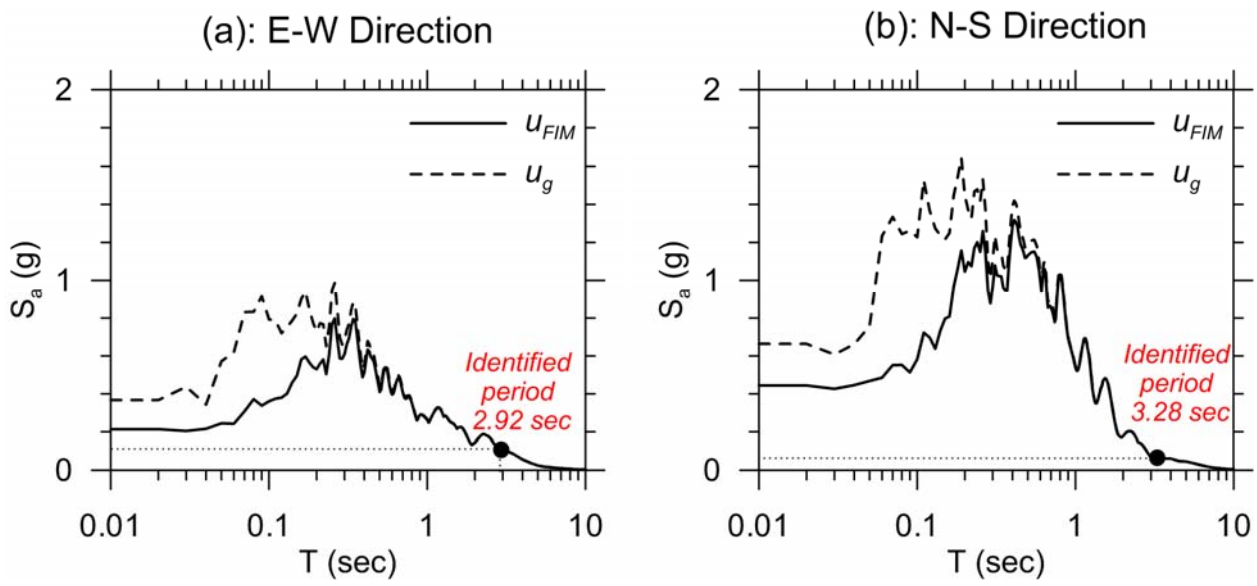

Figure 4-8 **Response spectra of u_{FIM} (recorded) and u_g (inferred) for Sherman Oaks building, 1994 Northridge earthquake**

An equivalent linear ground response analysis was performed in DeepSoil v4.0 to estimate the depth-variable ground responses adjacent to the embedded portion of the structure, taking the recording of u_{FIM} as input at 6.7 m (22 ft) with an elastic half-space[1]. Dynamic soil properties consisted of the V_s profile shown in Figure 4-6 and modulus reduction and damping curves appropriate for the overburden pressures and soil types as given by Darendeli (2001). DeepSoil does not update the shear modulus reduction of the elastic half-space as performed for the soil column above during the analysis. Therefore, the elastic half-space V_s parameter was updated through iterative runs until convergence with the V_s of the deepest layer of the soil column. Figure 4-9 shows the computed

[1] Input motions in ground response analyses can be specified as outcropping or within, the former requiring an elastic halfspace and the latter a rigid base (Kwok et al., 2007). For the Sherman Oaks building, the motion was recorded "within" the profile, but on a large foundation slab that could be interpreted as representing an outcropping condition. Analyses were performed for both conditions, with the outcropping results appearing more realistic.

variation of PGA and PGV with depth through the soil column. Note that PGA increases significantly over the embedment depth (approximately 50%) whereas the change in PGV is minor.

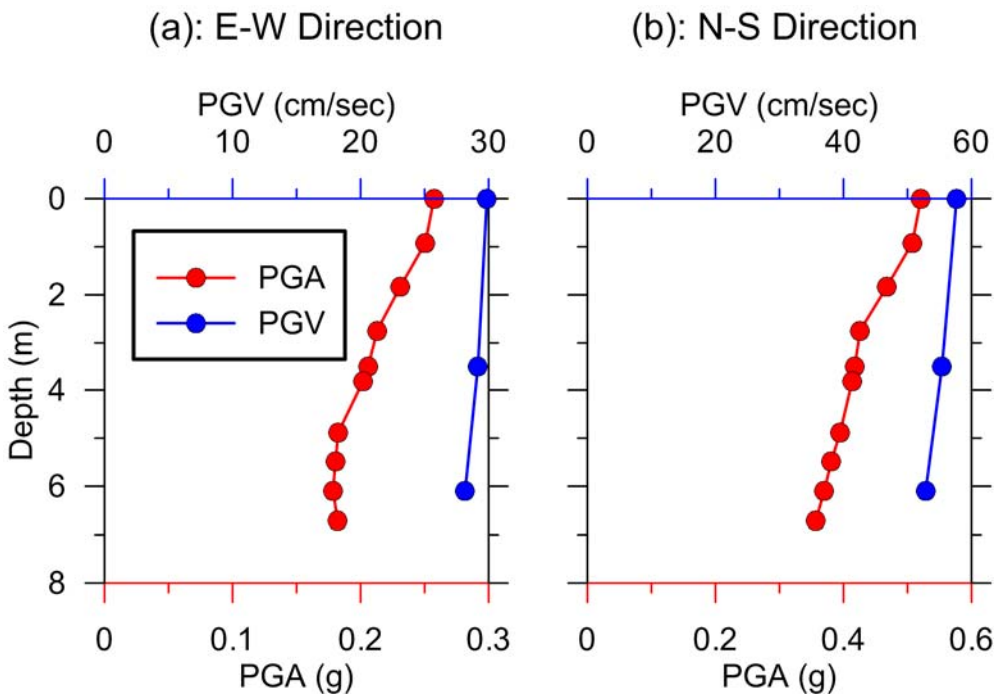

Figure 4-9 **Calculated variation of peak acceleration and velocity over the embedment depth for Sherman Oaks building, 1994 Northridge earthquake**

4.5.3 Foundation Conditions

We obtained construction drawings of the building from the California Strong Motion Implementation Program (CSMIP). The drawings are heavily pixilated and difficult to read, so our interpretation of structural details may not perfectly reflect the content of the original drawings. This subsection focuses on the foundation conditions that were captured for the MB. The foundation support with springs and dashpots is described in

4.5.4. Structural modeling is briefly discussed in Section 4.7, and further details are provided in Appendix A of the NIST report.

Figure 4-10 shows that the foundation is composed of variously configured bored pile groups connected with grade beams. The cast-in-place (bored) concrete piles are 51 cm (20 in) in diameter and extend to a depth of approximately 9.9 m (32.5 ft) below the lower subterranean level. Typical spacing of piles (center to center) is 0.9 to 1.2 m (3 to 4 ft). The foundation is rectangular in shape with plan dimensions of 36.3 by 57.6 m (119 by 189 ft). The dimensions of the main structure above the ground surface are 21.9 by 57.6 m (72 by 189 ft), although there is a widened section at the first floor matching the foundation dimension. Basement walls surround all embedded levels with the southern wall supported on approximately 36 0.6 m (2 ft) bored piles. Spacing for these piles is generally 1.8 m (6 ft) center to center with the exception of closer spacing near the elevator shaft.

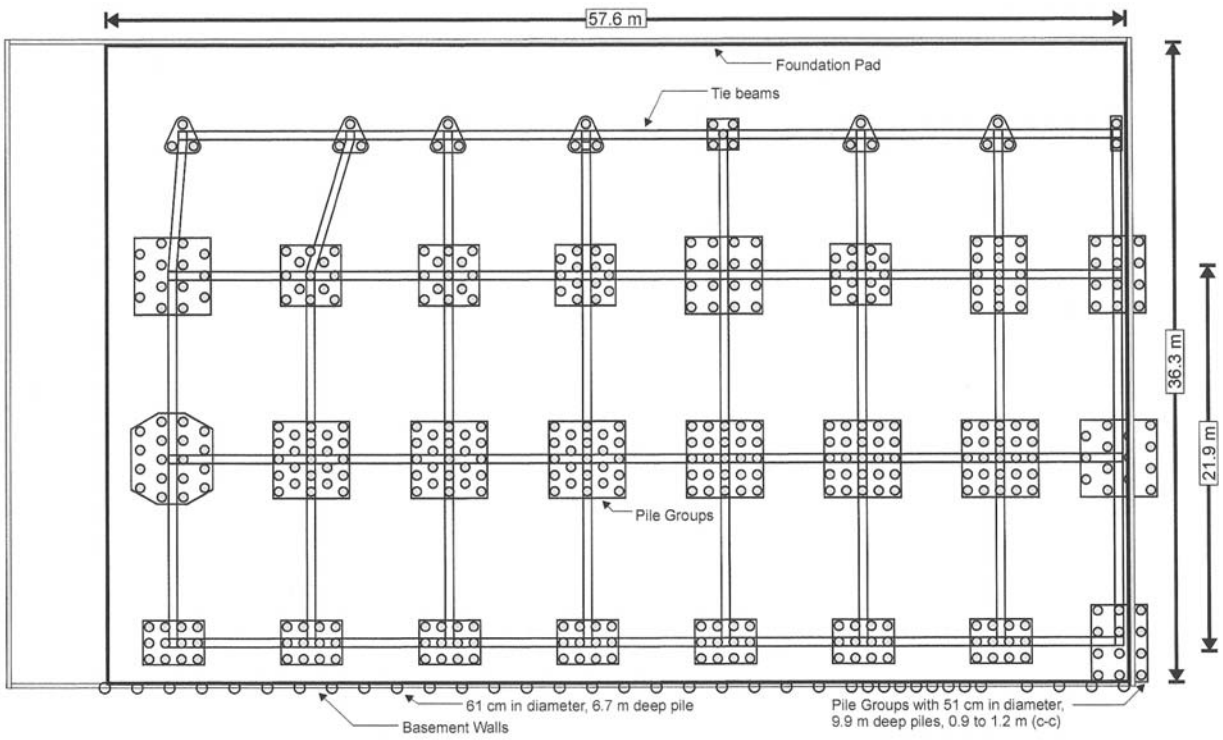

Figure 4-10 Sherman Oaks building foundation plan, based on construction drawings. 1 ft = 0.3048 m

4.5.4 Development of Foundation Springs and Dashpots

In this section, the development of foundation springs and dashpots is described using the input parameters given in Sections 4.5.1-4.5.3. The critical input parameters are foundation dimensions, structural period, soil properties, and input motion amplitudes. The analysis methodologies are described in Chapter 2 of the NIST report. Foundation-soil resistance from both shallow and deep foundation elements are considered in our analysis of springs and dashpots. Hence, it is assumed that the shallow foundation elements (principally grade beams) remain in contact with the soil, which is justified by

the sandy nature of the foundation soils and the presence of friction (not end bearing) piles. The following are emphasized in the present discussion:

- Identification of effective profile shear wave velocity for shallow foundation elements in consideration of foundation dimensions, overburden pressures from the structure, and nonlinear effects.
- The calculation of shallow foundation horizontal stiffness and damping and their separation into contributions from the base slab (derived principally from slab-soil frictional stresses) and passive pressures against the basement walls.
- The calculation of vertical stiffness and damping for a bed of springs under the base slab, emphasizing the proper representation of rotational impedance for shallow foundation elements.
- The distribution of shallow foundation springs and dashpots to the modeled structure nodes.
- The calculation of limiting spring forces (capacities).
- The contributions of pile groups to the vertical and lateral stiffness of the foundation system.

Effective Profile Velocity: As described in Section 2.2.2 of the NIST report, effective profile velocity is calculated by averaging velocities (as ratio of profile depth to shear wave travel time) across specified profile depths, z_p. Table 4-3 shows the values of z_p for each foundation vibration mode along with the depth range used for the calculation of effective velocity. The maximum depth considered is not equal to z_p because of the

foundation embedment (D). The depth range is taken from the ground surface to z_p+D for each vibration mode. For the specific case of the horizontal base spring, a narrower depth interval starting at the base of the foundation is used, as described further below.

Table 4-3 Effective Profile Depths and Velocities for Calculation of Static Stiffness. 1 ft=0.3048 m

Vibration Mode	Eq. for z_p (from Eq. 2.46[a]	z_p (m)	Depth Range (m)	V_{s0}[b] (m/s)
Horizontal Translation (x & y), overall	$\sqrt{BL}$	17.8	0 to 24.0	254.2
Horizontal Translation (x & y), base spring	$\sqrt{BL}$	17.8	6.2 to 24.0	296.2
Vertical Translation (z)	$\sqrt{BL}$	17.8	0 to 24.0	254.2
Rocking along x-axis (xx)	$\sqrt[4]{B^3L}$	14.0	0 to 20.2	243.0
Rocking along y-axis (yy)	$\sqrt[4]{BL^3}$	22.6	0 to 28.8	277.7

[a] B=11 m (foundation half width in short direction), L=28.8 m (half-length). Foundation depth D=6.2 m.
[b] V_{s0} is the free-field, non-overburden corrected average shear wave velocity.

As described in Section 2.2.2 of the NIST report, free-field velocities V_{s0} should be increased to account for the increased overburden provided by structure weight. For the Sherman Oaks building, the mass of the excavated soil for the basement is slightly greater than the structural mass (using values from Section 4.5.3), so no overburden correction is needed. The nonlinear shear modulus reduction factor is 0.5 per Table 4-1 and the Northridge earthquake peak acceleration of about 0.4g (Site Class D). No modulus reduction is required for other events.

Horizontal Stiffness and Damping: Table 4-4 shows the calculation of horizontal static stiffnesses and damping values. Horizontal static stiffnesses, including embedment effects, are calculated based on the gross foundation dimensions of 21.9 m by 57.6 m. As shown in Figure 4-10, the foundation plan for the structure includes pile-caps interconnected with grade beams and a surficial slab. The use of gross foundation

dimensions to calculate static stiffnesses assumes that stress-transfer from pile caps and grade beams occurs in stress bulbs that overlap at modest depth, so that the shallow foundation components effectively act as a unified system. This assumption does not require load transfer from the relatively thin foundation slab to the soil. The horizontal stiffness has contributions from base shear and passive pressure against basement walls. Because the base shear reaction mobilizes only soil below the embedment depth D, the effective profile velocity for the base spring is taken from D to $D+z_p$, as shown in Table 4-3. These horizontal base spring stiffnesses, which are given in Table 4-4, are then subtracted from the overall horizontal stiffness to evaluate the contribution from passive pressures against the basement walls.

Table 4-4 is organized to first present the reduced shear modulus used for the spring calculations, which are derived from the velocities in Table 4-3 along with the mass density (20 kN/m^3/g) and the shear modulus reduction (0.5 for Northridge). Static stiffnesses are then computed as the product of a surface stiffness (Table 2-1a) and embedment factor (Table 2-1b); both values are given in Table 4-4. Dimensionless frequency a_0 is calculated, from which dynamic modifiers of stiffness (α_x, α_y) and radiation damping coefficients (β_x, β_y) are computed. The damping ratio used for dashpot calculations is the sum of the radiation damping coefficient and hysteretic damping, which is evaluated from Darendeli (2001) as 0.088 for Northridge and 0.009 for other events. The calculation of dynamically modified spring stiffness and dashpot coefficient from these results is detailed in Table 4-4.

Table 4-4 Evaluation of the Impedance Functions For Sherman Oaks Building. Static Stiffness Results Shown are for Case of Northridge Earthquake, Which Uses a Shear Modulus Reduction Factor of G/G_0=0.5. Shear Moduli (G) and Static Stiffnesses (K_{sur}) for Other Earthquakes are Doubled Relative to Those Shown In This Table (G/G_0=1 for Those Events)

Spring/Dashpot	G (MPa)	Table 2-1a K_{sur} (kN/m)[a] or (kN.m/rad)[b]	Table 2-1b η	Eq. 2-7b a_0[c]	Table 2-1a α	Table 2-1a β_{sur}	Table 2-1b β_{emb}	Dynamic Stiffness	Dashpot
Horizontal, overall x-direction $(k_{x,total}\ \&\ c_{x,total})$	65.2	6.48e6	1.45	0.13	1	0.076	0.114	$k_{x,total} = \alpha_x K_{x,sur} \eta_x$	$c_{x,total} = k_{x,total}\left(\frac{2\beta_{emb} + \beta_s}{\omega}\right)$
Horizontal, overall y-direction $(k_{y,total}\ \&\ c_{y,total})$	65.2	7.04e6	1.45	0.13	1	0.070	0.106	$k_{y,total} = \alpha_y K_{y,sur} \eta_y$	$c_{y,total} = k_{y,total}\left(\frac{2\beta_{emb} + \beta_s}{\omega}\right)$
Horizontal, base spring x-direction $(k_{x,base}\ \&\ c_{x,base})$	88.6	8.81e6	N/A	0.11	1	0.065	N/A	$k_{x,base} = \alpha_x K_{x,sur}$	$c_{x,base} = k_{x,base}\left(\frac{2\beta_{sur} + \beta_s}{\omega}\right)$
Horizontal, base spring y-direction $(k_{y,base}\ \&\ c_{y,base})$	88.6	9.56e6	N/A	0.11	1	0.060	N/A	$k_{y,base} = \alpha_y K_{y,sur}$	$c_{y,base} = k_{y,base}\left(\frac{2\beta_{sur} + \beta_s}{\omega}\right)$
Vertical, z $(k_z\ \&\ c_z)$	65.2	8.55e6	1.22	0.13	1	N/A	0.132	$k_z = \alpha_z K_{z,sur} \eta_z$	$c_z = \left(\frac{2(\beta_{emb} + \beta_s)k_z}{\omega}\right)$
Rocking about x-axis $(k_{xx}\ \&\ c_{xx})$	58.0	1.05e9	1.74	0.14	1	N/A	0.010	$k_{xx} = \alpha_{xx} K_{xx,sur} \eta_{xx}$	$c_{xx} = \left(\frac{2(\beta_{emb} + \beta_s)k_{xx}}{\omega}\right)$
Rocking about y-axis $(k_{yy}\ \&\ c_{yy})$	73.9	5.55e9	1.58	0.12	0.99	N/A	0.003	$k_{yy} = \alpha_{yy} K_{yy,sur} \eta_{yy}$	$c_{yy} = \left(\frac{2(\beta_{emb} + \beta_s)k_{yy}}{\omega}\right)$

[a] Translation static stiffnesses calculated using B=11 m, L/B=2.625, and ν=0.33.

[b] Rotational Static stiffnesses calculated using B=11 m, L/B=2.625, and ν=0.33.

[c] Calculated at frequency corresponding to first-mode period of structure, taken as T = 2.7 sec.

Vertical Stiffness and Damping: Overall vertical and rotational stiffnesses are computed using the profile velocities given in Table 4-3 with the results in Table 4-4. Distributed vertical springs are provided over the base of the foundation, as shown in Figure 4-10. The springs are provided in the form of a vertical stiffness intensity, which is stiffness normalized by area (e.g., Equation 2-19 of the NIST report). The stiffness of any individual spring is computed as the product of stiffness intensity and the tributary area for the spring. As described in Section 2.2.3 of the NIST report, stiffness intensities are adjusted near the edges of the foundation to match the overall rocking stiffness values given in Table 4-4 (using Equation 2-20a-b of the NIST report). End length ratio R_e = 0.4 was used for these calculations.

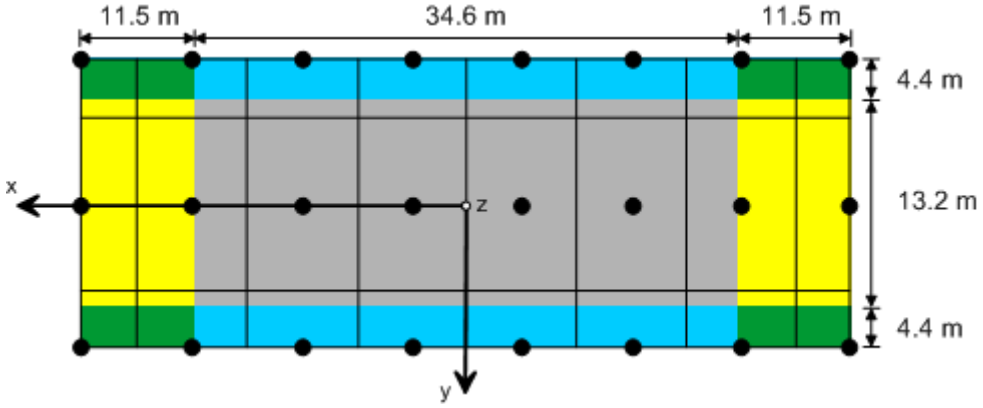

	$k_z^i\ (kN/m^3)$	$c_z^i\ (kN.sec/m^3)$
	8,202	715
	29,361	2,454
	36,524	3,209
	43,687	3,964

Figure 4-11 **Vertical spring and dashpot intensities and areas distinguished by color. Solid lines represent tributary area boundaries in which stiffness and dashpot values were distributed to the column node of each area. Solid circles represent column nodes. 1 ft = 0.3048 m**

The vertical stiffness intensities in the gray central zone in Figure 4-11 are computed from Equation 2-19 of the NIST report and reflect the vertical impedance. The edge intensities in the blue and yellow zones are increased by factor R_k = 5.33 for the *xx* direction and 3.58 for the *yy* direction. Stiffness intensities for corner zones were evaluated as the average of the *xx* and *yy* intensities. Dashpot intensities are calculated from stiffness intensities as $c_z^i = 2R_c\beta k_z^i/\omega$, where R_c represents the reduction factor to capture rotational rocking (Equation 2-20c-d of the NIST report).

Pile Groups: Pile group horizontal and vertical stiffness and damping were evaluated in accordance with Section 2.3 of the NIST report. As shown in Table 4-5, active pile length L_a is evaluated separately for the two vibration modes and is longer for vertical than horizontal (the calculation is iterative using results from Syngros, 2004). Effective shear wave velocity is calculated over the depth interval D to $D+L_a$; shear modulus is calculated from effective velocity and reduced for large strain effects (reduction factor of 0.5 for Northridge; 1.0 otherwise). Static single pile stiffnesses are calculated using Equation 2-21b and Table 2-3a of the NIST report. Dynamic group factors are then evaluated from Figure 2-12 of the NIST report; results are given in Table 4-5 for 3x3 and 4x4 group sizes. Those results were applied to individual pile groups (shown in Figure 4-3), with 3x3 results applied to groups with N_{pile}=12 and 4x4 results applied to groups with $N_{pile}\geq$13. Per Figure 2-12 of the NIST report, the stiffnesses of individual groups (k^G) are then calculated as the product of the group stiffness ratio, static single pile stiffness, and N_{pile}.

Table 4-5 Calculation of Pile Group Stiffnesses for Horizontal and Vertical Vibration. Modulus Applies for Case of Northridge Earthquake with G/G_0=0.5

Spring, dashpot	Active length, L_a (m)	V_{s0} (m/s)	G (MPa)	Static SP stiffness $K_j^p \left(\frac{MN}{m}\right)$	Group stiffness ratio, Fig 2-11[a]	Group Radiation Damp., β_j Fig 2-11[a]
Hor., x&y (3x3 grp)	4.1	180.1	63.4	237.3	0.47	0.2
Vert., z (3x3)	9.9	183.7	67.6	859.3	0.43	0.25
Hor., x&y (4x4 grp)	4.1	180.1	63.4	237.3	0.36	0.05
Vert., z (4x4)	9.9	183.7	67.6	859.3	0.30	0.29

Note: Static single pile (SP) stiffnesses calculated for E_p = 474.8 MN/m and d=0.6 m.

[a] Figure is in the NIST report (NIST, 2012)

Nodal Distribution: As shown in Figure 4-12, the horizontal springs and dashpots were distributed across nodes on the basement walls (representing passive pressures) and base slab (representing base shear). Vertical springs and dashpots were distributed across nodes on the base slab. There are a total of 68 nodes on the foundation having springs and dashpots. The basement walls nodes are positioned at the columns lines at the foundation floor, 1st subterranean floor and ground surface floor, resulting in each wall containing 3×8 and 3×3 nodes, in the longitudinal and transverse directions, respectively. Based on column locations, the foundation slab has 3×8 nodes, with the 22 perimeter nodes also being used for the basement walls.

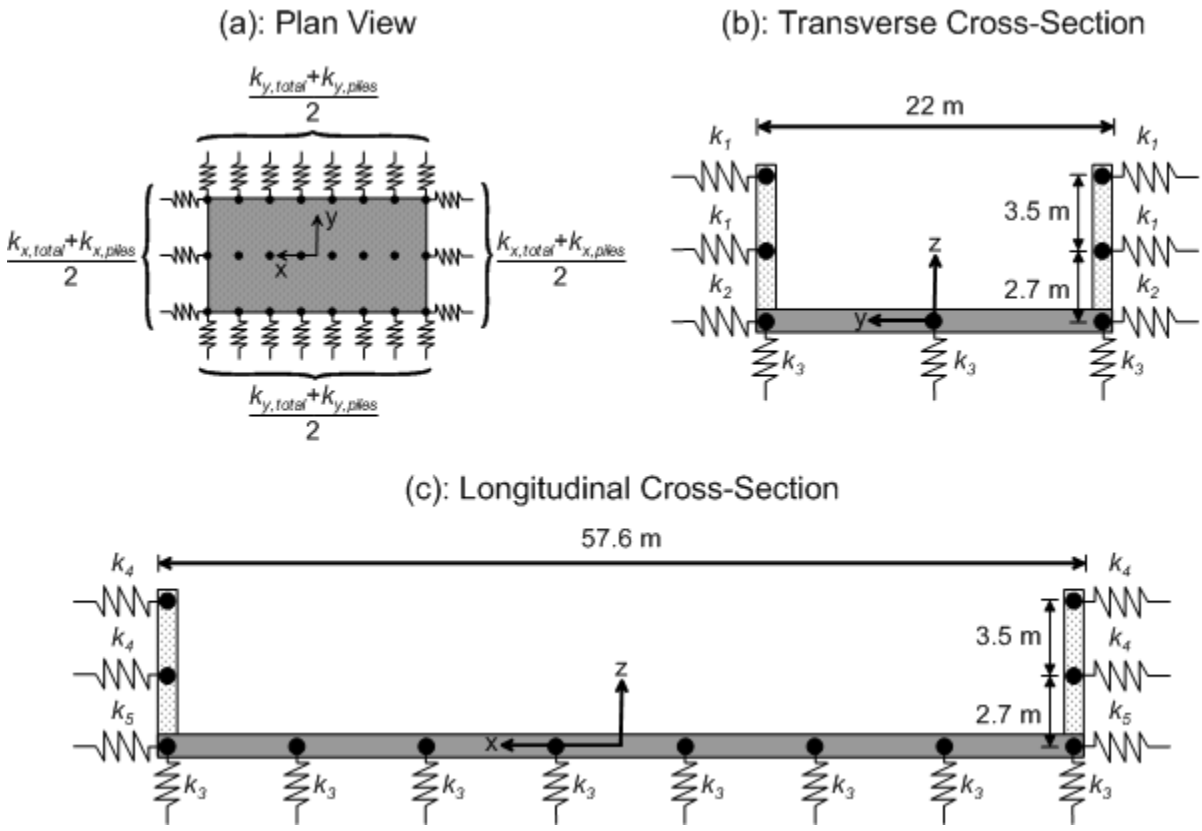

Pile Group Contribution	$k_{y,piles} = \sum k_y^G$	$k_{x,piles} = \sum k_x^G$
Translation in the y-direction	$k_1 = \frac{k_{y,total} - k_{y,base}}{48}$	$k_2 = k_1 + \frac{k_{y,base}}{16} + \frac{k_{y,piles}}{16}$
Translation in the x-direction	$k_4 = \frac{k_{x,total} - k_{x,base}}{27}$	$k_5 = k_4 + \frac{k_{x,base}}{6} + \frac{k_{x,piles}}{6}$
Translation in the z-direction	$k_3 = k_z^G + k_z$ Note: k_3 is not a constant value, k_z^G is a function of N_{piles} and k_z is a function of intensities in Figure 4-11.	

Figure 4-12 Distribution of nodes on foundation and calculation of individual spring stiffnesses.

The overall horizontal stiffness, combining the attributes from base shear, passive pressure against basement walls and pile groups, was distributed to the foundation perimeter (i.e., interior nodes have no horizontal springs). Half the overall horizontal stiffness was distributed to each edge of the foundation for a given direction as shown in Figure 4-12a. As described previously, the total stiffness is partitioned vertically into a base stiffness and a wall stiffness for a given direction. Wall stiffnesses are equally distributed to each basement wall node. Base stiffnesses are equally distributed along the sides of the foundation. These distributions are shown in cross-sections in Figure 4-12b and 4-12c with their respective calculations for each elevation. The vertical stiffness was modeled at all 24 foundation nodes as the contribution of the aforementioned stiffness intensity areas in Figure 4-11 and the columns respective vertical pile group stiffness (k_z^G). Dashpots were distributed in the same manner as their respective springs as shown in Figure 4-12.

Capacities of individual springs were evaluated using conventional vertical and lateral pile group capacity analysis (e.g., Salgado, 2006). The pile group capacities were assigned to nodes in the manner described above for stiffness. These capacities are compared to spring force demands in the following section.

4.6 Walnut Creek Building

The Walnut Creek office building has 10 stories above the ground surface and no subterranean levels. The building is 39.2 m (129 ft) tall from the ground surface to the roof. The height of the first floor is 4.9 m (14 ft), while all other floors above are 3.8 m (12.5 ft). Lateral loads are carried by an interior concrete shear wall core that is

embedded 3 m (10 ft) and an exterior precast and cast-in-place concrete frame. Vertical loads are carried by 7 cm (2.75 in) lightweight concrete over 7 cm (2.75 in) precast panel slabs supported by a precast, prestressed reinforced concrete beams. The building was designed in 1970.

The ratio of structure to soil stiffness for this building is $h/(V_sT) = 0.11$ using effective building height, soil shear wave velocity, and period values given in subsequent sections. Because this ratio is > 0.1, potentially significant inertial SSI effects in the form of period lengthening and foundation damping are expected. Other motivating factors for analyzing this building include the dual-system configuration of the structure and the presence of two vertical instruments at the foundation level that can be used to infer rocking of the core shear wall system.

4.6.1 Site Description

Figure 4-13 shows a plan view of the site. The ground surface elevation is approximately 51.8 m (170 ft) above mean sea level (AMSL). Portions of a geotechnical report, prepared by Harding, Miller, Lawson & Associates (1970), were obtained for the modeled structure and adjacent parking structure. A geotechnical report with seismic refraction investigation of the subsurface soils, prepared by Raney Geotechnical (1983), was obtained for the property adjacent to the aforementioned parking structure.

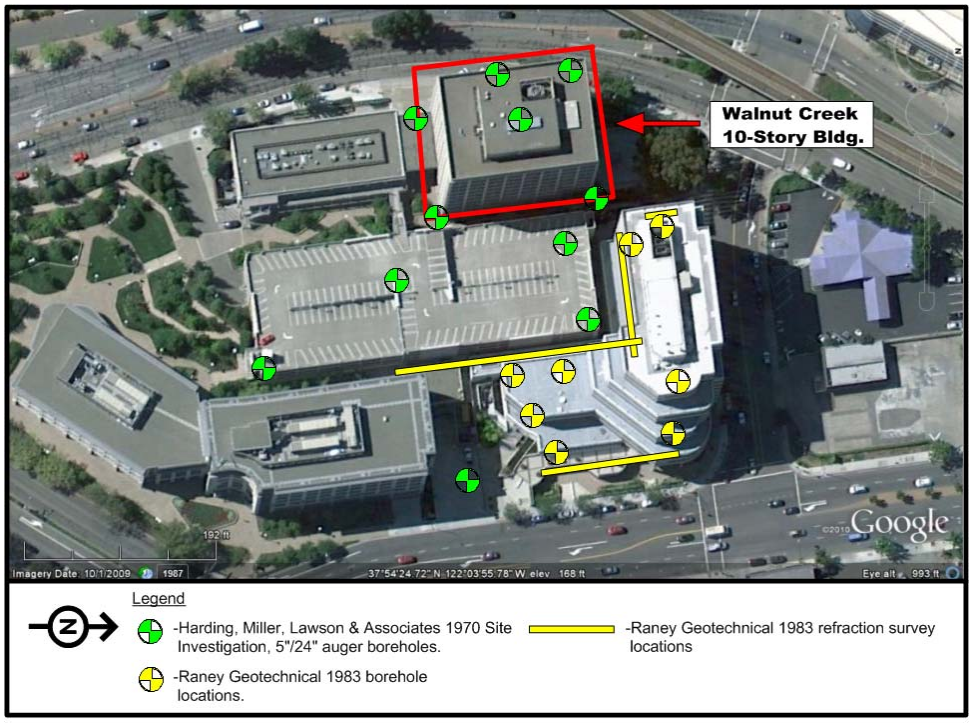

Figure 4-13 **Site plan of Walnut Creek office building showing locations of borings and refraction lines**

As shown in Figure 4-13, the reports contained six borings in and around the ground surface footprint of the Walnut Creek building, five borings at the parking structure, and eight borings at the adjacent property. Four seismic refraction surveys were performed and the two closest to the modeled site were utilized for analysis of the soils' seismic properties. Boring depths ranged from 1.5 to 17.4 m (5 to 57 ft). The borings indicate predominantly west dipping contacts of sandy clays and silts with variable thickness of 0.6 to 5.5 m (2 to 18 ft) overlying siltstone and sandstone of the Orinda Formation. Figure 4-14 shows the material profile based on the aforementioned reports at the location of the interior core foundation.

The geophysical data at the neighboring site was developed from seismic refraction surveys; interpreted shear wave velocity results for the modeled site are shown

in Figure 4-14. The shear wave velocities in the soils were estimated based on correlations by Fumal and Tinsley (1985), while the shear wave velocity in the rock was based on the seismic refraction data presented by Raney Geotechnical. Based on the reports, average moist unit weight is approximately 18.1 kN/m^3 (115 lb/ft^3). The water table depth was measured between 6.1 to 12.2 m (20 to 40 ft) below the ground surface.

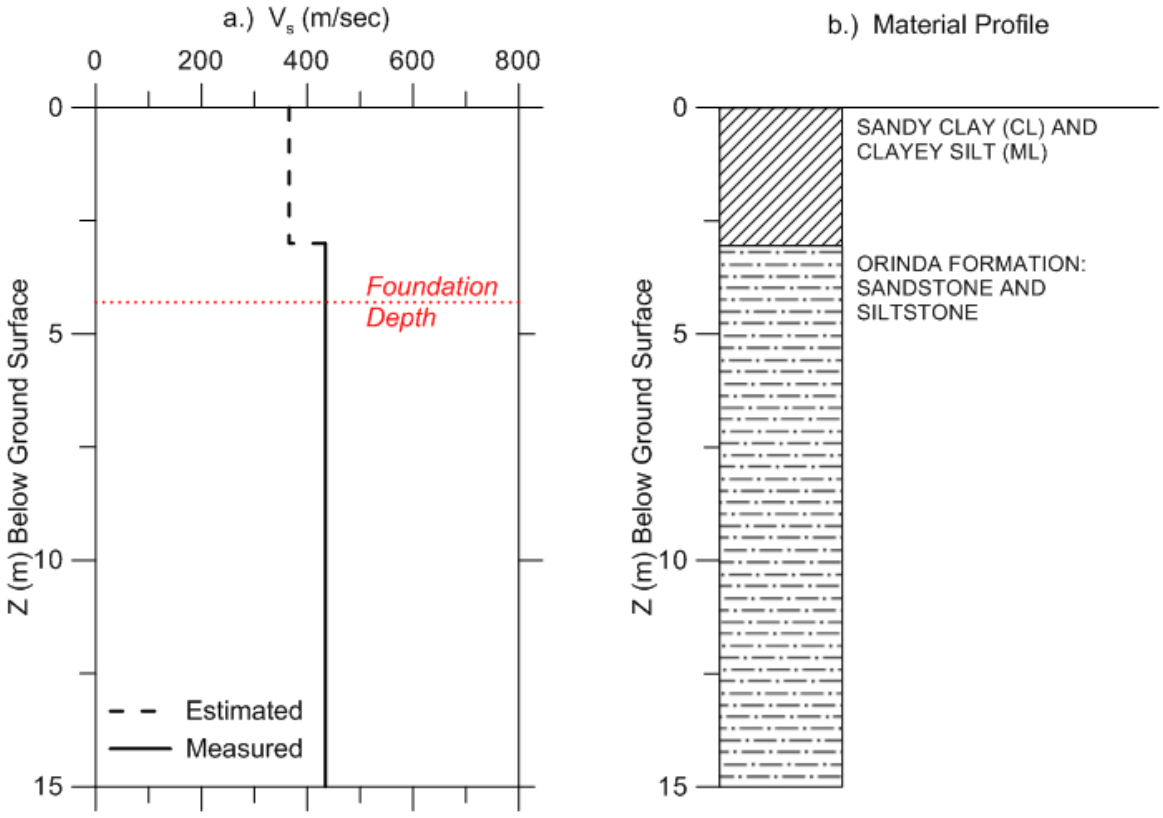

Figure 4-14 **Subsurface characteristics based site and adjacent site explorations of the Walnut Creek building: a) shear wave velocity profile and b) material profile**

4.6.2 Ground Motion Recordings

The Walnut Creek building is designated as CSMIP Station No. 58364. It contains 16 accelerometers at the locations shown in Figure 4-15 and has been instrumented since 1979. The accelerometers are located on four levels: ground surface, 3rd, 8th and roof

levels. There are two vertical sensors at the ground level, allowing the base rocking to be measured. There is no free-field ground instrument in the vicinity of the site.

The Center for Engineering Strong Motion Data (CESMD) has cataloged and reviewed five sets of recorded motions at this building since 1979. The recorded earthquake events and peak accelerations for the ground floor and roof are presented in Table 4-6.

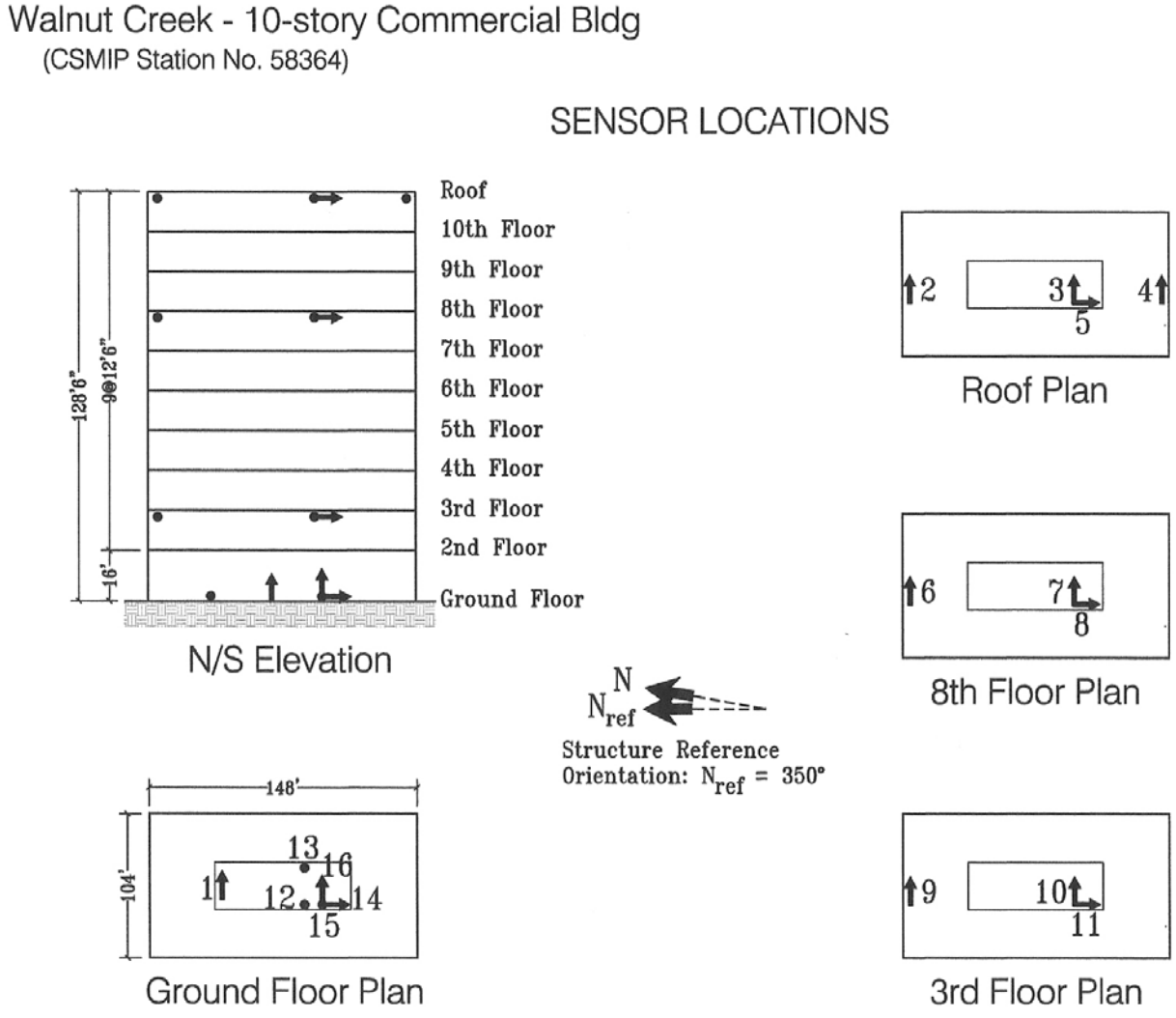

Figure 4-15 **CSMIP Station No. 58364: Walnut Creek 10-Story commercial building, sensor location sketch.**

Table 4-6 Summary of Recorded Earthquake Events and Peak Accelerations at Three Levels

Earthquake	Ground Floor				Roof		
	NS	EW	V1	V2	NS	EW	V
Livermore 80A	0.030	0.033	0.022	0.023	0.116	0.108	----
Livermore 80B	0.061	0.048	0.024	0.018	0.137	0.192	----
1989 Loma Prieta	0.102	0.046	0.053	0.047	0.208	0.164	----
2007 AlumRock	0.005	0.003	------	------	0.018	0.015	----
2008 Alamo	0.029	0.018	------	------	0.057	0.034	----

*NS, EW, and V = north-south, east-west, and vertical, respectively. V1=Chan. 12 (west) and V2=Chan. 13 (East)

The horizontal translations recorded at the ground level of the building were assumed to incorporate the base slab averaging component of kinematic interaction, but not the embedment component [the differential elevation between the ground and foundation levels is 4.2 m (14 ft)]. Transfer functions derived using the embedment procedures in Section 3.3.2 were used to modify the recorded translation to the foundation input motion (u_{FIM}). No free-field ground motions (u_g) were recorded, so the recordings from the ground level of the structure were divided by a transfer function for base slab averaging (calculated using the procedures in Section 3.3.2) to infer u_g. Figure 4-16 shows the u_{FIM} and u_g response spectra for the Loma Prieta earthquake.

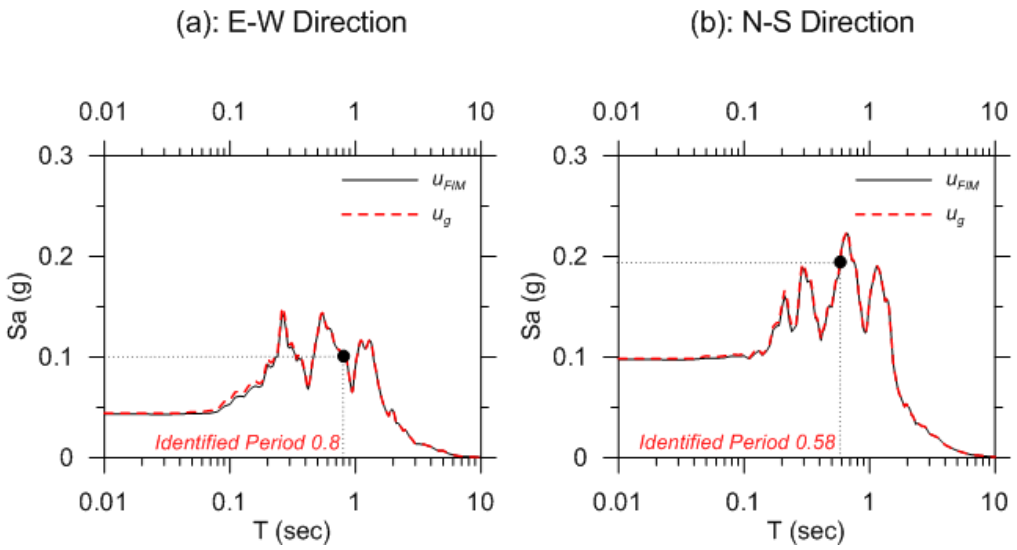

Figure 4-16 **Response spectra of the u_{FIM} and u_g for Walnut Creek building, 1989 Loma Prieta earthquake**

4.6.3 Foundation Conditions

Construction drawings of the building were obtained from CSMIP. In this section, the foundation conditions are described. The representation of the foundation support with springs and dashpots is provided in Section 4.6.4. Structural modeling details are briefly discussed in Section 4.7, with details provided in Appendix C of the NIST report.

Figure 4-17 provides the North-South elevation view of the Walnut Creek building. This illustrates how the shear wall core extends below the ground level to a foundation slab. Frame elements terminate at ground line, where they are supported on spread footings or drilled shafts inter-connected with grade beams. The core wall extends 3 m (10 feet) below the ground level and the footing is 1.2 m (4 feet) thick, so the base of the core wall footing is a total of 4.3 m (14 feet) below the ground level surface. This figure also shows that the ground surface is not level and that the left columns are slightly

longer than the right columns; for simplicity, this is not represented in the structural model and all columns are terminated at the same level (labeled as "Ground" in Figure 4-13).

Figure 4-18 shows that the foundation includes spread footings, drilled shafts, and mat elements. The mat foundation supporting the core walls has lateral dimensions of 11.6 by 25.6 m (38 by 84 ft), whereas the dimensions of the core walls are 7.3 by 21.3 m (24 by 70 ft). Between the top of the mat and ground surface, the mat is backfilled with concrete and sand. The distribution of spread footings and drilled shafts for support of exterior columns is shown in Figure 4-18.

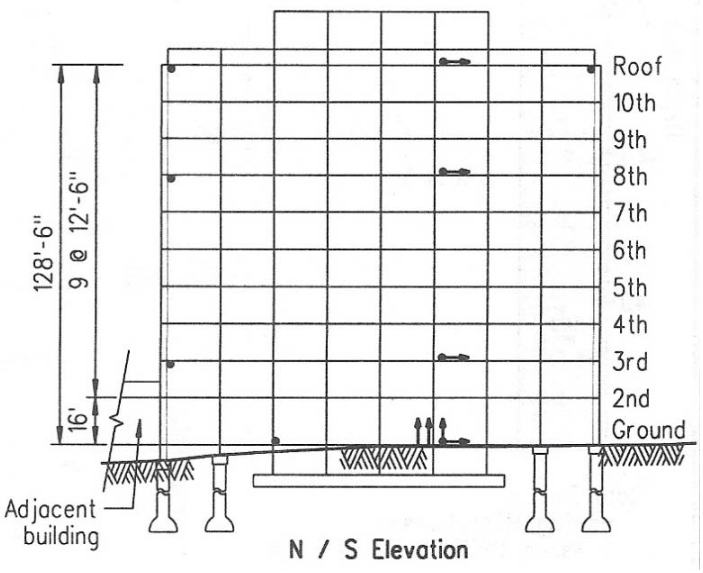

Figure 4-17 **Overall north-south elevation view of the Walnut Creek building (from Stewart and Stewart, 1997).**

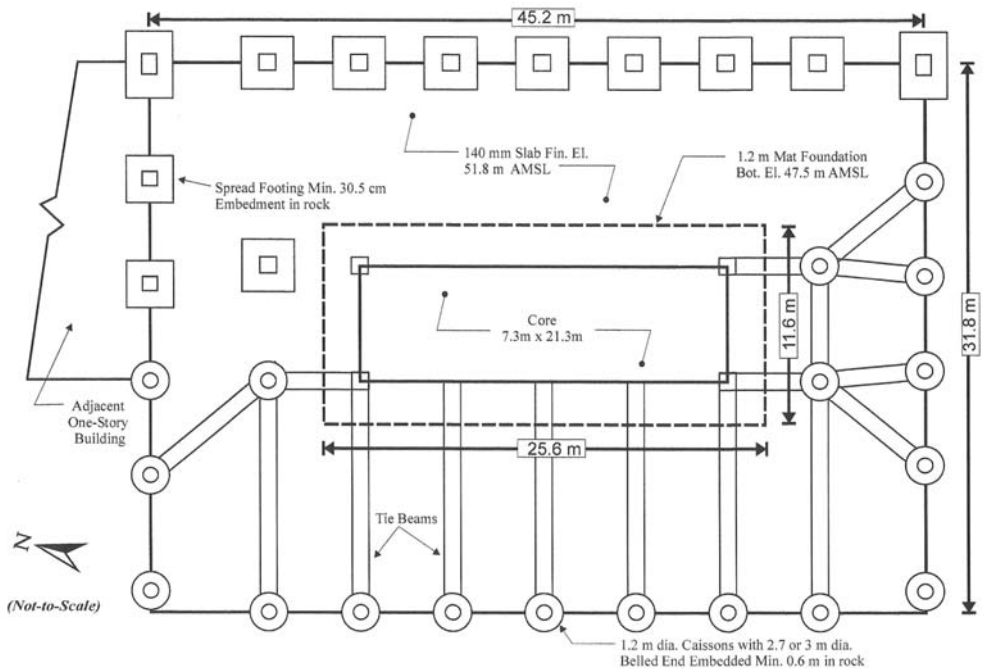

Figure 4-18 Walnut Creek building foundation plan (from construction drawings).

4.6.4 Development of Foundation Springs and Dashpots

In this section the development of foundation springs and dashpots is described using the input parameters described in Sections 4.6.1-4.6.3. The critical input parameters are foundation dimensions, structural period, soil properties, and input motion amplitudes. The analysis methodologies are as described in Chapter 2 of the NIST report. The following is emphasized below:

- Identification of the potential effect of foundation element flexibility on foundation impedance.
- Identification of effective profile shear wave velocity in consideration of foundation dimensions, overburden pressures from the structure, and nonlinear effects.
- The calculation of the interior mat foundation horizontal stiffness and damping.

- The calculation of vertical stiffness and damping for a bed of springs under the base slab, emphasizing the proper representation of rotational impedance for shallow foundation elements.
- The distribution of mat foundation springs and dashpots to the modeled structure nodes.
- The calculation of springs and dashpots for the footings and drilled shafts that support the moment frame.

Foundation Flexibility: As described in Section 2.2.1 of the NIST report, standard impedance function models apply for rigid foundations. The Walnut Creek building has a central core consisting of effectively rigid shear walls supported by an underlying reinforced concrete slab that is larger in plan dimension that the core. As discussed in Section 2.2.3 of the NIST report, flexibility in the mat beyond the limits of the effectively rigid core can reduce stiffness and radiation damping in the rocking mode (Iguchi and Luco, 1982).

To evaluate impedance reduction relative to the rigid case ($k/[k_{\psi=0}]$), plots from Iguchi and Luco (1982) that are similar to Figure 2-7 of the NIST report were utilized, but for a ratio of core/foundation radius equal to 0.75. The results of this calculation are shown in Table 4-7, which indicate that the foundation stiffness ratios are close to one, indicating little deviation from the rigid foundation case. Therefore the full mat dimensions of 11.6 by 25.6m (38 by 84 ft) were used for the analysis of foundation impedance.

Table 4-7 Evaluation of Soil-to-Foundation Stiffness and Foundation Flexibility. 1 ft=0.3048 m

Vibration Mode	Eq. for r_f	Core r_c (m)	Slab r_f (m)	$\frac{r_c}{r_f}$	ψ (Eq. 2-19)[a]	$\frac{k}{(k,\psi=0)}$
Vertical Translation (z)	$\sqrt{A_f/\pi}$	7.0	9.7	0.72	127	0.9
Rocking along x-axis (xx)	$\sqrt[4]{4I_f/\pi}$	9.3	12.0	0.78	188	0.8
Rocking along x-axis (yy)	$\sqrt[4]{4I_f/\pi}$	5.5	8.1	0.68	58	0.8

E_f=22,894.7 MPa, t_f = 1.22 m, ν_f = 0.2, a_0 = 0.13, and G = 347.5 MPa (based on $V_{s,avg}$ = 14 m/s)

Note: $k/(k_{,\psi=0})$ assessed from Iguchi and Luco (1982) plots using r_c/r_f = 0.75 and ψ = 100.

[a] Figures are in the NIST report (NIST, 2012)

Effective Profile Velocity: As described in Section 2.2.2 of the NIST report, effective profile velocity is calculated by averaging velocities (as ratio of profile depth to shear wave travel time) across specified profile depths, z_p. Table 4-8 shows the values of z_p for each foundation vibration mode along with the depth range used for the calculation of effective velocity. The maximum depth considered is not equal to z_p because of the foundation embedment (D). The depth range is taken from the ground surface to z_p+D for each vibration mode. For the specific case of the horizontal base spring, a narrower depth interval starting at the base of the foundation is used, as described further below.

Table 4-8 Effective Profile Depths and Velocities for Calculation of Static Stiffness

Vibration Mode	Eq. for z_p (from 2.46)	z_p (m)	Depth Range (m)	V_{s0}[b] (m/s)
Horizontal Translation (x & y)	$\sqrt{BL}$	8.6	4.3 to 12.9	434.3
Vertical Translation (z)	$\sqrt{BL}$	8.6	0 to 12.9	415.9
Rocking along x-axis (xx)	$\sqrt[4]{B^3L}$	7.1	0 to 11.3	413.5
Rocking along y-axis (yy)	$\sqrt[4]{BL^3}$	10.5	0 to 14.8	418.2

[a] B=5.8 m (foundation half width in short direction), L=12.8 m (half-length). Foundation depth D=4.3 m.

[b] V_{s0} is the free-field, non-overburden corrected average shear wave velocity.

As described in Section 2.2.2 of the NIST report, free-field velocities V_{s0} should be increased to account for the increased overburden provided by structure weight. The overburden-corrected $V_{s,f}$ is evaluated as described in Equation 2-16 of the NIST report. The increase in vertical stress from the structural weight ($\Delta\sigma_v$) was evaluated at two-foot intervals using the 2V:1H method (Holtz et al., 2011, Sec. 10.3). The velocity change was calculated using Equation 2-16 of the NIST report and the adjusted velocities were averaged over the depth ranges from Table 4-8 to provide the results presented in Table 4-9.

Table 4-9 Velocity Correction for Structural Overburden Weight

Z	V_{s0}[a] (m/s)	$V_{s,f}$[b] (m/s)
Horizontal Translation (x & y)	434.3	517.8
Vertical Translation (z)	415.9	463.7
Rocking along x-axis (xx)	413.5	460.8
Rocking along y-axis (yy)	418.2	465.5

[a] V_{s0} is the free-field, non-overburden corrected average shear wave velocity.
[b] V_{sf} is the overburden corrected average shear wave velocity.

The nonlinear shear modulus reduction factor is 0.95 per Table 4-1 of the NIST report and the Loma Prieta earthquake peak acceleration of about 0.1g (Site Class C). No modulus reduction is required for other events.

Mat Foundation Horizontal Stiffness and Damping: Table 4-10 shows the calculation of horizontal static stiffnesses and damping values. Based on the geometric configuration of the building the horizontal stiffness values for the interior core were modeled from the contribution of the base shear and neglected any passive pressure along the embedded portion of the core walls. Because the base shear reaction mobilizes only

soil below the embedment depth D, the effective profile velocity for the horizontal base spring is taken from D to $D+z_p$, as shown in Table 4-9.

Table 4-10 is organized to first present the reduced shear modulus used for the spring calculations, which are derived from the velocities in Table 4-9 along with the mass density (18.1 kN/m^3/g) and the shear modulus reduction (0.95 for Loma Prieta). Static stiffnesses are then computed as the product of a surface stiffness (Table 2-1a) and embedment factor (Table 2-1b); both values are given in Table 4-10. Dimensionless frequency a_0 is calculated, from which dynamic modifiers of stiffness (α_x, α_y) and radiation damping coefficients (β_x, β_y) are computed. The damping ratio used for dashpot calculations is the sum of the radiation damping coefficient and hysteretic damping, which is evaluated from Menq (2003) as 0.01. The calculation of dynamically modified spring stiffness and dashpot coefficient from these results is detailed in Table 4-10.

Table 4-10 Evaluation of the Impedance Functions for Walnut Creek Building. Static Stiffness Results Shown are for Case of Loma Prieta Earthquake

Spring/Dashpot	G (MPa)	Table 2-1a K_{sur} (kN/m)[a] or (kN.m/rad)[b]	Table 2-1b η	Eq. 2-7b a_0[c]	Table 2-2a α	Table 2-2a β_{sur}	Table 2-2b β_{emb}	Dynamic Stiffness	Dashpot
Horizontal, base spring x-direction $(k_{x,base}$ & $c_{x,base})$	469.4	2.24e7	N/A	0.11	1	0.057	N/A	$k_{x,base} = \alpha_x K_{x,sur}$	$c_{x,base} = k_{x,base}\left(\frac{2\beta_{sur} + \beta_s}{\omega}\right)$
Horizontal, base spring y-direction $(k_{y,base}$ & $c_{y,base})$	469.4	2.40e7	N/A	0.11	1	0.053	N/A	$k_{y,base} = \alpha_y K_{y,sur}$	$c_{y,base} = k_{y,base}\left(\frac{2\beta_{sur} + \beta_s}{\omega}\right)$
Vertical, z $(k_z$ & $c_z)$	376.4	2.35e7	1.22	0.12	1	N/A	0.111	$k_z = \alpha_z K_{z,sur}\eta_z$	$c_z = \left(\frac{2(\beta_{emb} + \beta_s)k_z}{\omega}\right)$
Rocking about x-axis $(k_{xx}$ & $c_{xx})$	371.6	8.49e8	1.70	0.12	1	N/A	0.005	$k_{xx} = \alpha_{xx} K_{xx,sur}\eta_{xx}$	$c_{xx} = \left(\frac{2(\beta_{emb} + \beta_s)k_{xx}}{\omega}\right)$
Rocking about y-axis $(k_{yy}$ & $c_{yy})$	379.3	2.78e9	1.54	0.12	0.99	N/A	0.002	$k_{yy} = \alpha_{yy} K_{yy,sur}\eta_{yy}$	$c_{yy} = \left(\frac{2(\beta_{emb} + \beta_s)k_{yy}}{\omega}\right)$

[a] Translation static stiffnesses calculated using B=5.8 m, L/B=2.2, and ν=0.33.

[b] Rotational Static stiffnesses calculated using B=5.8 m, L/B=2.2, and ν=0.33.

[c] Calculated at frequency corresponding to first-mode period of structure, taken as T = 0.66 sec

Mat Foundation Vertical Stiffness and Damping: Overall vertical and rotational stiffnesses are computed using the profile velocities given in Table 4-9 with the results in Table 4-10. Distributed vertical springs are provided over the base of the mat, as shown in Figure 4-19. The springs are provided in the form of a vertical stiffness intensity, which is stiffness normalized by area (e.g., Equation 2-19 of the NIST report). The stiffness of any individual spring is computed as the product of stiffness intensity and the tributary area for the spring. As described in Section 2.2.3, stiffness intensities are adjusted near the edges of the foundation to match the overall rocking stiffness values given in Table 4-10 (using Equation 2-20a-b of the NIST report). End length ratio R_e = 0.4 was used for these calculations.

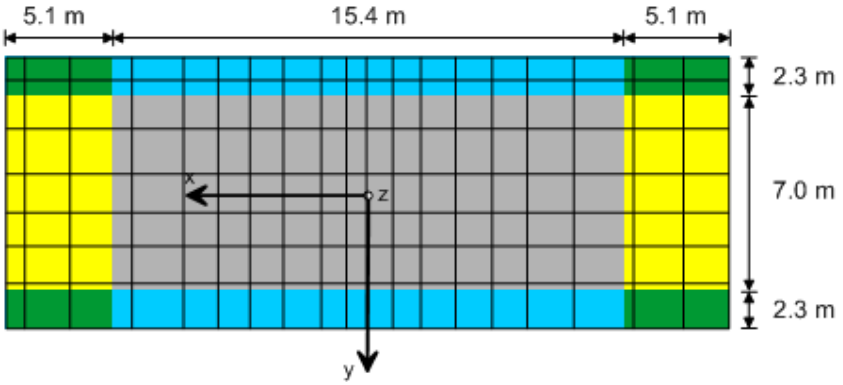

	$k_z^i\ (MN/m^3)$	$c_z^i\ (kN.sec/m^3)$
	96	275
	308	778
	418	1,235
	526	1,697

Figure 4-19 **Vertical spring and dashpot intensities and areas distinguished by color. Solid lines represent tributary area boundaries in which stiffness and dashpot values were distributed to each area. 1 ft = 0.3048 m**

The vertical stiffness intensities in the gray central zone in Figure 4-19 are computed from Equation 2-19 of the NIST report and reflect the vertical impedance. The edge intensities in the blue and yellow zones are increased by factor R_k = 5.48 for

the *xx* direction and 3.21 for the *yy* direction. Stiffness intensities for corner zones were evaluated as the average of the *xx* and *yy* intensities. Dashpot intensities are calculated from stiffness intensities as $c_z^i = 2R_c\beta k_z^i/\omega$, where R_c represents the reduction factor to capture rotational rocking (Equation 2-20c-d of the NIST report).

Springs and Dashpots Representing Footings and Grade Beams: Single valued springs and dashpots were provided for the translational modes (horizontal and vertical) for the exterior spread footings and piles. For simplicity the spread footings and belled pile heads were treated as individual shallow rectangular foundations with dimensions of 3.05 m (10 ft) by 3.05 m (10 ft). The calculations were similar to those for the interior mat, as described in Table 4-10; the same shear moduli *G* were used, but foundation half-width (*B*) was taken as 1.52 m (5 ft). The horizontal springs (k_x and k_y) and vertical springs (k_z) were calculated as 3.91e6 kN/m and 4.97e6 kN/m, respectively. The horizontal dashpots (c_x and c_y) and vertical dashpots (c_z) were calculated as 1.68e3 kN-s/m and 2.75e4 kN-s/m, respectively. The dimensionless frequency utilized for these calculations was a_0=0.02.

4.7 Baseline Model and Comparison to Recordings

Open System for Earthquake Engineering Simulation (OpenSees) software was used to perform response history analyses of a three-dimensional (3-D) model of the Sherman Oaks and Walnut Creek buildings. OpenSees is an open-source software package that was developed at the University of California, Berkeley for simulations of structural and geotechnical responses to earthquakes (OpenSees 2011). The structural conditions of the buildings are described in the NIST report with reference

to their representation in OpenSees models. The development of foundation springs and dashpots for both MBs is described in Sections 4.5.4 and 4.6.4 of this document.

The original OpenSees structural model for the Sherman Oaks building was provided by Erol Kalkan of the CSMIP and the US Geological Survey (personal communication, 2011). The original structural model was improved with inclusion of the subterranean levels and foundation springs and dashpots for the MB, but otherwise the initial structural properties were those from the Kalkan model. The response history recording data from the 1994 Northridge, 1992 Landers and 1987 Whittier earthquakes were used for the Sherman Oaks building.

The Walnut Creek OpenSees model was generated as part of this research. Because of the modest embedment of the Walnut Creek core wall foundation and the lack of subterranean levels, multi-support excitation along embedded portion of the foundation was not considered, causing the baseline model (MB) to match the bathtub model (Model 4) in this case. The implementation of the bathtub model for this structure is illustrated in Figure 4-20. The other models considered are fixed-base models analogous to Models 1 and 2 from Figure 4-3 (implementation for Walnut Creek building is shown in Figure 4-19). To expedite the analyses and the post-processing, the model was reduced to two-dimensional (2-D). The 2-D model includes all the elevations spanning the East-West direction.

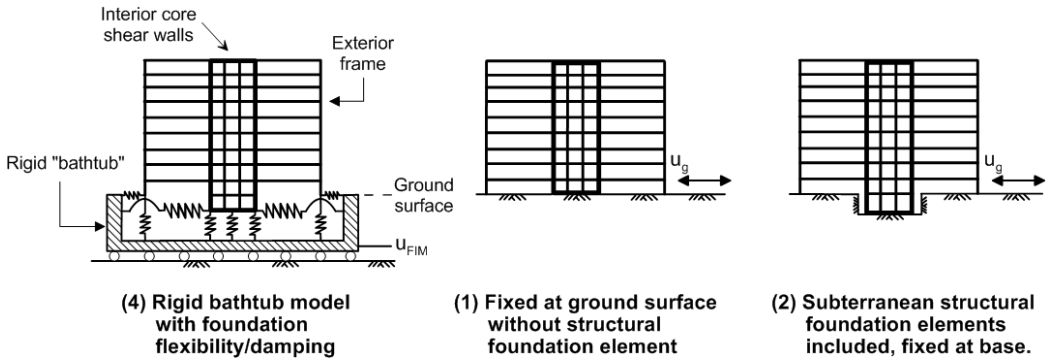

Figure 4-20 Schematic illustration of modeling approaches for modeling Walnut Creek building.

Displacement histories for both directions and multiple floor levels obtained from the calibrated Sherman Oaks MB are compared to recordings in Figures 4-21 for the Northridge earthquake. Figure 4-22 shows the peak displacements and accelerations. The match in both horizontal directions at the foundation and ground levels is excellent. Elsewhere over the height of the building, the quality of the match is generally better in the longitudinal direction than transverse (e.g. Channel 1 fit at roof level has a better match of phasing and amplitudes than Channel 2). The calibration process began with expanding the original structural model by Kalkan to include the sub-grade levels, where shear stiffness of the reinforced concrete walls was of concern. To keep the calibration approach simple, a multiplier on the theoretical shear modulus of the uncracked concrete (G_c) was taken as the calibration parameter, with the goal of matching near-ground response. A multiplier of 0.25 was used (which is a reasonable value to reflect the cracked stiffness properties of the walls), however, the near-ground response was not highly sensitive to this parameter over the range of 0.25-0.40 that was considered. The next step in the calibration was to seek to match the building period through adjustments of the structural stiffness

and mass. The real stiffnesses of a reinforced concrete element is highly variable (Haselton et. al 2011). Therefore the rebar stiffness (as a proxy for overall element flexural stiffness) was modified by 0.7 from the original value, whereas the mass was not modified.

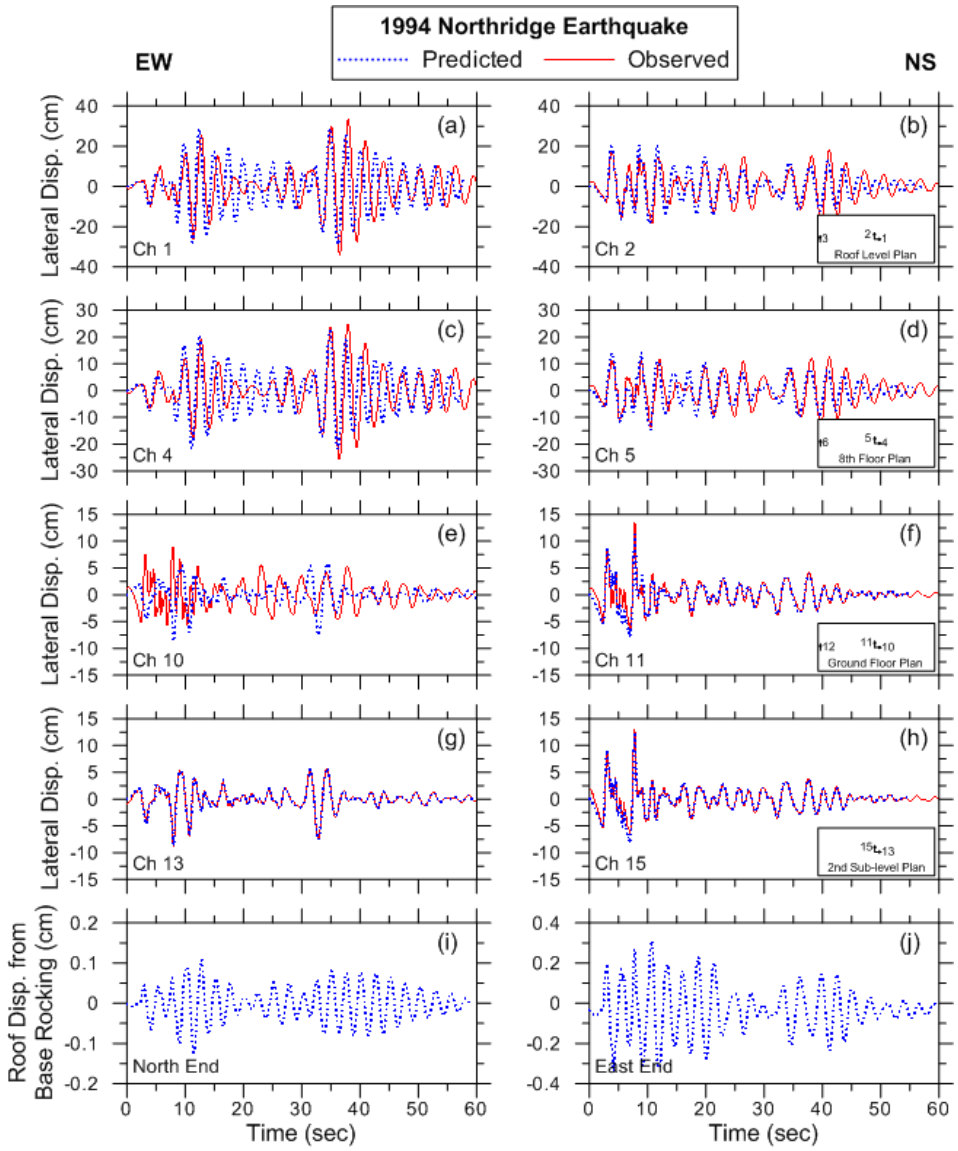

Figure 4-21 **Comparison of recorded displacement histories at roof, 8th floor, ground level and base level with those predicted using the Baseline Model (MB). Northridge earthquake.**

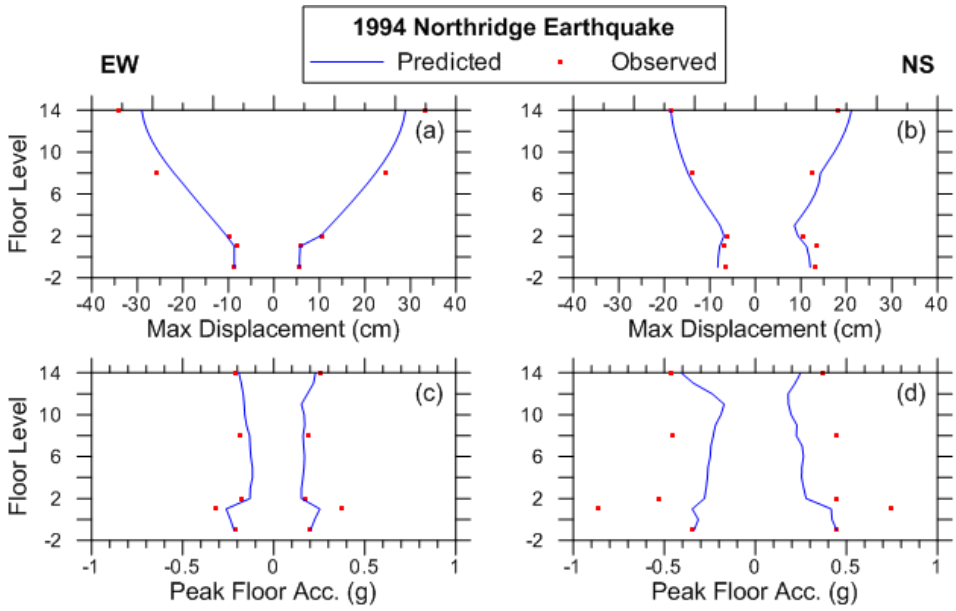

Figure 4-22 **Comparison of recorded peak displacements over the height (X and Y direction) with those predicted using the baseline model (MB). Northridge earthquake.**

A comparison of the relative displacement and absolute accelerations of the Walnut Creek MB and the measured data from the Loma Prieta earthquake at the different floors are shown in Figures 4-23. The plots in this figure indicate that the numerical model is a reasonable representation of the dynamic response of the physical structure. The relative displacement and absolute acceleration profiles are compared between the model and the recorded data in Figure 4-24. This model used a factor of 0.3 between cracked and uncracked concrete stiffness. The stiffness reduction of 30% was applied to the elastic modulus of the columns and shear wall components (modeled as trusses as described in the NIST report). No further calibration was performed and all other properties represented best estimates developed prior to viewing analysis results and analysis-data comparisons.

Because two vertical instruments are present at the ground floor level of the Walnut Creek building, it is possible to compute base rocking as the difference between the two verticals divided by their horizontal separation distance. As shown in Figure 4-24, low frequency noise causes base rocking evaluated in this manner from the CSMIP data to have unrealistic features. Accordingly, the vertical records were filtered using high-pass Butterworth filters with a corner frequency of 0.4 Hz, which was selected through examination of displacement histories with different corners as shown in Figure 4-25. Following the recommendations of Bommer and Boore (2005), the minimum filter corner that removes the low frequency noise features in the rocking displacement history was selected.

Figure 4-26 compares the filtered base rocking from recordings to that computed from simulations. The numerical model captures the observed rocking reasonably well. In Figure 4-27, the rotation at the base of the numerical model was multiplied by the vertical distance from the foundation-to-roof (39.2 m) to compute the rocking contribution to the lateral roof displacement. The rocking-induced lateral displacement accounts for approximately 10% of the total roof displacement.

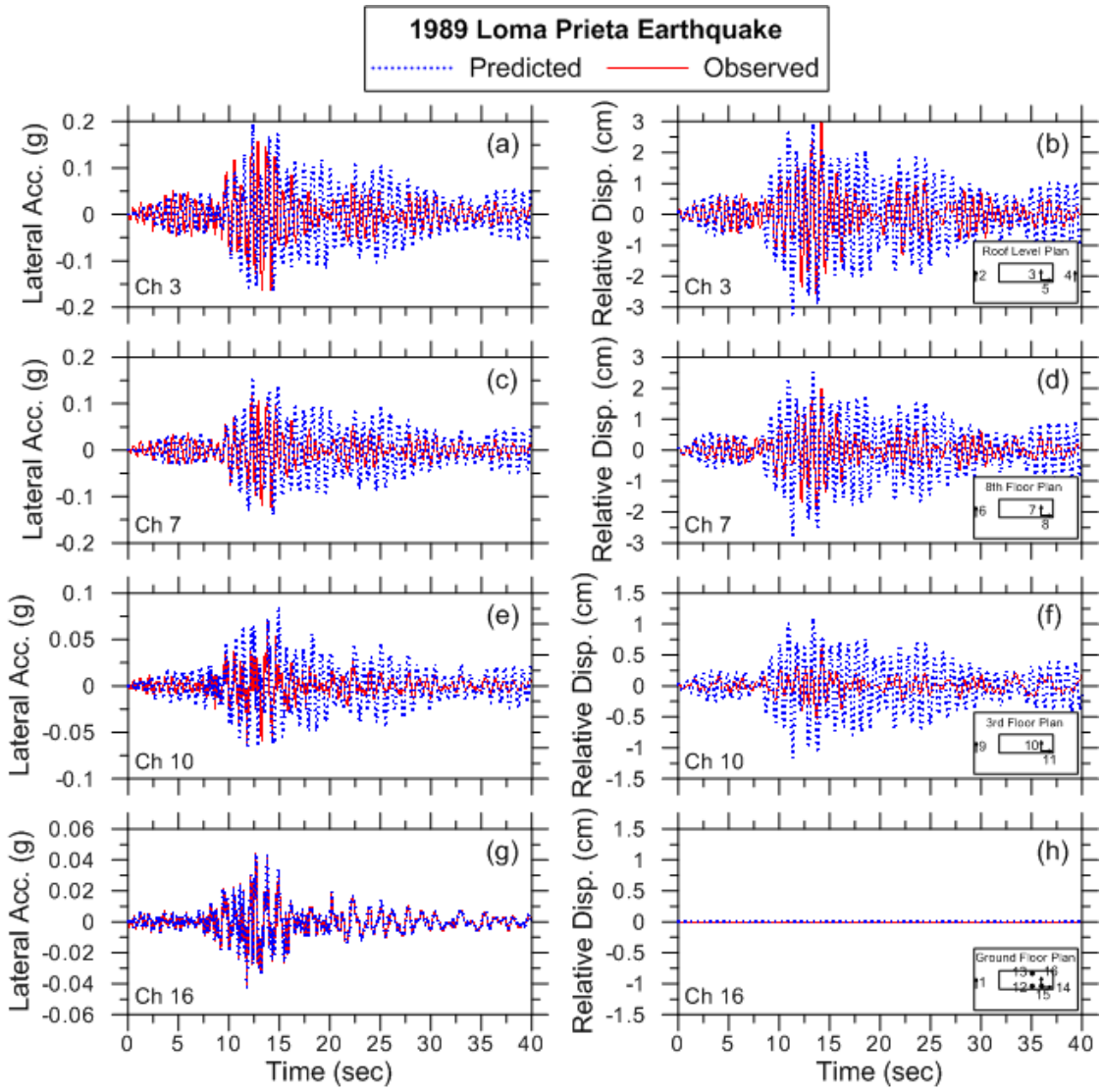

Figure 4-23 **Comparison of recorded lateral acceleration and relative displacement histories at roof, 8th floor, 3rd floor and ground level with those predicted using the Baseline Model (MB). Loma Prieta earthquake.**

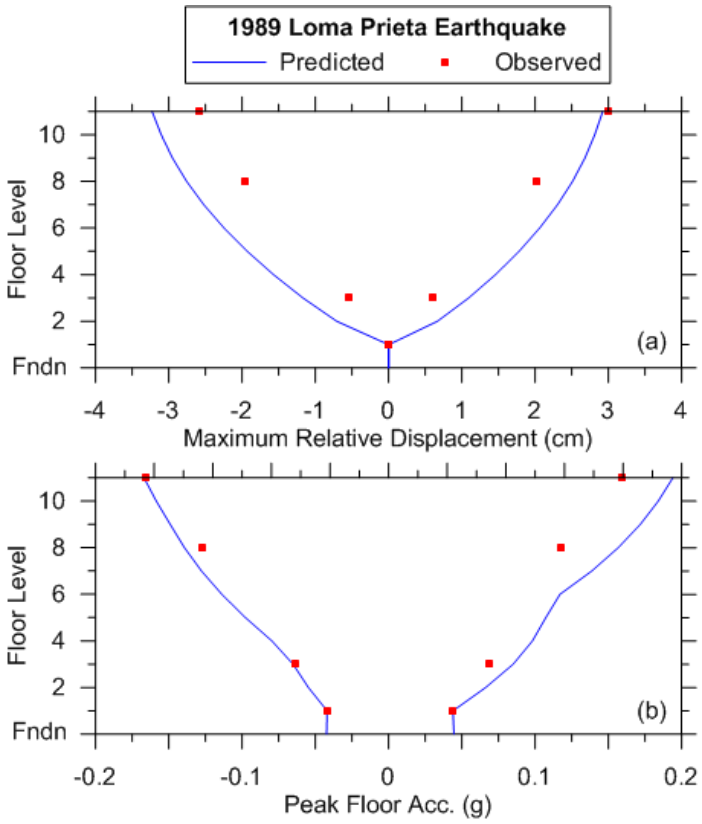

Figure 4-24 **Comparison of maximum floor relative displacement and absolute acceleration between model and recorded response. Loma Prieta earthquake.**

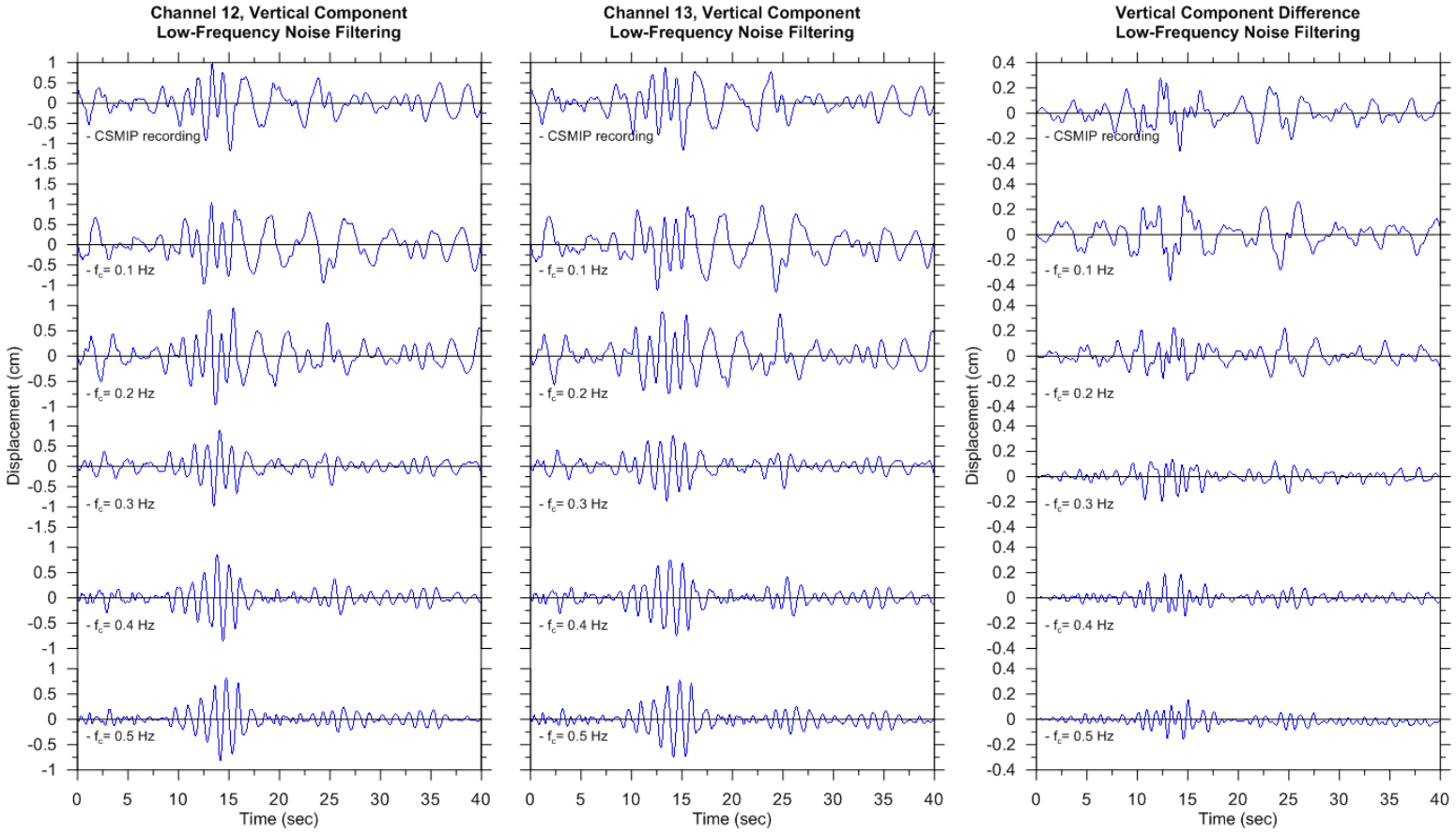

Figure 4-25 **High-pass filtering of Walnut Creek building vertical motions at the base level. Figure shows the effect of the corner frequency on displacement histories and rocking history for the Walnut Creek building.**

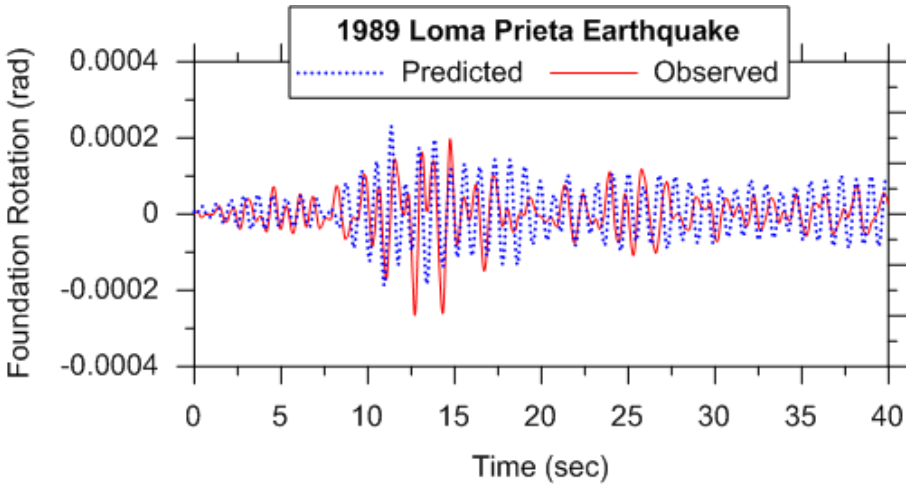

Figure 4-26 **Comparison of the foundation rotation from base rocking of the baseline model and recorded data for the Walnut Creek building.**

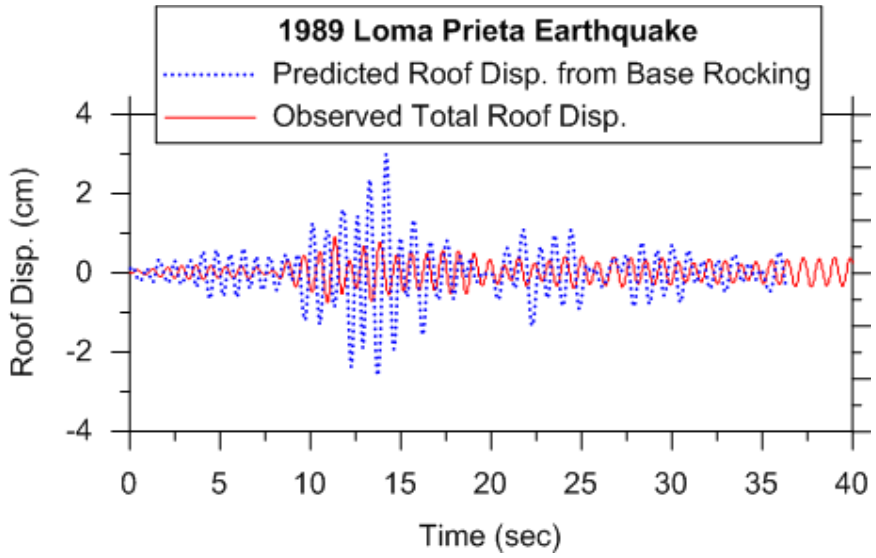

Figure 4-27 **Comparison of the baseline model roof displacement from base rocking compared to the total roof displacement from the recorded data for the Walnut Creek building.**

Based on the favorable comparisons of the response histories (Figure 4-23), maximum accelerations and displacement (Figure 4-24) and contribution to roof displacement from base rocking (Figures 4-27), the MBs provide a reasonable

approximation of the soil-structure system response and to provide a suitable basis for model to model comparisons presented in the next section.

4.8 Model to Model Comparison

Table 4-11 shows the 1st mode periods for the alternative model configurations for the Sherman Oaks and Walnut Creek structures. As expected, fixed base models have shorter periods than flexible-base models, although the changes are relatively modest, especially for the Sherman Oaks structure. Many of the changes in response that we compute can be related to the change in period coupled with spectral shape near the first mode period.

Table 4-11 Comparison of 1st Mode Periods for Alternative Model Configurations (for both models)

	Fundamental Period (sec)	
Model Type	Sherman Oaks Bldg., Norhtridge Earthquake	Walnut Creek Bldg., Loma Prieta Earthquake
MB (Baseline Model)	2.72	0.83
1 (fixed @ ground surface)	2.67	0.78
2 (fixed @ base)	2.71	0.78
3 (fixed horizontal spring)	2.65	N/A
4 (bathtub)	2.72	0.83

N/A = not applicable

4.8.1 Sherman Oaks Analysis Results

This section presents detailed Sherman Oaks model-to-model comparisons of the displacement time series and peak EDPs of maximum displacements, inter-story drift, story shear coefficients (C_s) and floor accelerations. Figures 4-28 through 4-32 show the Sherman Oaks MB compared individually to each simplified and alternative model discussed in Section 4.3.2.

Figure 4-28 shows the bathtub model introduces changes in displacement history response throughout the height that are negligible (e.g., less than 3.6% at roof level). Changes in maximum inter-story drift and story shear force profiles are also small both above and below ground level. The engineering demand parameter most affected by model-to-model variations is peak floor accelerations, which are relatively unaffected above ground line but are sensitive to the use of kinematic versus free-field ground motions. This can be seen by examination of the results marked '4a' and '4b' (i.e., use of u_{FIM} in lieu of u_g) in Figure 4-28. Similar trends are observed for MB.1 and MB.2 (Figure A-5 of the NIST report).

Ignoring the subterranean levels by assuming a rigid base at ground level (Model 1) alters the vibration period of the building (Table 4-11). As a result, displacement history responses are more out of phase than other configurations considered as shown in Figure 4-29, although the differences are small. Differences in above-ground story drifts, story shears, and peak floor accelerations are relatively large in some cases (up to a 50% change).

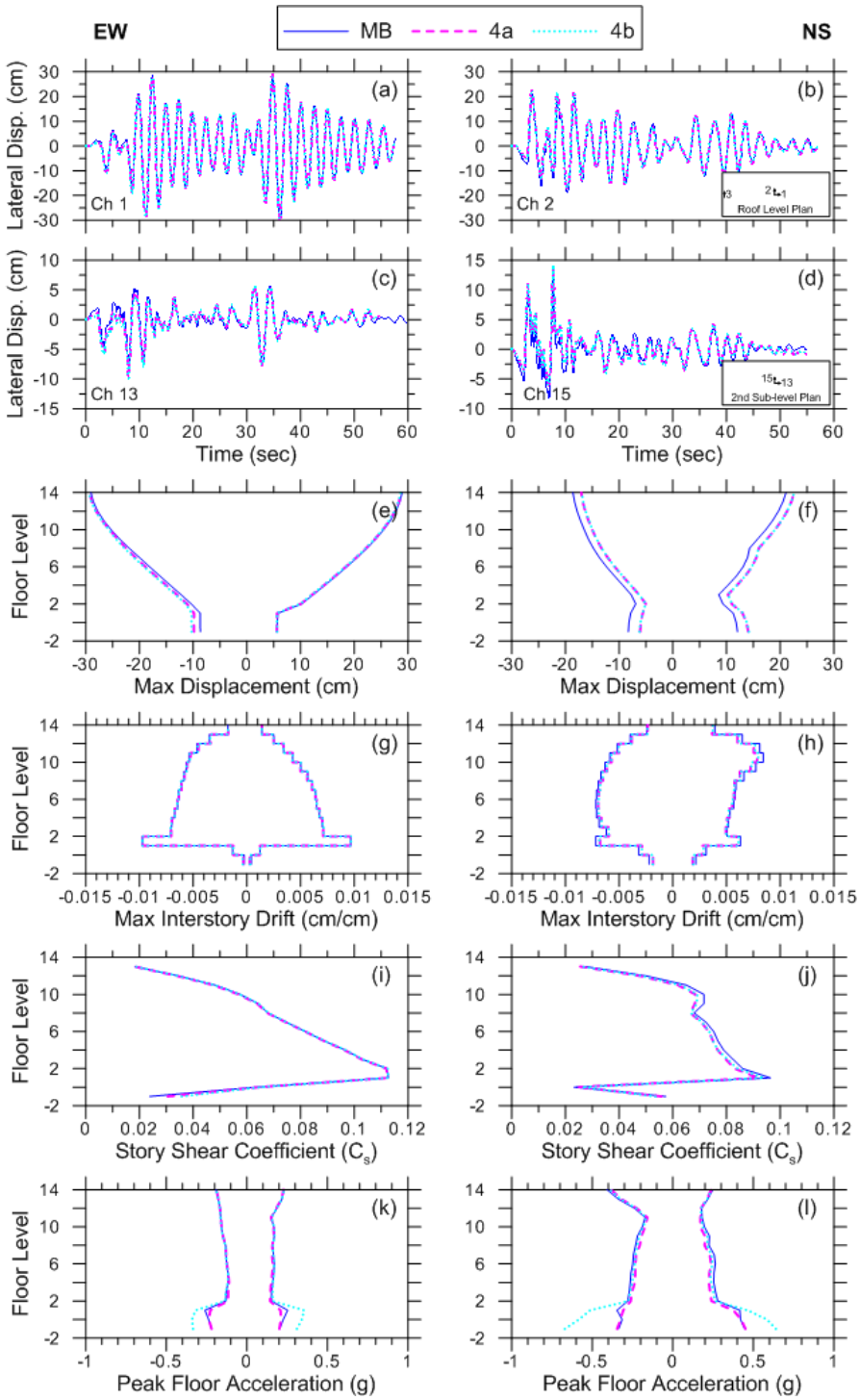

Figure 4-28 **Comparison of displacement histories, drift ratios, and story shears obtained from MB and Model 4 (bathtub) for the Sherman Oaks building.**

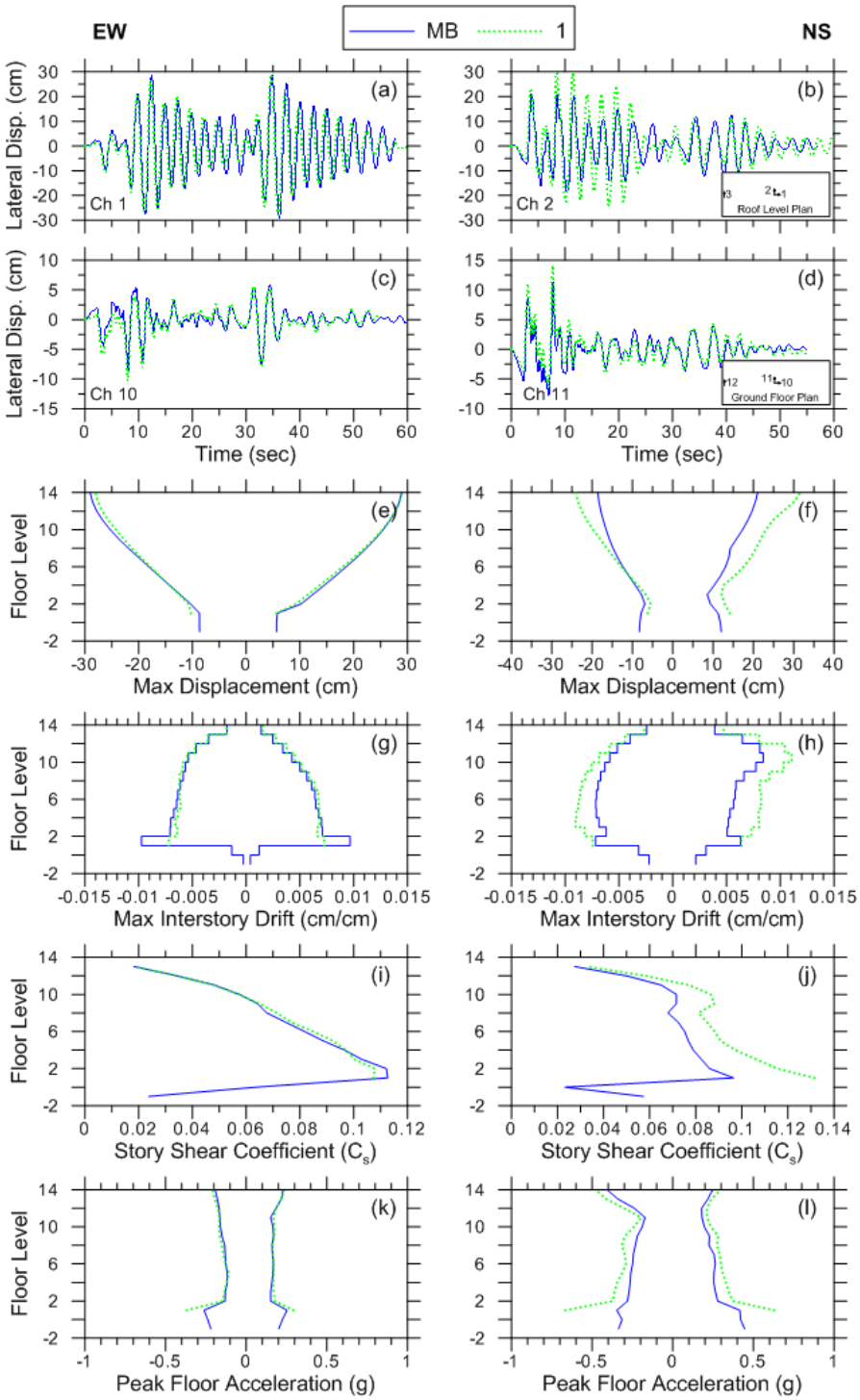

Figure 4-29 **Comparison of displacement histories, drift ratios, and story shears obtained from MB and Model 1 (fixed at ground line) for the Sherman Oaks building.**

Ignoring the embedment effect by running the structure down to a fixed base at the foundation level (Model 2) provides good matches to MB in vibration periods (Table 4-11), but drift, story shear, and peak floor acceleration profiles are significantly changed in Model 2 relative to MB (Figure 4-30). The differences are less than those for Model 1 and are generally larger below ground line than above.

The worst results were obtained with Model 3, in which upper-level foundation springs are fixed against displacement and input motions are applied at the base level with rocking allowed. Large differences in vibration periods, displacement histories, and drift/shear distributions are encountered, as shown in Figure 4-31. This model should not be used.

Figure 4-32 compares the MB results to those computed for models identical to MB except for rigid foundation structural elements (MB.1) and gapping allowed at the basement wall-soil interface (MB.2). These are not models used in practice, per Chapter 6 of the NIST report, but were investigated to gain insight into the importance of these effects in foundation modeling. The results show that allowing geometric nonlinearities (gap formation) has no discernible impact on the results. This supports the equivalent-linear foundation/soil modeling assumptions used in this work. The use of a rigid foundation increases responses, likely due to period change.

In Figure 4-33, the results are synthesized from each of the considered alternative practical configurations along with the MB as profiles of drift, inter-story drift, and story shear for transverse response (y-direction). The Model 3 results are clear outliers for each of the engineering demand parameters considered. Among the other models, Model 4 is closest to MB, followed by Model 2, and then Model 1. Differences in EDPs are generally greater below ground line than above.

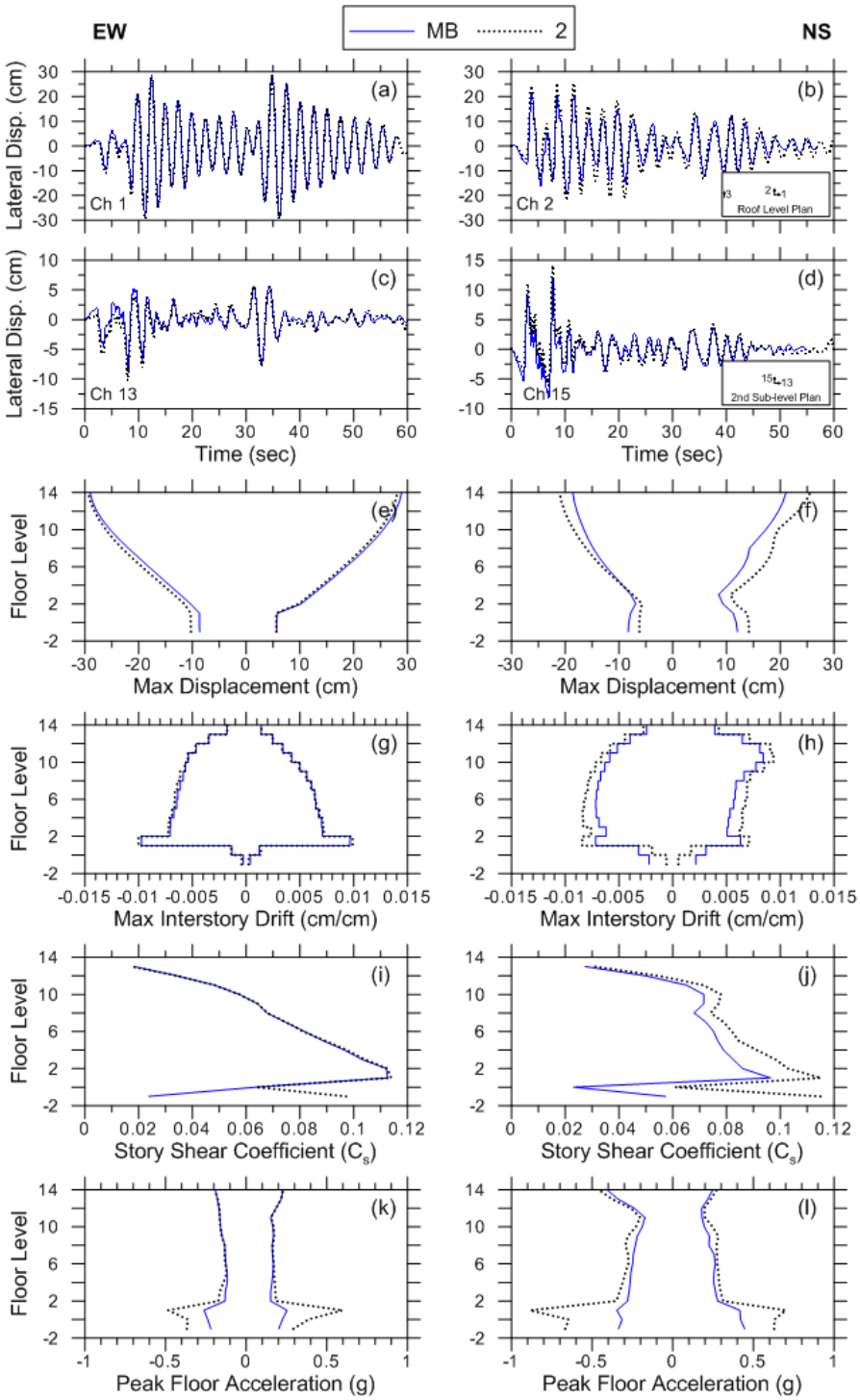

Figure 4-30 **Comparison of displacement histories, drift ratios, and story shears obtained from MB and Model 2 (fixed at base) for the Sherman Oaks building.**

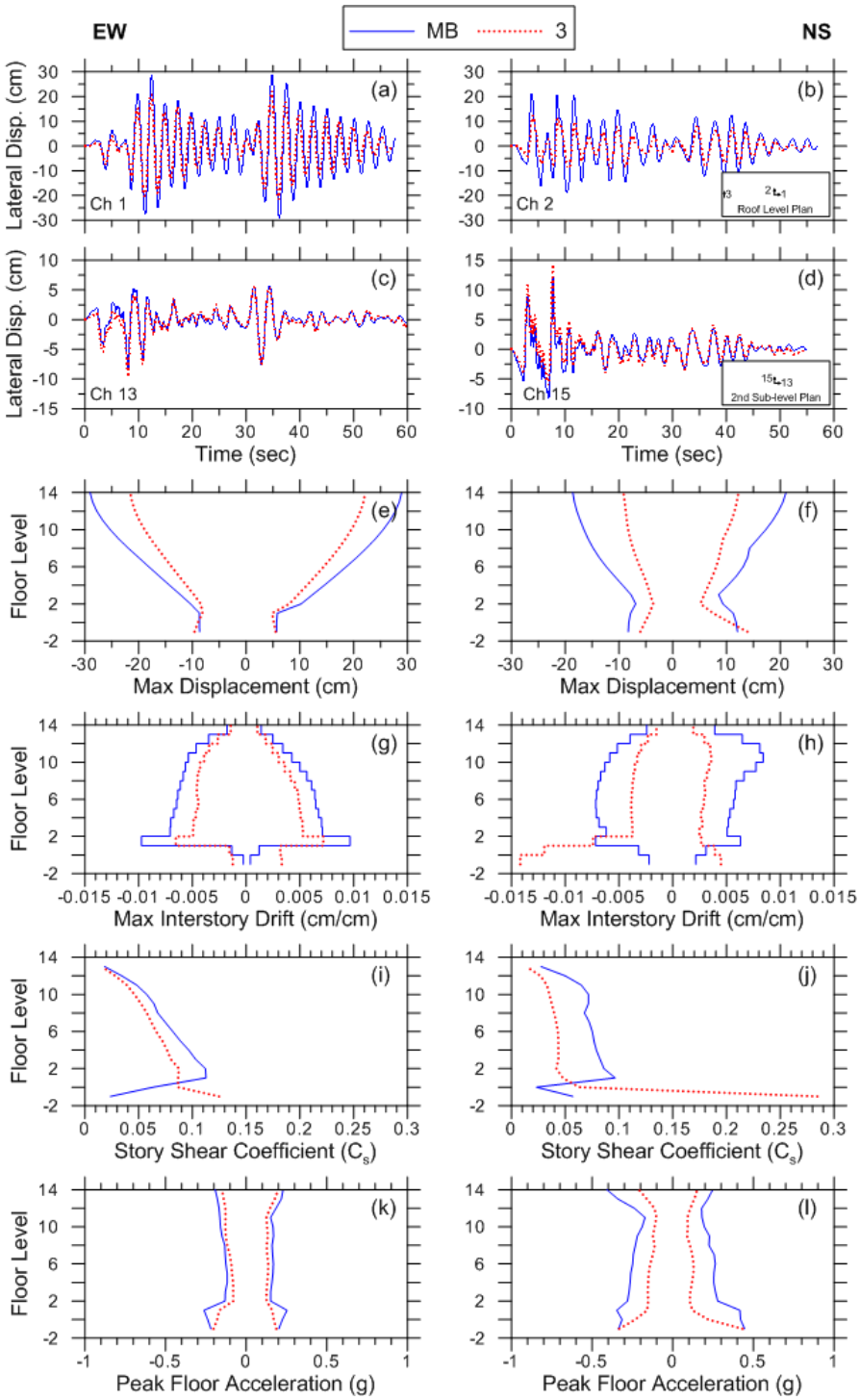

Figure 4-31 **Comparison of displacement histories, drift ratios, and story shears obtained from MB and Model 3 (fixed horizontal springs) for the Sherman Oaks building.**

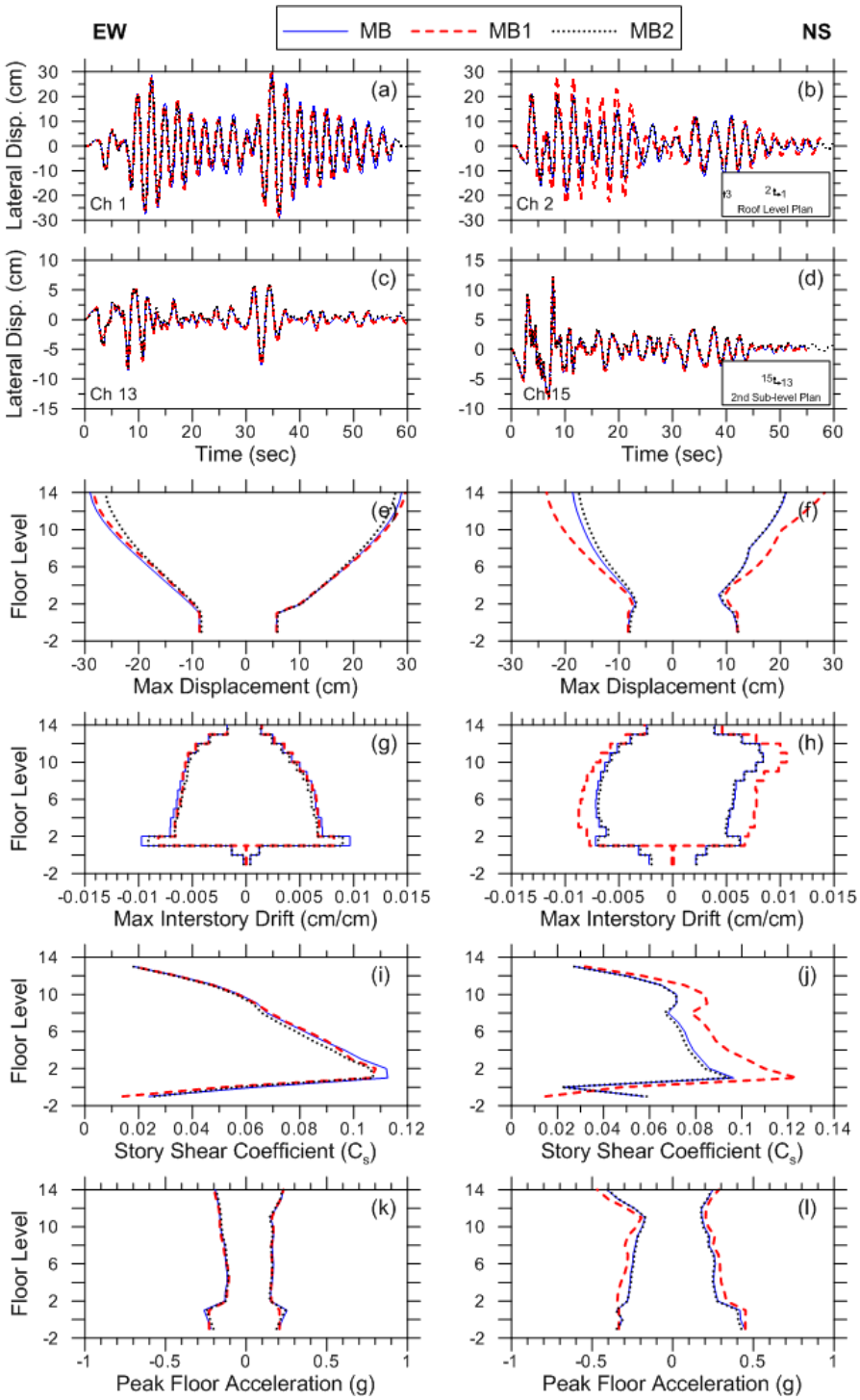

Figure 4-32 **Comparison of displacement histories, drift ratios, and story shears for MB, MB.1 (rigid foundations), and MB.2 (gaps) for the Sherman Oaks building.**

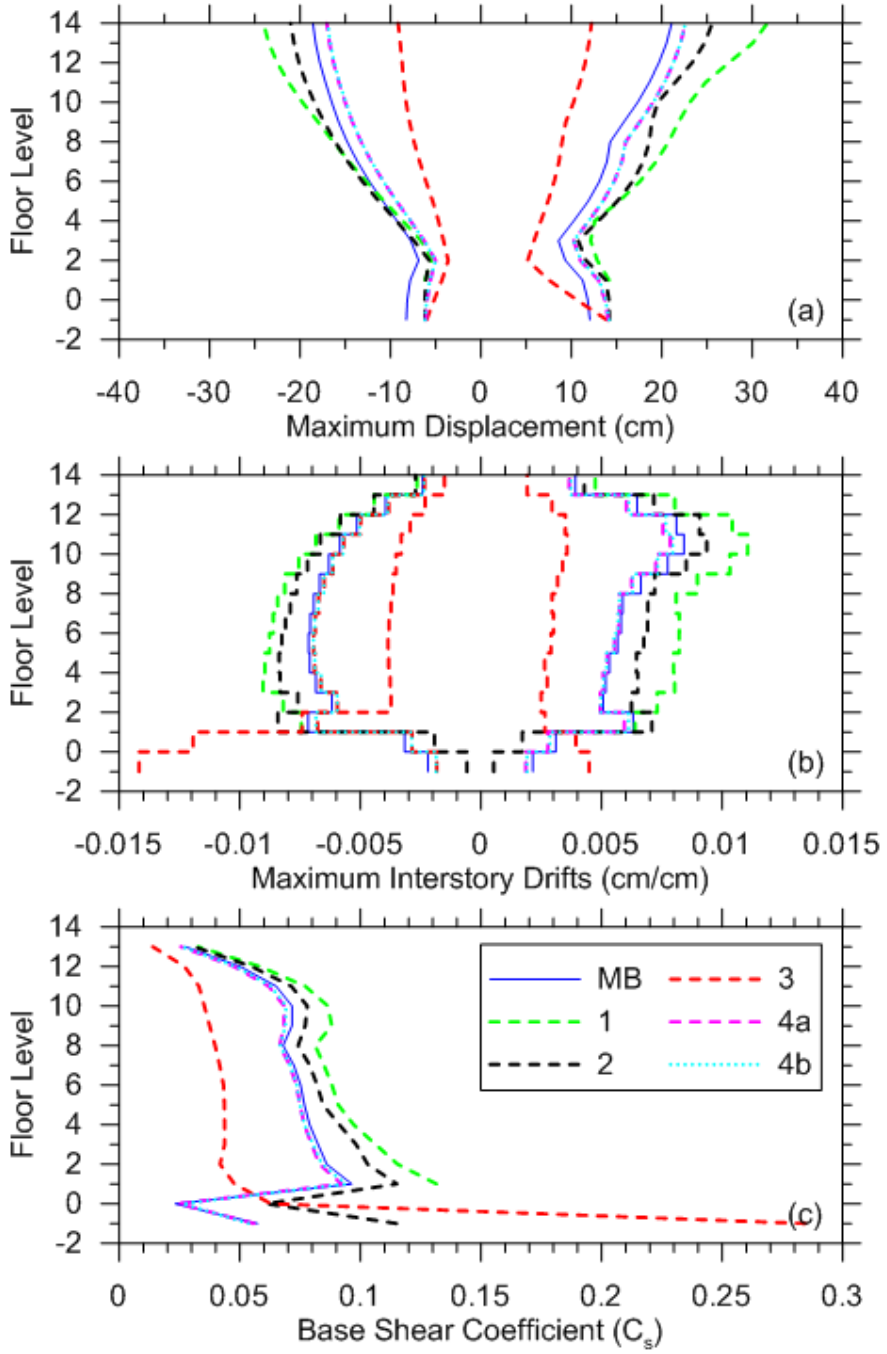

Figure 4-33 **Comparison of peak displacement over height, drift ratios, and story shears in transverse direction from all models of the Sherman Oaks building.**

4.8.2 Walnut Creek Analysis Results

A set of EDPs similar to those for the Sherman Oaks building were computed for the Walnut Creek building. However, the buildings configuration only allowed for the development of the two fixed-base modeling schemes (Model 1 and 2) for comparison to the MB. The MB matches the bathtub model (Model 4), as described in Section 4.7.

Figure 4-34 compares roof accelerations and displacements for the three models. The fixed-base models (Models 1 and 2) capture MB peak roof accelerations and displacements reasonably well, but the phasing of the recorded and computed roof motions is quite different. These phasing variations are likely due to differences in higher mode responses. Note that Models 1 and 2 are nearly identical in this case (unlike Sherman Oaks), because of the small embedment.

Figure 4-35 presents profiles of the peak EDPs of maximum displacement, inter-story drift, and floor accelerations. There is a general trend towards over-prediction of response by the fixed-base models (Models 1 and 2) relative to MB. The differences are largest in peak floor accelerations, and likely result from differences in higher-mode effects as a result of SSI.

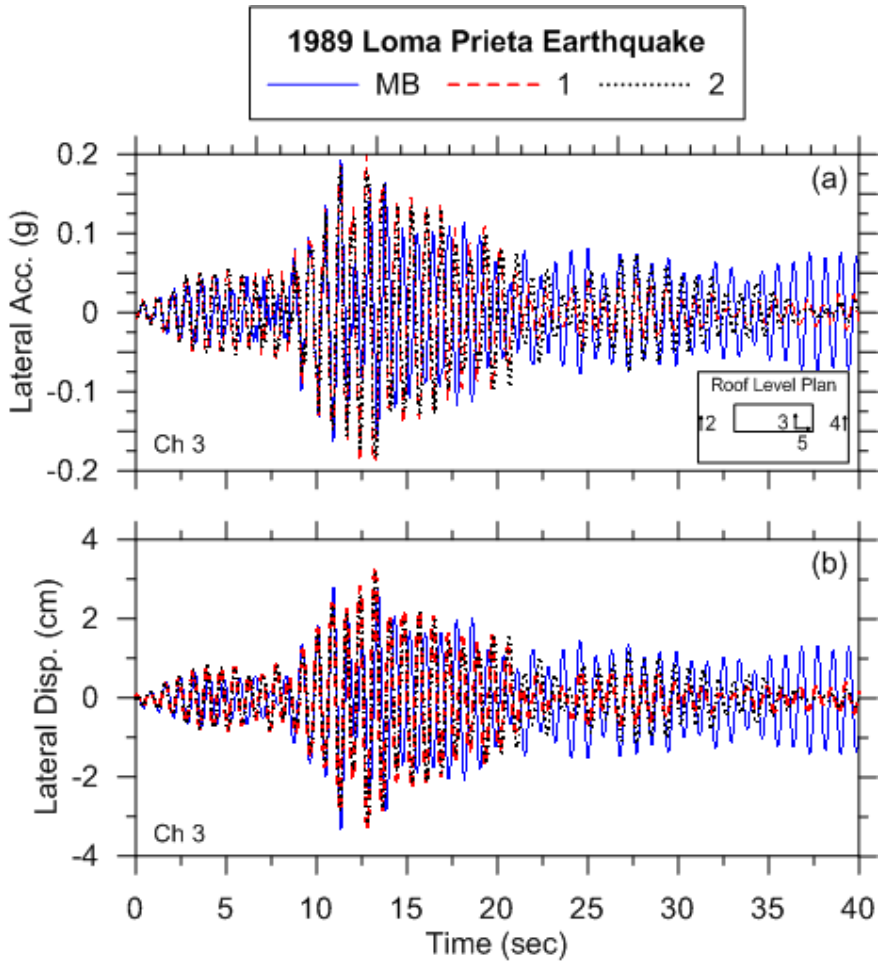

Figure 4-34 **Comparison of the roof acceleration and displacement histories for the reference model (MB, equivalent to Model 4) and Models 1 and 2 of the Walnut Creek building.**

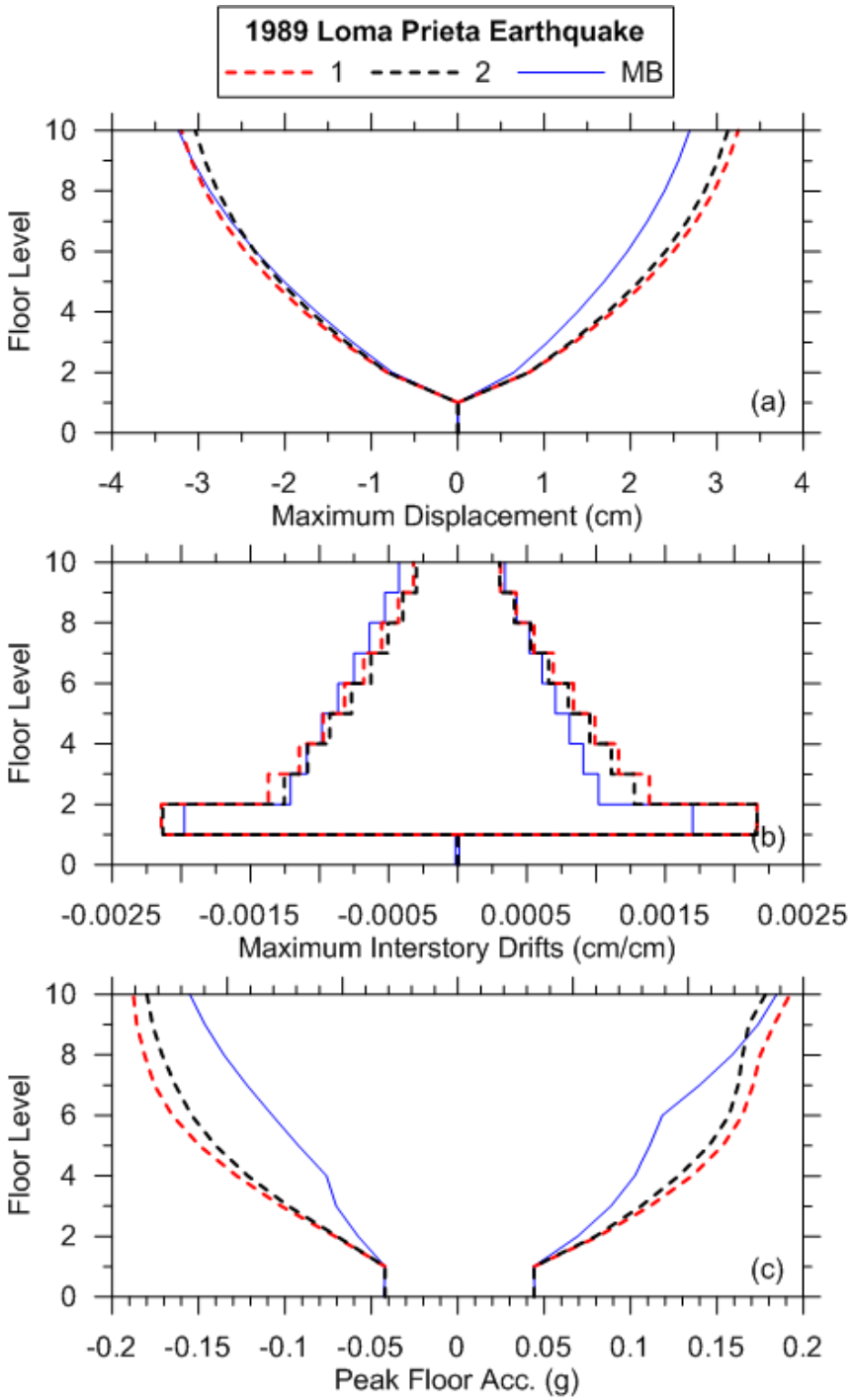

Figure 4-35 **Comparison of profiles of maximum displacement, maximum interstory drift, and peak floor acceleration for the reference model (MB, equivalent to Model 4) and Models 1 and 2 of the Walnut Creek building.**

4.9 Interpretation and Conclusions

Drawing upon the previous findings from Naeim et al (2008), Tileylioglu et al. (2010) and the present work, several consistencies can be observed. First, MB-type models have an encouraging ability to match observed responses with only modest tuning of structural parameters (i.e., damping ratios, element masses or stiffnesses). In particular, the SSI portion of the models appears to be performing well for each of the investigated structures having recordings of foundation rocking (two from prior work and Walnut Creek in the present work). These results suggest that the relatively simple equivalent-linear spring/dashpot approach for SSI modeling presented in the NIST report can provide satisfactory predictions of foundation response for the levels of excitation in these case studies.

Second, there are varying levels of performance for some of the simplified approaches used in practice. The worst-performing approach is Model 3, which should not be used for response history analysis. Model 1 is the next least-desirable option, with the level of difference from the MB being greatest for stiff structures or deeply embedded structures. The errors are especially noticed in under-prediction of building periods, variations in profiles of inter-story drifts, story shears and peak floor accelerations, and phasing errors in response histories. The best-performing models relative to MB are Model 2 and Model 4 (bathtub).

Our third general finding concerns the portions of a structure whose response is significantly affected by the SSI modeling. For the buildings considered, above-ground building responses, as measured for example by envelopes such as drift or story shear profiles, were modestly to insignificantly affected by SSI. The largest effects of SSI on above-ground enveloped responses were for the stiffest structures. In

contrast, below-ground enveloped responses (e.g. basement wall shear forces and below-ground inter-story drifts) were much more sensitive to SSI. Both the kinematic ground motion description and spring distributions contribute to these effects. This sensitivity was observed for all structures, whether flexible or relatively stiff.

Considering all of the above, it is observed that none of the simplified approaches either currently used or proposed for use in practice (Models 1-4 in Figure 4-3) can mimic the MB response over the full height of the structure for the range of structural conditions that have been considered to date. For flexible structures with modest embedment, any approach other than Model 3 would likely provide acceptable results above the ground line. More generally, the bathtub approach (Model 4) appears to be the most generally applicable and reliable among the simplifications considered. However, even Model 4 does a poor job below the ground line because the application of depth-variable ground motion or kinematic rocking can significantly affect EDPs for deeply embedded structures (approximately two levels or more). When it is desired to avoid the use of foundation springs, Model 2 has been shown to provide reasonably good results, especially for embedded, flexible structures and EDPs associated with the portion of the structure above the ground line.

5.0 FORCED VIBRATION TESTING OF A SHALLOW FOUNDATION FIELD TEST STRUCTURE

5.1 Introduction

Following the devastating 1971 San Fernando earthquake, the engineering community realized the need to instrument buildings with accelerometers to study their seismic response. In 1972, the California Legislature established the California Strong Motion Instrumentation Program (CSMIP) in which hundreds of buildings have been instrumented with arrays of accelerometers. The US Geological Survey also instruments buildings, including the influential ANSS program currently in operation. Unfortunately, configurations of the arrays in a manner to enable the evaluation of SSI is (in general) poorly understood and has not typically been a considered a high priority. The evaluation of SSI effects on buildings requires the horizontal accelerometers at the free-field, foundation, and roof and two vertical accelerometers on the foundation to evaluate rocking response (Stewart and Fenves, 1998). There are about 12 buildings in California that meet all of these criteria, although approximately 60 meet enough of the criteria that some SSI effects can be evaluated (Stewart et al., 1999b). These structures have variable levels of inertial and kinematic interaction effects, from strong to practically negligible. There is some indication that CSMIP

and USGS may improve their instrumentation arrays to include SSI-type sensor implementation plans, and data from such structures is particularly useful for response history analysis studies, investigations of period lengthening and foundation damping, and investigations of kinematic interaction.

One issue that is not easily investigated with building seismic arrays is inference of impedance functions. As explained by Tileylioglu et al. (2011), the measurement of horizontal impedance requires relative displacements between the foundation and free-field. Such measurements will be highly noisy in a seismic setting, but can be effectively made in forced vibration testing of structures in the field.

Forced vibration testing of a steel and reinforced concrete structure has been performed to evaluate soil-structure interaction (SSI) systems at multiple George E. Brown, Jr. Network for Earthquake Engineering Simulations (NEES) sites. This work has been completed as part of a multi-institutional National Science Foundation (NSF) grand challenge (NSF 06-504 Program) project called, "Mitigation of Collapse Risk in Vulnerable Concrete Buildings." This project has been documented in the Network for Earthquake Engineering Simulations Research (NEESR) website, known as NEEShub, as project NEES-2008-0637. The SSI test series consisted of three test sites: University of California, Los Angeles Laboratory (LAB), Wildlife Liquefaction Array (WLA), and Garner Valley Downhole Array (GVDA). This NSF program presented a unique opportunity for research in that until this series of tests no single structure had been tested with different types of underlying materials to evaluate their influence to the structural response.

The sequence of testing at the three sites investigates the response of SSI systems involving varying degrees of base flexibility. The LAB represents an effectively fixed-base condition with structural columns attached to the existing laboratory strong-floor. The WLA site, with a soft clay layer overlying loose, liquefiable sands, and the GVDA site, with firm lake-bed alluvium material, represents flexible base conditions having variable levels of soil stiffness. The three sites were chosen to represent a spectrum of SSI effects based on the foundation conditions, with practically no SSI effect expected at the LAB to moderate effects at the GVDA site, to a strong SSI influence at the WLA.

This chapter discusses the forced vibration testing performed at GVDA in which the author was involved in the field testing. The forced vibration testing at WLA and LAB was presented by Star (2011). This chapter first describes the field test setup and instrumentation used at GVDA. Secondly, the forced vibration testing schemes and data processing types are discussed. Then a review of the structural response histories from the forced vibration testing is presented in Section 5.4. The chapter finishes with some concluding remarks about the forced vibration testing performed at GVDA.

5.2 Test Setup and Instrumentation

5.2.1 Garner Valley Downhole Array (GVDA) Test Site

The Garner Valley Downhole Array (GVDA) site has been well studied since 1989 and is well documented at the NEES@UCSB site (http://nees.ucsb.edu/facilities/gvda). Figure 5-1 shows a plan view of the site. The ground surface elevation is approximately 1,329 m (4,360 ft) above mean sea level (AMSL). Documents indicate relatively consistent soil conditions, consisting of 18.3

m (60 ft) to 25.3 m (83 ft) of thick lake-bed alluvium overlying decomposed granite that extends to about 91.4 m (300 ft) where weathered granodiorite bedrock is encountered. Figure 5-2 shows our interpretation of the soil layering at the site based on the NEES@UCSB data. This site was chosen based on its accessibility, existing instrumentation and infrastructure, the availability of site data, and its distinct geotechnical conditions relative to the other two NEES sites considered in prior work (WLA and LAB).

Previously published geophysical data for the site has been developed from Spectral-Analysis-of-Surface-Waves (SASW) measurements (Stokoe et al. 2004). Locations of SASW tests are shown in Figure 5-1; the resulting interpretation of the shear wave velocity (V_s) profile is shown in Figure 5-2. Based on the NEES@UCSB data, the average moist unit weight of the soil is approximately 17.3 kN/m^3 (110 lb/ft^3) to 19.6 kN/m^3 (125 lb/ft^3). The water table is typically at approximately 3 m (10 ft) below the ground surface.

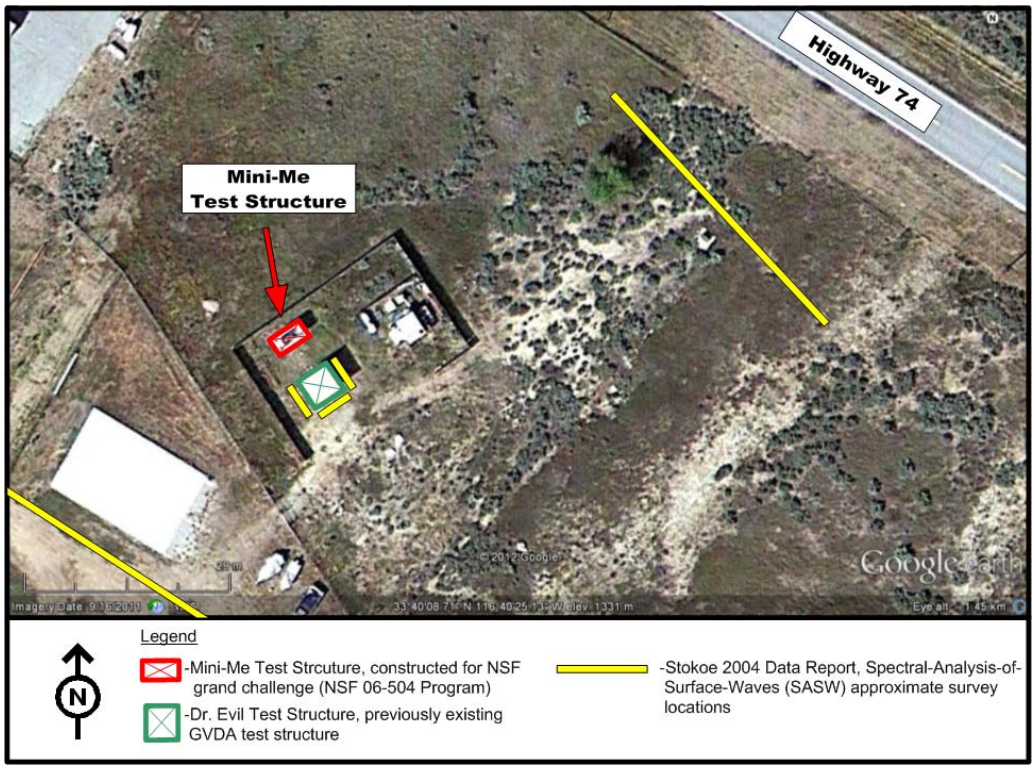

Figure 5-1 **Plan view of the GVDA site showing the approximate locations of the SASW test locations.**

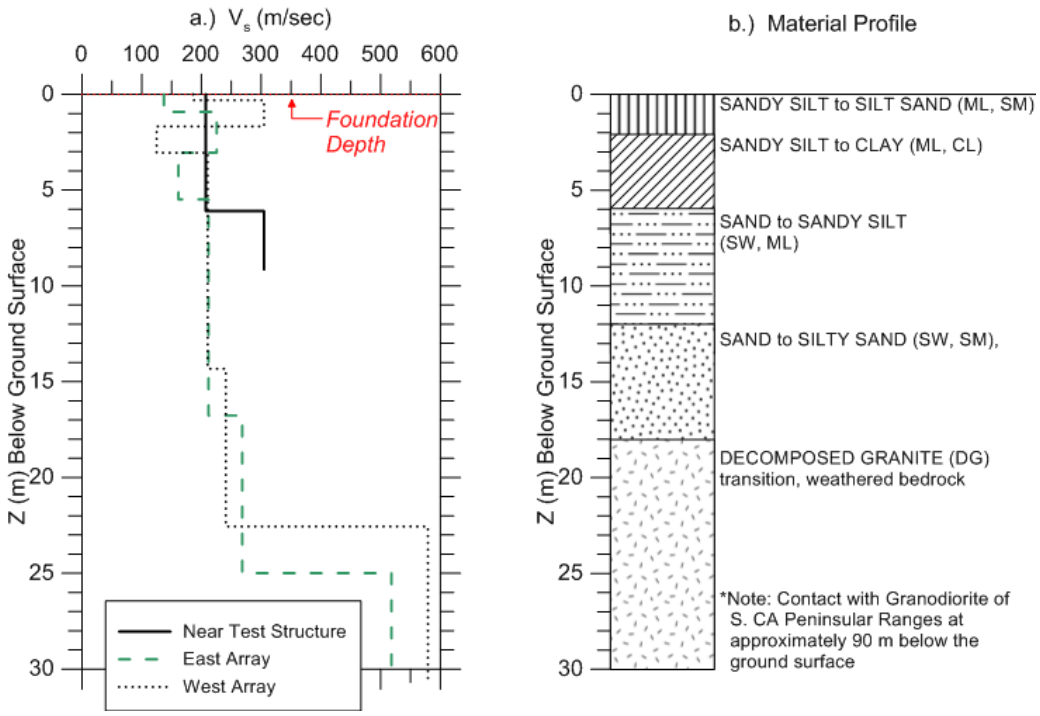

Figure 5-2 **Subsurface characteristics based on site exploration of the GVDA site: a) shear wave velocity profile and b) material profile.**

Crosshole seismic surveys were completed as part of this study to evaluate the soil shear wave velocity within the upper 2 m (6.6 ft) of the soil column below the structural footprint. The testing was performed on May 26, 2011 and the resulting soil shear wave velocity profiles are shown in Figure 5-3. The survey was conducted in two phases in an effort to evaluate the influence of the structural weight. Initial crosshole testing was performed across the structural footprint with only the weight of the foundation. Secondly, testing was performed following installation of the full structure. In addition to the measured results, Figure 5-3 provides velocity profile model names that will be used for analyses presented in Chapter 6.

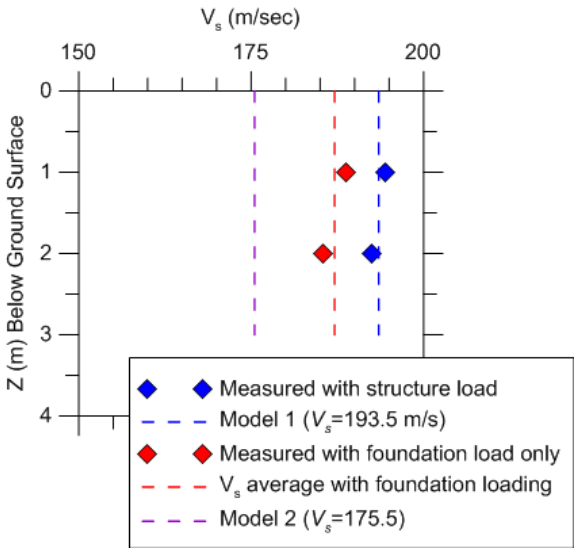

Figure 5-3 **Soil shear wave velocity profiles based on crosshole seismic surveys performed on May 26, 2011.**

Crosshole testing in which the weight of the structure is acting on the soil between the geophones produced an average velocity of V_s = 193.5 m/s (634.8 ft/s), which is referred to as "Model 1." Testing with the foundation, but not the structure, in place produced a slower velocity of V_s = 187.1 m/s (537.6 ft/s). Based on these results, the scaling of V_s with overburden pressure can be evaluated as follows (adapted from Tileylioglu et al., 2011):

$$\frac{(V_s)_1}{(V_s)_2} = \left(\frac{\sigma'_{v0} + (\Delta\sigma_v)_1}{\sigma'_{v0} + (\Delta\sigma_v)_2} \right)^{n/2} \quad (5\text{-}1)$$

where $(V_s)_1$ and $(V_s)_2$ are the overburden-corrected shear wave velocity for a particular depth z, σ_{v0}' is the effective stress from the soil's self-weight at depth z, and $(\Delta\sigma_v)_1$ and $(\Delta\sigma_v)_2$ are the increment of vertical stress at depth z from varying structural weights (e.g., for combined foundation/structure and foundation alone, respectively). The $\Delta\sigma_v$ quantities can be computed using classical 'Boussinesq-type' stress distribution theory (e.g., Fadum, 1948). The n value typically varies from approximately 0.5 for granular soils to 1.0 for cohesive soils with plasticity index PI > 6.5 (Yamada et al., 2008). A site-specific n value of 0.6 was back-calculated for a depth of 1.5 m (5 ft) below ground surface (BGS) from Eq. (5-1) using the aforementioned crosshole velocities and conditions where σ_{v0}' = 25 kN/m^2, $(\Delta\sigma_v)_1$ = 10 kN/m^2 and $(\Delta\sigma_v)_2$ = 6.3 kN/m^2. The GVDA site-specific n value determined for sandy and silty materials corresponds well to the Yasuda et al., 2008 recommended range of n values.

The velocity that is expected at the site prior to foundation placement (referred to as Model 2) was derived in a similar manner to Eq. (5-1):

$$V_s \approx V_{s0} \left(\frac{\sigma'_{v0} + \Delta\sigma_v}{\sigma'_{v0}} \right)^{n/2} \quad (5\text{-}2)$$

where V_{so} denotes the shear wave velocity measured in the free-field. The back-calculated V_{so} profile is shown in Figure 5-2. The V_{so} = 175.5 m/s (575.8 ft/s) was back-calculated for a depth of 1.5 m (5 ft) BGS from Eq. (5-2) using the site-specific n = 0.6, V_s = 193.5 m/s (634.8 ft/s), σ_{v0}' = 25 kN/m^2 and $\Delta\sigma_v$ = 10 kN/m^2.

5.2.2 Test Structures

The test structure that was used at all test sites for forced vibration testing is referred to as "Mini-Me." Mini-Me is a rectangular shaped steel moment frame with removable cross-bracing consisting of reinforced concrete roof and foundation, as shown in Figure 5-4. Unembedded reinforced concrete foundations were constructed at each field tests site and were cast-in-place to ensure realistic foundation-soil contact. The foundations were 0.61 m (2 ft) thick, 4.28 m (14 ft) long and 2.13 m (7 ft) wide and were designed to be nearly rigid. The foundation mat is composed of nominal 27.6 MPa (4,000 psi) concrete reinforced with #5 rebar. Prior to construction of the foundation, the pad was cleared and grubbed to remove surficial top soils and organics. The foundation mat was constructed on site and had more than 28 days to cure before testing. Based on the dimensions, the foundation has an estimated mass of 13,340 kg (29,409.4 lbs).

Nine 2.54 cm (1") diameter threaded rods were used to anchor the base plate of each column of the super structure to the foundation. The anchors were pre-drilled and secured using epoxy. The upper deck (roof) is composed of nominal 27.6 MPa (4,000 psi) concrete reinforced with #7 rebar and has similar dimensions to the foundation mat. The braced frame columns are constructed from four 30.5 cm x 30.5 cm x 1.3 cm (12"x12"x1/2") square hollow steel sections (HSS) that are 2.13 m (7 ft) tall and have a mass of approximately 250 kg (551 lbs) each. The super structure was constructed in September, 2008 and was transported from site-to-site. Removable cross-bracing can be added to the structure in order to modify the stiffness of the structure system. The braces are constructed from HSS 10.2 cm x 10.2 cm x 1.3 cm (4" x 4"x 1/2") steel sections. The total mass of the braces is approximately 800 kg

(1,763.7 lbs). The super structure and foundation together are 3 m (9.8 ft) tall. Braced and unbraced conditions were investigated as part of this experiment. As of this writing, the structure still exists and is present at GVDA.

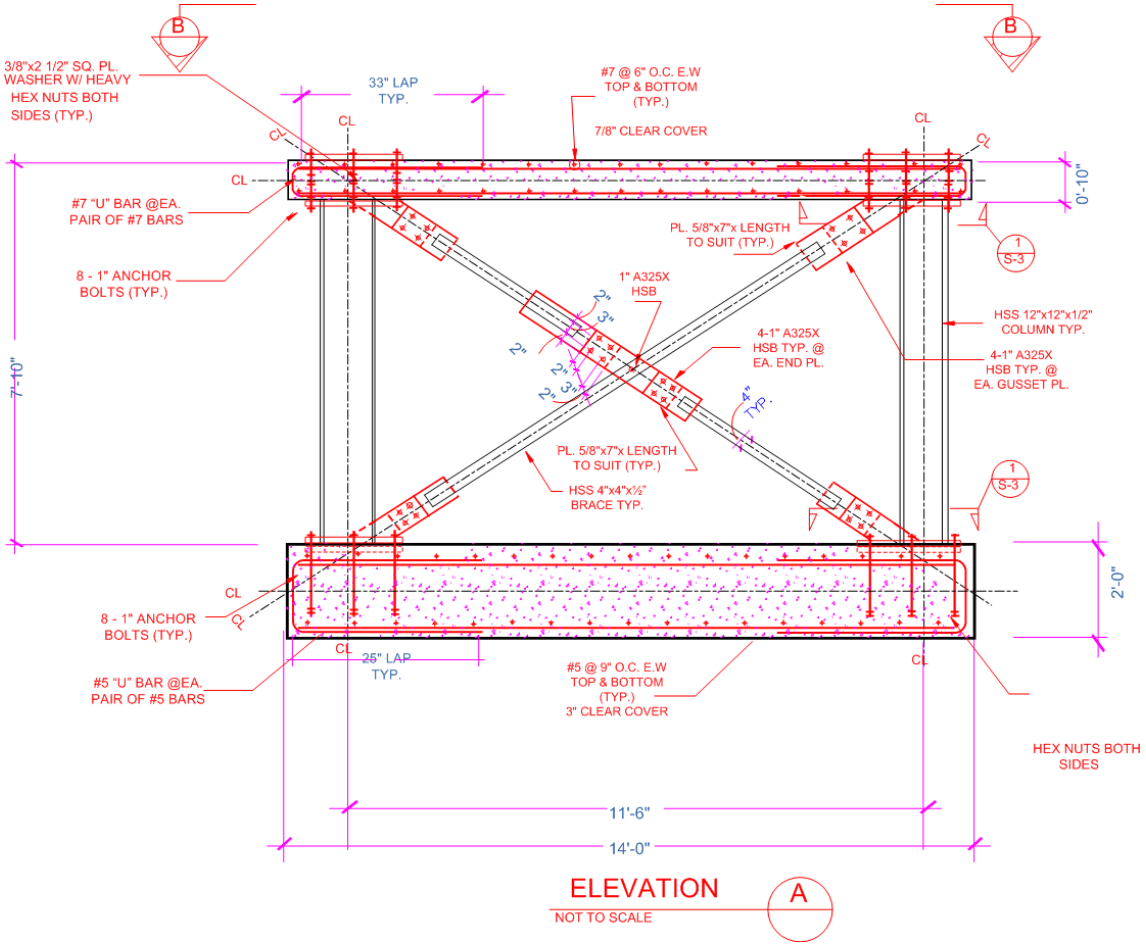

Figure 5-4 Construction plan cross-section of the test structure Mini-Me.

The GVDA site was previously improved with a similar type test structure for evaluate of SSI effects, referred to here as "Dr. Evil." Dr. Evil is a square shaped steel moment frame with removable cross-bracing consisting of reinforced concrete roof and foundation. Details on the dimensions and mass of this structure are provided in Tileylioglu et al. (2011) and at NEES@UCSB. During the testing period of this

experiment Dr. Evil was unbraced. Dr. Evil is situated approximately 4.6 m (14 ft) to the south of Mini-Me. The construction materials are similar to Mini-Me.

The construction drawings for Mini-Me are located in the NEEShub for this project. The foundation geometry adopted for testing is shown in Figure 5-5. Vibration modes for translation is represented by *x*, *y* and *z*, while rotation about theses axis, respectively, are *xx*, *yy* and *zz*. Figure 5-6 shows a photograph of the test structures at GVDA. With the exception of the foundation, the same "Mini-Me" super structure (columns, bracing, and roof) was used at GVDA, WLA, and LAB.

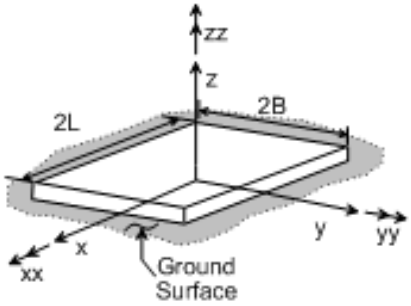

Figure 5-5 **Sketch showing the geometry adapted for the rectangular foundation** $(L \geq B)$.

Figure 5-6 **Photograph showing the test structure Mini-Me (right) and the previously constructed structure Dr. Evil (left) located at GVDA**

5.2.3 Sensors

In an effort to capture the response of the structure during the forced vibration testing at GVDA a total of 42 Episensor accelerometers were installed to monitor the response of Mini-Me, Dr. Evil and the adjacent soil. Figure 5-7 shows the sensor location plan along with a structure location plan. Mini-Me was instrumented with eight Kinemetrics Episensor ES-T triaxial accelerometers. The accelerometers are 13.3 cm (5.2 in) diameter (cylinder) and 6.2 cm (2.4 in) high. The accelerometers have a selected output range of +/- 20 V, for an amplitude range of +/- 4.0 g. The bandwidth is DC to 200 Hz. The accelerometers have a calibrated sensitivity of 5 Volts per g. One accelerometer was bolted in place at each corner of the structure top slab and foundation slab. Four Trans-Tek inc. model 0244-0000 DC_LVDTs (linear variable differential transformers) were installed near the corners of Mini-Me's foundation mat. The LVDTs have a measurement range of 5 cm (2 in). Dr. Evil was instrumented with four triaxial accelerometers. Additional triaxial accelerometers were installed in the soil near the structure. One was buried at the elevation of the foundation base in the longitudinal direction relative to the orientation of the structure (positive x-direction) and one in the direction transverse to the orientation of the structure (positive y-direction). All accelerometers sampled at a rate of 200 Hz.

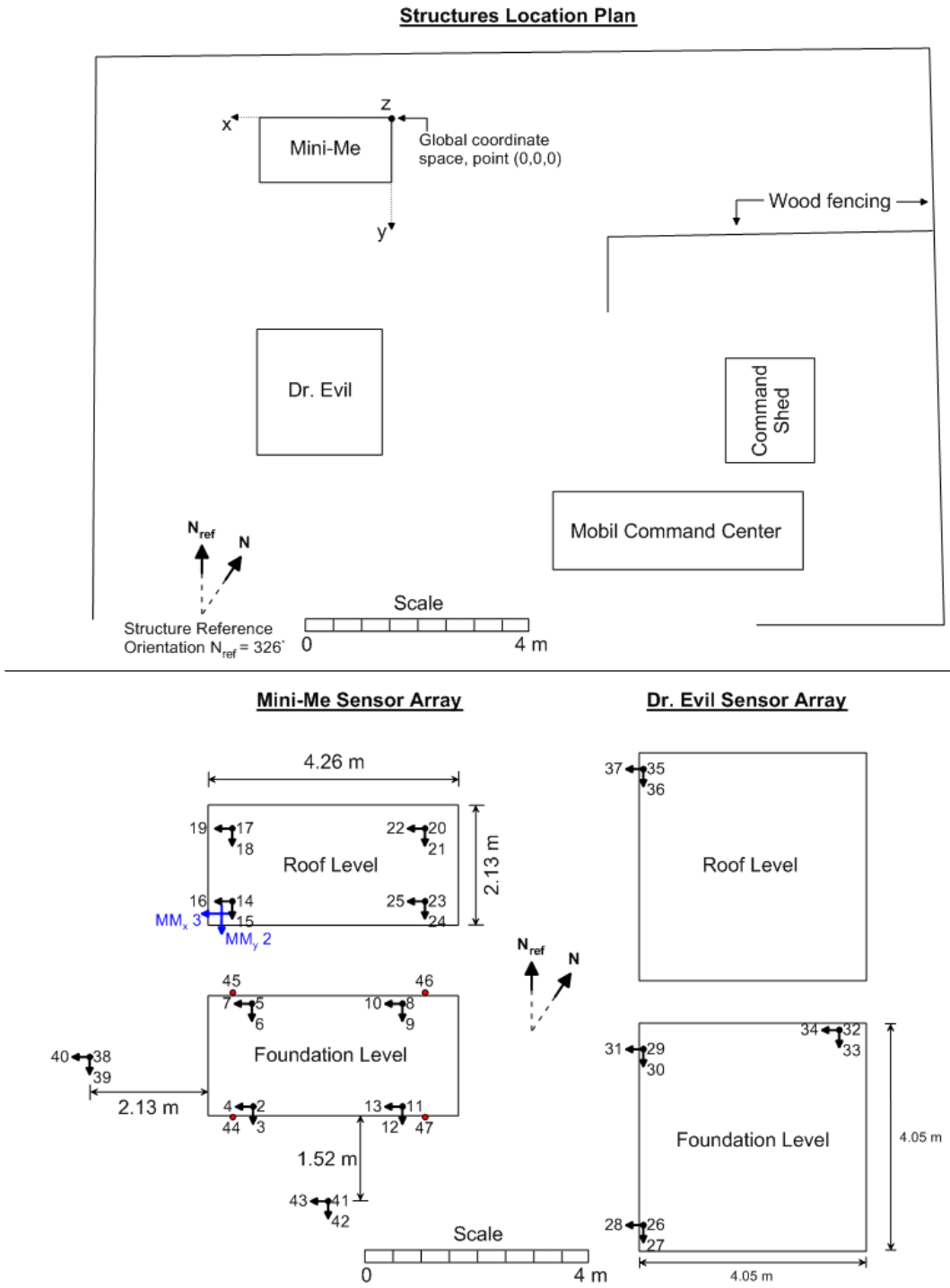

Figure 5-7 **Sketch showing the structures location and sensor arrays for testing at GVDA.**

The shaker forces were prescribed via the control system, however, it has been found that the prescribed input does not always equal the actual shaker response.

Therefore additional accelerometers were used to evaluate the input shaker force and ensure proper calibration for analysis. Two shakers were used for this experiment, which will be explained in detail in Section 5.2.4; a small linear shaker was instrumented with a single accelerometer in the direction of shaking and a larger eccentric mass shaker. During testing with the larger shaker two horizontal accelerometers were installed parallel to the existing accelerometers at the southwest corner of Mini-Me. Figure 5-7 shows the location of these two accelerometers in blue. This was done in order to allow the correlation of data on two separate acquisition systems.

The sensor implementation plan was prepared with support of NEES@UCLA. Details pertaining to the Episensor accelerometers and LVDTs can be found at http://nees.ucla.edu/equipment.html.

5.2.4 Forced Vibration Shakers

Mini-Me was subjected to forced vibration testing using two types of shakers. A small shaker referred to as "Atom-Ant," was used for *x*, *y* and torsion modal forced vibration testing at the roof and top of foundation mat levels. A larger shaker referred to as "Mighty Mouse," was used for *x* and *y* modal forced vibration testing at the roof level. The forced vibration testing was performed on June 22 through June 24, 2011 and August 1 through August 2, 2011.

Atom Ant is a small portable Acoustic Power System 'ELECTRO-SEIS long stroke shaker model 400. The shaker characteristics are described here because it is not NEES@UCLA equipment documented on the web site. Atom Ant is a 7.3 kg (161 lbs) shaker that has a maximum force of 444.8 N (100 lbf). The shaker was controlled by an APS Dynamic Inc. dual mode power amplifier model 144 and a HP Agilent

33220A, 2 Mhz function / arbitrary waveform generator. Forcing frequencies were controlled through the generator output by two methods: sweeps and steps. Sweeps consist of producing a consistent scan of frequency output that was controlled automatically for defined ranges. Sweeps frequencies ranged from 4 Hz to a maximum of 54 Hz. Steps consisted of producing constant frequencies in short sustained intervals at 0.5 Hz steps for the same frequency range as the sweeps. The steps were produced for redundancy to present individual frequency point comparisons to the sweep data.

Mighty Mouse is a large NEES 4600A eccentric mass shaker that consists of two sets of circular weights. The eccentricity of the circular weights can be adjusted from 0 to 110.7 N-m (980 lb-in.) and is intended for a frequency range of 0 to 20 Hz. The force is proportional to the eccentricity. Forcing frequencies were controlled by the Mobile Command Center using LabVIEW (described in Sec 5.2.5). For consistency with the forced vibration testing performed with the Atom Ant shaker, sweeps and steps were performed. Sweeps frequencies ranged from 0 to a maximum of 19 Hz. Steps consisted of short sustained intervals at 0.2 Hz steps for the same frequency range as the sweeps.

Atom Ant was on loan from Geovision Inc. during the testing phase and Mighty Mouse is maintained and operated by NEES@UCLA.

5.2.5 Data Acquisition Setup

Data collection was performed with the Mobile Command Center operated by NEES@UCLA. The sensors responses were collected by eight (8) Quanterra Q330 wireless data loggers. The Q330s have 6-channels, global positioning system (GPS) receivers, and a dynamic range of 135 dB RMS S/N with a time stamp accuracy of

<0.1 ms. The Q330 data was then collected using Rockhound data acquisition software in the Mobile Command Center located onsite. The sensor sampling rate was 200 Hz. The GVDA data acquisition channels have been described in Table 5-1 and are presented in Figure 5-7. In this report, the data from this acquisition system is referred to as "structural response data."

During forced vibration testing using Mighty Mouse, the shaker pulse and correlation accelerometer data was recorded using a DAQ which had a sampling rate of 5000 Hz. The higher sampling rate is necessary in order to determine phasing of the shaker force with adequate precision. The data acquisition (DA) channels used for data collection pertaining to testing with the Mighty Mouse shaker is described in Table 5-2. In this report, the data from this acquisition system is referred to as "Mighty Mouse shaker data." The Mighty Mouse shaker data includes two accelerometers used for correlation of the two different data acquisition systems. The accelerometer locations are presented in Figure 5-7 as blue arrows, parallel to accelerometers designated as channels 15 and 16 in the structural response data. The correlation method used is described in Section 5.3.3. Two tables have been presented for Table 5-2 because channel 4 and 5 were switched from the June to August testing. The prefix "MM" is used to distinguish the Mighty Mouse shaker data channels from the Structural Response data channels, shown in column 2 of Table 5-2.

Table 5-1 GVDA Sensor Locations plan for all forced vibration testing located at Garner Valley Downhole Array site in June and August of 2011.

DA Channel Number	Channel Name Corrected/Converted	Sensor Label	Sensor Type	Comments	Position			Position Units	Orientation			Coordinate Space	Serial Number	Sensor Measurement Units	Calibration Constant	
					X	Y	Z		I	J	K				Value	Units
1	1	Time	Position	Raw Data has Unix time	228	252	0	in	0	0	0	Global Coordinate Space	Time	s	1	s
2	2	MM Bottom_SW_Z	Accelerometer		136.5	78	24	in	0	0	1	Global Coordinate Space	1193	count	0.0000119	G/count
3	3	MM Bottom_SW_Y	Accelerometer		136.5	78	24	in	0	1	0	Global Coordinate Space	1193	count	0.0000119	G/count
4	4	MM Bottom_SW_X	Accelerometer		136.5	78	24	in	1	0	0	Global Coordinate Space	1193	count	0.0000119	G/count
5	5	MM Bottom_NW_Z	Accelerometer		136.5	6	24	in	0	0	1	Global Coordinate Space	1700	count	0.0000119	G/count
6	6	MM Bottom_NW_Y	Accelerometer		136.5	6	24	in	0	1	0	Global Coordinate Space	1700	count	0.0000119	G/count
7	7	MM Bottom_NW_X	Accelerometer		136.5	6	24	in	1	0	0	Global Coordinate Space	1700	count	0.0000119	G/count
8	8	MM Bottom_NE_Z	Accelerometer		31.5	6	24	in	0	0	1	Global Coordinate Space	1550	count	0.0000119	G/count
9	9	MM Bottom_NE_Y	Accelerometer		31.5	6	24	in	0	1	0	Global Coordinate Space	1550	count	0.0000119	G/count
10	10	MM Bottom_NE_X	Accelerometer		31.5	6	24	in	1	0	0	Global Coordinate Space	1550	count	0.0000119	G/count
11	11	MM Bottom_SE_Z	Accelerometer		31.5	78	24	in	0	0	1	Global Coordinate Space	1701	count	0.0000119	G/count
12	12	MM Bottom_SE_Y	Accelerometer		31.5	78	24	in	0	1	0	Global Coordinate Space	1701	count	0.0000119	G/count
13	13	MM Bottom_SE_X	Accelerometer		31.5	78	24	in	1	0	0	Global Coordinate Space	1701	count	0.0000119	G/count
14	14	MM Top_SW_Z	Accelerometer		151.5	67.5	118	in	0	0	1	Global Coordinate Space	1444	count	0.0000119	G/count
15	15	MM Top_SW_Y	Accelerometer		151.5	67.5	118	in	0	1	0	Global Coordinate Space	1444	count	0.0000119	G/count
16	16	MM Top_SW_X	Accelerometer		151.5	67.5	118	in	1	0	0	Global Coordinate Space	1444	count	0.0000119	G/count
17	17	MM Top_NW_Z	Accelerometer		151.5	16.5	118	in	0	0	1	Global Coordinate Space	1443	count	0.0000119	G/count
18	18	MM Top_NW_Y	Accelerometer		151.5	16.5	118	in	0	1	0	Global Coordinate Space	1443	count	0.0000119	G/count
19	19	MM Top_NW_X	Accelerometer		151.5	16.5	118	in	1	0	0	Global Coordinate Space	1443	count	0.0000119	G/count
20	20	MM Top_NE_Z	Accelerometer		16.5	16.5	118	in	0	0	1	Global Coordinate Space	1190	count	0.0000119	G/count
21	21	MM Top_NE_Y	Accelerometer		16.5	16.5	118	in	0	1	0	Global Coordinate Space	1190	count	0.0000119	G/count
22	22	MM Top_NE_X	Accelerometer		16.5	16.5	118	in	1	0	0	Global Coordinate Space	1190	count	0.0000119	G/count
23	23	MM Top_SE_Z	Accelerometer		16.5	67.5	118	in	0	0	1	Global Coordinate Space	1883	count	0.0000119	G/count
24	24	MM Top_SE_Y	Accelerometer		16.5	67.5	118	in	0	1	0	Global Coordinate Space	1883	count	0.0000119	G/count
25	25	MM Top_SE_X	Accelerometer		16.5	67.5	118	in	1	0	0	Global Coordinate Space	1883	count	0.0000119	G/count
26	26	DE Bottom_SW_Z	Accelerometer		158.7	394	24	in	0	0	1	Global Coordinate Space	1702	count	0.0000119	G/count
27	27	DE Bottom_SW_Y	Accelerometer		158.7	394	24	in	0	1	0	Global Coordinate Space	1702	count	0.0000119	G/count
28	28	DE Bottom_SW_X	Accelerometer		158.7	394	24	in	1	0	0	Global Coordinate Space	1702	count	0.0000119	G/count
29	29	DE Bottom_NW_Z	Accelerometer		158.7	270.5	24	in	0	0	1	Global Coordinate Space	1192	count	0.0000119	G/count
30	30	DE Bottom_NW_Y	Accelerometer		158.7	270.5	24	in	0	1	0	Global Coordinate Space	1192	count	0.0000119	G/count
31	31	DE Bottom_NW_X	Accelerometer		158.7	270.5	24	in	1	0	0	Global Coordinate Space	1192	count	0.0000119	G/count
32	32	DE Bottom_NE_Z	Accelerometer		18	255.3	24	in	0	0	1	Global Coordinate Space	3849	count	0.0000119	G/count
33	33	DE Bottom_NE_Y	Accelerometer		18	255.3	24	in	0	1	0	Global Coordinate Space	3849	count	0.0000119	G/count
34	34	DE Bottom_NE_X	Accelerometer		18	255.3	24	in	1	0	0	Global Coordinate Space	3849	count	0.0000119	G/count
35	35	DE Top_W_Z	Accelerometer		158.7	264	117	in	0	0	1	Global Coordinate Space	1445	count	0.0000119	G/count
36	36	DE Top_W_Y	Accelerometer		158.7	264	117	in	0	1	0	Global Coordinate Space	1445	count	0.0000119	G/count
37	37	DE Top_W_X	Accelerometer		158.7	264	117	in	1	0	0	Global Coordinate Space	1445	count	0.0000119	G/count
38	38	Field W_Z	Accelerometer		336	42	-1	in	0	0	1	Global Coordinate Space	1442	count	0.0000119	G/count
39	39	Field W_Y	Accelerometer		336	42	-1	in	0	1	0	Global Coordinate Space	1442	count	0.0000119	G/count
40	40	Field W_X	Accelerometer		336	42	-1	in	1	0	0	Global Coordinate Space	1442	count	0.0000119	G/count
41	41	Field S_Z	Accelerometer		84	252	-1	in	0	0	1	Global Coordinate Space	1446	count	0.0000119	G/count
42	42	Field S_Y	Accelerometer		84	252	-1	in	0	1	0	Global Coordinate Space	1446	count	0.0000119	G/count
43	43	Field S_X	Accelerometer		84	252	-1	in	1	0	0	Global Coordinate Space	1446	count	0.0000119	G/count
44	44	SW corner	LVDT	Mult Conv. Data by 10	153	85	22	in	0	0	1	Global Coordinate Space	D29	count	3.08E-07	in/count
45	45	NW corner	LVDT		153	-1	22	in	0	0	1	Global Coordinate Space	D8	count	2.36E-07	in/count
46	46	NE corner	LVDT	Mult Conv. Data by 10	15	-1	22	in	0	0	1	Global Coordinate Space	D15	count	2.43E-07	in/count
47	47	SE corner	LVDT	Mult Conv. Data by 10	15	85	22	in	0	0	1	Global Coordinate Space	D17	count	2.50E-07	in/count
48	48	AA Weight Acc	Accelerometer		42	84	118	in	1	1	0	Global Coordinate Space	548	count	0.0000119	G/count

* MM: Mini-Me test structure; AA: Atom Ant Shaker; DE: Dr. Evil test structure; Bottom: sensor located on bottom (foundation) slab; Top: sensor located on top (roof) slab;

* SW, SE, NE, NW: Relative directional in "Sensor Label" and locatin for "Position," based on referenced north in Structures Location Plan (Figure 7);

*X, Y, Z: Sensor direction and location based on global coordinate system shown in the Structures Location Plan (Figure 7)

*G: Gravity; in: inches; s: seconds; LVDT: linear variable differential transformer; I, J, K: Represents orientation of sensor, respectively, in X, Y, and Z direction

*Note converted LVDT data (Chs. 44, 46, and 47) has an error that can be corrected by multipling processed channels by a factor of 10.

Table 5-2a Mighty Mouse Shaker Data plan for vibration testing using Mighty Mouse shaker located at Garner Valley Downhole Array site in June of 2011.

DA Channel Number	Channel Name Corrected/Converted	Sensor Label	Sensor Type	Comments	Position			Position Units	Orientation			Coordinate Space	Serial Number	Sensor Measurement Units	Calibration Constant	
					X	Y	Z		I	J	K				Value	Units
1	MM 1	Time	Position		228	252	0	in	0	0	0	Global Coordinate Space	Time	s	1	s
2	MM 2	MM Top_SW_ X_Correlation	Accelerometer	Correlation to channel 16 of GVDA Mini-Me Sensor Locations	163	67.5	118	in	1	0	0	Global Coordinate Space	551	count	0.0000119	G/count
3	MM 3	MM Top_SW_ Y_Correlation	Accelerometer	Correlation to channel 15 of GVDA Mini-Me Sensor Locations	151.5	82	118	in	0	1	0	Global Coordinate Space	542	count	0.0000119	G/count
4	MM 4	MM Control Frequecy	N/A	1 Pulse Per Revolution	228	252	0	in	0	0	0	Global Coordinate Space	Pulse1	V	1	V
5	MM 5	Shaker Pulses	N/A	10 Pulses Per Revolution	228	252	0	in	0	0	0	Global Coordinate Space	Pulse10	V	1	V

* MM: Mini-Me test structure; Top: sensor located on top (roof) slab;
* SW Relative southwest location based on referenced north in Structures Location Plan (Figure 5-7);
*X, Y, Z: Sensor direction in "Senosr Label" and location for "Position," based on global coordinate system shown in the Structures Location Plan (Figure 7)
*G: Gravity; V: volts; in: inches; s: seconds; N/A: not applicable; I, J, K: Represents orientation of sensor, respectively, in X, Y, and Z direction

Table 5-2b Mighty Mouse Shaker Data plan for vibration testing using Mighty Mouse shaker located at Garner Valley Downhole Array site in August of 2011.

DA Channel Number	Channel Name Corrected/Converted	Sensor Label	Sensor Type	Comments	Position			Position Units	Orientation			Coordinate Space	Serial Number	Sensor Measurement Units	Calibration Constant	
					X	Y	Z		I	J	K				Value	Units
1	MM 1	Time	Position		228	252	0	in	0	0	0	Global Coordinate Space	Time	s	1	s
2	MM 2	MM Top_SW_ X_Correlation	Accelerometer	Correlation to channel 16 of GVDA Mini-Me Sensor Locations	163	67.5	118	in	1	0	0	Global Coordinate Space	551	count	0.0000119	G/count
3	MM 3	MM Top_SW_ Y_Correlation	Accelerometer	Correlation to channel 15 of GVDA Mini-Me Sensor Locations	151.5	82	118	in	0	1	0	Global Coordinate Space	542	count	0.0000119	G/count
4	MM 4	Shaker Pulses	N/A	10 Pulses Per Revolution	228	252	0	in	0	0	0	Global Coordinate Space	Pulse10	V	1	V
5	MM 5	MM Control Frequecy	N/A	1 Pulse Per Revolution	228	252	0	in	0	0	0	Global Coordinate Space	Pulse1	V	1	V

* MM: Mini-Me test structure; Top: sensor located on top (roof) slab;
* SW Relative southwest location based on referenced north in Structures Location Plan (Figure 7);
*X, Y, Z: Sensor direction in "Senosr Label" and location for "Position," based on global coordinate system shown in the Structures Location Plan (Figure 5-7)
*G: Gravity; V: volts; in: inches; s: seconds; N/A: not applicable; I, J, K: Represents orientation of sensor, respectively, in X, Y, and Z direction

5.3 Trials and Data Processing Procedures

The experiment consists of four (4) trials distinguished by the type of loading (i.e., type of shaker) and structural stiffness (braced or unbraced condition) as follows:

- Trial 1: Braced Structure, Atom Ant Shaker
- Trial 2: Braced Structure, Mighty Mouse Shaker
- Trial 3: Unbraced Structure, Atom Ant Shaker
- Trial 4: Unbraced Structure, Mighty Mouse Shaker

The forced vibration testing where Mini-Me was braced was performed in June 2011, while the unbraced condition was tested in August 2011.

Each trial consisted of forced vibration testing of Mini-Me in multiple modal directions (x, y, and torsion). All data has been uploaded to the NEEShub. Each trial contains unprocessed data, converted data and corrected data files.

This section begins with a discussion of the field test logs, which have labeling corresponding to the data files located at the NEEShub. Section 5.3.2 describes the different file types and the processes taken in preparation of the data files from unprocessed data to corrected data. Section 5.3.3 describes how the Mighty Mouse shaker and structural response data acquisition systems were synchronized. Then Sections 5.3.4 through 5.3.6 describe the specific data file types that are located at the NEEShub in detail.

5.3.1 Field Test Logs

Tables 5-3 through 5-6 show field testing logs for the forced vibration testing of Mini-Me that were performed on June 22 through June 24, 2011 and August 1 through August 2, 2011. Mini-Me was in a braced condition during the June testing, where both Atom Ant and Mighty Mouse shakers were utilized. The August testing

consisted of forced vibration testing of Mini-Me in an unbraced condition, where both Atom Ant and Mighty Mouse shakers were utilized.

The highlighted blue rows in Tables 5-3 through 5-6 represent the unprocessed data files. These unprocessed data files contain several different forced vibration testing runs. The underlying non-highlighted rows represent the subevents that were determined by shaking direction, shaking force (or shaker type), shaking duration, and shaker pulsing type (steeps or sweeps) as indicated in the loading description column. Each subevent was categorized with a subevent identification number based on the test location, trial, order location in the series of testing, and repetitions. The three test locations have the following numbering 1=LAB, 2=WLA and 3=GVDA. The trial number corresponds to the aforementioned list of bracing and shaking type condition. The order number was based on the chronology of testing in a particular trial. If the subevent labeling has a letter following the order number, this letter represents the order of repetition of the type of forced vibration force, duration and pulsing type. For example, in Table 5-3, Exp.3.1.1b represents experiment at GVDA, trial 1, first forced vibration test of the trial, and 'b' represents redundancy with this test being the second of its type.

Table 5-3 GVDA forced vibration testing logs for testing on June 22, 2011 (Trial 1: Mini-Me in braced condition with forcing from Atom Ant shaker).

							Local Time Recorded in Field				
Subevent #	**Local Date**	**Recorded Data File Name**	**Subevent File Name**	**Description**	**Loading Description**	**GMT**	**First Sample**	**Last Sample**	**Sweep Frequency Range**	**Snipped Subevent Time Length**	**Snipped Unix time**
-	6/22/2011	20110622161102.GV3									
1a	"	"	Exp3.1.1a.txt	Braced	X AA sweep top	17:10	10:10:06 AM		4-54 Hz	50 s	1308762590
-		20110622171102.GV3									
1b	"		Exp3.1.1b.txt	Braced	X AA sweep top	17:12	10:12:00 AM		4-54 Hz	50 s	1308762710
1c	"		Exp3.1.1c.txt	Braced	X AA sweep top	17:13	10:13:50 AM		4-54 Hz	50 s	1308762800
1d	"		Exp3.1.1d.txt	Braced	X AA sweep top	17:15	10:15:30 AM		4-54 Hz	200 s	1308762930
1e	"		Exp3.1.1e.txt	Braced	X AA sweep top	17:19	10:19:30 AM		4-54 Hz	200 s	1308763175
2	"		Exp3.1.2.txt	Braced	X AA step 0.5 Hz top	17:24	10:24:00 AM	10:41:15 AM	4-54 Hz	1035 s	1308763440
3a	"		Exp3.1.3a.txt	no rope on shaker	X AA sweep top	17:48	10:48:30 AM		4-54 Hz	50 s	1308764900
3b	"		Exp3.1.3b.txt	Braced	X AA sweep top	17:49	10:49:30 AM		4-54 Hz	50 s	1308764960
-		20110622181102.GV3									
4a	"		Exp3.1.4a.txt	Braced	Y AA torsion 42" sweep top	18:12	11:12:30 AM		4-54 Hz	50 s	1308766338
4b	"		Exp3.1.4b.txt	Braced	Y AA torsion 42" sweep top	18:14	11:14:00 AM		4-54 Hz	50 s	1308766428
4c	"		Exp3.1.4c.txt	Braced	Y AA torsion 42" sweep top	18:15	11:15:15 AM		4-54 Hz	50 s	1308766503
4d	"		Exp3.1.4d.txt	Braced	Y AA torsion 42" sweep top	18:22	ambient	11:22:15 AM	4-54 Hz	200 s	1308766925
4e	"		Exp3.1.4e.txt	Braced	Y AA torsion 42" sweep top	18:26	11:26:00 AM		4-54 Hz	200 s	1308767150
5	"		Exp3.1.5.txt	Braced	Y AA torsion step 0.5 Hz top	18:30	11:30:30 AM		4-44 Hz	1000 s	1308767405
6a	"		Exp3.1.6a.txt	Braced	Y AA sweep top	18:59	11:59:45 AM		4-54 Hz	50 s	1308769173
6b	"		Exp3.1.6b.txt	Braced	Y AA sweep top	19:01	12:01:00 PM		4-54 Hz	50 s	1308769248
6c	"		Exp3.1.6c.txt	Braced	Y AA sweep top	19:02	12:02:15 PM		4-54 Hz	50 s	1308769323
6d	"		Exp3.1.6d.txt	Braced	Y AA sweep top	19:03	12:03:30 PM		4-54 Hz	200 s	1308769400
6e	"		Exp3.1.6e.txt	Braced	Y AA sweep top	19:07	12:07:30 PM		4-54 Hz	200 s	1308769640
-		20110622191102.GV3									
7	"		Exp3.1.7.txt	Braced	Y AA step 0.5 Hz top	19:12	12:12:30 PM	12:25:00 PM	4-44 Hz	800 s	1308769920
-		20110622201102.GV3									
8a	"		Exp3.1.8a.txt	Braced, Shaker untied	X AA sweep bottom	20:21	1:21:15 PM		4-54 Hz	50 s	1308774063
8b	"		Exp3.1.8b.txt	Braced, Shaker untied	X AA sweep bottom	20:26	1:26:00 PM		4-54 Hz	50 s	1308774348
8c	"		Exp3.1.8c.txt	Braced, Shaker untied	X AA sweep bottom	20:27	1:27:30 PM		4-54 Hz	50 s	1308774438
8d	"		Exp3.1.8d.txt	Braced, Shaker untied	X AA sweep bottom	20:29	1:29:25 PM		4-54 Hz	50 s	1308774553
8e	"		Exp3.1.8e.txt	Braced, Shaker untied	X AA sweep bottom	20:31	1:31:50 PM		4-54 Hz	200 s	1308774705
8f	"		Exp3.1.8f.txt	Braced, Shaker untied	X AA sweep bottom	20:35	1:35:50 PM		4-54 Hz	200 s	1308774945
8g	"		Exp3.1.8g.txt	Braced, Shaker untied	X AA sweep bottom	20:39	1:39:50 PM		4-54 Hz	200 s	1308775185
-	"		Void	Braced, Shaker untied	X AA step .5 Hz bottom	20:46	1:46:30 PM	Void	4-44 Hz	N/A	VOID
9	"		Exp3.1.9.txt	Braced, Shaker untied	X AA step .5 Hz bottom	20:50	1:50:55 PM	2:09:45 PM	4-44 Hz	1100 s	1308775900
-		20110622211102.GV3									
10a	"		Exp3.1.10a.txt	Braced, Shaker untied	X AA sweep bottom	21:11	2:11:30 PM		4-54 Hz	50 s	1308777078
10b	"		Exp3.1.10b.txt	Braced, Shaker untied	X AA sweep bottom	21:12	2:12:55 PM		4-54 Hz	200 s	1308777170
11a	"		Exp3.1.11a.txt	Braced, Shaker untied	Y AA sweep bottom	21:21	2:21:40 PM		4-54 Hz	50 s	1308777686
11b	"		Exp3.1.11b.txt	Braced, Shaker untied	Y AA sweep bottom	21:22	2:22:50 PM		4-54 Hz	50 s	1308777756
11c	"		Exp3.1.11c.txt	Braced, Shaker untied	Y AA sweep bottom	21:24	2:24:00 PM		4-54 Hz	50 s	1308777826
11d	"		Exp3.1.11d.txt	Braced, Shaker untied	Y AA sweep bottom	21:25	2:25:30 PM	2:28:50 PM	4-54 Hz	200 s	1308777918
11e	"		Exp3.1.11e.txt	Braced, Shaker untied	Y AA sweep bottom	21:29	2:29:30 PM	2:32:50 PM	4-54 Hz	200 s	1308778158
12	"		Exp3.1.12.txt	Braced, Shaker untied	Y AA step .5 Hz bottom	21:34	2:34:30 PM	2:51:30 PM	4-44 Hz	1040 s	1308778456
13a	"		Exp3.1.13a.txt	Braced, Shaker untied	Y AA Torsion 42" sweep bottom	22:02	3:02:30 PM		4- 54 Hz	50 s	1308780138
13b	"		Exp3.1.13b.txt	Braced, Shaker untied	Y AA Torsion 42" sweep bottom	22:03	3:03:45 PM		4- 54 Hz	50 s	1308780213
13c	"		Exp3.1.13c.txt	Braced, Shaker untied	Y AA Torsion 42" sweep bottom	22:04	3:04:50 PM		4- 54 Hz	50 s	1308780278
13d	"		Exp3.1.13d.txt	Braced, Shaker untied	Y AA Torsion 42" sweep bottom	22:06	3:06:50 PM		4- 54 Hz	200 s	1308780398
13e	"		Exp3.1.13e.txt	Braced, Shaker untied	Y AA Torsion 42" sweep bottom	22:10	3:10:30 PM		4- 54 Hz	200 s	1308780618
-		20110622221102.GV3									
13f	"		Exp3.1.13f.txt	Braced, Shaker untied	Y AA Torsion 42" sweep bottom	22:14	3:14:30 PM		4- 54 Hz	200 s	1308780858
14	"		Exp3.1.14.txt	Braced, Shaker untied	Y AA Torsion 42" Step .5 Hz bottom	22:21	3:21:30 PM	3:38:00 PM	4-44 Hz	1000s	1308781278

* Blue highlight shows raw data file, in which snipped files below came from; X, Y and Torsion are direction of shaking; AA: Atom Ant shaker used; MM: Mighty Mouse shaker used;

* step: shaker increments stepped at a defined frequency (given directly after step label) was used; sweep: increment of shaker frequency was provided in across a defined frequency zone and then brought back to zero;

*Bottom: indicates shaker was located on the bottom concrete deck; Top: indicates shaker was located on the top concrete deck; % ecc 980: indicated percent eccentricity of the 980 lb weight used during forcing.

Table 5-4a GVDA forced vibration testing logs for testing on June 23 and 24, 2011 (Trial 2: Mini-Me in braced condition with forcing from Mighty Mouse shaker).

							Local Time Recorded in Field				
Subevent #	**Local Date**	**Recorded Data File Name**	**Subevent File Name**	**Description**	**Loading Description**	**GMT**	**First Sample**	**Last Sample**	**Sweep Frequency Range**	**Snipped Subevent Time Length**	**Snipped Unix time**
		20110623163939.GV3									
1a	6/23/2011		Exp3.2.1a.txt	Braced	Y 10% ecc, 980 Force, sweep	17:16	10:16:40 AM	10:23:00 AM	0-19 Hz	400	1308849445
1b	6/23/2011		Exp3.2.1b.txt	Braced	Y 10% ecc, 980 Force, sweep	17:25	10:25:00 AM	10:32:00 AM	0-19 Hz	400	1308849945
1c	6/23/2011		Exp3.2.1c.txt	Braced	Y 10% ecc, 980 Force, sweep	17:32	10:32:00 AM	10:39:00 AM	0-19 Hz	400	1308850378
		20110623173939.GV3									
2a	6/23/2011		Exp3.2.2a.txt	Braced	Y 25% ecc, 980 Force, sweep	17:56	10:56:00 AM	11:03:00 AM	0-19 Hz	400	1308851805
2b	6/23/2011		Exp3.2.2b.txt	Braced	Y 25% ecc, 980 Force, sweep	18:03	11:03:00 AM	11:10:00 AM	0-19 Hz	400	1308852255
2c	6/23/2011		Exp3.2.2c.txt	Braced	Y 25% ecc, 980 Force, sweep	18:11	11:11:00 AM	11:18:00 AM	0-19 Hz	400	1308852720
		20110623183939.GV3									
3	6/23/2011		Exp3.2.3.txt	Braced	Y 25% ecc, 980 Force, step 0.2 Hz	18:39	11:39:00 AM	11:46:00 AM	1-19 Hz	450	1308854440
Void	6/23/2011		Void	Braced	X 25% ecc, 980 Force, sweep	19:06	12:06:00 PM	12:13:00 PM	Error	Void	Void
4a	6/23/2011		Exp3.2.4a.txt	Braced	X 25% ecc, 980 Force, sweep	19:17	12:17:00 PM	12:23:00 PM	1-19 Hz	400	1308856680
4b	6/23/2011		Exp3.2.4b.txt	Braced	X 25% ecc, 980 Force, sweep	19:25	12:25:00 PM	12:32:00 PM	1-19 Hz	400	1308857160
5	6/23/2011		Exp3.2.5.txt	Braced	X 25% ecc, 980 Force,step 0.2 Hz	19:33	12:33:00 PM	12:41:00 PM	1-19 Hz	420	1308857700
		20110623193939.GV3									
6a	6/23/2011		Exp3.2.6a.txt	Braced	X 10% ecc, 980 Force, sweep	20:03	1:03:00 PM	1:10:00 PM	1-19 Hz	400	1308859440
6b	6/23/2011		Exp3.2.6b.txt	Braced	X 10% ecc, 980 Force, sweep	20:11	1:11:00 PM	1:18:00 PM	1-19 Hz	400	1308859920
6c	6/23/2011		Exp3.2.6c.txt	Braced	X 10% ecc, 980 Force, sweep	20:18	1:18:00 PM	1:25:00 PM	1-19 Hz	400	1308860340
Void	6/23/2011		Void	Braced	X 10% ecc, 980 Force, step 0.2 Hz	Error	Void	Void	Error	Void	Void
Void	6/23/2011		Void	Braced	X 5% ecc, 980 Force, sweep	Error	Void	Void	Error	Void	Void
		20110623220430.GV3									
7a	6/23/2011		Exp3.2.7a.txt	Braced	X 5% ecc, 980 Force, sweep	22:09	3:09:00 PM		0-19 Hz	400	1308867000
7b	6/23/2011		Exp3.2.7b.txt	Braced	X 5% ecc, 980 Force, sweep	22:25	3:25:00 PM		0-19 Hz	400	1308867960
7c	6/23/2011		Exp3.2.7c.txt	Braced	X 5% ecc, 980 Force, sweep	22:33	3:33:00 PM		0-19 Hz	400	1308868440
8	6/23/2011		Exp3.2.8.txt	Braced	X 5% ecc, 980 Force, step 0.2 Hz	22:41	3:41:00 PM		0-19 Hz	420	1308868940
		20110623230430.GV3									
9a	6/23/2011		Exp3.2.9a.txt	Braced	Y 5% ecc, 980 Force, sweep	23:09	4:09:00 PM	4:18:00 PM	0-19 Hz	400	1308870600
9b	6/23/2011		Exp3.2.9b.txt	Braced	Y 5% ecc, 980 Force, sweep	23:19	4:19:00 PM	4:24:00 PM	0-19 Hz	400	1308871050
9c	6/23/2011		Exp3.2.9c.txt	Braced	Y 5% ecc, 980 Force, sweep	23:25	4:25:00 PM		0-19 Hz	400	1308871520
10	6/23/2011		Exp3.2.10.txt	Braced	Y 5% ecc, 980 Force, step 0.2 Hz	23:32	4:32:00 PM		0-19 Hz	450	1308872020
Void	6/23/2011		Void	Braced	Y 50% ecc, 980 Force, sweep	23:54	4:54:00 PM		Error	Void	Void
		20110624000037.GV3									
Void	6/23/2011		Void	Braced	Y 50% ecc, 980 Force, sweep	0:24	5:24:00 PM		Error	Void	Void
11	6/23/2011		Exp3.2.11.txt	Braced	Y 50% ecc, 980 Force, sweep	0:28	5:28:00 PM	5:36:00 PM	0-17.5 Hz	400	1308875340
Void	6/23/2011		Void	Braced	Y 50% ecc, 980 Force, sweep	0:42	5:42:00 PM		Error	Void	Void
Void	6/23/2011		Void	Braced	Y 50% ecc, 980 Force, sweep	0:54	5:54:00 PM		Error	Void	Void
		20110624010037.GV3									
Void	6/23/2011		Void	Braced	X 50% ecc, 980 Force, sweep	1:17	6:17:00 PM		Error	Void	Void
		20110624161014.GV3									
		20110624171014.GV3									
12a	6/24/2011		Exp3.2.12a.txt	Braced	X 50% ecc, 980 Force, sweep	17:12	10:12:00 AM		0-16 Hz	360	1308935590
12b	6/24/2011		Exp3.2.12b.txt	Braced	X 50% ecc, 980 Force, sweep	17:26	10:26:00 AM	10:33:00 AM	0-16.5 Hz	360	1308936430
13	6/24/2011		Exp3.2.13.txt	Braced	X 50% ecc, 980 Force, step 0.2 Hz	17:36	10:36:00 AM		0-16.5 Hz	360	1308937100
14	6/24/2011		Exp3.2.14.txt	Braced	X 100% ecc, 980 Force, sweep	18:00	11:00:00 AM	11:08:00 AM	0-14 Hz	397	1308938483
		20110624181014.GV3									
15	6/24/2011		Exp3.2.15.txt	Braced	Y 100% ecc, 980 Force, sweep	18:53	11:53:00 AM		0-14 Hz	419	1308941641
		20110624191014.GV3									
16	6/24/2011		Exp3.2.16.txt	Braced	Y 100% ecc, 980 Force, step 0.2 Hz	19:22	12:22:00 PM		0-14 Hz	398	1308943442

* Blue highlight shows raw data file, in which snipped files below came from; X, Y and Torsion are direction of shaking; AA: Atom Ant shaker used; MM: Mighty Mouse shaker used;

* step: shaker increments stepped at a defined frequency (given directly after step label) was used; sweep: increment of shaker frequency was provided in across a defined frequency zone and then brought back to zero;

*Bottom: indicates shaker was located on the bottom concrete deck; Top: indicates shaker was located on the top concrete deck; % ecc 980: indicated percent eccentricity of the 980 lb weight used during forcing.

Table 5-4b Mighty Mouse shaker data logs for testing on June 23 and 24, 2011 (Trial 2: Mini-Me in braced condition with forcing from Mighty Mouse shaker).

										Cross-Correlation Data	
Subevent #	Local Date	Recorded Data File Name	Subevent File Name	Description	Loading Description	Notes	Sweep Frequency Range	Snipped Subevent Time Length	Snipped time	First Snipped Sample (Point Location)	First Snipped Sample (Time Location, sec)
		GV_11_06_23_1015									
1a	6/23/2011		Exp3.2.1a.txt	Braced	Y 10% ecc, 980 Force, sweep		0-19 Hz	418	112	1556	0.3112
1b	6/23/2011		Exp3.2.1b.txt	Braced	Y 10% ecc, 980 Force, sweep		0-19 Hz	398	612	1562	0.3124
1c	6/23/2011		Exp3.2.1c.txt	Braced	Y 10% ecc, 980 Force, sweep		0-19 Hz	424	1045	1567	0.3134
		GV_11_06_23_1055									
2a	6/23/2011		Exp3.2.2a.txt	Braced	Y 25% ecc, 980 Force, sweep		0-19 Hz	420	50	2231	0.4462
2b	6/23/2011		Exp3.2.2b.txt	Braced	Y 25% ecc, 980 Force, sweep		0-19 Hz	440	505	2237	0.4474
2c	6/23/2011		Exp3.2.2c.txt	Braced	Y 25% ecc, 980 Force, sweep		0-19 Hz	416	965	2239	0.4478
		GV_11_06_23_1139									
3	6/23/2011		Exp3.2.3.txt	Braced	Y 25% ecc, 980 Force, step 0.2 Hz		1-19 Hz	470	90	789	0.1578
Void	6/23/2011		Void	Braced	X 25% ecc, 980 Force, sweep	Error Encountered	Error	Void	Void		
		GV_11_06_23_1217									
4a	6/23/2011		Exp3.2.4a.txt	Braced	X 25% ecc, 980 Force, sweep	X-Acc Rev. for Corr.	1-19 Hz	427	30	1806	0.3612
4b	6/23/2011		Exp3.2.4b.txt	Braced	X 25% ecc, 980 Force, sweep	X-Acc Rev. for Corr.	1-19 Hz	409	511	1809	0.3618
5	6/23/2011		Exp3.2.5.txt	Braced	X 25% ecc, 980 Force,step 0.2 Hz	X-Acc Rev. for Corr.	1-19 Hz	452	1048	11813	2.3626
		GV_11_06_23_1303									
6a	6/23/2011		Exp3.2.6a.txt	Braced	X 10% ecc, 980 Force, sweep	X-Acc Rev. for Corr.	1-19 Hz	406	54	9529	1.9058
6b	6/23/2011		Exp3.2.6b.txt	Braced	X 10% ecc, 980 Force, sweep	X-Acc Rev. for Corr.	1-19 Hz	385	535	4532	0.9064
6c	6/23/2011		Exp3.2.6c.txt	Braced	X 10% ecc, 980 Force, sweep	X-Acc Rev. for Corr.	1-19 Hz	427	953	14535	2.907
Void	6/23/2011		Void	Braced	X 10% ecc, 980 Force, step 0.2 Hz	Error Encountered	Error	Void	Void		
Void	6/23/2011		Void	Braced	X 5% ecc, 980 Force, sweep	Error Encountered	Error	Void	Void		
		GV_11_06_23_1509									
7a	6/23/2011		Exp3.2.7a.txt	Braced	X 5% ecc, 980 Force, sweep	X-Acc Rev. for Corr.	0-19 Hz	436	32	2095	0.419
		GV_11_06_23_1525									
7b	6/23/2011		Exp3.2.7b.txt	Braced	X 5% ecc, 980 Force, sweep	X-Acc Rev. for Corr.	0-19 Hz	435	25	11421	2.2842
7c	6/23/2011		Exp3.2.7c.txt	Braced	X 5% ecc, 980 Force, sweep	X-Acc Rev. for Corr.	0-19 Hz	420	495	11424	2.2848
8	6/23/2011		Exp3.2.8.txt	Braced	X 5% ecc, 980 Force, step 0.2 Hz	X-Acc Rev. for Corr.	0-19 Hz	459	1004	16424	3.2848
		GV_11_06_23_1609									
9a	6/23/2011		Exp3.2.9a.txt	Braced	Y 5% ecc, 980 Force, sweep		0-19 Hz	419	40	1226	0.2452
9b	6/23/2011		Exp3.2.9b.txt	Braced	Y 5% ecc, 980 Force, sweep		0-19 Hz	430	489	6223	1.2446
9c	6/23/2011		Exp3.2.9c.txt	Braced	Y 5% ecc, 980 Force, sweep		0-19 Hz	415	960	1218	0.2436
10	6/23/2011		Exp3.2.10.txt	Braced	Y 5% ecc, 980 Force, step 0.2 Hz		0-19 Hz	460	1460	1213	0.2426
Void	6/23/2011		Void	Braced	Y 50% ecc, 980 Force, sweep	Error Encountered	Error	Void	Void		
Void	6/23/2011		Void	Braced	Y 50% ecc, 980 Force, sweep	Error Encountered	Error	Void	Void		
		GV_11_06_23_1728									
11	6/23/2011		Exp3.2.11.txt	Braced	Y 50% ecc, 980 Force, sweep		0-17.5 Hz	408	48	1920	0.384
Void	6/23/2011		Void	Braced	Y 50% ecc, 980 Force, sweep	Error Encountered	Error	Void	Void		
Void	6/23/2011		Void	Braced	Y 50% ecc, 980 Force, sweep	Error Encountered	Error	Void	Void		
Void	6/23/2011		Void	Braced	X 50% ecc, 980 Force, sweep	Error Encountered	Error	Void	Void		
		GV_11_06_24_1011									
12a	6/24/2011		Exp3.2.12a.txt	Braced	X 50% ecc, 980 Force, sweep	X-Acc Rev. for Corr.	0-16 Hz	384	72	2406	0.4812
		GV_11_06_24_1026									
12b	6/24/2011		Exp3.2.12b.txt	Braced	X 50% ecc, 980 Force, sweep	X-Acc Rev. for Corr.	0-16.5 Hz	408	62	3456	0.6912
13	6/24/2011		Exp3.2.13.txt	Braced	X 50% ecc, 980 Force, step 0.2 Hz	X-Acc Rev. for Corr.	0-16.5 Hz	375	732	3465	0.693
		GV_11_06_24_1100									
14	6/24/2011		Exp3.2.14.txt	Braced	X 100% ecc, 980 Force, sweep	X-Acc Rev. for Corr.	0-14 Hz	419	35	5980	1.196
		GV_11_06_24_1153									
15	6/24/2011		Exp3.2.15.txt	Braced	Y 100% ecc, 980 Force, sweep		0-14 Hz	411	43	3774	0.7548
		GV_11_06_24_1222									
16	6/24/2011		Exp3.2.16.txt	Braced	Y 100% ecc, 980 Force, step 0.2 Hz		0-14 Hz	389	65	3939	0.7878

* Blue highlight shows raw data file, in which snipped files below came from; X, Y and Torsion are direction of shaking; AA: Atom Ant shaker used; MM: Mighty Mouse shaker used;

* step: shaker increments stepped at a defined frequency (given directly after step label) was used; sweep: increment of shaker frequency was provided in across a defined frequency zone and then brought back to zero;

*Bottom: indicates shaker was located on the bottom concrete deck; Top: indicates shaker was located on the top concrete deck; % ecc 980: indicated percent eccentricity of the 980 lb weight used during forcing.

Table5-5 GVDA forced vibration testing logs for testing on August 1 and 2, 2011 (Trial 3: Mini-Me in unbraced condition with forcing from Atom Ant shaker).

							Local Time Recorded in Field				
Subevent #	**Local Date**	**Recorded Data File Name**	**Subevent File Name**	**Description**	**Loading Description**	**GMT**	**First Sample**	**Last Sample**	**Sweep Frequency Range**	**Snipped Subevent Time Length**	**Snipped Unix time**
		20110801213133.GV4									
1	8/1/2011		Exp3.3.1a.txt	Not Braced	X AA sweep top	22:55	2:55:30 PM		4-54 Hz	50 s	1312235714
2	8/1/2011		Exp3.3.1b.txt	Not Braced, Med Amplitude	X AA sweep top	22:57	2:57:00 PM		4-54 Hz	50 s	1312235805
3	8/1/2011		Exp3.3.1c.txt	Not Braced,	X AA sweep top	22:58	2:58:25 PM		4-54 Hz	50 s	1312235890
4	8/1/2011		Exp3.3.1d.txt	Not Braced,	X AA sweep top	23:00	3:00:00 PM		4-54 Hz	200 s	1312235985
5	8/1/2011		Exp3.3.1e.txt	Not Braced, Med Amp	X AA sweep top	23:05	3:05:30 PM		4-54 Hz	200 s	1312236318
6	8/1/2011		Exp3.3.2.txt	Not Braced	X AA step 0.5 Hz top, may have slipped @ 25Hz	23:10	3:10:15 PM		4-35 Hz	760 s	1312236580
7	8/1/2011		Exp3.3.2f.txt	Not Braced	X AA sweep top	23:27	3:27:45 PM		4-54 Hz	50 s	1312237652
		20110801223133.GV4									
8	8/1/2011		Exp3.3.3a.txt	Not Braced	Y AA torsion 47" top	23:43	3:43:25 PM		4-54 Hz	50 s	1312238592
9	8/1/2011		Exp3.3.3b.txt	Not Braced	Y AA torsion 47" top	23:44	3:44:40 PM		4-54 Hz	50 s	1312238667
10	8/1/2011		Exp3.3.3c.txt	Not Braced	Y AA torsion 47" top	23:46	3:46:20 PM		4-54 Hz	200 s	1312238767
11	8/1/2011		Exp3.3.3d.txt	Not Braced	Y AA torsion 47" top	23:50	3:50:13 PM		4-54 Hz	200 s	1312239001
12	8/1/2011		Exp3.3.4.txt	Not Braced	Y AA torsion step 1.0 Hz top	23:55	3:55:00 PM	4:06:20 PM	4-44 Hz	700 s	1312239278
13	8/1/2011		Exp3.3.5a.txt	Not Braced	Y AA, Sweep,Shaker Acc Direction Switch	0:22	4:22:15 PM		4-54 Hz	50 s	1312240925
14	8/1/2011		Exp3.3.5b.txt	Not Braced	Y AA, Sweep,Shaker Acc Direction Switch	0:24	4:24:00 PM		4-54 Hz	50 s	1312241028
15	8/1/2011		Exp3.3.5c.txt	Not Braced	Y AA, Sweep,Shaker Acc Direction Switch	0:29	4:29:45 PM		4-54 Hz	200 s	1312241373
		20110801233133.GV4									
16	8/1/2011		Exp3.3.5d.txt	Not Braced	Y AA, Sweep,Shaker Acc Direction Switch	0:33	4:33:25 PM		4-54 Hz	200 s	1312241593
17	8/1/2011		Exp3.3.6.txt	Not Braced	Y AA, 1 Hz Steps,Shaker Acc Direction Switch	0:38	4:38:00 PM	4:48:00 PM	4-44Hz	600 s	1312241868
		20110802000036.GV4									
18	8/1/2011		Exp3.3.7a.txt	Not Braced	X AA sweep bottom	1:09	5:09:50 PM		4-54 Hz	50 s	1312157380
19	8/1/2011		Exp3.3.7b.txt	Not Braced	X AA sweep bottom	1:11	5:11:15 PM		4-54 Hz	50 s	1312243863
20	8/1/2011		Exp3.3.7c.txt	Not Braced	X AA sweep bottom	1:12	5:12:25 PM		4-54 Hz	200 s	1312243933
21	8/1/2011		Exp3.3.7d.txt	Not Braced	X AA sweep bottom	1:16	5:16:10 PM		4-54 Hz	200 s	1312244158
22	8/1/2011		Exp3.3.8.txt	Not Braced	X AA step 1 Hz bottom	1:20	5:20:30 PM	5:27:35 PM	4-44 Hz	450 s	1312244418
23	8/1/2011		Exp3.3.9a.txt	Not Braced	Y AA sweep bottom	1:36	5:36:50 PM		4-54 Hz	50 s	1312245402
24	8/1/2011		Exp3.3.9b.txt	Not Braced	Y AA sweep bottom	1:38	5:38:04 PM		4-54 Hz	50 s	1312245470
25	8/1/2011		Exp3.3.9c.txt	Not Braced	Y AA sweep bottom	1:39	5:39:30 PM		4-54 Hz	200 s	1312245558
26	8/1/2011		Exp3.3.9d.txt	Not Braced	Y AA sweep bottom	1:43	5:43:25 PM		4-54 Hz	200 s	1312245792
27	8/1/2011		Exp3.3.10.txt	Not Braced	Y AA step 1 Hz bottom	1:47	5:47:20 PM	5:54:25 PM	4-44 Hz	450 s	1312246028
		20110802150036.GV4									
28	8/2/2011		Exp3.3.11a.txt	Not Braced	Y AA torsion 47" bottom	16:47	8:47:07 AM		4-54 Hz	50 s	1312300012
29	8/2/2011		Exp3.3.11b.txt	Not Braced	Y AA torsion 47" bottom	16:48	8:48:08 AM		4-54 Hz	50 s	1312300070
		20110802161037.GV4									
30	8/2/2011		Exp3.3.11c.txt	Not Braced	Y AA torsion 47" bottom	17:12	9:12:10 AM		4-54 Hz	200 s	1312300208
31	8/2/2011		Exp3.3.11d.txt	Not Braced	Y AA torsion 47" bottom	17:16	9:16:00 AM		4-54 Hz	200 s	1312300426
32	8/2/2011		Exp3.3.12.txt	Not Braced	Y AA torsion step 1.0 Hz bottom	17:20	9:20:00 AM	9:26:50 AM	4-44 Hz	420 s	1312300673

* Blue highlight shows raw data file, in which snipped files below came from; X, Y and Torsion are direction of shaking; AA: Atom Ant shaker used; MM: Mighty Mouse shaker used;

* step: shaker increments stepped at a defined frequency (given directly after step label) was used; sweep: increment of shaker frequency was provided in across a defined frequency zone and then brought back to zero;

*Bottom: indicates shaker was located on the bottom concrete deck; Top: indicates shaker was located on the top concrete deck; % ecc 980: indicated percent eccentricity of the 980 lb weight used during forcing.

Table 5-6a GVDA forced vibration testing logs for testing on August 2, 2011 (Trial 4: Mini-Me in unbraced condition with forcing from Mighty Mouse shaker).

							Local Time Recorded in Field				
Subevent #	Local Date	Recorded Data File Name	Subevent File Name	Description	Loading Description	GMT	First Sample	Last Sample	Sweep Frequency Range	Snipped Subevent Time Length	Snipped Unix time
		20110802161037.GV4									
1	8/2/2011		Exp3.4.1a.txt	Not Braced	Y 5% ecc, 980 Force, sweep	16:46	9:46:00 AM	9:54:00 AM	0-19 Hz	399	1312303611
2	8/2/2011		Exp3.4.1b.txt	Not Braced	Y 5% ecc, 980 Force, sweep	16:54	9:54:00 AM	10:02:00 AM	0-19 Hz	398	1312304072
3	8/2/2011		Exp3.4.2.txt	Not Braced	Y 5% ecc, 980 Force, step 0.2 Hz	17:05	10:05:00 AM	10:12:00 AM	0-19 Hz	400	1312304750
		20110802171037.GV4									
4	8/2/2011		Exp3.4.3a.txt	Not Braced	Y 10% ecc, 980 Force, sweep	17:23	10:23:00 AM	10:31:00 AM	0-19 Hz	390	1312305840
5	8/2/2011		Exp3.4.3b.txt	Not Braced	Y 10% ecc, 980 Force, sweep	17:31	10:31:00 AM	10:39:00 AM	0-19 Hz	400	1312306310
6	8/2/2011		Exp3.4.4.txt	Not Braced	Y 10% ecc, 980 Force, step 0.2 Hz	17:39	10:39:00 AM	10:47:00 AM	0-19 Hz	420	1312306850
7	8/2/2011		Exp3.4.5a.txt	Not Braced	Y 25% ecc, 980 Force, sweep	17:58	10:58:00 AM	11:06:00 AM	0-19 Hz	400	1312307920
8	8/2/2011		Exp3.4.5b.txt	Not Braced	Y 25% ecc, 980 Force, sweep	18:06	11:06:00 AM	11:14:00 AM	0-19 Hz	399	1312308371
		20110802181037.GV4									
9	8/2/2011		Exp3.4.6.txt	Not Braced	Y 25% ecc, 980 Force, step 0.2 Hz	18:14	11:14:00 AM	11:23:00 AM	0-19 Hz	417	1312308938
10	8/2/2011		Exp3.4.7a.txt	Not Braced	X 5% ecc, 980 Force, sweep	18:39	11:39:00 AM	11:48:00 AM	0-19 Hz	400	1312310425
11	8/2/2011		Exp3.4.7b.txt	Not Braced	X 5% ecc, 980 Force, sweep	18:48	11:48:00 AM	11:56:00 AM	0-19 Hz	400	1312310905
12	8/2/2011		Exp3.4.8.txt	Not Braced	X 5% ecc, 980 Force, step 0.2 Hz	18:58	11:58:00 AM	12:07:00 PM	0-19 Hz	419	1312311611
		20110802191037.GV4									
13	8/2/2011		Exp3.4.9a.txt	Not Braced	X 10% ecc, 980 Force, sweep	19:19	12:19:00 PM	12:27:00 PM	0-19 Hz	399	1312312781
14	8/2/2011		Exp3.4.9b.txt	Not Braced	X 10% ecc, 980 Force, sweep	19:27	12:27:00 PM	12:36:00 PM	0-19 Hz	400	1312313250
15	8/2/2011		Exp3.4.10.txt	Not Braced	X 10% ecc, 980 Force, step 0.2 Hz	19:41	12:41:00 PM	12:49:00 PM	0-19 Hz	440	1312314160
16	8/2/2011		Exp3.4.11a.txt	Not Braced	X 25% ecc, 980 Force, sweep	19:58	12:58:00 PM	1:06:00 PM	0-19 Hz	400	1312315140
17	8/2/2011		Exp3.4.11b.txt	Not Braced	X 25% ecc, 980 Force, sweep	20:06	1:06:00 PM	1:13:00 PM	0-19 Hz	400	1312315610
		20110802201037.GV4									
18	8/2/2011		Exp3.4.12.txt	Not Braced	X 25% ecc, 980 Force, step 0.2 Hz	20:14	1:14:00 PM	1:23:00 PM	0-19 Hz	440	1312316125
19	8/2/2011		Exp3.4.13a.txt	Not Braced	X 50% ecc, 980 Force, sweep	20:38	1:38:00 PM	1:46:00 PM	0-14 Hz	400	1312317520
20	8/2/2011		Exp3.4.13b.txt	Not Braced	X 50% ecc, 980 Force, sweep	20:46	1:46:00 PM	1:55:00 PM	0-14 Hz	396	1312318004
21	8/2/2011		Exp3.4.14.txt	Not Braced	X 50% ecc, 980 Force, step 0.2 Hz	20:54	1:54:00 PM	2:02:00 PM	0-14 Hz	417	1312318493
		20110802211037.GV4									
22	8/2/2011		Exp3.4.15a.txt	Not Braced, step	X 100 % ecc, east weight slipped to 95% ecc	21:19	2:19:00 PM	2:27:00 PM	0-14 Hz	391	1312320009
23	8/2/2011		Exp3.4.15b.txt	Not Braced, step	X 100 % ecc, east weight slipped to 95% ecc	21:45	2:45:00 PM	2:53:00 PM	0-14 Hz	393	1312321547
24	8/2/2011		Exp3.4.16.txt	Not Braced, sweep 0.2 Hz	X 100 % ecc, east weight slipped to 95% ecc	21:53	2:53:00 PM	3:01:00 PM	0-14 Hz	410	1312322040
		20110802221037.GV4									
25	8/2/2011		Exp3.4.17a.txt	Not Braced, step	Y-Dir, 50 % ecc, directional sensor off 60 deg	22:22	3:22:00 PM	3:29:00 PM	0-14 Hz	399	1312323751
26	8/2/2011		Exp3.4.17b.txt	Not Braced, step	Y-Dir, 50 % ecc, directional sensor off 60 deg	22:29	3:29:00 PM	3:36:00 PM	0-14 Hz	399	1312324201
27	8/2/2011		Exp3.4.18.txt	Not Braced, sweep 0.2 Hz	Y-Dir, 50 % ecc, directional sensor off 60 deg	22:37	3:37:00 PM	3:45:00 PM	0-14 Hz	419	1312324681
28	8/2/2011		Exp3.4.19a.txt	Not Braced	Y 100% ecc, 980 Force, sweep	23:00	4:00:00 PM	4:07:00 PM	0-12 Hz	399	1312326031
		20110802231037.GV4									
29	8/2/2011		Exp3.4.19b.txt	Not Braced	Y 100% ecc, 980 Force, sweep	23:07	4:07:00 PM	4:14:00 PM	0-12 Hz	400	1312326480
30	8/2/2011		Exp3.4.20.txt	Not Braced	Y 100% ecc, 980 Force, step 0.2 Hz	23:16	4:16:00 PM		0-12 Hz	419	1312326961

* Blue highlight shows raw data file, in which snipped files below came from; X, Y and Torsion are direction of shaking; AA: Atom Ant shaker used; MM: Mighty Mouse shaker used;

* step: shaker increments stepped at a defined frequency (given directly after step label) was used; sweep: increment of shaker frequency was provided in across a defined frequency zone and then brought back to zero;

*Bottom: indicates shaker was located on the bottom concrete deck; Top: indicates shaker was located on the top concrete deck; % ecc 980: indicated percent eccentricity of the 980 lb weight used during forcing.

Table 5-6b Mighty Mouse shaker data logs for testing on August 2, 2011 (Trial 4: Mini-Me in unbraced condition with forcing from Mighty Mouse shaker).

										Cross-Correlation Data	
Subevent #	Local Date	Recorded Data File Name	Subevent File Name	Description	Loading Description	Notes	Sweep Frequency Range	Snipped Subevent Time Length	Snipped Unix time	First Snipped Sample (Point Location)	First Snipped Sample (Time Location, sec)
		GV_11_08_02_0945_1									
1	8/2/2011		Exp3.4.1a.txt	Not Braced	Y 5% ecc, 980 Force, sweep	Y-Acc Rev. for Corr.	0-19 Hz	411	49	4485	0.897
2	8/2/2011		Exp3.4.1b.txt	Not Braced	Y 5% ecc, 980 Force, sweep	Y-Acc Rev. for Corr.	0-19 Hz	405	510	4486	0.8972
		GV_11_08_02_1003_1									
3	8/2/2011		Exp3.4.2.txt	Not Braced	Y 5% ecc, 980 Force, step 0.2 Hz	Y-Acc Rev. for Corr.	0-19 Hz	410	138	2443	0.4886
		GV_11_08_02_1023_1									
4	8/2/2011		Exp3.4.3a.txt	Not Braced	Y 10% ecc, 980 Force, sweep	Y-Acc Rev. for Corr.	0-19 Hz	428	32	15813	3.1626
5	8/2/2011		Exp3.4.3b.txt	Not Braced	Y 10% ecc, 980 Force, sweep	Y-Acc Rev. for Corr.	0-19 Hz	416	504	5814	1.1628
6	8/2/2011		Exp3.4.4.txt	Not Braced	Y 10% ecc, 980 Force, step 0.2 Hz	Y-Acc Rev. for Corr.	0-19 Hz	445	1044	5815	1.163
		GV_11_08_02_1057_1									
7	8/2/2011		Exp3.4.5a.txt	Not Braced	Y 25% ecc, 980 Force, sweep	Y-Acc Rev. for Corr.	0-19 Hz	416	64	8560	1.712
8	8/2/2011		Exp3.4.5b.txt	Not Braced	Y 25% ecc, 980 Force, sweep	Y-Acc Rev. for Corr.	0-19 Hz	434	516	3561	0.7122
9	8/2/2011		Exp3.4.6.txt	Not Braced	Y 25% ecc, 980 Force, step 0.2 Hz	Y-Acc Rev. for Corr.	0-19 Hz	439	1083	3561	0.7122
		GV_11_08_02_1139_1									
10	8/2/2011		Exp3.4.7a.txt	Not Braced	X 5% ecc, 980 Force, sweep		0-19 Hz	426	34	3808	0.7616
11	8/2/2011		Exp3.4.7b.txt	Not Braced	X 5% ecc, 980 Force, sweep		0-19 Hz	421	513	8808	1.7616
		GV_11_08_02_1158_1									
12	8/2/2011		Exp3.4.8.txt	Not Braced	X 5% ecc, 980 Force, step 0.2 Hz		0-19 Hz	414	116	2466	0.4932
		GV_11_08_02_1219_1									
13	8/2/2011		Exp3.4.9a.txt	Not Braced	X 10% ecc, 980 Force, sweep		0-19 Hz	423	37	4762	0.9524
14	8/2/2011		Exp3.4.9b.txt	Not Braced	X 10% ecc, 980 Force, sweep		0-19 Hz	424	506	4762	0.9524
		GV_11_08_02_1240_1									
15	8/2/2011		Exp3.4.10.txt	Not Braced	X 10% ecc, 980 Force, step 0.2 Hz		0-19 Hz	455	98	1773	0.3546
16	8/2/2011		Exp3.4.11a.txt	Not Braced	X 25% ecc, 980 Force, sweep		0-19 Hz	Missing	Missing		0
17	8/2/2011		Exp3.4.11b.txt	Not Braced	X 25% ecc, 980 Force, sweep		0-19 Hz	Missing	Missing		0
18	8/2/2011		Exp3.4.12.txt	Not Braced	X 25% ecc, 980 Force, step 0.2 Hz		0-19 Hz	Missing	Missing		0
		GV_11_08_02_1337_1									
19	8/2/2011		Exp3.4.13a.txt	Not Braced	X 50% ecc, 980 Force, sweep		0-14 Hz	421	39	4802	0.9604
20	8/2/2011		Exp3.4.13b.txt	Not Braced	X 50% ecc, 980 Force, sweep		0-14 Hz	417	523	4802	0.9604
21	8/2/2011		Exp3.4.14.txt	Not Braced	X 50% ecc, 980 Force, step 0.2 Hz		0-14 Hz	412	1012	4802	0.9604
		GV_11_08_02_1418_1									
22	8/2/2011		Exp3.4.15a.txt	Not Braced, step	X 100 % ecc, east weight slipped to 95% ecc		0-14 Hz	441	68	6602	1.3204
		GV_11_08_02_1444_1									
23	8/2/2011		Exp3.4.15b.txt	Not Braced, step	X 100 % ecc, east weight slipped to 95% ecc		0-14 Hz	414	46	8859	1.7718
24	8/2/2011		Exp3.4.16.txt	Not Braced, sweep 0.2 Hz	X 100 % ecc, east weight slipped to 95% ecc		0-14 Hz	360	540	3858	0.7716
		GV_11_08_02_1521_1									
25	8/2/2011		Exp3.4.17a.txt	Not Braced, step	Y-Dir, 50 % ecc, directional sensor off 60 deg	Y-Acc Rev. for Corr.	0-14 Hz	427	46	14	0.0028
26	8/2/2011		Exp3.4.17b.txt	Not Braced, step	Y-Dir, 50 % ecc, directional sensor off 60 deg	Y-Acc Rev. for Corr.	0-14 Hz	423	497	11	0.0022
27	8/2/2011		Exp3.4.18.txt	Not Braced, sweep 0.2 Hz	Y-Dir, 50 % ecc, directional sensor off 60 deg	Y-Acc Rev. for Corr.	0-14 Hz	418	977	6	0.0012
		GV_11_08_02_1559_1									
28	8/2/2011		Exp3.4.19a.txt	Not Braced	Y 100% ecc, 980 Force, sweep	Y-Acc Rev. for Corr.	0-12 Hz	423	42	2981	0.5962
29	8/2/2011		Exp3.4.19b.txt	Not Braced	Y 100% ecc, 980 Force, sweep	Y-Acc Rev. for Corr.	0-12 Hz	469	491	2976	0.5952
30	8/2/2011		Exp3.4.20.txt	Not Braced	Y 100% ecc, 980 Force, step 0.2 Hz	Y-Acc Rev. for Corr.	0-12 Hz	408	972	2972	0.5944

* Blue highlight shows raw data file, in which snipped files below came from; X, Y and Torsion are direction of shaking; AA: Atom Ant shaker used; MM: Mighty Mouse shaker used;

* step: shaker increments stepped at a defined frequency (given directly after step label) was used; sweep: increment of shaker frequency was provided in across a defined frequency zone and then brought back to zero;

*Bottom: indicates shaker was located on the bottom concrete deck; Top: indicates shaker was located on the top concrete deck; % ecc 980: indicated percent eccentricity of the 980 lb weight used during forcing.

Two data acquisition systems were used for Trial 2 (braced structure, Mighty Mouse shaker) and Trial 4 (unbraced structure, Mighty Mouse shaker). The structural response test logs, corresponding to the data acquisition system attributes described in Table 5-1, are shown in Tables 5-4a and 5-6a. The Mighty Mouse shaker test logs, corresponding to the data acquisition system described in Table 5-3, are described in Tables 5-4b and 5-6b.

The last few columns of Tables 5-3 through 5-6 represent the location where the subevents were cropped from the unprocessed data files. The last few columns of Tables 5-4b and 5-6b present additional information regarding cross-correlation analyses performed to synchronize the structural response data files with the Mighty Mouse data files. Details of the cross-correlation analysis are presented in Section 5.3.3.

5.3.2 Data Processing

Several types of data files were prepared as part of this experiment. The workflow and development of the data files differ, dependent on the type of shaker used for forced vibration testing. The different workflow schemes used for processing the data in this study are shown in Figures 5-8 and 5-9. The solid rectangular boxes in Figures 5-8 and 5-9 represent the different types of data files (with file name type indicated in brackets), while the dashed rectangular boxes represent the work required to create the next type of data file in the processing procedure.

5.3.2.1 Structural Response Data Processing

Table 5-1 shows the attributes of the structural response data acquisition system. The attributes include the data acquisition (DA) channel, sensor type, sensor location, and

sensor orientation. Table 5-1 was used for the forced vibration testing with the small shaker (Atom Ant) and large shaker (Mighty Mouse). Figure 5-8 shows the processing of the structural response data from unprocessed data to corrected data. The unprocessed data files contain multiple events as indicated by the non-highlighted rows in Tables 5-3 and 5-5. The unprocessed structural response data collected in the field was divided into subevents based on vibration modes and duration of shaking. When the data was divided into subevents the data was also converted to engineering units and was documented as converted data files. Then the converted data files were baseline corrected. The baseline correction consisted of determining the mean responses and removing them from the records. The baseline corrected data has been saved as the corrected data to be used for analysis. Shown graphically in Figure 5-8 is an example of the data processing using channel 15 of the structural response data. The data files shown in Figure 5-8 from top to bottom are the unprocessed data file: "20110802221037.txt"; the converted data file: "Exp.3.4.19a_GVDA_08.02.2011_Unbraced_1312326030_MM_Y_400_

Sweep_100ecc_TopDeck.txt"; and the corrected data file: "Exp.3.4.19a_GVDA_08.02.2011_

Unbraced_1312326030_MM_Y_400_Sweep_100ecc_TopDeck_MeanCorrected.txt."

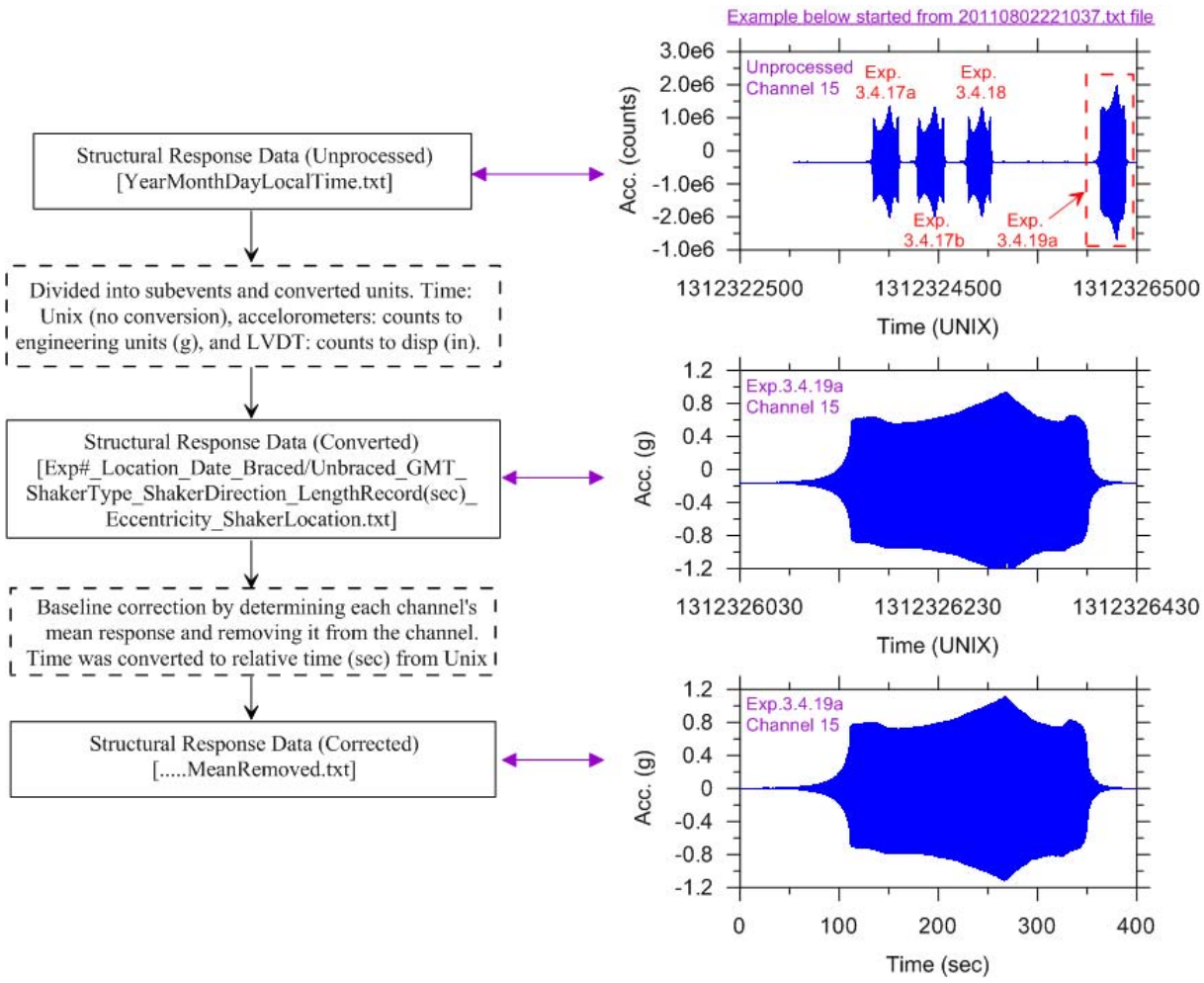

Figure 5-8 **Flowchart describing the workflow and associated data files for the structural response data files. The graphical example is for experiment 3.4.19a as described in Table 5-6. The solid boxes in the flowchart describe the data file types with file name descriptions in brackets, while the dashed boxes describe the effort taken to achieve the underlying processed data file.**

5.3.2.2 Mighty Mouse Shaker Data Processing

Table 5-2 shows the attributes of the Mighty Mouse shaker data acquisition system and Table 5-1 shows the attributes of the structural response data acquisition. Attributes shown in Tables 5-1 and 5-2 are the data acquisition (DA) channel, sensor type, sensor location, and sensor orientation. Figure 5-9 shows at the left branch of the workflow how

the Mighty Mouse shaker unprocessed data was processed directly to corrected data file types. The unprocessed data files contain multiple events as indicated by the non-highlighted rows in Tables 5-4b and 5-6b. The unprocessed Mighty Mouse data files were divided into subevents based on different shaker force intensities and modes of vibration. During segregation of these subevents the data was converted from field counts to engineering units along with a baseline correction (removal of mean response). This data has been uploaded to the NEEShub as Mighty Mouse corrected data. However, the two corrected data files needed to be combined at a common sampling frequency for analysis. Therefore, the high frequency Mighty Mouse shaker data was decimated and then synchronized with the low frequency structural response data. Synchronization was performed using cross-correlation, as described in Section 5.3.3. The final corrected data shown at the bottom of Figure 5-9 contains additional data including calculated shaker forces, frequency, angle of rotating mass and response of parallel accelerometer used for data acquisition correlation, which is described in Section 5.3.6. This final corrected data that combines the two acquisition systems together is referred to as "Synchronized Structural Response and Mighty Mouse Shaker Data."

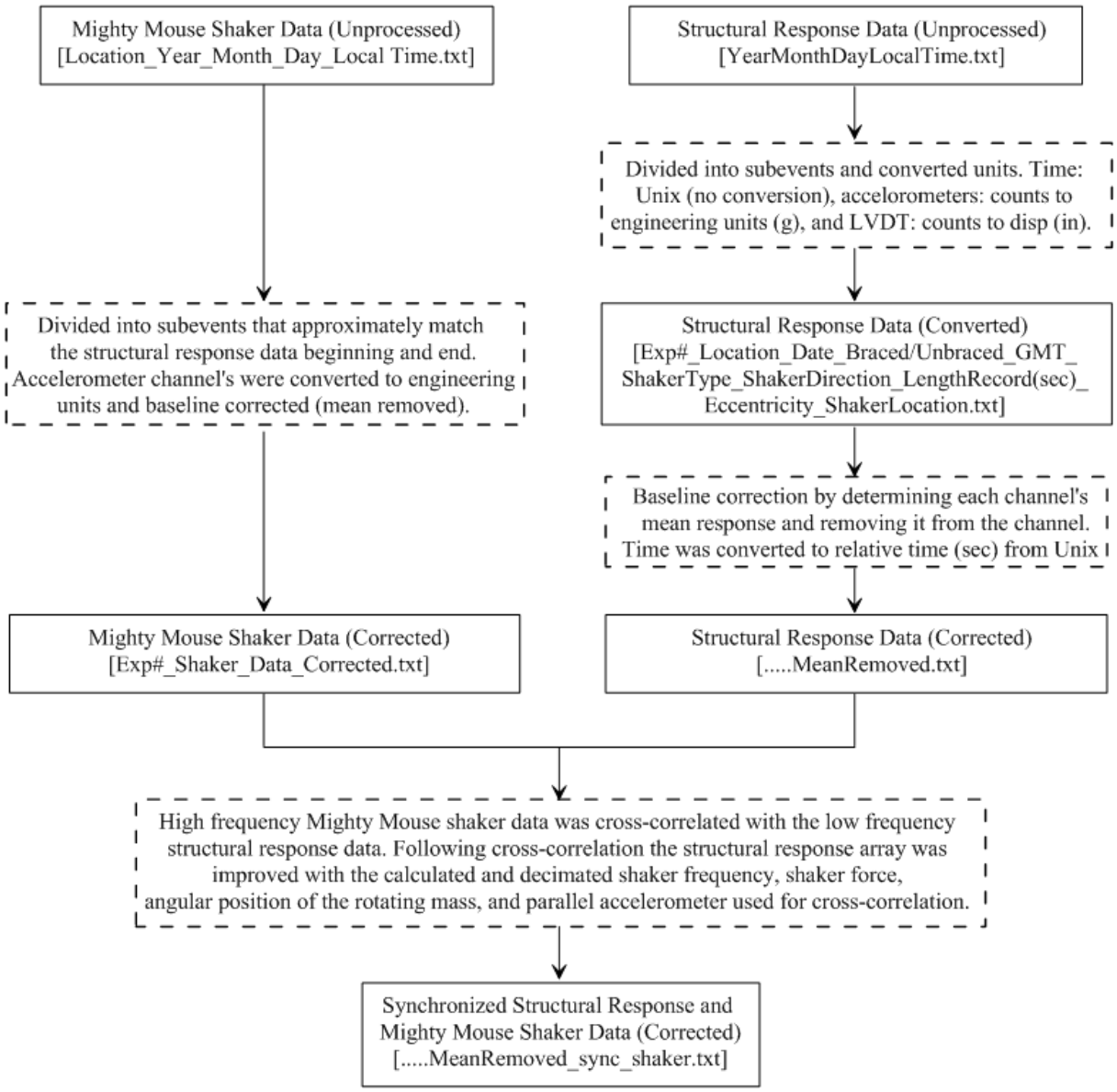

Figure 5-9 **Flowchart describing the workflow and associated data files for the Mighty Mouse data files and corresponding structural response data files (described in Figure 8). The solid boxes in the flowchart describe the data file types with file name descriptions in brackets, while the dashed boxes describe the effort taken to achieve the underlying processed data file.**

5.3.3 Cross-Correlation of the Data Acquisition Systems

A cross-correlation analysis was performed to synchronize the two different data acquisition systems used for testing the large Mighty Mouse shaker. As described in Section 5.2.5, the Mighty Mouse shaker data was collected at a faster sampling rate compared to the structural responses data (5000 Hz vs. 200 Hz). The Mighty Mouse shaker DA system collected data using a relative time signature from start of recording and required synchronization to the structural response data acquisition, which used a GPS time signature. This synchronization was achieved by comparing adjacent parallel accelerometers recording to the respective DA systems in the direction of shaking. The accelerometers used for correlation were located on the roof at the southwest corner of Mini-Me, as shown in Figure 5-7.

The cross-correlation analysis was performed using decimated corrected Mighty Mouse shaker data and unaltered corrected structural response data as described in Section 5.3.3. The cross-correlation analysis was performed by comparing an approximate 20 sec structural response window at the middle of the response. This window of comparison was selected to avoid artificial noise that exists near the ends of the windows of time in which measured responses occur. The responses typically have an approximate 50 or 400 sec duration. However, the 20 sec window was compared to a more robust window encompassing most of the record and both sets were found to produce equivalent record-to-record lags. Therefore the 20 sec window was used to reduce computational effort. Two examples of the cross-correlation analysis are provided in Figures 5-10 and 5-11.

Figure 5-10 shows the cross-correlation analysis for experiment 3.4.1a (unbraced condition with 5% eccentricity force in the *y*-direction). Figure 5-10a and 5-10b shows the corrected data for the adjacent parallel accelerometers used for the cross-correlation analysis. Since loading for this test was in the *y*-direction, structural response data channel 15 and Mighty Mouse shaker data channel 2 (see Figure 5-7) were correlated. Figure 5-10c shows the graphical result of the cross-correlation, where the peak represents the time-lag (Δt) between accelerometers, found to be 0.897 sec. Figure 5-10c shows the correlated accelerometer responses superimposed in a short time window from 342-345 sec. This short time window is used to present how the Mighty Mouse shaker data files can be adjusted by Δt to synchronize with the structural response data.

Figure 5-11 shows the synchronized results for experiment 3.4.1a using the same accelerometers. Figure 5-11a shows an unaltered structural response from Figure 5-10a, while Figure 5-11b shows the corrected Mighty Mouse data. The Mighty Mouse data was shifted by Δt and decimated to match the sampling frequency of the structural response data. Figure 5-11c shows the final match of the data sets in a short time window of 342-345 sec. The Mighty Mouse shaker acceleration time series contains visible levels of noise as shown in Figure 5-10b. However, following a time shift of Δt and decimation to the structural response sampling frequency, synchronization was achieved and the noise was reduced as a result of the low-pass filter association with the decimation routine (see Figure 5-11c).

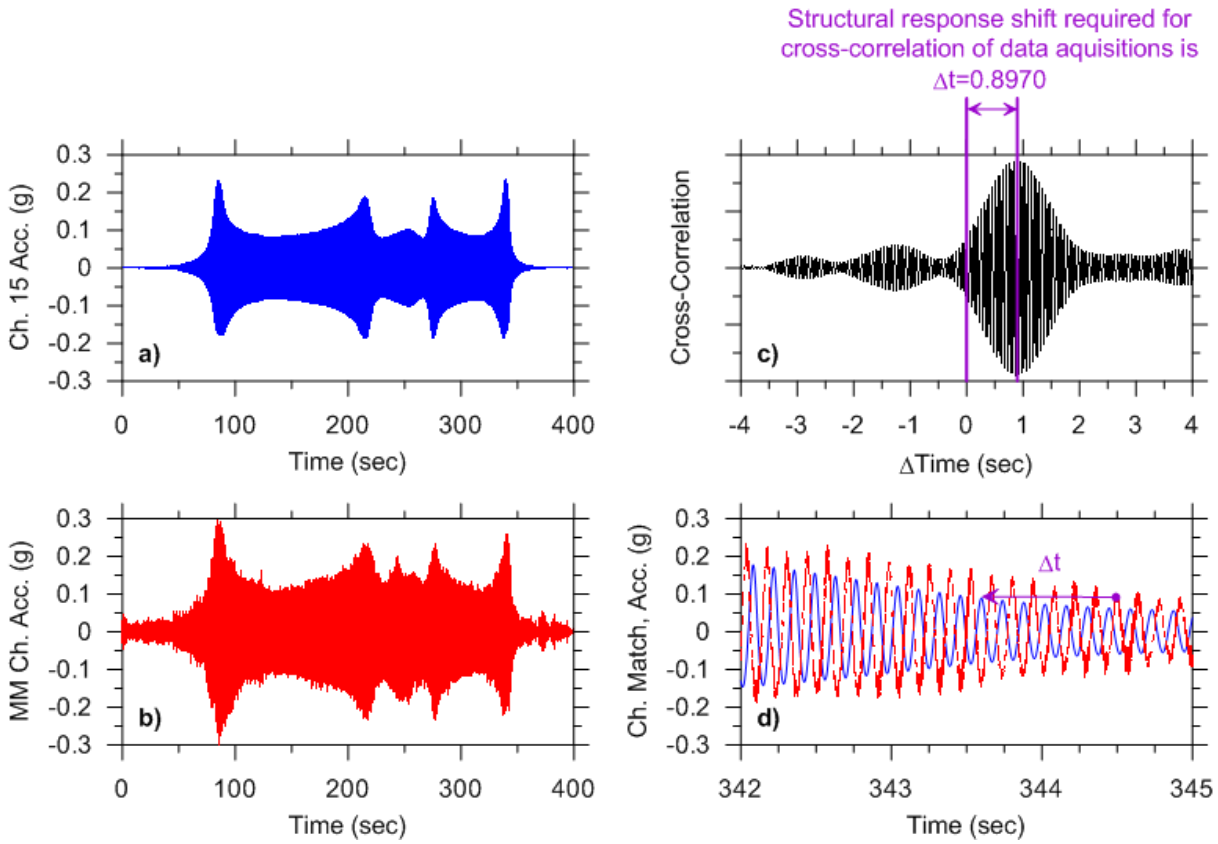

Figure 5-10 **Experiment 3.4.1a cross-correlations analysis components: (a) structural response data channel 15 accelerometer, (b) parallel Mighty Mouse shaker data channel 2, (c) cross-correlation graphical result, and (d) short time window showing required time-shift for correlation.**

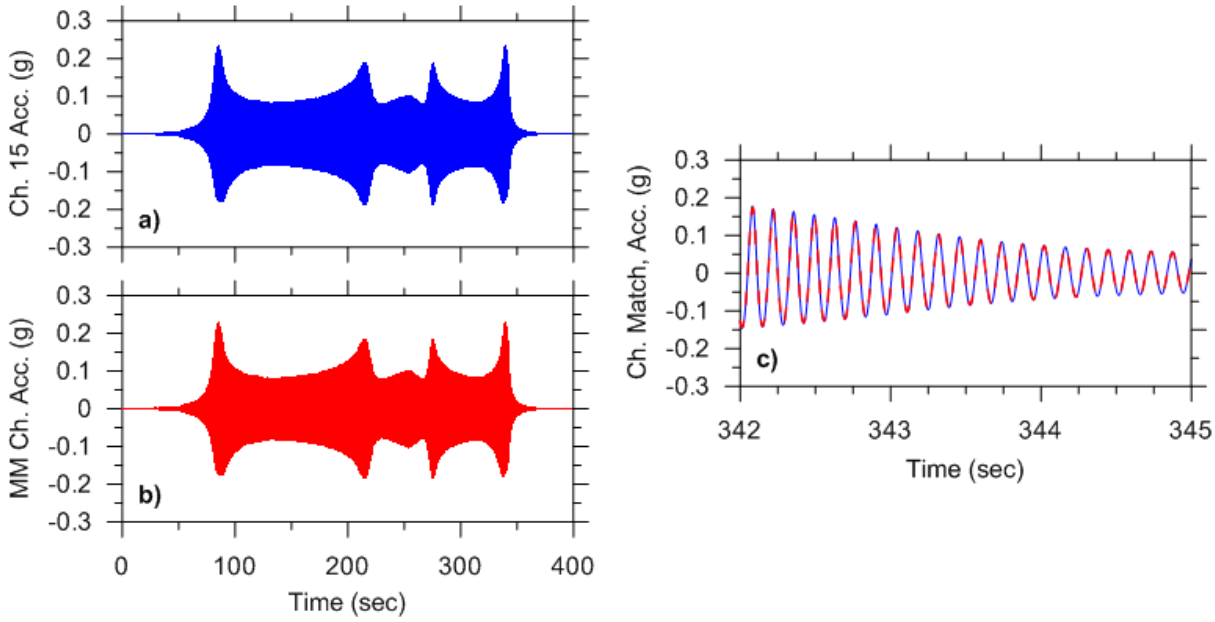

Figure 5-11 **Experiment 3.4.1a results following application of time-lag: (a) structural response data channel 15 accelerometer, (b) parallel Mighty Mouse shaker data channel 2 adjusted by Δt=0.8907, and (c) short time window showing correlation of adjusted Mighty Mouse shaker data to structural response data.**

Figure 5-12 shows the cross-correlation analysis for experiment 3.4.19a (unbraced condition with 100% eccentricity force in the *y*-direction). Figure 5-12a and 5-12b shows the corrected data for the adjacent parallel accelerometers used for the cross-correlation analysis. Since loading for this test was in the *y*-direction, structural response data channel 15 and Mighty Mouse shaker data channel 2 (see Figure 5-7) were correlated. Figure 5-12c shows the graphical result of the cross-correlation, where the peak represents the time-lag (Δt) between accelerometers, found to be 0.5962 sec. Figure 5-12c shows the synchronized accelerograms superimposed for a short time window from 110-113 sec.

Figure 5-13 shows the synchronized results for experiment 3.4.19a using the same accelerometers. Figure 5-13a shows an unaltered structural response from Figure 5-12a, while Figure 5-13b shows the corrected Mighty Mouse data. The Mighty Mouse data was shifted by Δt and decimated to match the sampling frequency of the structural response data. Figure 5-13c shows the final match of the data sets in a short time window of 110-113 sec.

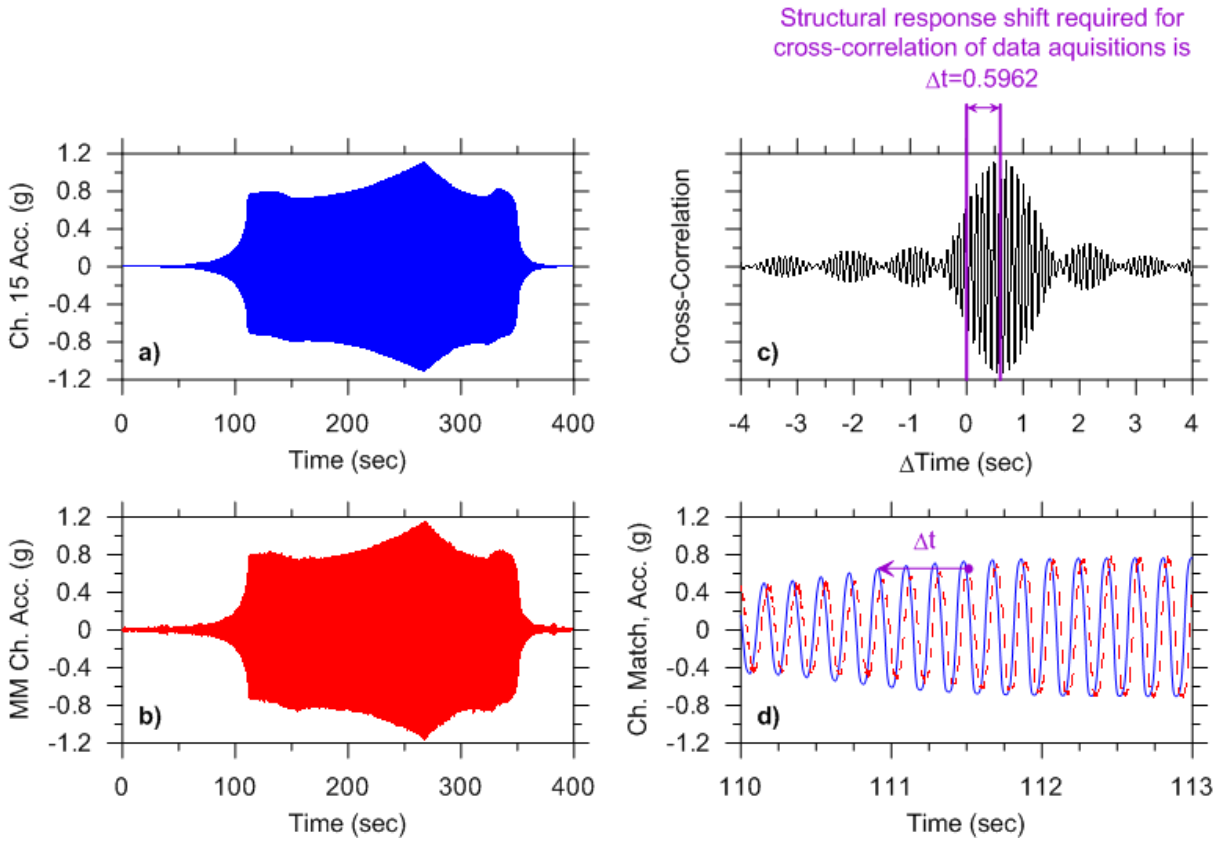

Figure 5-12 **Experiment 3.4.19a cross-correlations analysis components: (a) structural response data channel 15 accelerometer, (b) parallel Mighty Mouse shaker data channel 2, (c) cross-correlation graphical result, and (d) short time window showing required time-shift for correlation.**

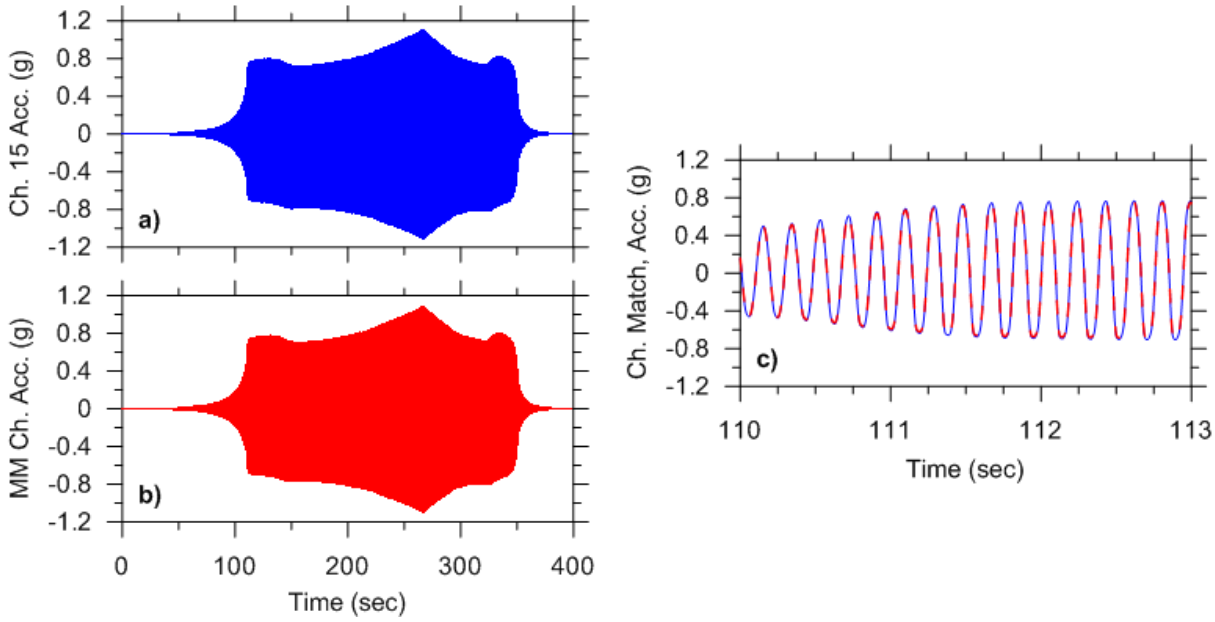

Figure 5-13 **Experiment 3.4.19a results following application of time-lag: (a) structural response data channel 15 accelerometer, (b) parallel Mighty Mouse shaker data channel 2 adjusted by Δt=0.8907, and (c) short time window showing correlation of adjusted Mighty Mouse shaker data to structural response data.**

5.3.4 Unprocessed Data Files

The unprocessed data files contain raw data as obtained from in the field from the two DA systems described in Section 5.2.5. At NEEShub, the unprocessed data has been stored in two folders: "Structural Response Data" and "Mighty Mouse Shaker Data." Applicable units for the raw data are Unix time or relative time, counts, and pulses. The structural response unprocessed data and Mighty Mouse shaker unprocessed data files are described in the following Sections.

5.3.4.1 Unprocessed Structural Response Data Files

Unix time and counts are the units that were used for recording the unprocessed data of the structural response in the field. Unix time is a system describing time in sec from

Thursday, January 1, 1970 in the Greenwich Mean Time (GMT) zone. It should be noted that the testing was performed at GVDA in California which is located in the Pacific Standard Time (PST) zone that is eight hours behind GMT. The June testing was during daylight savings and used Pacific Daylight Time (PDT) which is seven hours behind GMT.

The unprocessed data is labeled according to the date and GMT (YYYYMMDDGMT) when the recording began. For example, a test recorded with a beginning GMP time of 6:39 pm and 39 seconds on June 23, 2011 would have a text file name of 20110623183939.txt. The structural response unprocessed data files are listed and highlighted blue in Tables 5-3, 5-4a, 5-5 and 5-6a. A brief summary of the documented channels (columns) of data in the structural response data plan (see Table 5-2) are listed below.

- Channel 1: Time (Unix time)
- Channels 2 through 43: Accelerometers (Counts)
- Channels 44 through 47: LVDTs (Counts)
- Channel 48: Accelerometer for Atom Ant shaker mass in direction of loading (Counts)

5.3.4.2 Unprocessed Mighty Mouse Shaker Data Files

Relative time (sec) from the beginning of data recording, counts and pulses are the units that were used for recording the unprocessed data for the Mighty Mouse shaker data. During excitation with Mighty Mouse, the aforementioned channel 48 of the structural response data files described in Section 5.3.4.1 was unused and slated with zeros.

The unprocessed Mighty Mouse shaker data is labeled according to the date and PST/PDT (GV_YY_MM_DD_PST/PDT) when the recording begun. For example, a test

recorded with a beginning time using PST/PDT at 10:15 am (seconds are not included) on June 23, 2011 would have a text file name of GV_11_06_23_1015.txt. A brief summary of the documented channels (columns) of the Mighty Mouse shaker data are listed below.

- Channel 1: Time (sec)
- Channels 2 and 3: Correlation accelerometers (volts)
- Channels 4 and 5: Shaker pulses (10 pulses per revolution) and shaker control frequency (1 pulse per revolution)

Channels 4 and 5 of the unprocessed Mighty Mouse shaker data were switched during the different testing dates. The switch has been noted in Tables 5-2. During the June (braced condition, Trial 2) testing, channel 4 is the shaker control frequency data and channel 5 is the shaker pulses data. However, during the August (unbraced condition, Trial 4) testing, channel 4 is the shaker pulses data and channel 5 is the shaker control frequency data.

5.3.5 Converted Data Files

Converted data was produced by separating the unprocessed data into subevents for each sweep or step testing interval, and then converting the data to engineering units. First the start times for sweep and step subevents were identified from the test logged PST/PDT converted to Unix time. Then through visual inspection using Matlab graphical tools, appropriate segments were cropped from the unprocessed data file to encompass the duration of loading and response for each respective subevent. The data within the subevent segments were then converted to engineering units.

5.3.5.1 Converted Structural Response Data Files

Following conversion, the units used for the accelerometers and LVDTs are provided in Tables 5-1 and 5-2. Conversion was performed by first dividing $2^{24}/40$ counts per volt. Acceleration signals in volts were converted to 'g' using the differential gain of 5 volts per g. Displacement signals from LVDTs were converted to volts as done with the acceleration signals and then converted to inches using the calibration of each LVDT based on volts per in. It should be noted that three of the LVDT converted data files (Chs. 44, 46, and 47) located at the NEEShub contain an artificial error that can be corrected by multiplying the response by a factor of 10. (Following processing it was found that these LVDT conversion factors were off by a tenth). The converted acceleration and displacement data channels are similar to the unprocessed data discussed in Section 5.3.4. However, it is presented in Unix time, acceleration in g, and inches as shown below. The time signature channel (column) of the converted data was not converted to standard sec and remains in Unix time. The time signature was unchanged during this process so that the location of each subevent is well documented during the cropping procedure.

- Channel 1: Time (Unix time)
- Channels 2 through 43: Accelerometers (g)
- Channels 44 through 47: LVDTs (in)
- Channel 48: Accelerometer for Atom Ant shaker mass in direction of loading (g)

When the structural response converted data was obtained for forced vibration testing using Mighty Mouse shaker, channel 48 was slated with zeros. This was done for both Trial 2 and Trial 4.

5.3.5.2 Converted Mighty Mouse Shaker Data Files

No converted Mighty Mouse shaker data files were created. As shown in Figure 5-8, the Mighty Mouse Shaker data was converted in conjunction with corrective measures. Therefore the conversion details of the Mighty Mouse data are described below in Section 5.3.2.2.

5.3.6 Corrected Data Files

Three types of corrected data files were created: (1) structural response (2) Mighty Mouse shaker (3) synchronized structural response and Mighty Mouse shaker. As shown in Figures 5-8 and 5-9, the procedure used to obtain the corrected structural response data was identical for all trials. However, the preparation of the corrected Mighty Mouse shaker data consisted of performing both the conversion and time shift correction simultaneously, as shown in Figure 5-9 on the left branch. The synchronized structural response and Mighty Mouse shaker corrected data sets were created by the cross-correlation procedure described in Section 5.3.3. The time signature of all subevent data files were converted from Unix time to relative time (sec) from the beginning of subevent.

5.3.6.1 Corrected Structural Response Data Files

The corrected structural response data (accelerations and displacements) were created by applying mean removal to the converted data prepared in the manner discussed in Section 5.3.5.1. The mean was computed using Matlab built-in functions across the subevent time window. This type of baseline correction just shifts the responses relative to the horizontal axis. The corrected structural response data file signals have units identical to

those for the converted data, with the exception of time that is in sec relative to the window start time (not Unix time).

5.3.6.2 Corrected Mighty Mouse Shaker Data Files

The corrected Mighty Mouse shaker data files were separated into subevents and acceleration signals were converted to engineering units and baseline corrected. The subevents start and end times were chosen to be consistent with the structural response data files discussed in Section 5.3.6.1. The time signature was re-established to relative time (in sec) from the beginning of each subevent. The conversion of the accelerometers to gravity (g) units required division by the sensitivity factor of 5 volts/g. The pulsing data is used to identify the beginning of the sine wave and no conversion was required. The baseline correction consisted of mean removal, as before. The converted data fields are similar to the unprocessed data discussed in Section 5.3.2 as shown below.

- Channel 1: Time (sec)
- Channels 2 and 3: Correlation accelerometers (g)
- Channels 4 and 5: Shaker pulses and shaker control frequency

Channels 4 and 5 of the corrected Mighty Mouse shaker data were switched between testing dates. The details of this switch are provided in Table 5-2. During the June (braced condition, Trial 2) testing channel 4 is the shaker control frequency data and channel 5 is the shaker pulses data. However, during the August (unbraced condition, Trial 4) testing channel 4 is the shaker pulses data and channel 5 is the shaker control frequency data. No conversion was performed to these channels.

5.3.6.3 Corrected Synchronized Structural Response and Mighty Mouse Shaker Data Files

The forced vibration testing using Mighty Mouse for excitation required synchronizing and merging of the two data acquisition file types as discussed in Section 5.3.3. Channels 2 and 3 of the Mighty Mouse shaker data were compared, respectively, to channels 16 and 15 of the structural response data. The signals used in the comparison have a common direction of vibration. Based on the time shift from cross-correlation, Δt, the beginning of the corrected Mighty Mouse shaker data was truncated to correlate with the corrected structural response data. The cross-correlation Δt was determined as described in Section 5.3.3 and presented in the last column of Tables 5-4b and 5-6b.

The correlated Mighty Mouse Shaker data was then evaluated for the shaker frequency, angular position of the shaker's rotating mass, and shaker harmonic force. The shaker frequency and angular position of the rotating mass were determined directly from the frequency of the shaker control frequency data. The shaker force was determined based on

$$F = m_r r \omega^2 \cos\theta \tag{5-2}$$

where m_r is the rotating mass, ω is the angular frequency, θ is the angular position of the rotating mass, and r is the radius from the center of rotation to the centroid of the rotating mass. The shaker control frequency channel of the Mighty Mouse shaker data, as shown in Table 5-2, records a single pulse per revolution of the forcing weight. This pulse is recorded when the weight is aligned in the positive direction of loading. Therefore, an

angular position of $\theta = 0$ represents when the weights are pointed in the positive direction of shaking (see Figure 5-7).

The corrected synchronized structural response and Mighty Mouse shaker data files are similar to the corrected structural response data files, however, they have been supplemented with the shaker angular frequency, shaker force, angular position of the shaker's rotating mass, and the respective Mighty Mouse shaker data accelerometer that was used for cross-correlation. The agreement of the cross-correlation for the different acquisition systems can be obtained by comparing channel 52 with channel 15 or channel 16 dependent if the vibration mode is in the *y* or *x* direction, respectively. A summary of the corrected synchronized structural response and Mighty Mouse shaker data files is shown below.

- Channel 1: Time (sec)
- Channels 2 through 43: Accelerometers (g)
- Channels 44 through 47: LVDTs (in)
- Channel 48: Slated with zeros (column used for Atom Ant shaker mass acceleration)
- Channel 49: Shaker angular frequency
- Channel 50: Shaker force (N)
- Channel 51: Angular position (rad) of the shaker's rotating mass
- Channel 52: Mighty Mouse shaker data accelerometer (g) used for cross-correlation (from either channel 2 [x-direction] or channel 3 [y-direction])

5.4 Structural Response of Test Structure

In this section, the processed data is visually inspected to detect obvious errors and to provide insight into the structural response from forced vibration loading. While all records were subject to visual inspection, only three loading conditions are discussed in this section. These three tests represent a spectrum of the loading conditions applied to Mini Me at GVDA. Table 5-7 describes the test experiments chosen for this discussion along with the loading direction, shaker type, maximum force applied, and the intensity descriptor. The intensity descriptors represent the amplitude of forces applied during a particular test relative to other tests at GVDA (i.e., small, moderate, large). Figure 5-14 shows force histories in the time-domain for the tests referenced in this section. All three tests described in this section had the shaker installed on the roof with the shaking applied in the *y*-direction. Figures 5-15 through 5-17 show structural response histories for the force histories in Figure 5-14.

Table 5-7 Test Experiment Used for Presentation of Structural Responses Due to Forced Vibration Testing.

Test Experiment[a] (Figure Below)	Loading Direction	Loading Shaker[b]	Max Force[c] (kN)	Force Intensity[d]
Exp. 3.3.5a (Figure 5-15)	Y	AA	0.2	Small
Exp. 3.4.1a (Figure 5-16)	Y	MM	7.1	Moderate
Exp. 3.4.19a (Figure 5-17)	Y	MM	61.7	Large

[a] See subevent file name from Tables 5-3 to 5-6. Structural response from experiment shown in bracketed Figure no.

[b] AA=Atom Ant and MM=Mighty Mouse.

[c] Maximum force applied from the shaker. See Figure 5-14 for shaker force history.

[d] Force intensity is relative to the test forces at GVDA.

Figure 5-15 shows the structural response of the unbraced structure with loading from the Atom Ant shaker. The maximum force applied by the shaker during this

experiment was 201 N. This force level produces small shear stresses and shear strains in the foundation soil that would not be expected to induce nonlinear response in the foundation soil (discussed further in Chapter 6).

Figures 5-15a and Figure 5-15b show the horizontal structural responses near the four corners of the foundation and roof, respectively. The acceleration trends in Figures 5-15a and 5-15b look fairly consistent from channel to channel in any particular direction. An order of magnitude difference is observed between the maximum accelerations in the direction of applied shaking force (y-direction) and the perpendicular direction (x-direction). Comparing the responses shown in Figures 5-15a and 5-15b, it is observed that the roof acceleration in any given direction is about an order of magnitude greater than the foundation acceleration. These features are particularly evident at about 12 to 15 sec.

Figures 5-15c and 5-15d show the vertical response of the structure. Figure 5-15c shows that the foundation and roof vertical accelerations are similar to each other. Figure 5-15d shows displacements of the foundation from LVDTs. The displacements on the eastern side (channel nos. 46 and 47) are consistent with each other, having a maximum displacement of approximately 0.001 cm (0.0004 in). The western side (channel nos. 44 and 45) shows more displacement than the eastern side with having a maximum displacement of approximately 0.0013 cm (0.0006 in). It should be noted that Figure 5-15d accounted for the correction of the artificial errors as a result of incorrect calibration factors being used during data processing as discussed in Section 5.3.5.1. (Channel nos.

44, 46, and 47 were corrected by multiplication of the response history by 10 and then converted to cm form in for presentation).

Figure 5-15e shows the horizontal foundation accelerations for the adjacent structure (Dr. Evil), ground accelerations between the two structures, and foundation accelerations from Mini-Me. The accelerometers on Dr. Evil require a baseline correction that is time-dependent, opposed to the previously applied linear mean correction. In the direction of shaking, accelerations on the foundation of the Dr. Evil structure are approximately 5% of those on the Mini-Me foundation. Peak accelerations on the ground between the two structures are approximately 15% of those on the Mini-Me foundation.

Figure 5-16 shows the response of the unbraced structure with loading from the Mighty Mouse shaker (5% eccentricity). The maximum force applied by the shaker during this experiment was 7.1 kN, which can be described as a "moderate" force. This level of excitation could reasonably be expected to produce some nonlinearity in the response of the foundation soils (discussed further in Chapter 6).

Figures 5-16a and Figure 5-16b show the horizontal structural responses near the four corners of the foundation and roof, respectively. As before, the shaking is much stronger in the direction of applied shaking (*y*-direction) than in the perpendicular *x*-direction. A noteworthy feature in these plots is the different waveforms recorded by channels 6 and 9 (Figure 5-16a) during the approximate time intervals of 75-95 sec and 200-300 sec. In the former interval (near 85 sec), at the scale of the plot shown in Figure 5-16a, the responses appear to be reversed from each other (i.e., simultaneous peaks in Channel 6 and 9 of 0.04g and -0.04g). In the latter interval (between 200-300 sec), the

channel 9 signal exhibits a s plateau-type appearance while channel no. 6 lacks that plateau feature and gradually reduces in amplitude with time. These same features can be seen in the roof responses in Figure 5-16b. These distinct characteristics of the west and east signals may result from torsional responses of the structure, perhaps arising from loosening of bolts securing the columns to the top and bottom slabs (these bolts were periodically re-tightened in the field during the large amplitude tests). As expected, Figures 5-16a and 5-16b show that the roof accelerations are about an order magnitude larger than foundation accelerations.

Figure 5-16c and 5-16d show the vertical response of the structure. Figure 5-16c shows that the foundation and roof vertical accelerations are similar. Figure 5-16d shows foundation displacements from LVDT recordings. Displacements on the northeast corner (channel 46) were at the noise level so this instrument appears to have been disconnected. Channels from the south side (nos. 44 and 47) are fairly consistent, having maximum displacements around 0.013 cm (0.005 in), channel 44 at the southwestern corner has slightly larger displacements. The northwest LVDT (channel 45) is fairly consistent with channel 47. Figure 5-16d accounted for the aforementioned correction as applied for Figure 5-15d.

Figure 5-16e shows the horizontal accelerations of the adjacent structure (Dr. Evil), ground accelerations, and foundation accelerations from Mighty Mouse excitation of Mini-Me. As before, the foundation accelerograms from Dr. Evil have baseline drift. Compared to foundation accelerations on the excited structure, intermediate ground

accelerations are lower by a factor of 9 and Dr Evil foundation accelerations are lower by a factor of 40.

Figure 5-17 shows the structural response of the unbraced structure with loading from the Mighty Mouse shaker operating at maximum capacity that produced a peak force of 61.7 kN. This can be described as a "large" force. A substantial nonlinear response of the foundation soils is expected from this experiment (discussed further in Chapter 6).

Figures 5-17a and Figure 5-17b show horizontal structural accelerations near the four corners of the foundation and roof, respectively. A noteworthy feature in these plots is the different waveforms recorded by channels 15 and 24 (Figure 5-16b) during the approximate time intervals of 75-100 sec and 325-350 sec. At the scale of the plot shown in Figure 5-16b, the responses appear to be reversed from each other (i.e., simultaneous peaks in channels 15 and 24 of 0.25g and -0.25g). These same features can be seen in the foundation responses in Figure 5-17a. These distinct characteristics of the west and east signals may result from torsional responses of the structure, perhaps arising from loosening of bolts securing the columns to the top and bottom slabs (these bolts were periodically re-tightened in the field during the large amplitude tests). Structural accelerations perpendicular to the loading direction in Figure 5-17a and Figure 5-17b are about an order of magnitude lower in amplitude than those in the loading direction. The perpendicular accelerations peak at the same time intervals as the different horizontal responses noted previously, which supports the notion that these features are associated with a torsional mode response.

Figure 5-17c and 5-17d show the vertical response of the structure. Many of the trends are similar to those noted at lower shaking levels: (1) similar amplitudes at roof and foundation (Figure 5-17c), and (2) similar foundation displacements on the eastern and western sides (Figure 5-17d). A new features not seen in previous tests is that the LVDT displacements in Figure 5-17c are not symmetric, being much larger in the up direction (positive) than down (negative direction), implying the formation of gapping.

Figure 5-17e shows the horizontal accelerations of the adjacent structure (Dr. Evil), ground accelerations, and foundation accelerations from Mighty Mouse excitation of Mini-Me. As before, the foundation accelerograms from Dr. Evil have baseline drift. In the direction of shaking, accelerations on the foundation of the Dr. Evil structure are approximately 5% of those on the Mini-Me foundation. Peak accelerations on the ground between the two structures are approximately 14% of those on the Mini-Me foundation.

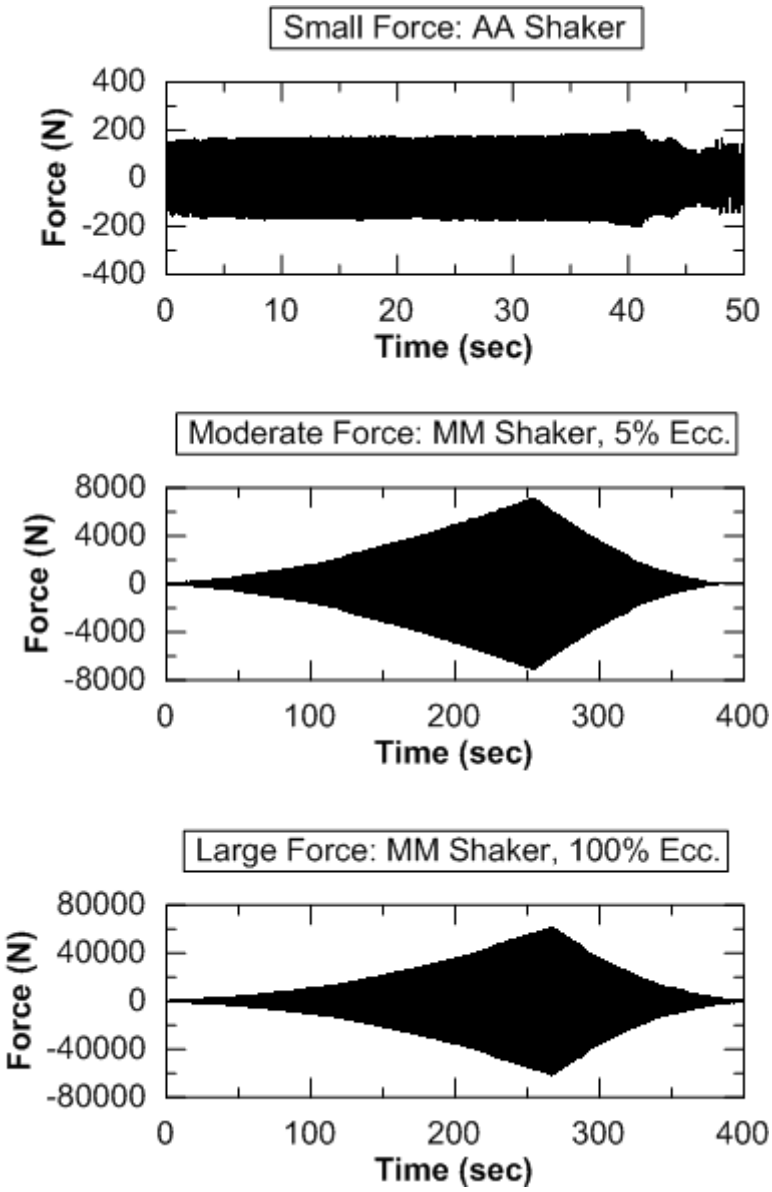

Figure 5-14 **Shaker force loading histories that represent the small, moderate and large forces used during forced vibration testing at GVDA. The titles of the shaker forces correspond to Table 5-7.**

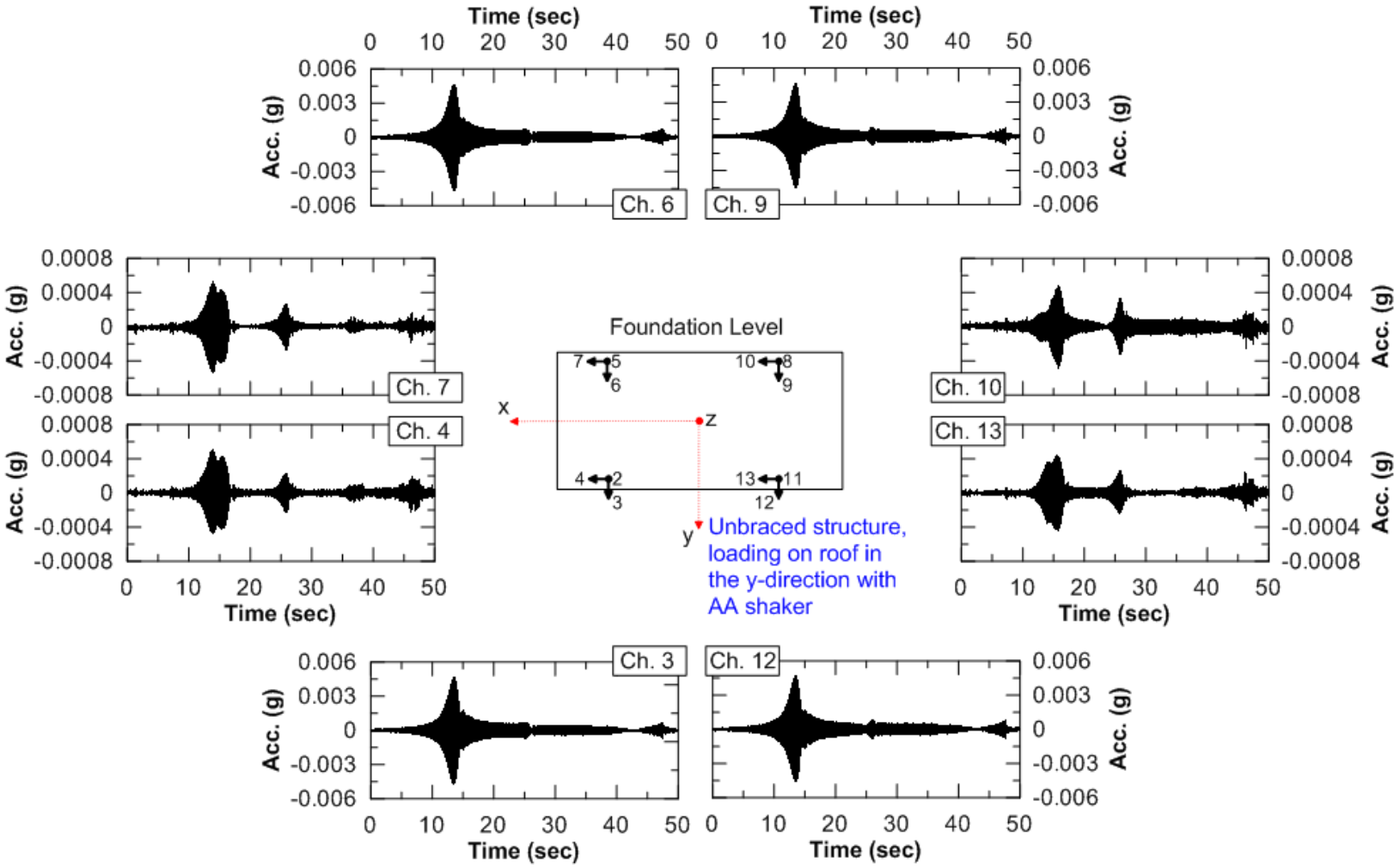

Figure 5-15a **The horizontal structural responses of the foundation are shown for Exp. 3.3.5a (Unbraced condition, Atom Ant shaker loading on the roof in the *y*-direction). The local axes along with channel identification are shown in the middle, while the structural responses are shown in the peripheral.**

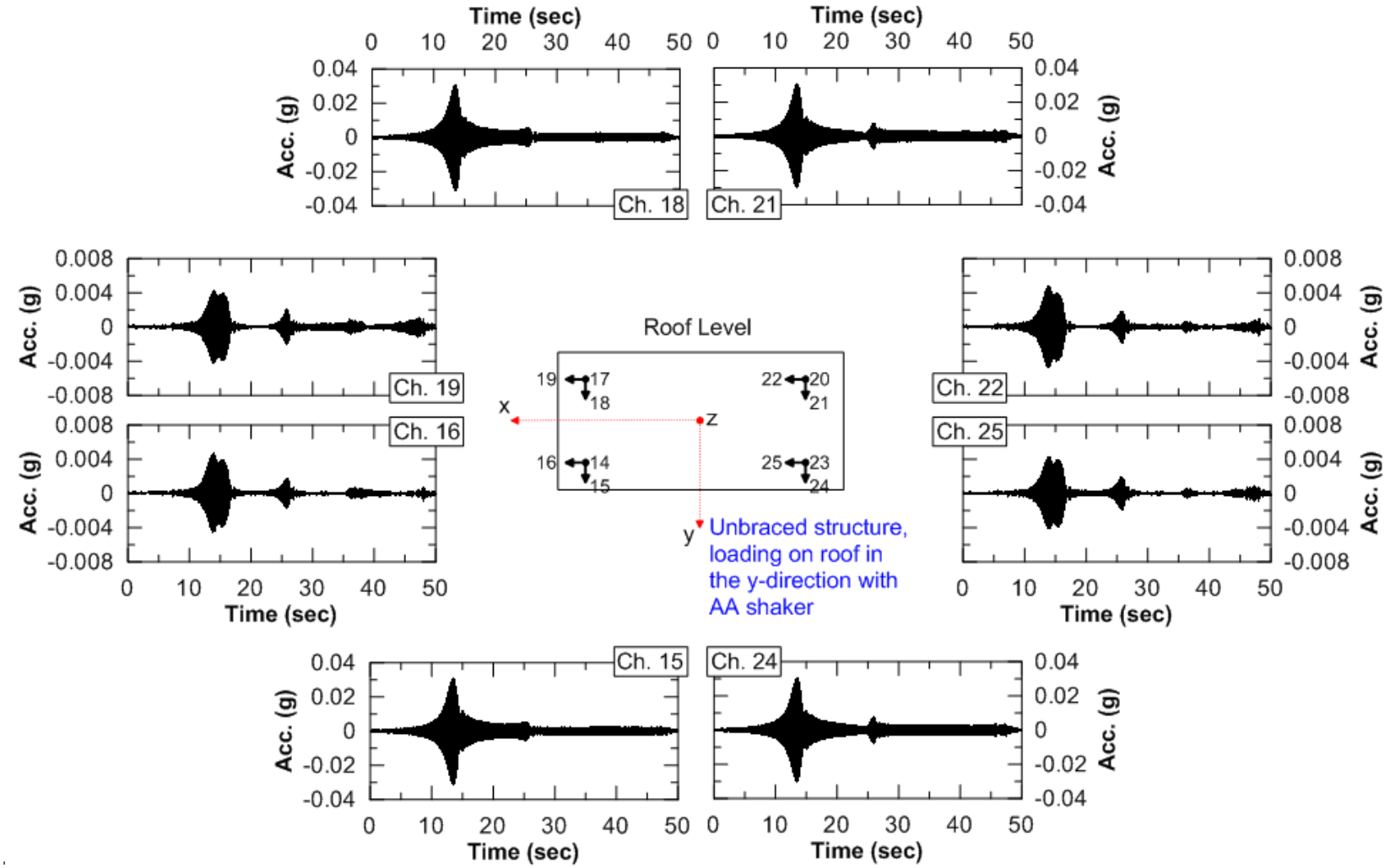

Figure 5-15b **The horizontal structural responses of the roof are shown for Exp. 3.3.5a (Unbraced condition, Atom Ant shaker loading on the roof in the *y*-direction). The local axes along with channel identification are shown in the middle, while the structural responses are shown in the peripheral.**

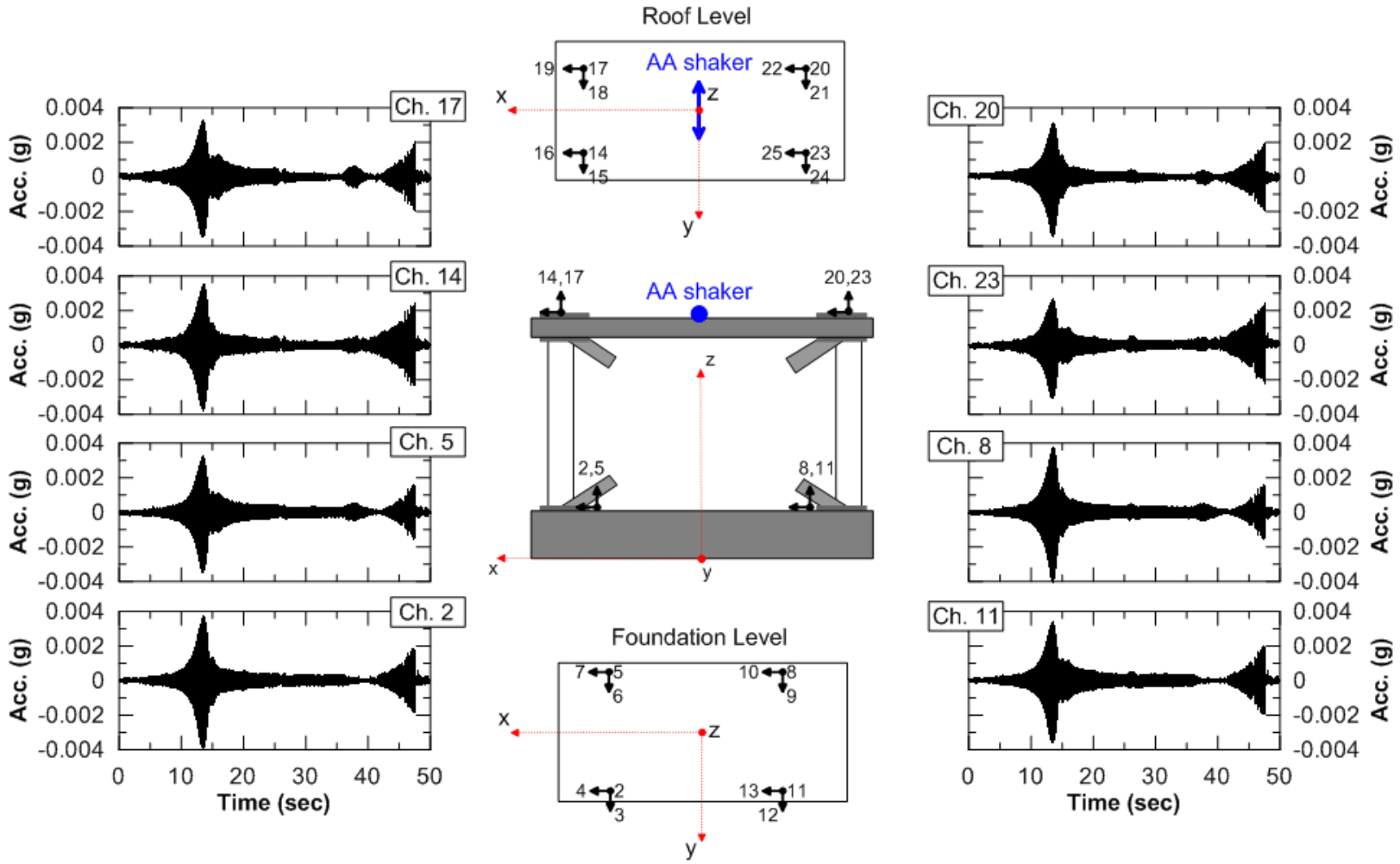

Figure 5-15c **The vertical structural responses are shown for Exp. 3.3.5a (Unbraced condition, Atom Ant shaker loading on the roof in the *y*-direction). The local axes along with channel identification are shown in the middle, while the structural responses are shown on at the sides.**

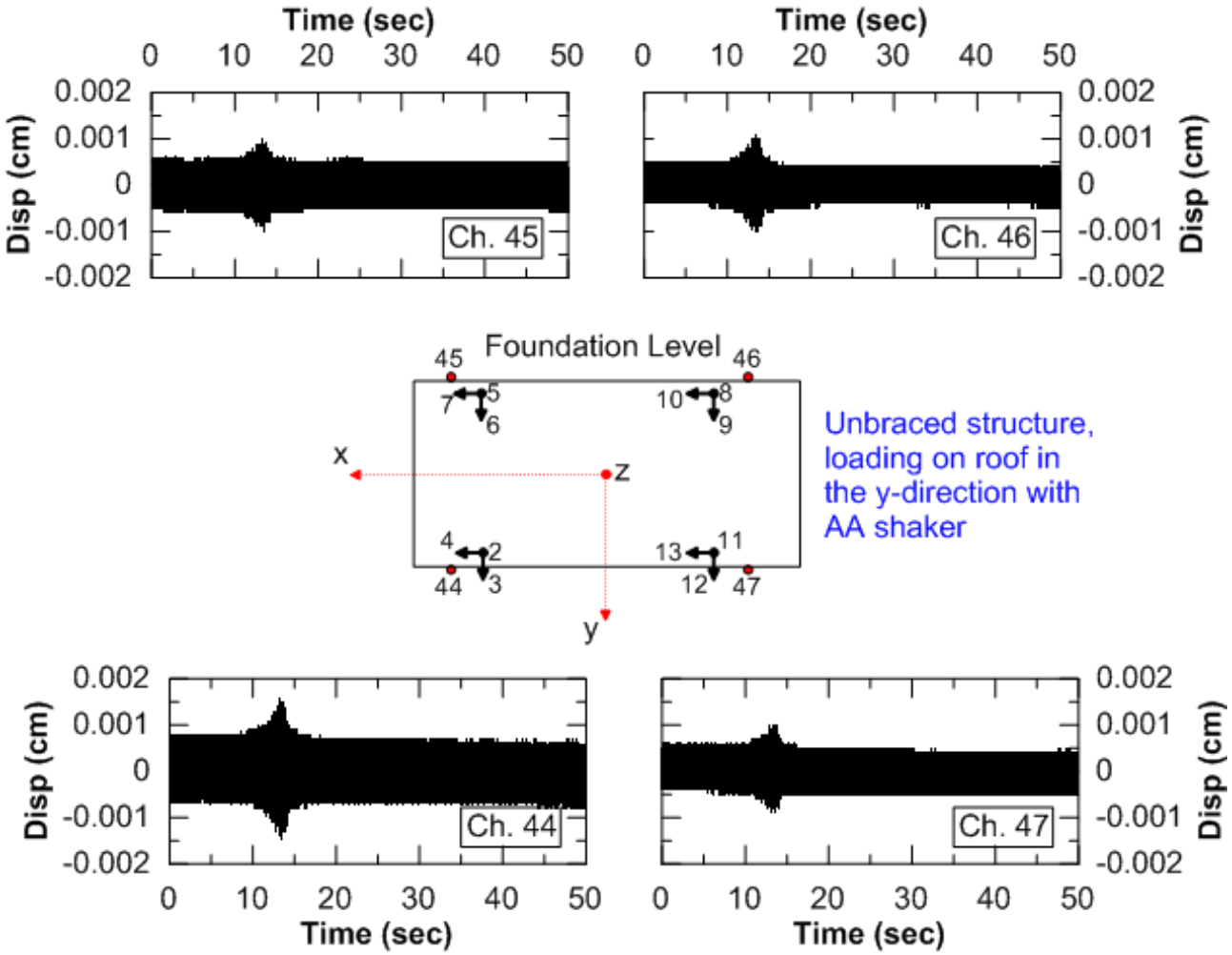

Figure 5-15d **The vertical structural displacements based on LVDT recordings are shown for Exp. 3.3.5a (Unbraced condition, Atom Ant shaker loading on the roof in the *y*-direction). The local axes along with channel identification are shown in the middle, while the structural responses are shown on above and below.**

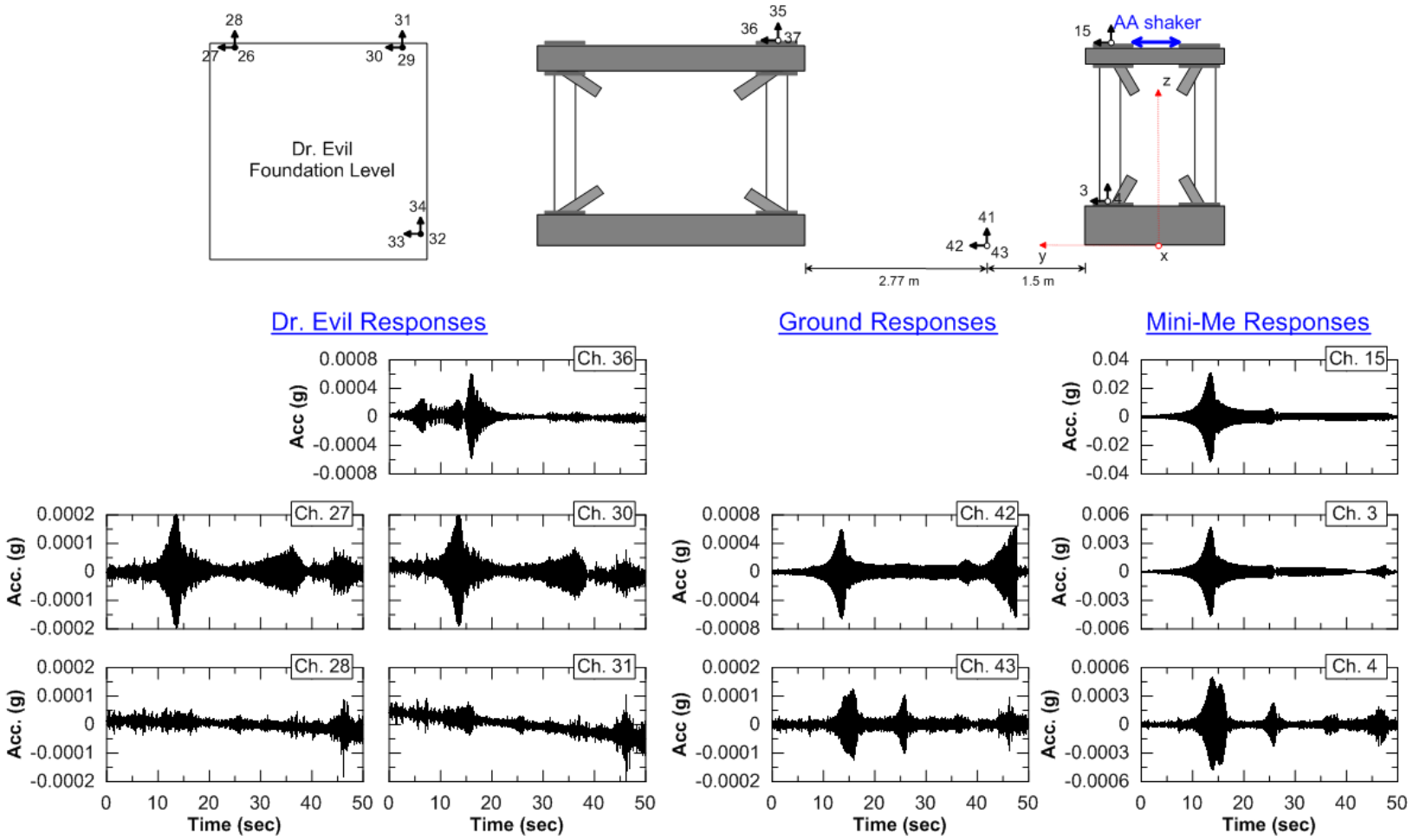

Figure 5-15e **The horizontal structural responses of the adjacent structure (Dr. Evil) are shown in comparison to the free-field and Mini-Me responses for Exp. 3.3.5a (Unbraced condition, Atom Ant shaker loading on the roof in the *y*-direction). The local axes of Mini-Me is shown along with channel identifications of the responses. Dr. Evil foundation plan view is shown at the top left and the cross-section relationship of the structures and free-field is shown at the top right.**

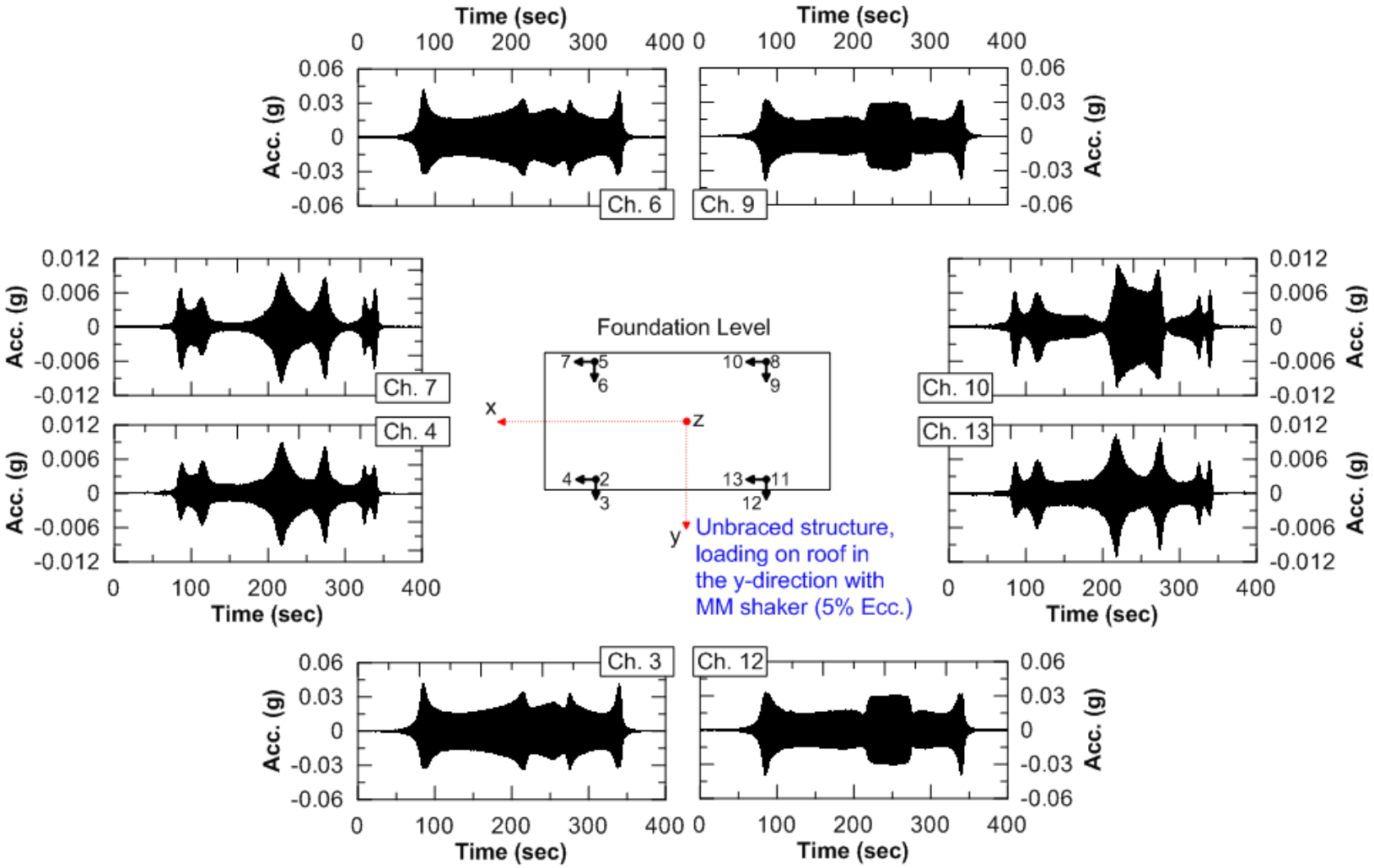

Figure 5-16a **The horizontal structural responses of the foundation are shown for Exp. 3.4.1a (Unbraced condition, Mighty Mouse shaker with 5% eccentricity loading on the roof in the *y*-direction). The local axes along with channel identification are shown in the middle, while the structural responses are shown in the peripheral.**

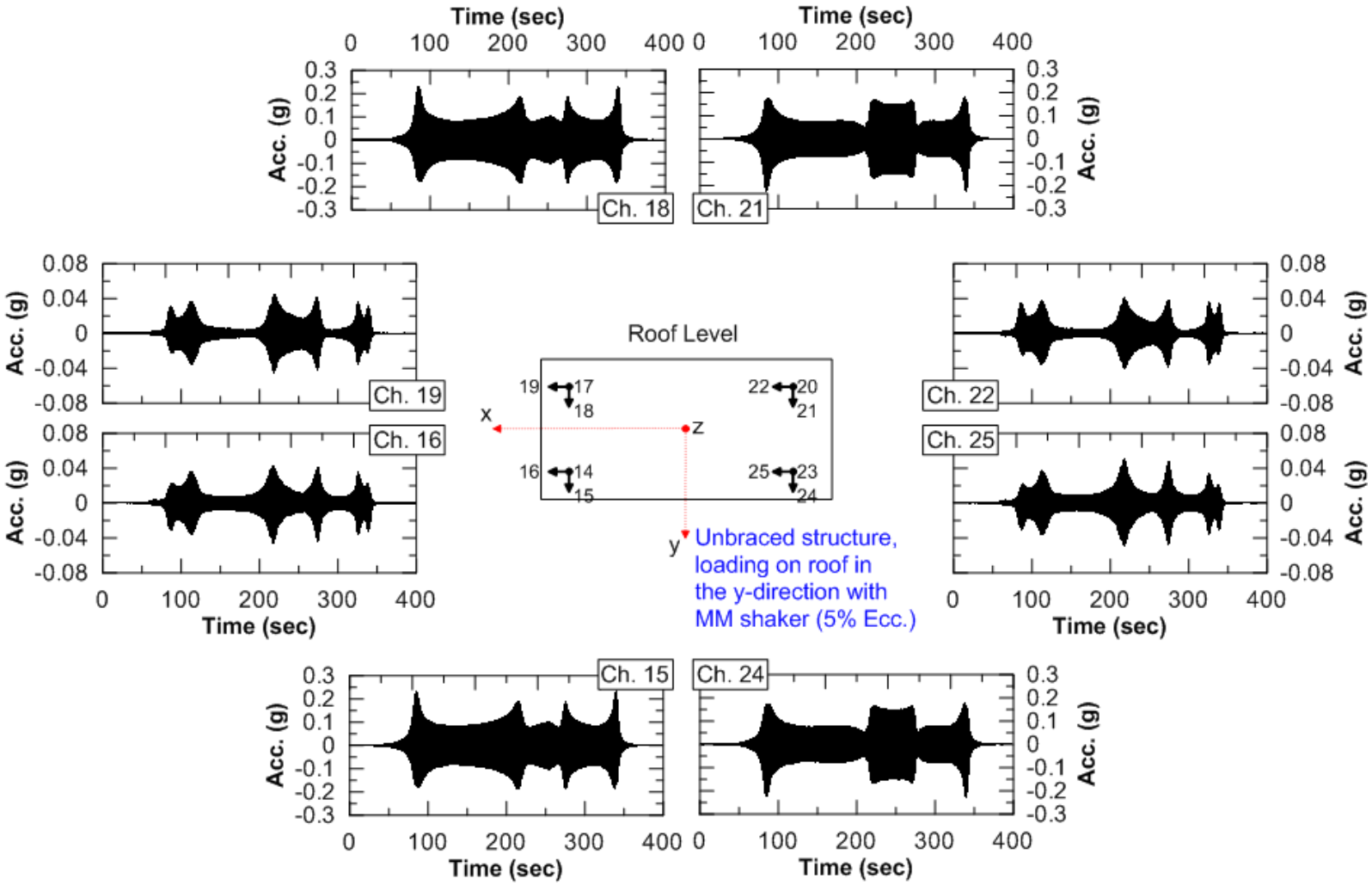

Figure 5-16b **The horizontal structural responses of the roof are shown for Exp. 3.4.1a (Unbraced condition, Mighty Mouse shaker with 5% eccentricity loading on the roof in the *y*-direction). The local axes along with channel identification are shown in the middle, while the structural responses are shown in the peripheral.**

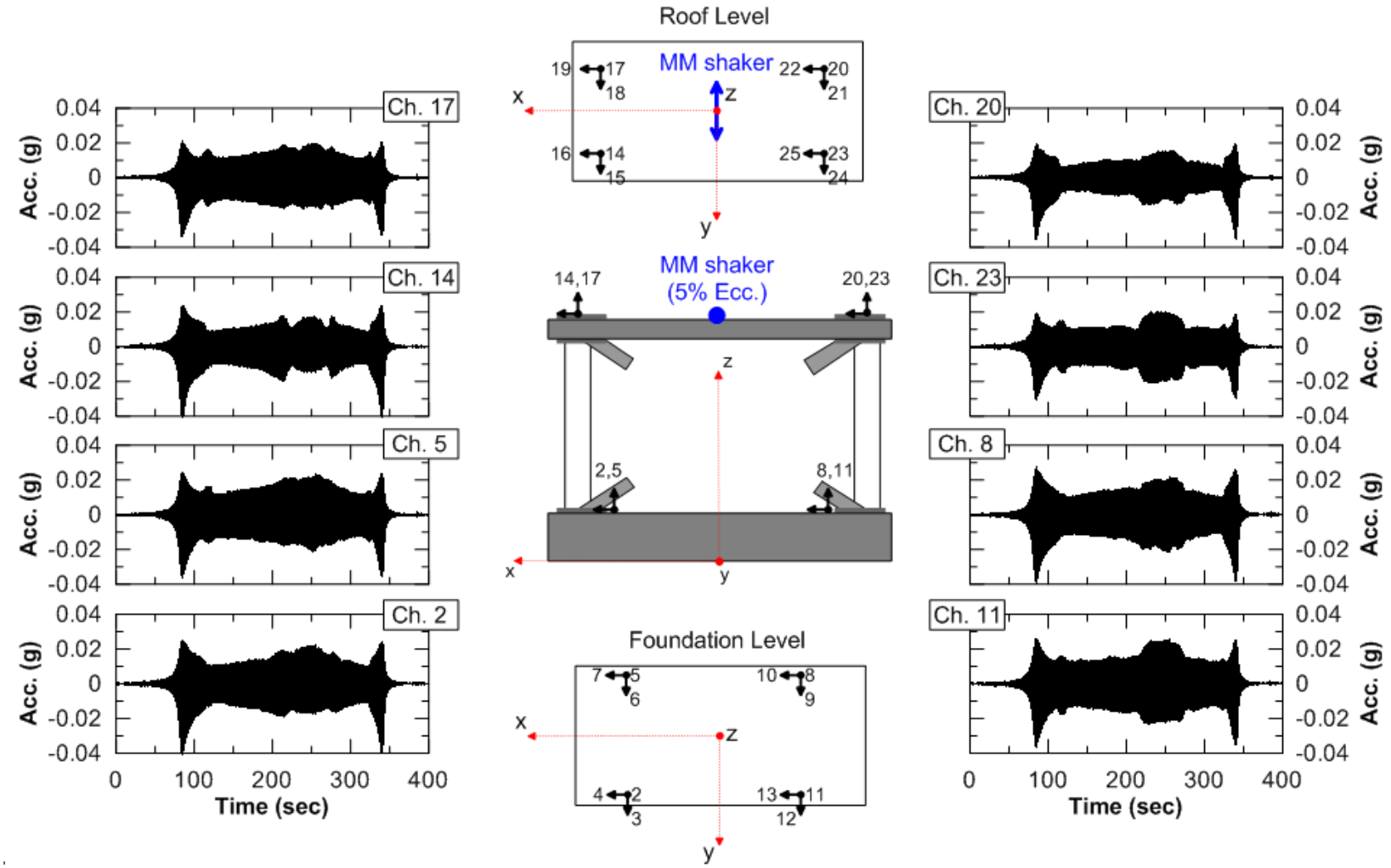

Figure 5-16c **The vertical structural responses are shown for Exp. 3.4.1a (Unbraced condition, Mighty Mouse shaker with 5% eccentricity loading on the roof in the *y*-direction). The local axes along with channel identification are shown in the middle, while the structural responses are shown on at the sides.**

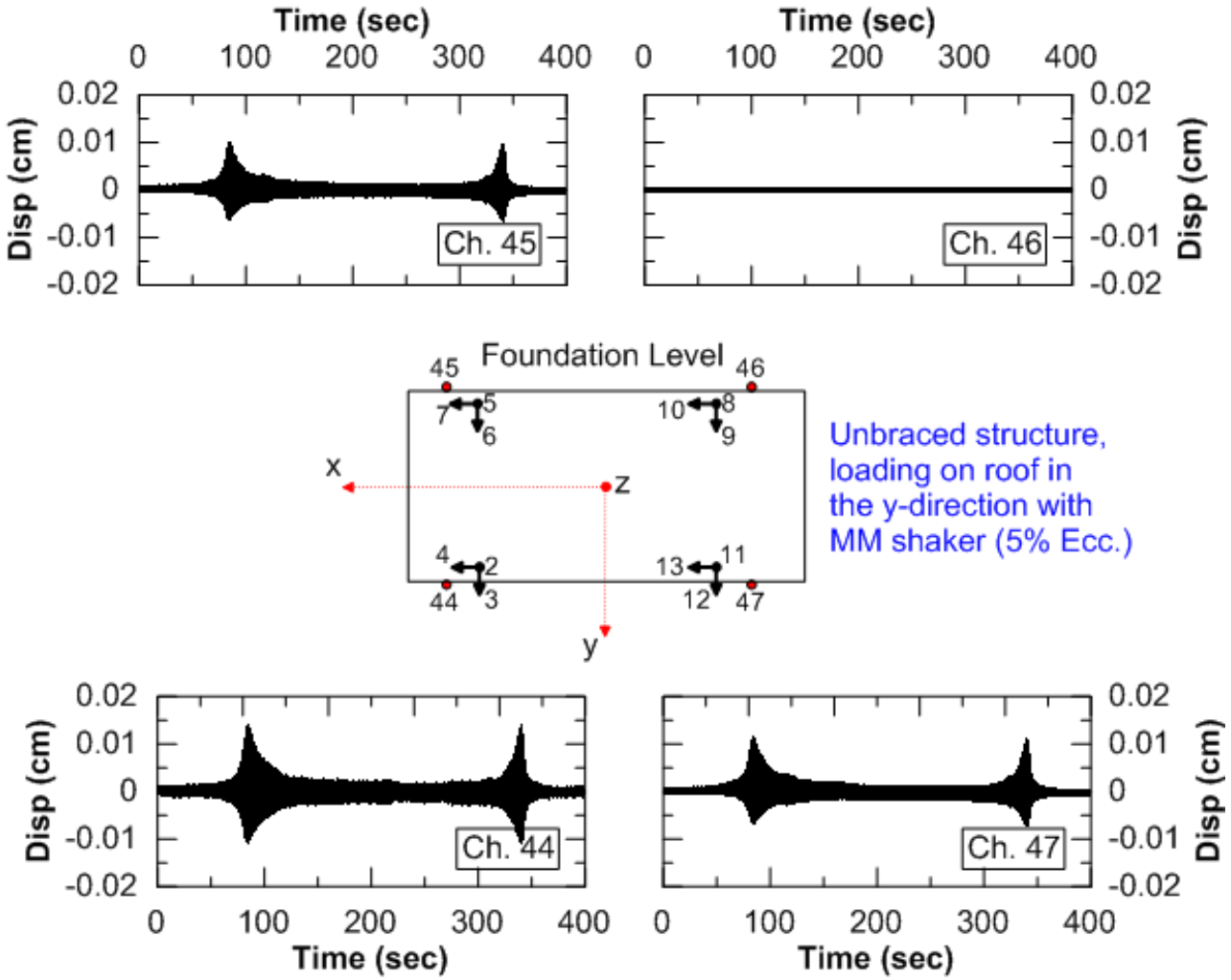

Figure 5-16d **The vertical structural displacements based on LVDT recordings are shown for Exp. 3.4.1a (Unbraced condition, Mighty Mouse shaker with 5% eccentricity loading on the roof in the *y*-direction). The local axes along with channel identification are shown in the middle, while the structural responses are shown on above and below.**

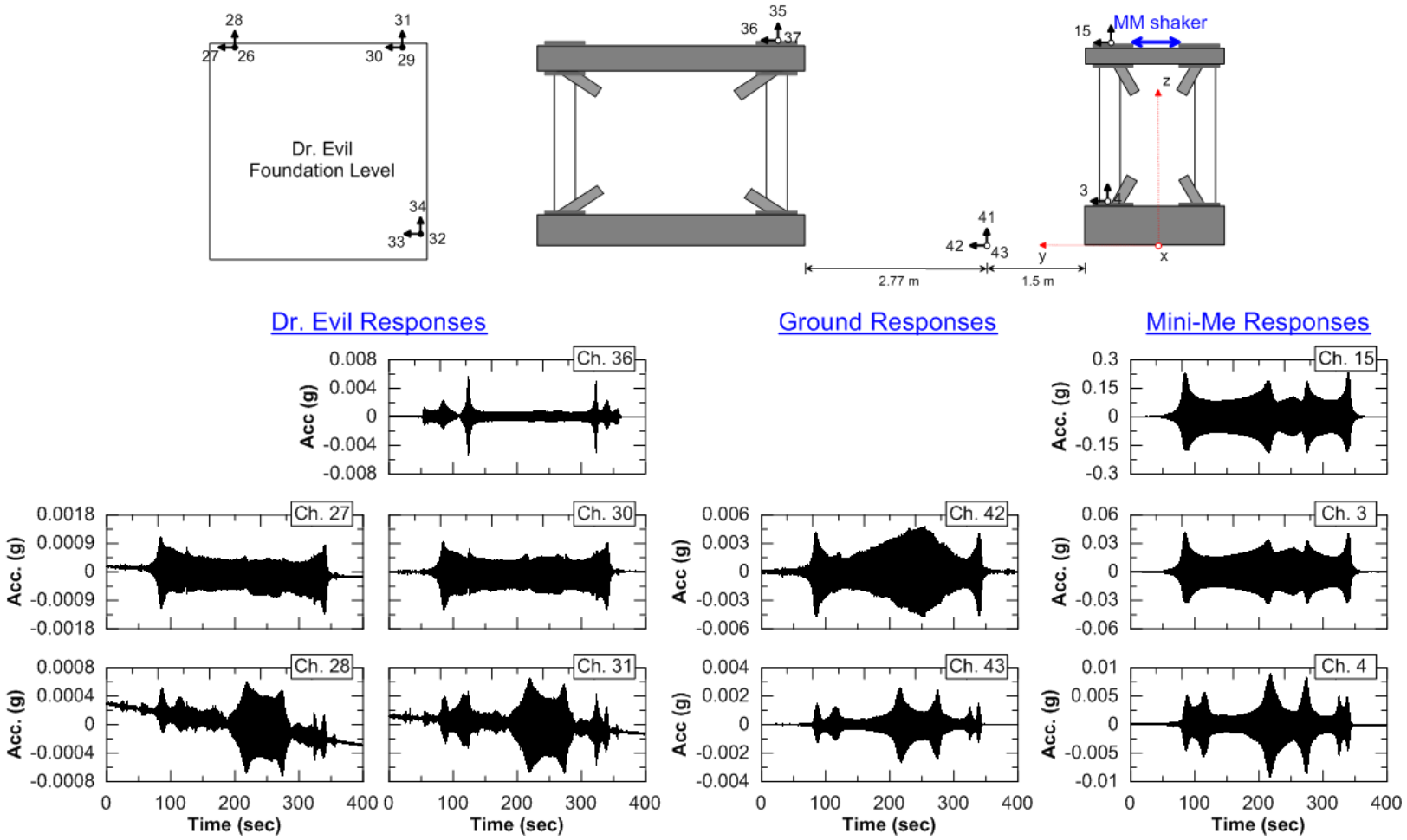

Figure 5-16e **The horizontal structural responses of the adjacent structure (Dr. Evil) are shown in comparison to the free-field and Mini-Me responses for Exp. 3.4.1a (Unbraced condition, Mighty Mouse shaker with 5% eccentricity loading on the roof in the *y*-direction). The local axes of Mini-Me is shown along with channel identifications of the responses. Dr. Evil foundation plan view is shown at the top left and the cross-section relationship of the structures and free-field is shown at the top right.**

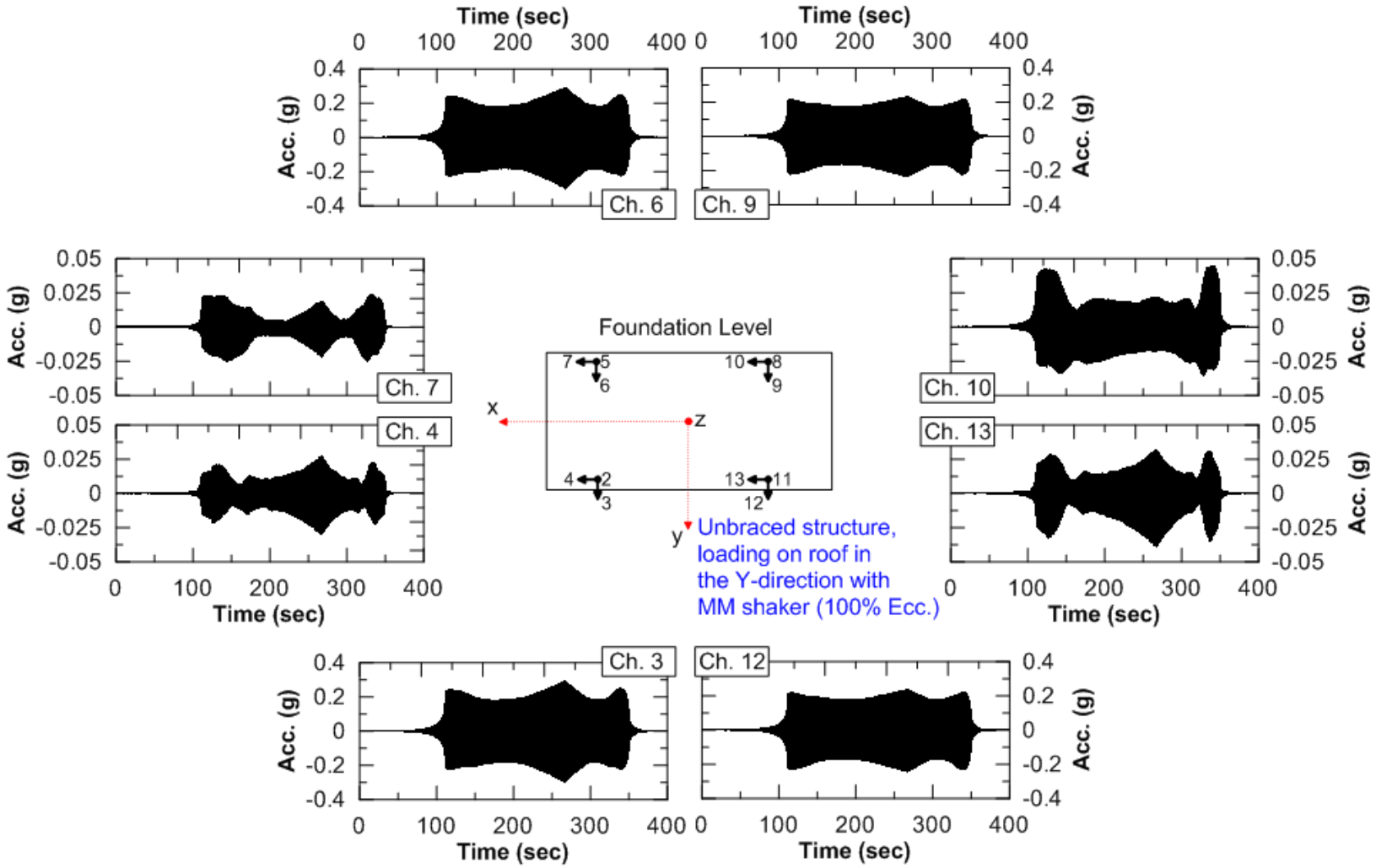

Figure 5-17a **The horizontal structural responses of the foundation are shown for Exp. 3.4.19a (Unbraced condition, Mighty Mouse shaker with 100% eccentricity loading on the roof in the *y*-direction). The local axes along with channel identification are shown in the middle, while the structural responses are shown in the peripheral.**

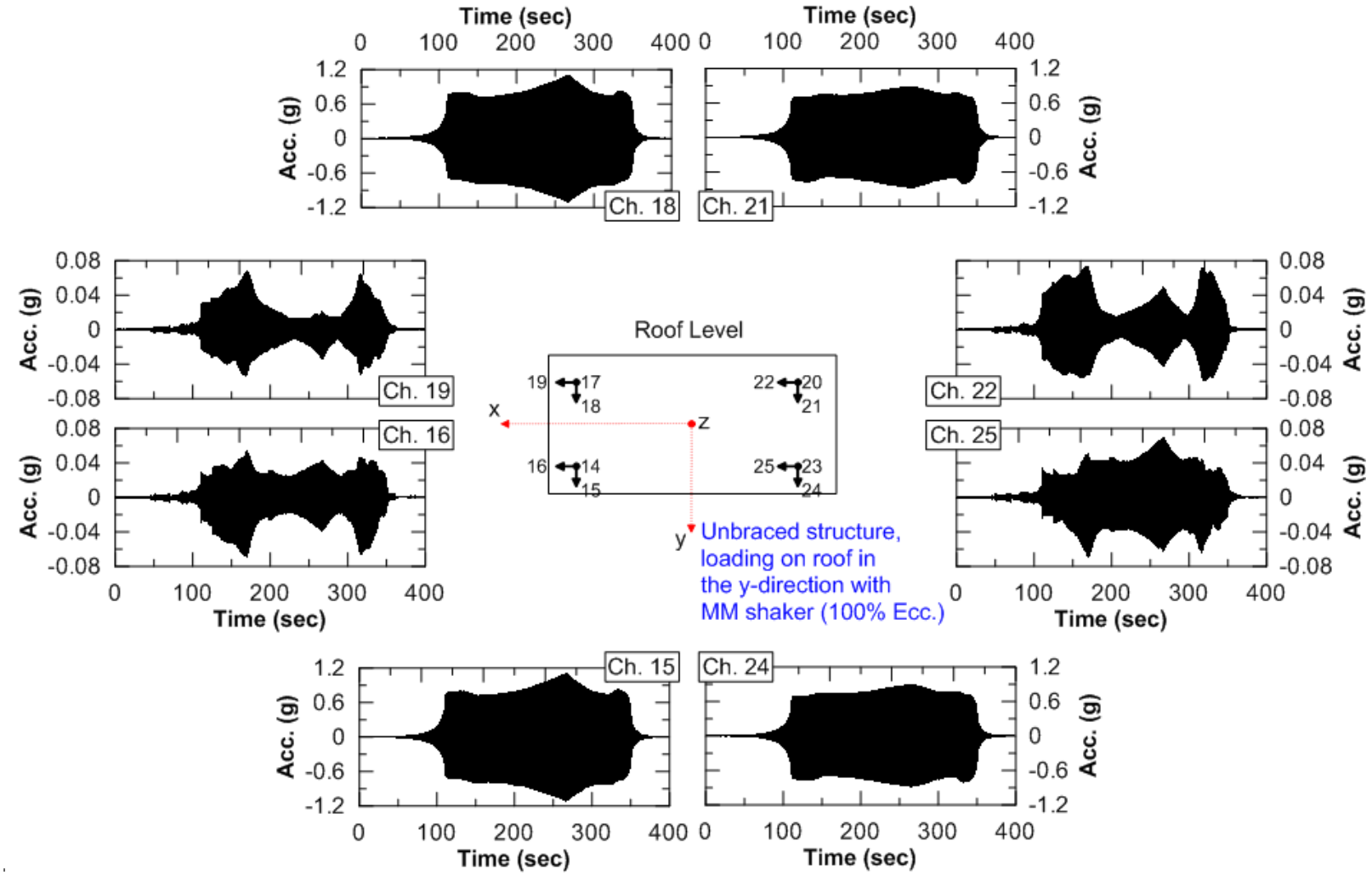

Figure 5-17b **The horizontal structural responses of the roof are shown for Exp. 3.4.19a (Unbraced condition, Mighty Mouse shaker with 100% eccentricity loading on the roof in the *y*-direction)The local axes along with channel identification are shown in the middle, while the structural responses are shown in the peripheral.**

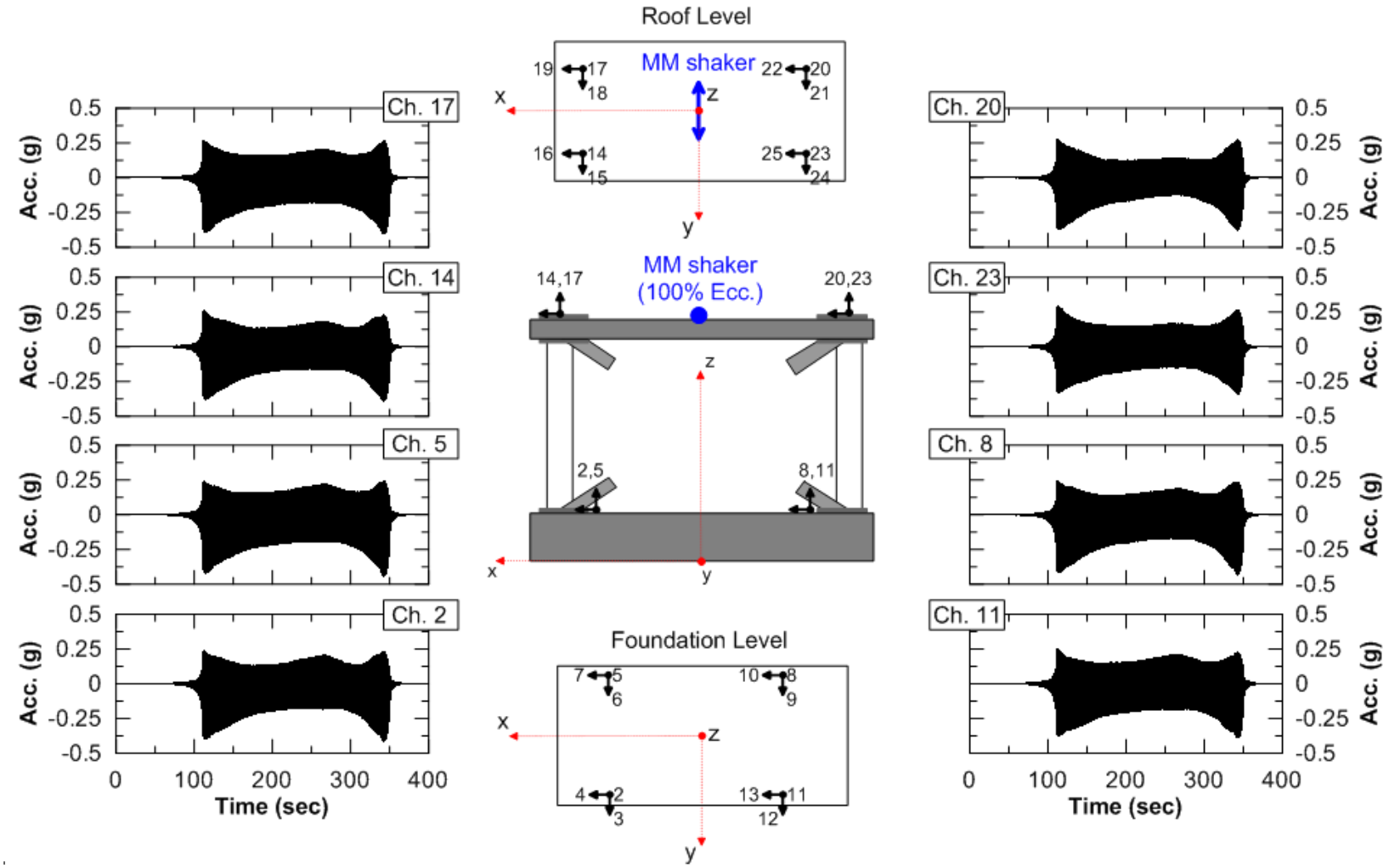

Figure 5-17c **The vertical structural responses are shown for Exp. 3.4.19a (Unbraced condition, Mighty Mouse shaker with 100% eccentricity loading on the roof in the *y*-direction). The local axes along with channel identification are shown in the middle, while the structural responses are shown on at the sides.**

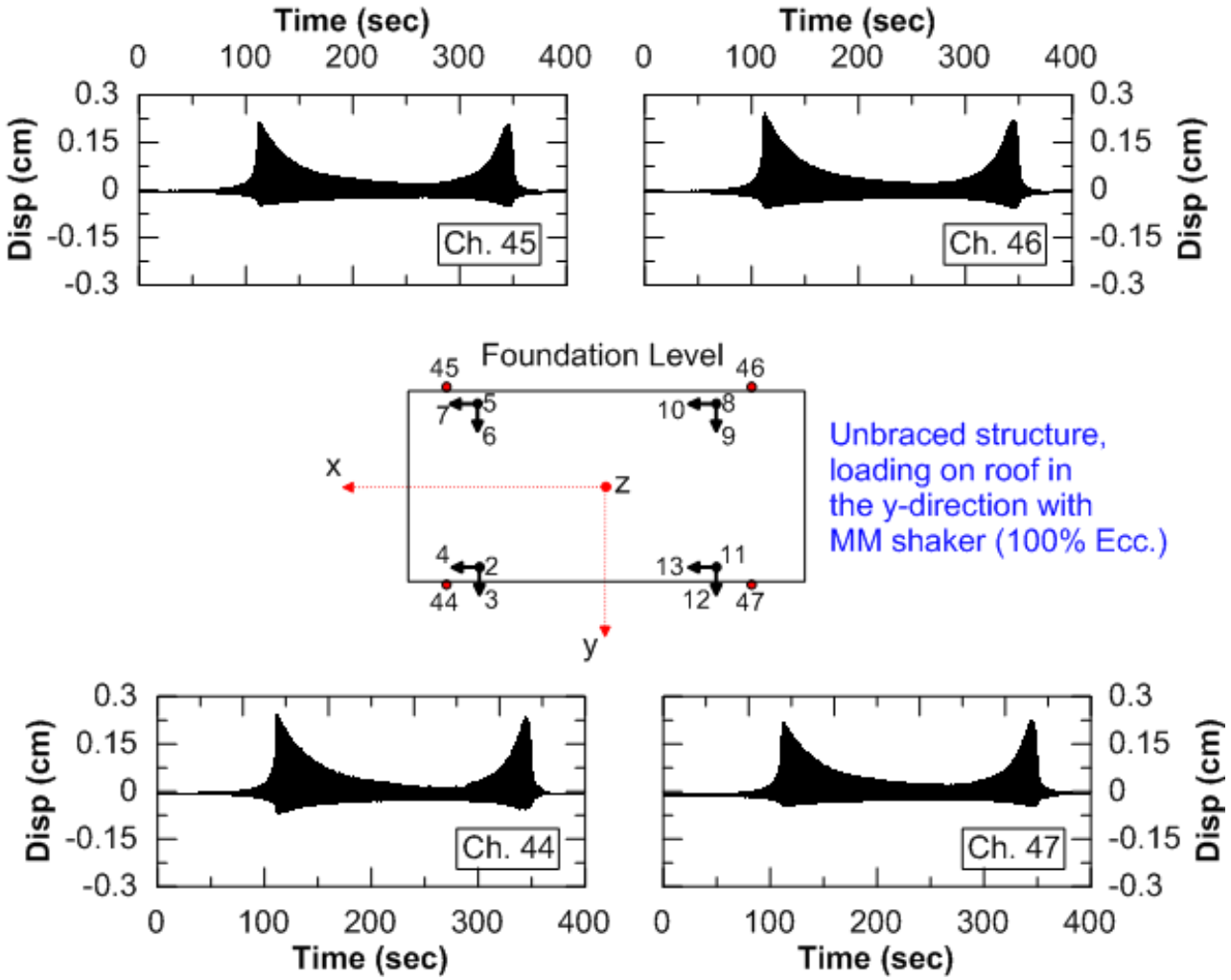

Figure 5-17d **The vertical structural displacement based on LVDTs are shown for Exp. 3.4.19a (Unbraced condition, Mighty Mouse shaker with 100% eccentricity loading on the roof in the *y*-direction). The local axes along with channel identification are shown in the middle, while the structural responses are shown on at the sides.**

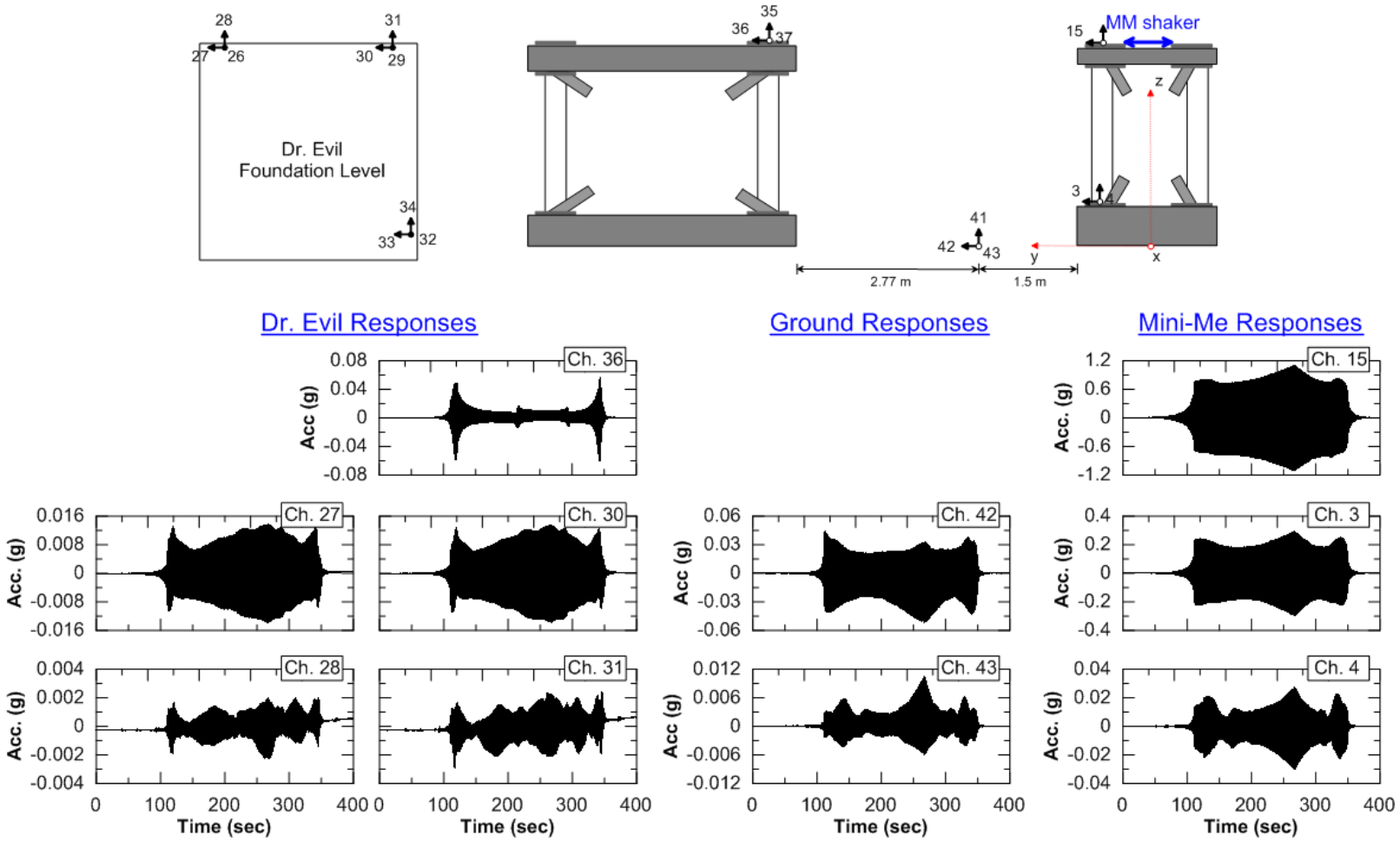

Figure 5-17e **The horizontal structural responses of the adjacent structure (Dr. Evil) are shown in comparison to the free-field and Mini-Me responses for Exp. 3.4.19a (Unbraced condition, Mighty Mouse shaker with 100% eccentricity loading on the roof in the *y*-direction). The local axes of Mini-Me is shown along with channel identifications of the responses. Dr. Evil foundation plan view is shown at the top left and the cross-section relationship of the structures and free-field is shown at the top right.**

5.5 Conclusions

Forced vibration testing of a shallow foundation field test structure was successfully performed at GVDA in June and August 2011. The structure was loaded cyclically by a small linear mass shaker that imparted consistent force amplitudes over the frequency range 0-50 Hz and by a large eccentric mass shaker that imparted frequency-dependent forces over the frequency range 0-19 Hz. The test structure was well instrumented with accelerometers and LVDTs to capture the structural response histories. The response histories have been processed from the unprocessed data files to convert to engineering units, convenient time formats, and to remove baseline errors. The data files created from the forced vibration testing at GVDA have been archived at the NEEShub (https://nees.org/warehouse/project/637).

This chapter provides a detailed description of GVDA soil conditions, test structures, sensor arrays, data acquisition systems, shaker types and forces, field test logs, and the data processing procedures used for the GVDA SSI force vibration testing.

Section 5.4 presented a review of the processed data files and the resultant structural responses from the forced vibration loading at GVDA. Visual inspection revealed several problems a disconnected LVDT (channel 46), baseline errors of accelerations from the foundation of adjacent structure Dr. Evil, and conversion error of three vertical foundation LVDTs (channels44, 46, and 47). The conversion error can be corrected by multiplying the converted data channels by a factor of 10.

The observed responses indicate no significant torsional response for the lowest shaking level, but asymmetric responses suggestive of a torsional response for the larger

shakers. Gapping was observed in the LVDT displacements applied by the strongest shaking, which is consistent with visual observations from the field.

6 EVALUATION OF SOIL-STRUCTURE INTERACTION EFFECTS FROM FORCED VIBRATION TESTING

6.1 Introduction

As described in Chapter 5, forced vibration testing of a well-instrumented test structure was performed to evaluate soil-structure interaction (SSI) effects. The experiments were performed at the Garner Valley Downhole Array (GVDA) site operated by NEES@UCSB. Forced vibration testing of our test structure, hereafter referred to as "Mini-Me," was previously performed at the Wildlife Liquefaction Array (WLA) and at the UCLA laboratory (Star, 2011). Mini-Me was the first structure to be tested with varying foundation conditions (i.e. different underlying soils), so that we could examine the impact of variable soil conditions on SSI effects. In addition, the GVDA site conditions allowed for instrumentation of the adjacent, existing structure and a large rectangular concrete slab during testing. The adjacent structure, hereafter referred to as "Dr. Evil," was instrumented for evaluation of structure-soil-structure interaction (SSSI) from the vibration of Mini-Me. Also, an existing concrete slab in the parking lot adjacent to the GVDA site was instrumented for evaluation of kinematic interaction effects.

6.2 Previous Forced Vibration Testing of Field Test Structures to Evaluate Impedance Functions

Limited full-scale forced vibration testing studies have been performed with the configuration of arrays necessary to evaluate SSI. As discussed in Section 5.1, the evaluation of SSI effects on buildings requires horizontal accelerometers at the free-field, foundation, and roof, and two vertical accelerometers on the foundation to evaluate rocking response (Stewart and Fenves, 1998). In the case of forced vibration testing, the free-field motion is not required since the external force is introduced directly to the structure's foundation or roof and the free-field motion is taken as zero. Table 6-1 shows the attributes of previous forced vibration testing studies involving large-scale test structures that have been instrumented to evaluate SSI. The studies listed in Table 6-1 investigated the responses of their respective structures to evaluate the real and imaginary parts of the SSI system impedance functions and to compare them to theoretical models. Recall from Section 2.3.1 that the soil-foundation stiffness is represented by only the real part, whereas the damping is represents by a ratio of the real and imaginary parts (Eq. 2-5).

Table 6-1 Summary of Field Forced Vibration Tests Used to Evaluate Foundation Impedance Functions (NIST, 2012)

				Excitation		Results			
Foundation Dimensions	Embed. (m)[1]	f_1 (Hz)[2]	V_S (m/s)[3]	Source	Freq. (Hz)[4]	$\tilde{T}/T$ [5]	Impedance obtained	Freq. range (Hz)[6]	Reference
3×3m	0-1.5	17.5	305	Shaker on ground	7-70	1.3 (D=1.5); 1.5 (D = 0)	k_x, c_x, k_{yy}, c_{yy}	modal freq. only	Lin and Jennings, 1984
25×25m	4-5.5	NS: 2.16; EW: 1.26	300	Shaker on roof	NS: 0.8-2.5; EW: 0.8-1.75	NS:1.06; EW:1.1	k_x, c_x, k_{yy}, c_{yy}	NS:0.8-2.5; EW:0.8-1.75	Luco et al., 1988; Wong et al., 1988
1.3×1.3m; 1.2×1.1m	0	n/a	120; 75	Shaker on fndn.	10-60	n/a	k_x, c_x, k_{yy}, c_{yy}	0-60	Crouse et al., 1990
diam = 10.8m	5.2	9.37	300	Shaker on roof & fndn	2-20	2	k_x, c_x, k_{yy}, c_{yy}, $k_{x\text{-}yy}$, $c_{x\text{-}yy}$, k_z, c_z	5-14	DeBarros and Luco, 1995
4.1×4.1m	0	6.0, 13	198	Shaker on roof	5-15	1.15, 1.29	k_x, c_x, k_{yy}, c_{yy}	5-15	Tileylioglu et al. 2011
4.3×2.1m	0	Braced NS: 31.2; EW: 23.0; Unbraced NS: 11.5; EW: 12.1	106; 98	Shaker on roof & fndn	4-45	Braced NS: 3.06; EW: 3.03; Unbraced NS: 1.35; EW: 1.81	k_x, c_x, k_{yy}, c_{yy}	4-45	Star 2011

[1]Foundation embedment depth; [2] Fundamental mode, fixed-base frequency; [3]Vs=Shear wave velocity of soil; [4]Frequency range and [5]Period lengthening. Symbols: D=embedment depth; n/a=not available; NS=North-South building axis; EW=East-West building axis; diam=diameter; and fndn.=foundaiton

Lin and Jennings (1984) constructed a square 3 m (10 ft) single story structure overlying 300 m (1,000 ft) of young river alluvial deposits with a V_s = 300 m/s (984 ft/s). The water table was located at 76 m (250 ft) below the ground surface. An external shaking force located 15 m (49 ft) from the structure was used to produce horizontal incident SH-waves. This was done in an attempt to represent earthquake excitation. Forced vibration was applied with the structure situated at three different embedment depths. The impedance results for translation and rocking of the nonembedded structure were found in good agreement with the analytical model of Veletsos and Wei (1971). However, the embedment effects of the testing were found to be larger than the analytical

models (Beredugo and Novak, 1972, Elsabee and Morray, 1977, Luco et al., 1975, and Permalee and Kudder, 1974).

A forced vibration test was performed at the roof of the Millikan Library Building to evaluate horizontal and rocking impedance functions (Luco et al, 1988 and Wong et al, 1988). The structure is a nine-story reinforced concrete building with approximately 5.5 m (18 ft) of embedment overlying firm soil that has a V_s = 300 m/s (984 ft/s). For modeling purposes, the foundation was considered rigid with an effective radius of 13.7 m (45ft). The lateral loads are resisted by a shear wall (NS direction) and a central core (EW direction). Based on the different active systems, the embedment into the soil was modeled as 4 m (13 ft) in the NS direction and 5.5 m (18 ft) in the EW direction. Figure 6-1 presents the Wong et al. (1988) experimental results versus the theoretical (Apsel and Luco, 1987) model for rocking and horizontal responses in both the NS and EW directions. The impedance functions in Figure 6-1 have been normalized by the characteristic foundation length. The study was confined to a limited frequency range (0.8-2.5 Hz), however, noteworthy trends were observed. The experimental rocking impedances (Figures 6-1a and 6-1c) match the theoretical results in both directions fairly well, with the exception of the underpredicted imaginary part of the EW direction. The horizontal impedance model overpredicted the experimental results by as much as 50% in the NS direction (Figure 6-1b).

Crouse et al (1990) performed forced vibration testing at two sites that had different foundations. The first site (known as “Cholame station”) consisted of a square 1.3 m (4 ft) reinforced concrete foundation that had 200 cm (8 in) diameter piers at the

four corners. The Cholame station site has a V_s = 120 m/s (390 ft/s). The Cholame station foundation was modeled as a rigid circular foundation with an equivalent radius of 0.73 m (2.4 ft). The concept of an equivalent radius was applied because of the impedance functions considered in the study, which assume circular foundation geometry.. The second site (known as "Station 6") consisted of a rectangular 1.2 m x 1.1 m (3.9 ft x 3.6 ft) reinforced concrete foundation at ground surface. Station 6 site has a V_s = 75 m/s (250 ft/s). The Station 6 foundation was modeled as rigid. Both foundations overlay soil deposits that are approximately 70 m (230 ft) of soft to moderately stiff Quaternary alluvial deposits. Forced vibration was applied at the roof between the frequencies of 10 to 60 Hz. Three theoretical impedance models were evaluated for comparison at these sites, as follows: 1) using the best estimate of V_s and damping properties: 2) correcting for overburden pressure from the structure by increasing the V_s values of the upper 0.6 m (2 ft) by 30%: 3) using Model 2 updated with a higher soil damping (8% instead of 1.5%) for the upper 0.9 m (3 ft). These models of soil properties were applied with impedance function solutions presented by Wong and Luco (1985) and Apsel and Luco (1987). Figures 6-2 and 6-3 show normalized results of the models compared to the experimentally derived impedance functions for the Cholame station and Station 6 sites, respectively. Real parts have been normalized by Gr (for translation) and Gr^3 (for rocking), while the imaginary parts are normalized by a_0, where r is the effective radius and $a_0^r = \omega r / V_s$. For comparison, the soil and foundation parameters used for normalization purposes are: G = 9.44 MPa (0.197 psf), r = 0.61 m (2 ft) and V_s = 73 m/s (240 fps) as described by Crouse and Hushmand (1989).

Crouse et al. (1990) showed that the impedance functions are frequency-dependent at both sites (Figures 6-2 and 6-3). The Cholame station (Figure 6-2) horizontal impedances are generally lower than the models, while the rocking impedances are larger than expected. Station 9 (Figure 6-3) showed both the horizontal and rocking impedances to be larger than expected. Crouse et al (1990) found a better theoretical fit to the experimental data by including the overburden pressure and by increasing the soil damping (Model 3). The predicted theoretical impedance functions based on no modification to the measured V_s or soil damping (Model 1) procedure typically had the worst comparison to the experimental data.

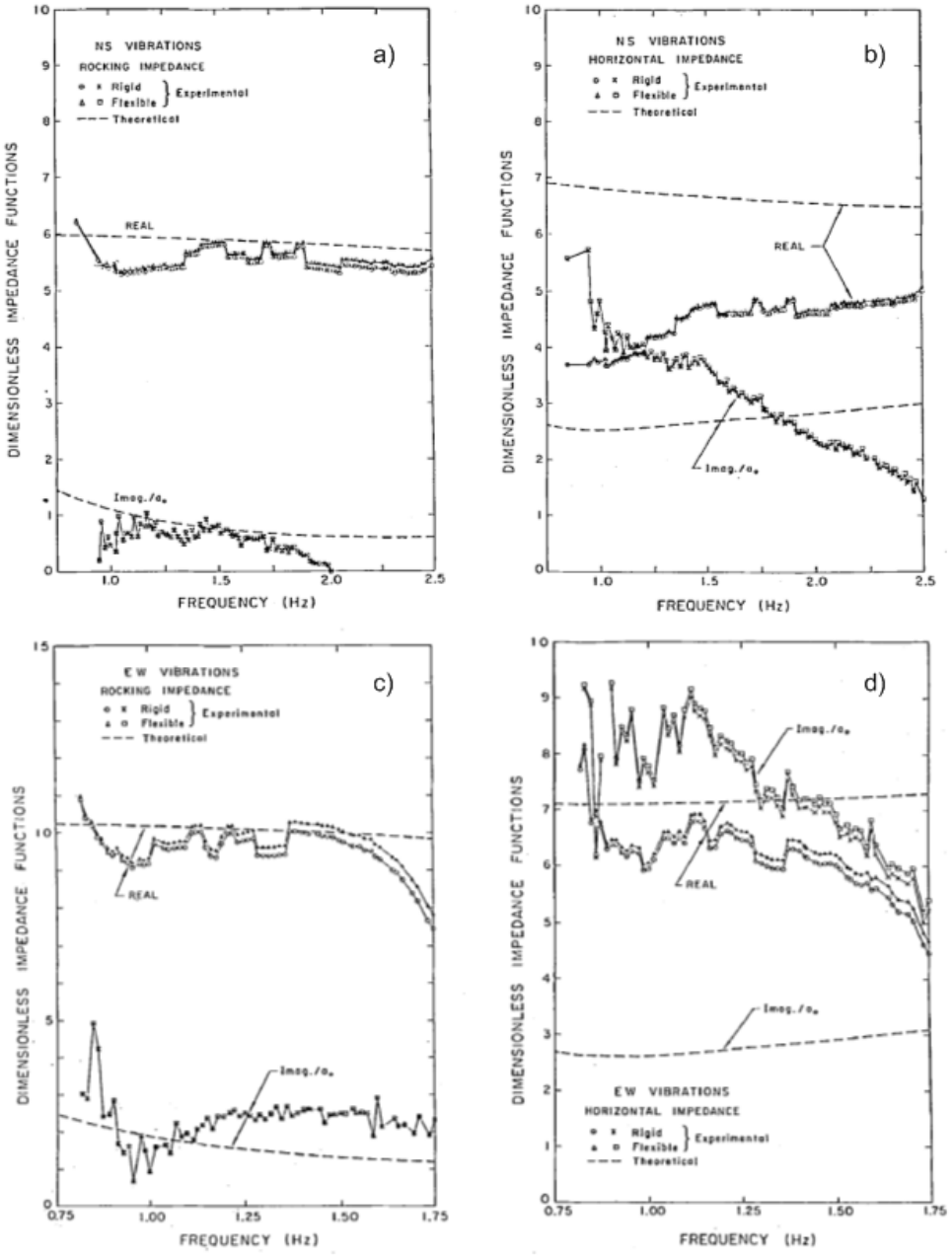

Figure 6-1 **Impedance functions derived from forced vibration testing of the Millikan Library Building (Wong et al., 1988). The figure shows the impedance functions in the north-south direction for a) rocking and b) horizontal and in the east-west for c) rocking and d) horizontal.**

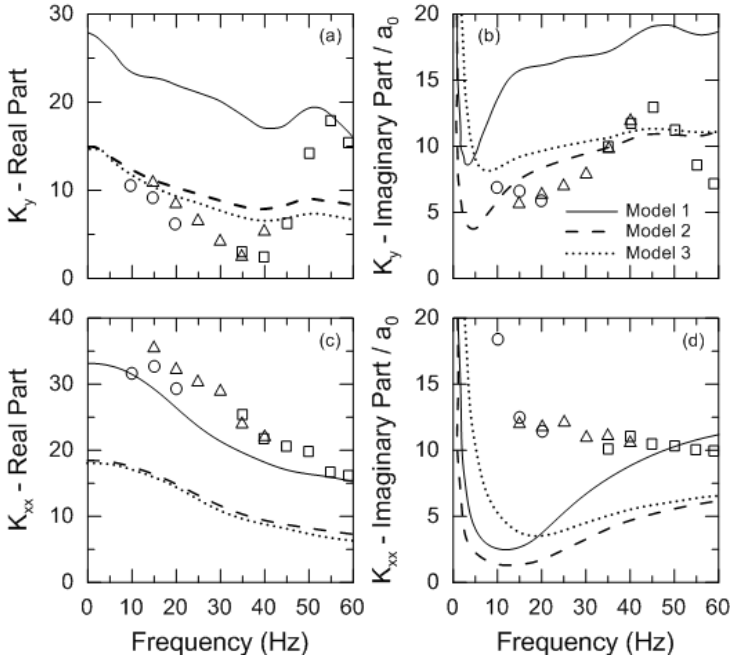

Figure 6-2 **Impedance functions for Cholame station in the horizontal (a-b) and rocking (c-d) modes of vibration. (Crouse et al., 1990).**

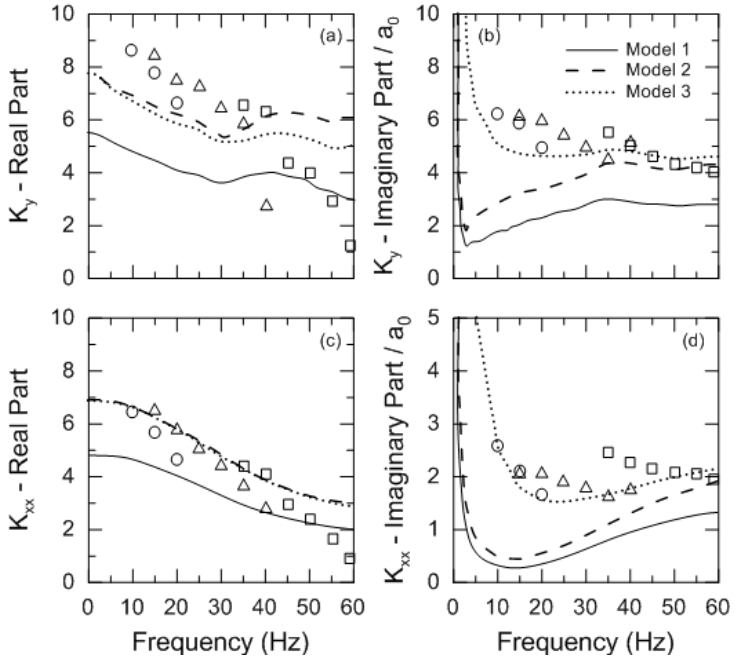

Figure 6-3 **Impedance functions for Station 6 in the horizontal (a-b) and rocking (c-d) modes of vibration. (Crouse et al., 1990).**

Further evaluation of the theoretical models was completed by forced vibration testing of the one-quarter scale Hualien containment model (de Barros and Luco, 1995). The Hualien model was constructed to evaluate the impedance functions for nuclear power plants. The Hualien model is 16.13 m (52.9 ft) tall, with a circular 10.82 m (35.5 ft) diameter foundation embedded to a depth of 5.15 m (16.9 ft). The soils at the site consist of sand and gravel that have been extensively studied by CRIEPI (Central Research Institute of Electric Power Industry, Japan) and IES (Institute of Earth Sciences, China). In an effort to validate the existing theoretical models evaluated in Crouse et al. (1990) and Luco and Wong (1990, 1992), multiple models varying the V_s based on existing conditions and structural overburden pressure were compared to the experimental impedance functions of the Hualien model. Figure 6-4 shows the impedance functions as stiffness and dashpot coefficients for the EW direction of the Hualien model. For comparison purposes, model-based impedances computed using two equivalent V_s values are also shown: 1) V_s = 317 m/s (1040 ft/s) for the soils below the foundation (neglecting structural overburden) and 2) V_s = 382 m/s (1250 ft/s) by updating Model 1 V_s by accounting for excavation and structural overburden effects. de Barros and Luco (1995) generally found the horizontal and rocking impedance functions were overpredicted. A noteworthy exception, as seen previously in Figures 6-1 through 6-3, is that the experimental rocking dashpot (or imaginary component) exceeded the theoretical models.

Impedance functions from forced vibration testing of the Dr. Evil test structure at GVDA have been previously studied by Tileylioglu et al. (2011). The details of the Dr.

Evil test structure and GVDA were described in Chapter 5. Figure 6-4 shows a normalized comparison of the experimentally derived impedance functions (as stiffness and damping ratios) and the Pais and Kausel (1988) theoretical model for rectangular foundations (Table 2-1). The test structure was in an unbraced condition and was loaded by a small linear mass shaker mounted to the bottom of the roof slab. Three suspension logging and spectral analysis of surface waves (SASW) arrays were situated adjacent to the structure and an averaged shear wave velocity of the soil was found to be V_s=198 m/s (650 ft/s), with a ± 15 m/s (50 ft/s) range. The theoretical horizontal impedance functions match well with only a slight overprediction, while the rocking damping was underpredicted.

The Mini-Me test structure discussed in Section 5.2.2 was previously situated and tested by forced vibrations at the WLA site (Star, 2011). The WLA site is maintained as part by NEES@UCSB and is composed of softer materials than GVDA. The WLA site soils are generally consistent with about a 2.5 m (0.76 ft) to 3.0 m (0.91 ft) thick layer of silty and clay underlain by a granular layer that is 3.5 m (1.07 ft) to 4.0 m (1.22 ft) thick. The granular layer is underlain by silt and clay. The forced vibration was applied with the linear mass shaker and large Mighty Mouse shaker described in Section 5.2.5. The use of the large shaker is unique in that the previous studies maintained small forces to avoid a nonlinear response of the soil. Figures 6-6 and 6-7 show the experimental results of the impedance functions (stiffness and damping ratios) compared to the theoretical Pais and Kausel (1988) model using two V_s evaluations: 1) V_s = 106 m/s (347.8 ft/s) accounting for structural overburden and 2) V_s = 98 m/s (321.7 ft/s) as determined from crosshole

seismic testing of the free-field material. Figure 6-6 shows the impedance functions produced from small forces. As with the other studies, the model tends to overpredict the stiffness slightly. Stable results for the impedance functions were found from about 4 Hz to 20 Hz. Figure 6-7 shows the influence of large forces on the impedance functions. At small frequencies the stiffness is similar to the small force tests, however as frequency increases there is a significant stiffness decrease. The softening of the stiffness is shown to correspond to the shearing of the soil and the induced nonlinearity. Figure 6-7 show the estimated soil nonlinearity for each mode of vibration. The process of estimating the soil strains and shear modulus reductions are explained in Section 6.6.2. The damping component response shows a similar underprediction to the models.

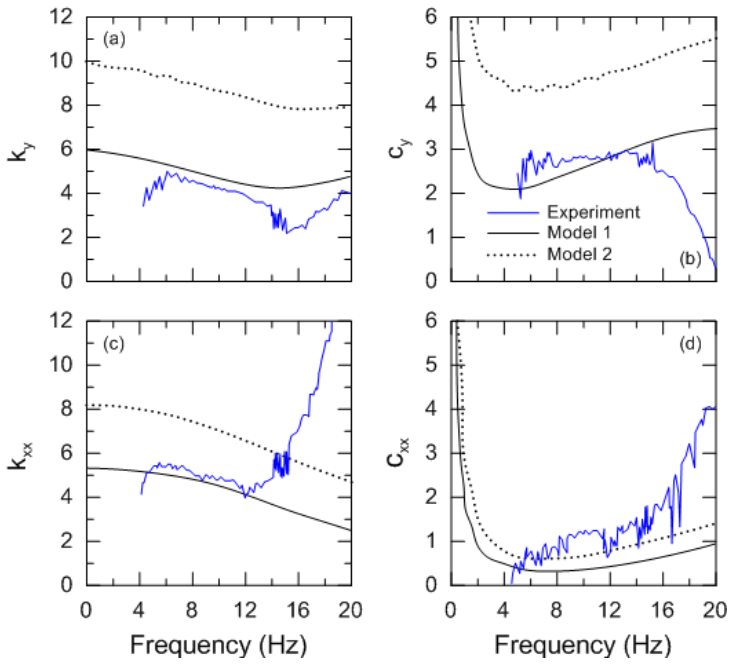

Figure 6-4 **Normalized impedance functions for Hualien containment model in the horizontal (a-b) and rocking (c-d) modes of vibration. (de Barros and Luco, 1995).**

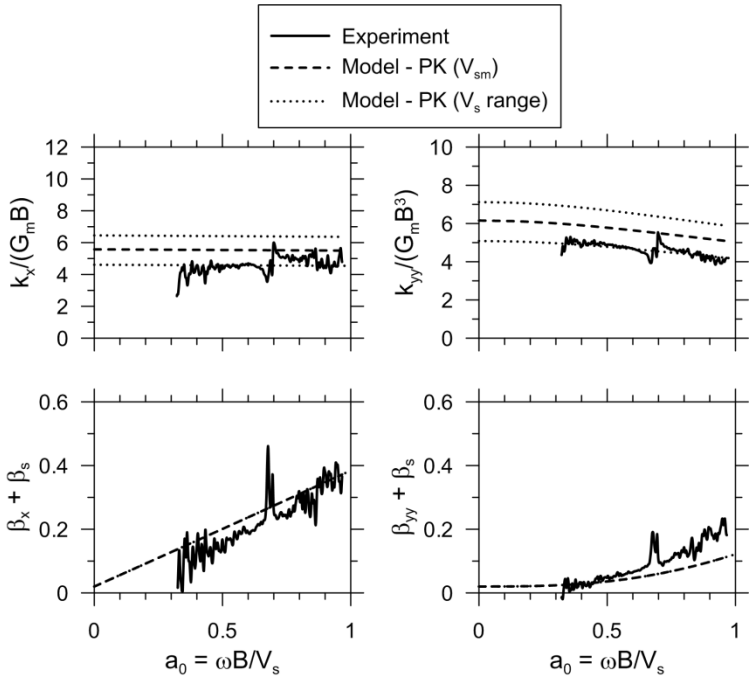

Figure 6-5 **Normalized impedance functions for testing of Dr. Evil as GVDA for horizontal (top) and rocking (bottom) modes of vibration. (Tileylioglu et al., 2011).**

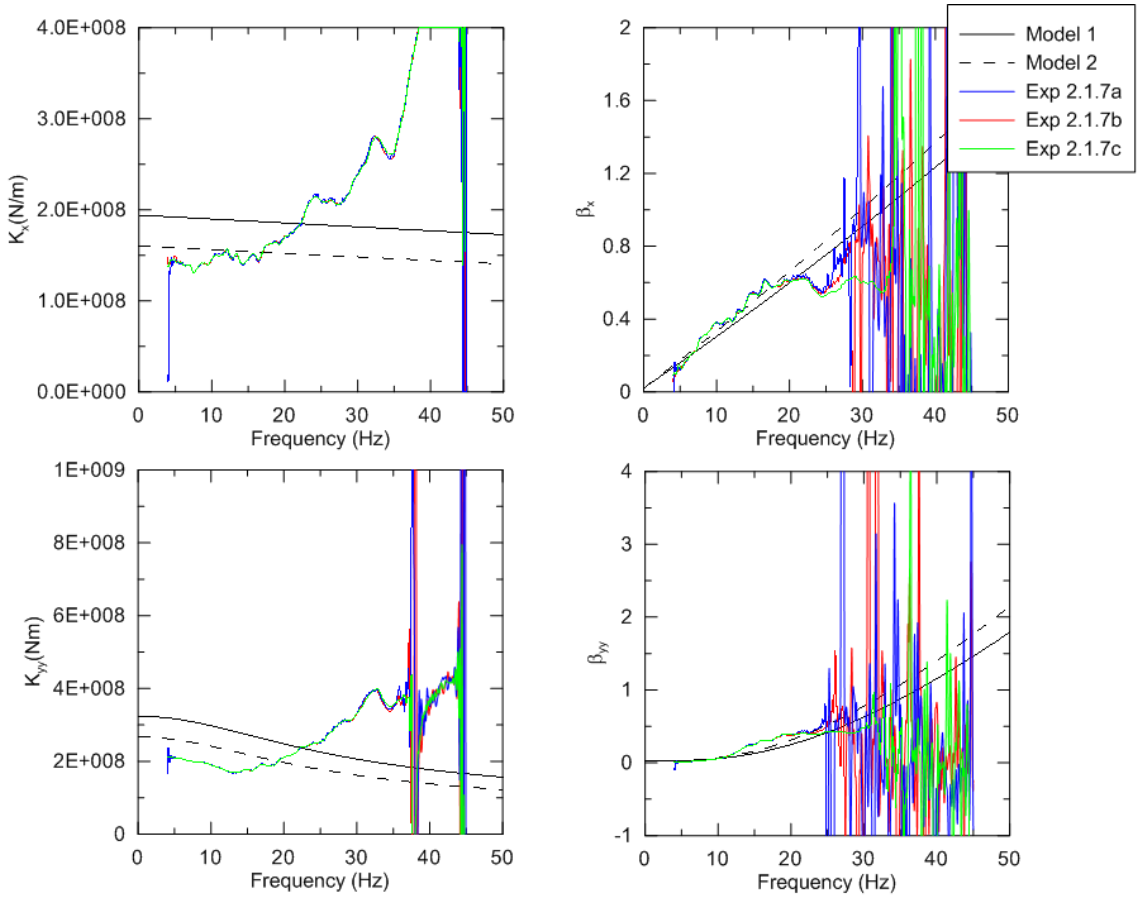

Figure 6-6 **Impedance functions for testing of Mini-Me at WLA for horizontal (top) and rocking (bottom) modes of vibration using small shaker. Exp 2.1.7 (Unbraced condition, Atom Ant shaker loading on the roof in the x-direction). (Star, 2011).**

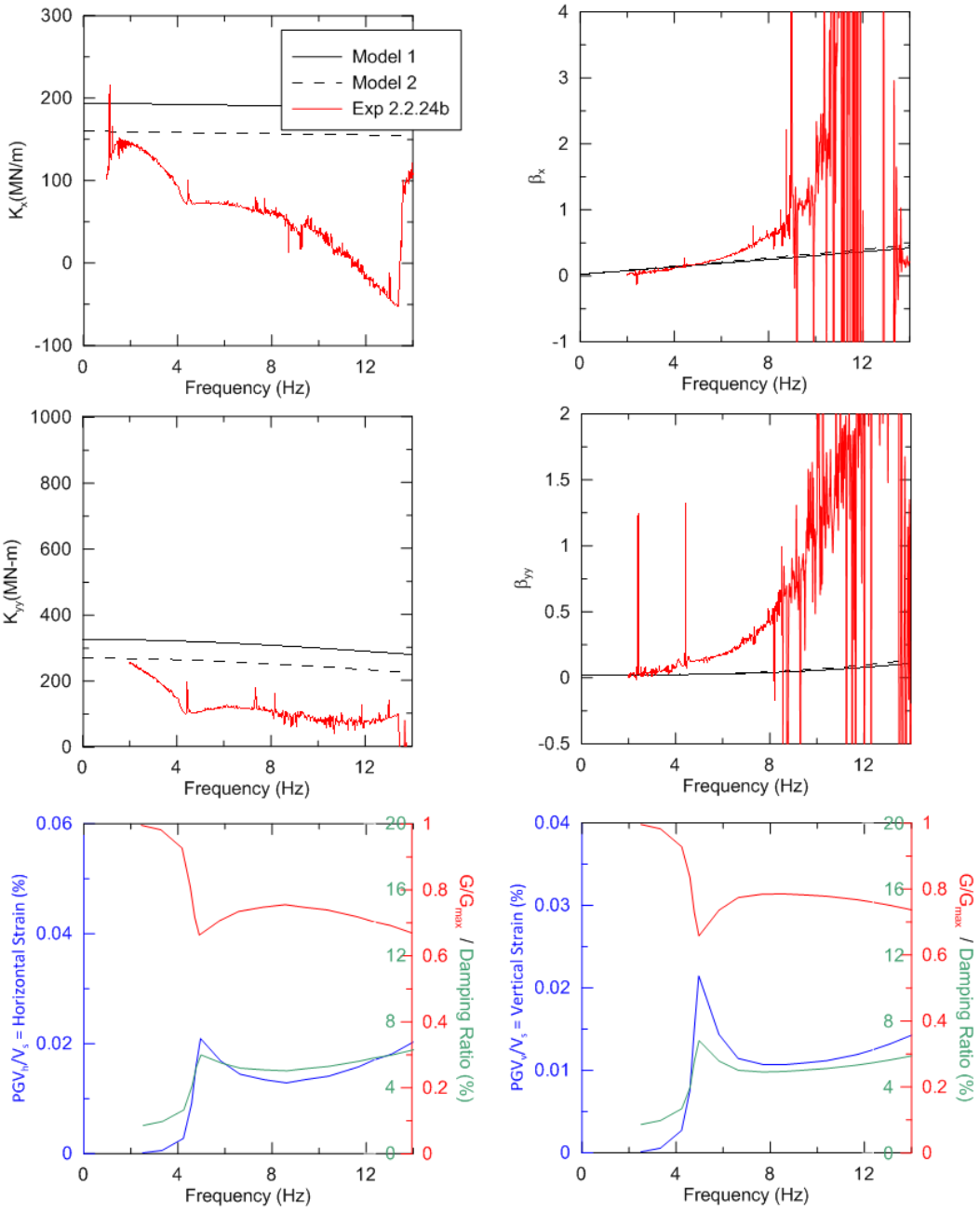

Figure 6-7 **Impedance functions for testing of Mini-Me at WLA for horizontal (top), rocking (middle) modes of vibration using a large shaker. The bottom graphic shows a representation of the soil nonlinearity during testing. Exp. 2.2.224b (Unbraced condition, Mighty Mouse shaker (100% ecc.) loading on the roof in the y-direction). (Star, 2011).**

6.3 Inversion Procedures for Evaluation of Impedance Ordinates from Forced Vibration Test Data

Several procedures have been presented for evaluating impedance functions from forced vibration testing of structures (Tileylioglu et al, 2011, de Barros and Luco, 1995, Crouse et al, 1990, etc.). This study uses the Tileylioglu et al (2011) approach, in which an above-ground single degree-of-freedom (SDOF) system was modeled to represent our field test structure. The SDOF system shown in Figure 6-8 represents the soil-foundation-structure system being excited by a shaker force (F_{shaker}).

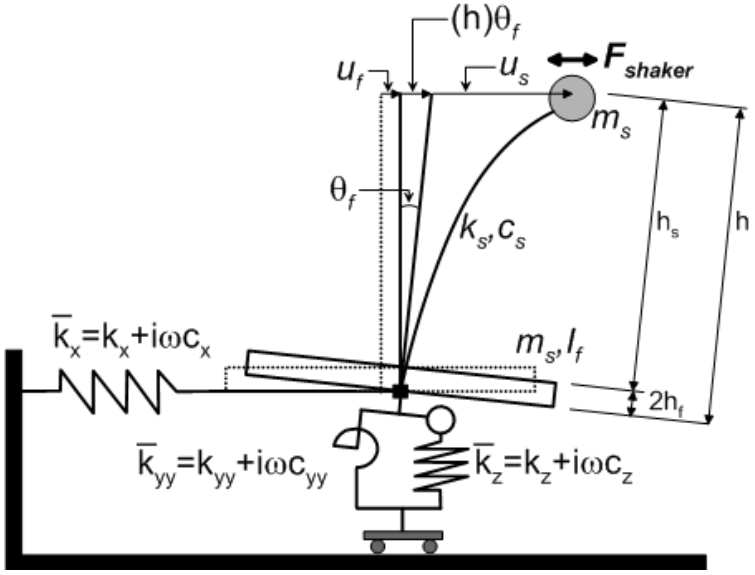

Figure 6-8 **Sketch showing the soil-structure interaction system used for determination of impedance functions from forced vibration testing based on Tileylioglu et al (2011).**

The Tileylioglu et al (2011) type model in Figure 6-8 shows the inclusion of the frequency-dependent impedance functions for horizontal translation ($\bar{k}_x$), vertical translation ($\bar{k}_z$) and rotation ($\bar{k}_{yy}$) where the overbar (-) represents a complex value. It

should be noted that the subscript notation assumes excitation in the *x*-*z* plane, however, excitation in the *y*-*z* plane can also be represented by reversing the *x* and *y* subscripts. Analysis of the impedance functions requires measurement of the foundation translation (u_f) and rotation (θ_f). The total roof displacement is:

$$u_{roof} = u_f + h\theta_f + u_s \tag{6-1}$$

Where h is the height of the center of the structural mass (m_s) for the SDOF, and u_s is the displacement of the top mass associated with the structural compliance as represented by structural stiffness (k_s) and damping (c_s) coefficients. The equation of motion for the system in Eq. (6-2) can be written as (Clough and Penzien, 1993):

$$M\ddot{U} + C\dot{U} + KU = F \tag{6-2}$$

where U represents the horizontal displacements and rotations of each degree of freedom: $U = [u_f \quad \theta_f \quad u_s]^T$. The vertical foundation and rotational superstructure displacements were not included for the horizontal response. The mass (M), dashpot (C) and stiffness (K) matrices given by Tileylioglu et al (2011) and Crouse et al. (2001) are:

$$M = \begin{pmatrix} m_f + m_s & m_f h_f + m_s h & m_s \\ m_f h_f + m_s h & I_f + m_f {h_f}^2 + m_s h^2 & m_s h \\ m_s & m_s h & m_s \end{pmatrix} \tag{6-3}$$

$$K = \begin{pmatrix} k_x & k_{yx} & 0 \\ k_{yx} & k_{yy} & 0 \\ 0 & 0 & k_s \end{pmatrix} \tag{6-4}$$

$$C = \begin{pmatrix} c_x & c_{yx} & 0 \\ c_{yx} & c_{yy} & 0 \\ 0 & 0 & c_s \end{pmatrix} \tag{6-5}$$

where m_f is the foundation mass, m_s is the superstructure mass, I_f is the mass moment of inertia about the foundation, h_f is the height of the foundation, and the subscripts *x*, *y*, *xy* and *yx* represent the modes of vibration. As discussed before, the notation for excitation in the *x*-*z* plane is shown with *x* representing vibration in the horizontal *x*-direction, *yy* representing rotation about the y-axis and *xy,* and *yx* representing coupling terms between the off-diagonal soil impedance terms. These coupling terms have been taken as zero for this study because the foundations are not embedded.

The aforementioned SDOF system equations can be divided into three distinct equations representing the foundation translation (Eq. 6-6), foundation rotation (Eq. 6-7) and structural translation (Eq. 6-8).

$$m_s(\ddot{u}_f + h\ddot{\theta}_f + \ddot{u}_s) + m_f(\ddot{u}_f + h_f\ddot{\theta}_f) + c_x\dot{u}_f + k_x u_f = F_s \tag{6-6}$$

$$m_s h(\ddot{u}_f + h\ddot{\theta}_f + \ddot{u}_s) + I_f\ddot{\theta}_f + m_f h_f(\ddot{u}_f + h_f\ddot{\theta}_f) + c_{yy}\dot{\theta}_f + k_{yy}\theta_f = hF_s \tag{6-7}$$

$$m_s(\ddot{u}_f + h\ddot{\theta}_f + \ddot{u}_s) + c_s\dot{u}_s + k_s u_s = F_s \tag{6-8}$$

The unknown impedance functions are contained in Eqs. (6-6) and (6-7). Through transformation to the frequency domain and presenting those equations as displacements, the foundation translation and rotation can be written as Eqs (6-9) and (6-10), respectively:

$$-\omega^2 m_s(\hat{u}_f + h\hat{\theta}_f + \hat{u}_s) - \omega^2 m_f(\hat{u}_f + h_f\hat{\theta}_f) + i\omega c_x\hat{u}_f + k_x\hat{u}_f = \hat{F}_s \tag{6-9}$$

$$-\omega^2 m_s h(\hat{u}_f + h\hat{\theta}_f + \hat{u}_s) - \omega^2 I_f \hat{\theta}_f - \omega^2 m_f h_f (\hat{u}_f + h_f \hat{\theta}_f) + i\omega c_{yy}\hat{\theta}_f + k_{yy}\hat{\theta}_f = h\hat{F}_s \quad (6\text{-}10)$$

where the hat symbol (^) represents a frequency domain variable. Recalling the definition of the impedance function from Eq. (2-3), then Eqs. (6-9a) and (6-10b) can be rewritten as:

$$-\omega^2 m_s (\hat{u}_f + h\hat{\theta}_f + \hat{u}_s) - \omega^2 m_f (\hat{u}_f + h_f \hat{\theta}_f) + \bar{k}_x \hat{u}_f = \hat{F}_s \quad (6\text{-}11)$$

$$-\omega^2 m_s h(\hat{u}_f + h\hat{\theta}_f + \hat{u}_s) - \omega^2 I_f \hat{\theta}_f - \omega^2 m_f h_f (\hat{u}_f + h_f \hat{\theta}_f) + \bar{k}_{yy}\hat{\theta}_f = h\hat{F}_s \quad (6\text{-}12)$$

Eqs. (6-11) and (6-12) can now be rearranged and expressed as a definition of the impedance functions as:

$$\hat{\bar{k}}_x = \frac{\hat{F}_s + \omega^2 m_s (\hat{u}_f + h\hat{\theta}_f + \hat{u}_s) + \omega^2 m_f (\hat{u}_f + h_f \hat{\theta}_f)}{\hat{u}_f} \quad (6\text{-}13)$$

$$\hat{\bar{k}}_{yy} = \frac{h\hat{F}_s + \omega^2 m_s h(\hat{u}_f + h\hat{\theta}_f + \hat{u}_s) + \omega^2 I_f \hat{\theta}_f + \omega^2 m_f h_f (\hat{u}_f + h_f \hat{\theta}_f)}{\hat{\theta}_f} \quad (6\text{-}14)$$

Eqs. (6-13) and (6-14) represent the complex-valued impedance functions for the modes of translation and rotation, respectively. As shown in Chapter 2, Eq. (2-5), a damping ratio (β_j) can be derived for each mode based on the real and imaginary parts of the complex-valued impedance function. Eq. (2-8) can be expressed using the complex-valued impedance as Eq. (6-15).

$$\beta_j = \frac{imag(\hat{\bar{k}}_j)}{2 * real(\hat{\bar{k}}_j)} \quad (6\text{-}15)$$

6.4 Forced Vibration and Inertial Responses of Test Structure at GVDA

Prior to analysis of the impedance functions, the input acceleration histories used in the evaluation of the translational impedance (Eq. 6-13) and rotational impedance (Eq. 6-14) are reviewed. The structural response histories used for the response characteristics have been described in Section 5.4. This section will present the frequency-domain structural response, forcing function and structural inertia components for the small, moderate, and large amplitude force cases presented in Figure 5-14. Each force-response figure is followed by load-deformation loops for the base shear versus horizontal displacement and foundation moment versus rotation at varying frequencies. The loops are diagnostic of the stiffness and damping produced from the forced vibration frequencies. For comparison of the accelerations in the force-response figures, the rocking and torsion responses are presented as linear acceleration quantities. The linear quantities are calculated by multiplying the rotation of the rocking by the height (h) and the torsion by the distance between accelerometers (L') where the subscripts represent the accelerometer distance on the roof (r) and foundation (f).. The forces (F) are described using subscript 's' for superstructure, 'f' for foundation and secondary subscript to indicate translation (y) or rocking (xx) mode of vibration.

The small amplitude forces and responses are shown in Figure 6-9. The shaker force is the predominant force at small (4-7 Hz) and high (>13 Hz) frequencies, while the translational inertia dominates around the resonant frequency. The foundation inertial rocking component is greater than the translational foundation inertia. As expected, the responses are greatest near the resonant frequency of the structure with the exception of

the torsional response. The torsion of the structure and foundation occur after the resonance frequency is reached at about 17 Hz. It is noteworthy that the horizontal forces produced from rocking are similar in trend and amplitude with the translational responses. The loops in Figure 6-10 show a fairly consistent inclination across the frequencies. This consistency indicates that the stiffness for both translation and rotation are frequency-independent for the small force amplitude testing. However the loops are not very smooth at small forces and might be presenting artificial results.

The moderate amplitude forces and responses are shown in Figure 6-11. The shaker force becomes larger as frequency increases. The foundation and structural inertia forces are relatively consistent from 5-12 Hz, with the dominant force of inertia is roof translation associated with the foundation rotation. The greatest response was the horizontal acceleration of the roof from the foundation rocking. The rocking response was about twice as large as the horizontal structural response, which is the next dominant response. There was a small amount of torsion displayed after the resonant frequency. The loops in Figure 6-12 show that the loops' inclination changes with frequency. This change shows a frequency-dependency of the stiffness for both translation and rotation during medium amplitude testing, unlike the case for the small amplitude testing. The loops for the medium forcing test are found to be smoother than the small forcing test due to the increase loading and deformations.

The medium amplitude forces and responses are shown in Figure 6-11. The shaker force becomes larger as frequency increases. The foundation and structural inertia forces are show a distinctive peak around 8 Hz and then the structural inertia force

follows a similar trend as the shaker force. The greatest responses are the horizontal acceleration of the roof from the foundation rocking and the horizontal structural response. These responses follow a similar amplitude and trend. There is significantly more torsion compared to the small amplitude tests, where a distinctive peak is observed at 16 Hz. The loops in Figure 6-12 show that the loops' inclination changes with frequency. This change shows a frequency-dependency of the stiffness for both translation and rotation during medium amplitude testing. The loops for the medium forcing test are found to be smoother than the small forcing test due to the increase loading and deformations.

The large amplitude forces and responses are shown in Figure 6-13. The shaker force becomes larger as frequency increases. The foundation and structural inertia forces are relatively consistent from 5-12 Hz, with the dominant force of inertia is roof translation associated with the foundation rotation. The greatest response was the horizontal acceleration of the roof from the foundation rocking. The rocking response was about twice as large as the horizontal structural response, which is the next dominant response. There was a small amount of torsion displayed after the resonant frequency. The loops in Figure 6-14 show that the loops' inclination changes with frequency. This change shows a frequency-dependency of the stiffness for both translation and rotation during large amplitude testing, similar to the observed load-deformation of the medium amplitude testing.

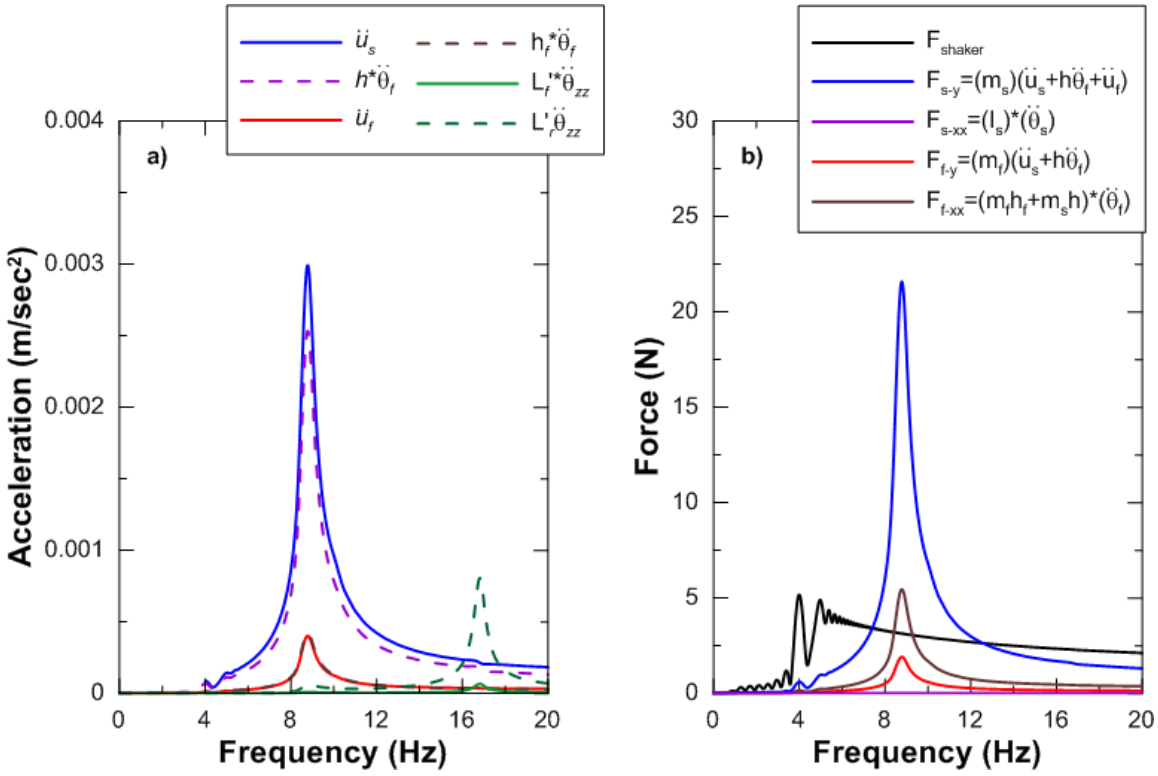

Figure 6-9 **Frequency domain presentation of the a) responses and b) force components of Exp. 3.3.5a (Unbraced condition, Atom Ant shaker loading on the roof in the y-direction). Refer to Figure 6-8 for definitions.**

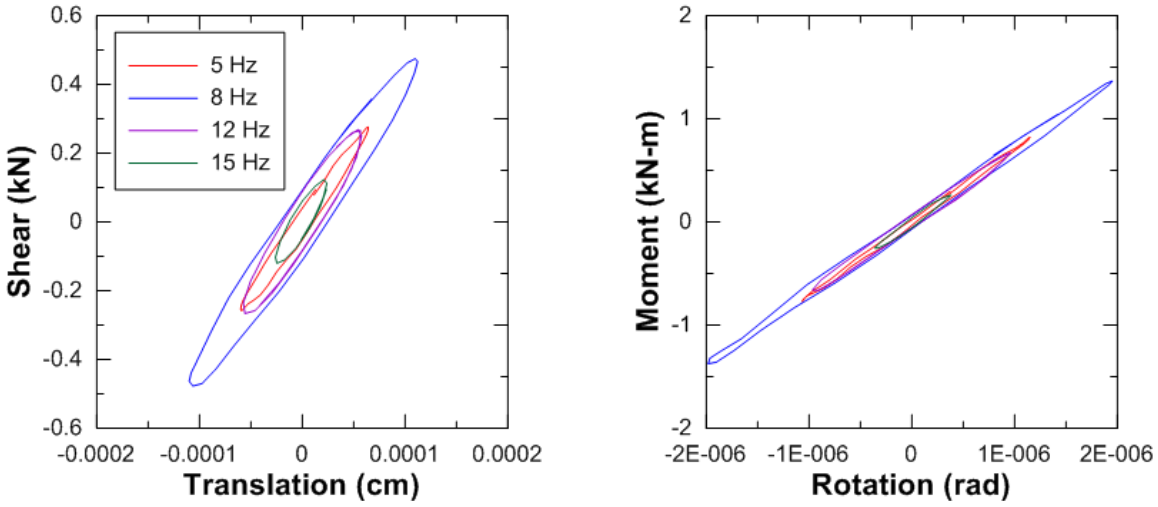

Figure 6-10 **Response correlation of the shear versus translation and moment versus rotation of Exp. 3.3.5a (Unbraced condition, Atom Ant shaker loading on the roof in the y-direction).**

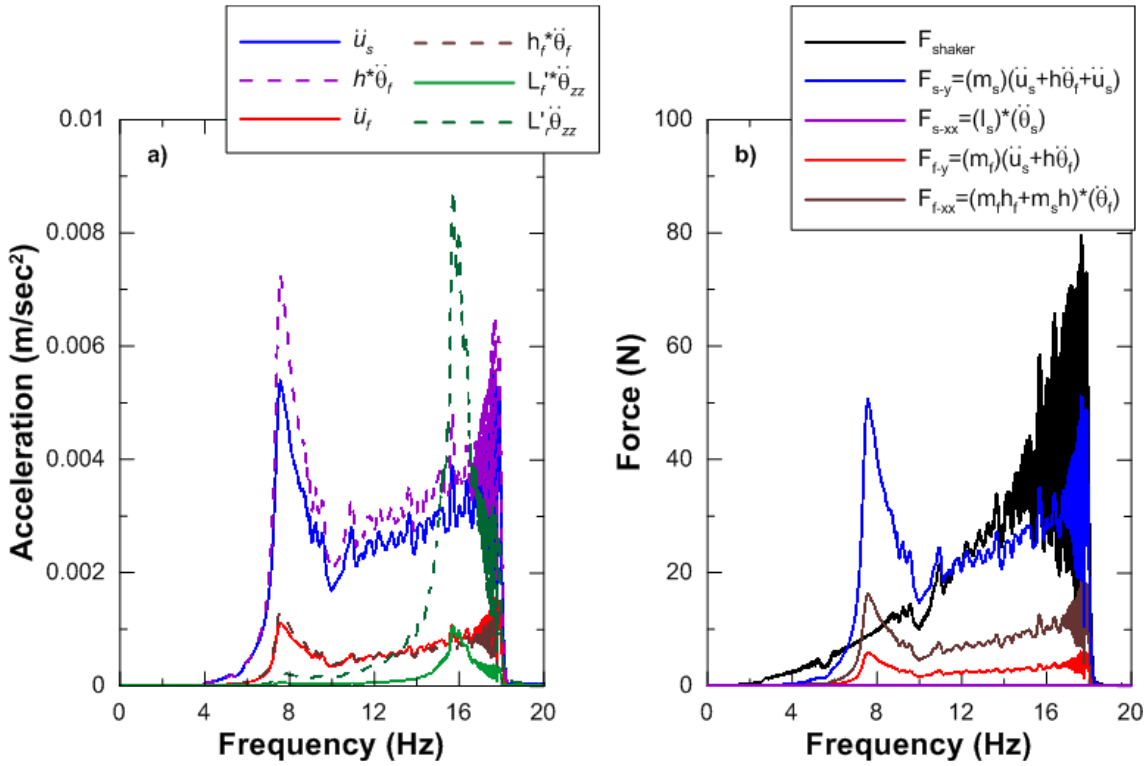

Figure 6-11 **Frequency domain presentation of the a) responses and b) force components of Exp. 3.4.1a (Unbraced condition, Mighty Mouse shaker (5% ecc.) loading on the roof in the y-direction). Refer to Figure 6-8 for definitions.**

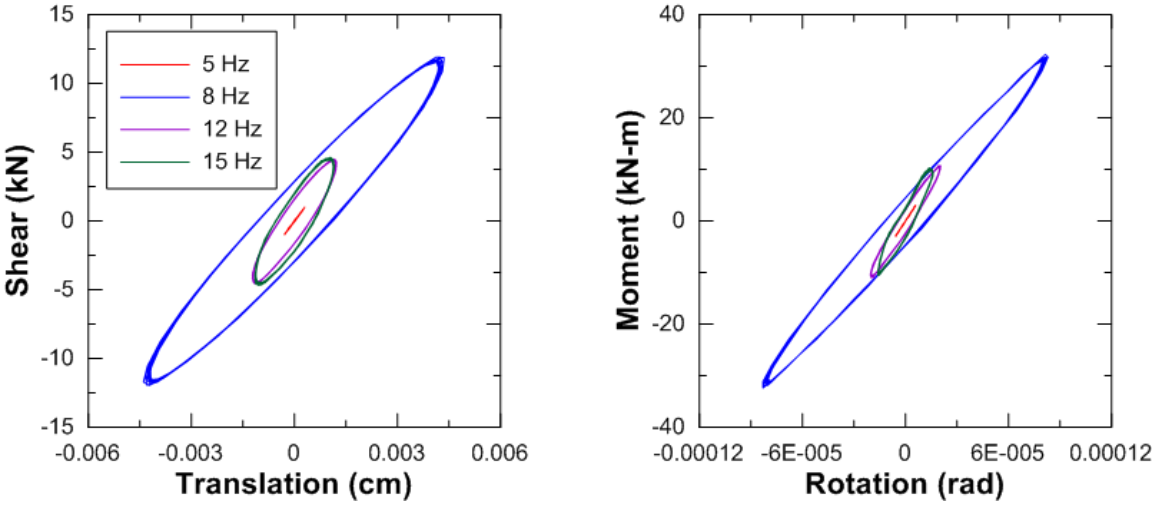

Figure 6-12 **Response correlation of the shear versus translation and moment versus rotation of Exp. 3.4.1a (Unbraced condition, Mighty Mouse shaker (5% ecc.) loading on the roof in the y-direction).**

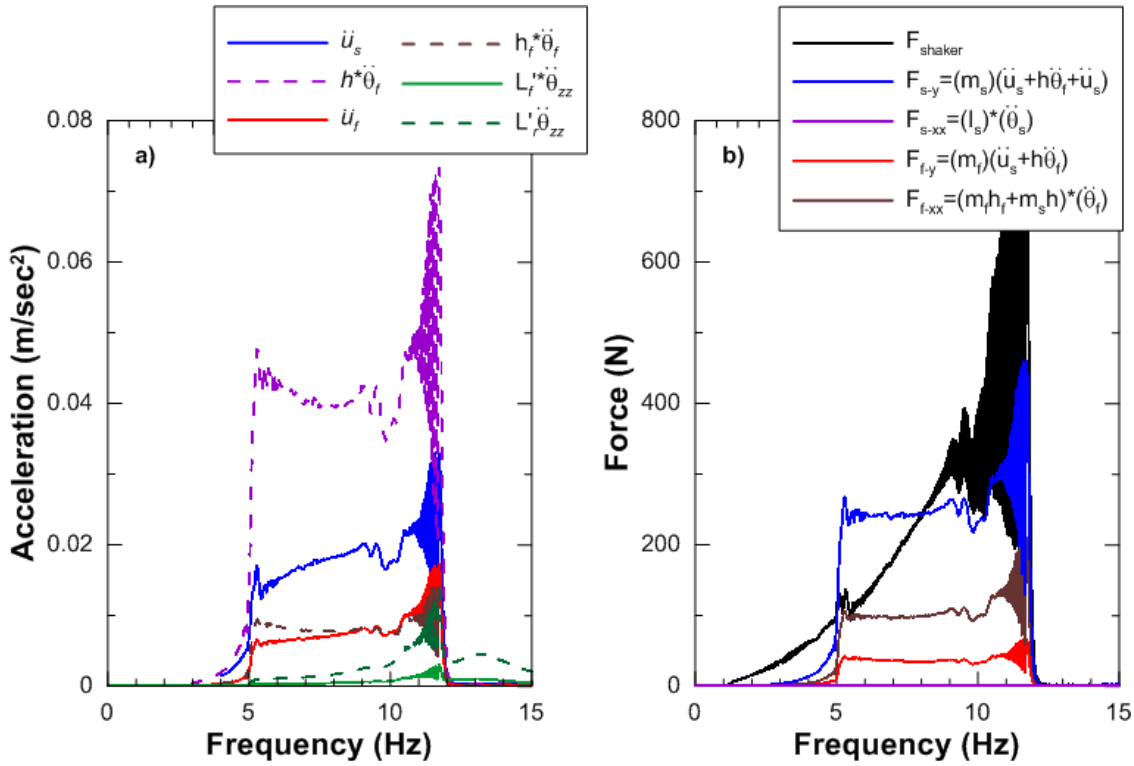

Figure 6-13 **Frequency domain presentation of the a) responses and b) force components of Exp. 3.4.19a (Unbraced condition, Mighty Mouse shaker (100% ecc.) loading on the roof in the y-direction). Refer to Figure 6-8 for definitions.**

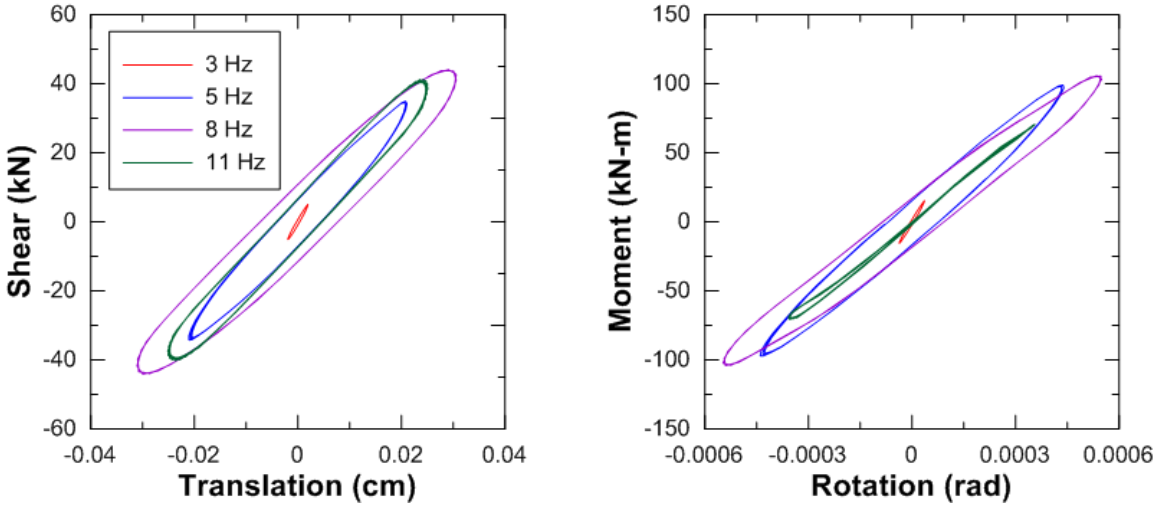

Figure 6-14 **Response correlation of the shear versus translation and moment versus rotation of Exp. 3.4.19a (Unbraced condition, Mighty Mouse shaker (100% ecc.) loading on the roof in the y-direction).**

6.5 Impedance Functions from Forced Vibration Testing

As discussed in Chapter 5, two shakers were used to apply harmonic loads to Mini-Me. A linear mass shaker was used to produce small-amplitude forces for which shear stresses and shear strains would be expected to be in the linear-elastic range. An eccentric mass shaker was used to produce relatively large-amplitude forces, for which nonlinear response of the foundation soils is expected.

Within this section, foundation stiffness and damping inferred from test data are compared to predictions from the impedance function model of Pais and Kausel (1988) (Tables 2-1 and 2-2). Two representations of the subsurface soil conditions were developed based on the V_s profiles discussed in Section 5.2.1: "Model 1" refers to the use of V_s = 193.5 m/s, which was directly measured from crosshole testing with the weight of the structure acting on the soil; "Model 2" refers to the use V_{s0} = 175.5 m/s (575.8 ft/s), which represents equivalent free-field velocities back-calculated using Eq. (5-2) with a site-specific *n*-value (free-field velocities were not directly measured).

6.5.1 Small Amplitude Forced Vibration Testing

The small amplitude forced vibration testing consisted of shaking Mini-Me in both the braced and unbraced stiffness conditions. Experimental impedance functions for a) translation and b) rotation were back-calculated using the Tileylioglu et al. (2011) and Crouse et al. (2001) method (Eqs. 6-15 and 6-16). The structural response acceleration histories and shaker force were used as input parameters. The force history was determined by multiplying the shaker mass (19.2 kg) by its acceleration history. When the force was applied at the roof the shaker was secured in place with rope, whereas no

restraint was applied when the shaker was mounted on the foundation slab (see Figure 6-15).

Figures 6-16 through 6-23 show the experimentally derived impedance functions for the SSI system. Frequency smoothing was applied using three passes of an 11-point hamming window based on methods described by Mikami et al. (2008). Repetitions of each test (shaking direction and location) were processed and are shown in Figures 6-15 through 6-18. The experiment numbers associated with each figure can be referenced to the testing details in Chapter 5 (Tables 5-3 and 5-5). A discussion about the interpretation of the data is in Section 6.9.1.

Figure 6-15 **Photographs showing the Atom Ant shaker on the left, secured in-place with rope during forcing tests at the roof slab and on the right free-standing during forcing test at the foundation slab.**

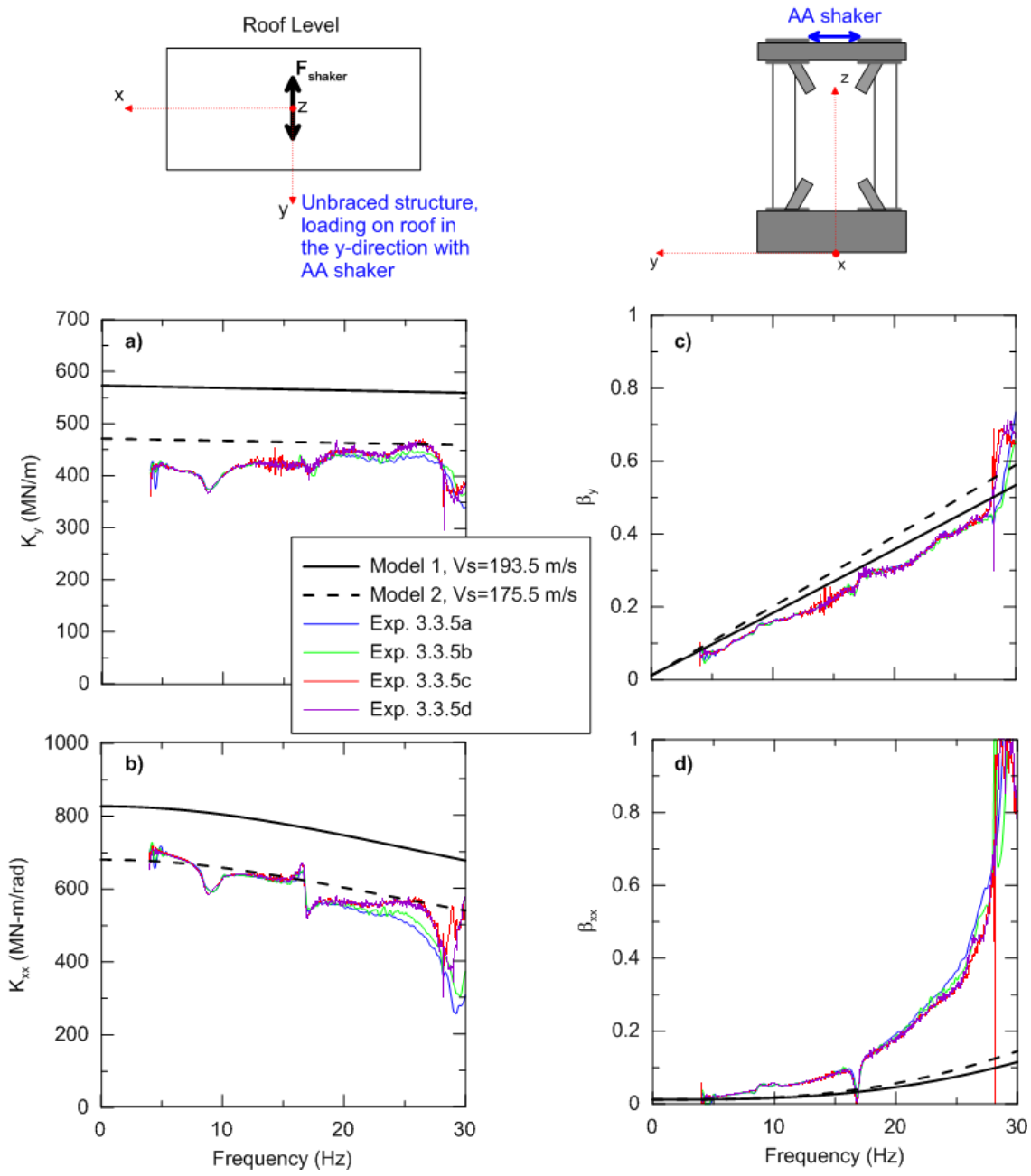

Figure 6-16 **Inverted impedance function results from analysis of Exp. 3.3.5 (Unbraced condition, Atom Ant shaker loading on the roof in the y-direction). The plots show a) the translation stiffness, b) rocking stiffness, c) translation damping ratio, and d) rocking damping ratio of the SSI system in the direction of loading.**

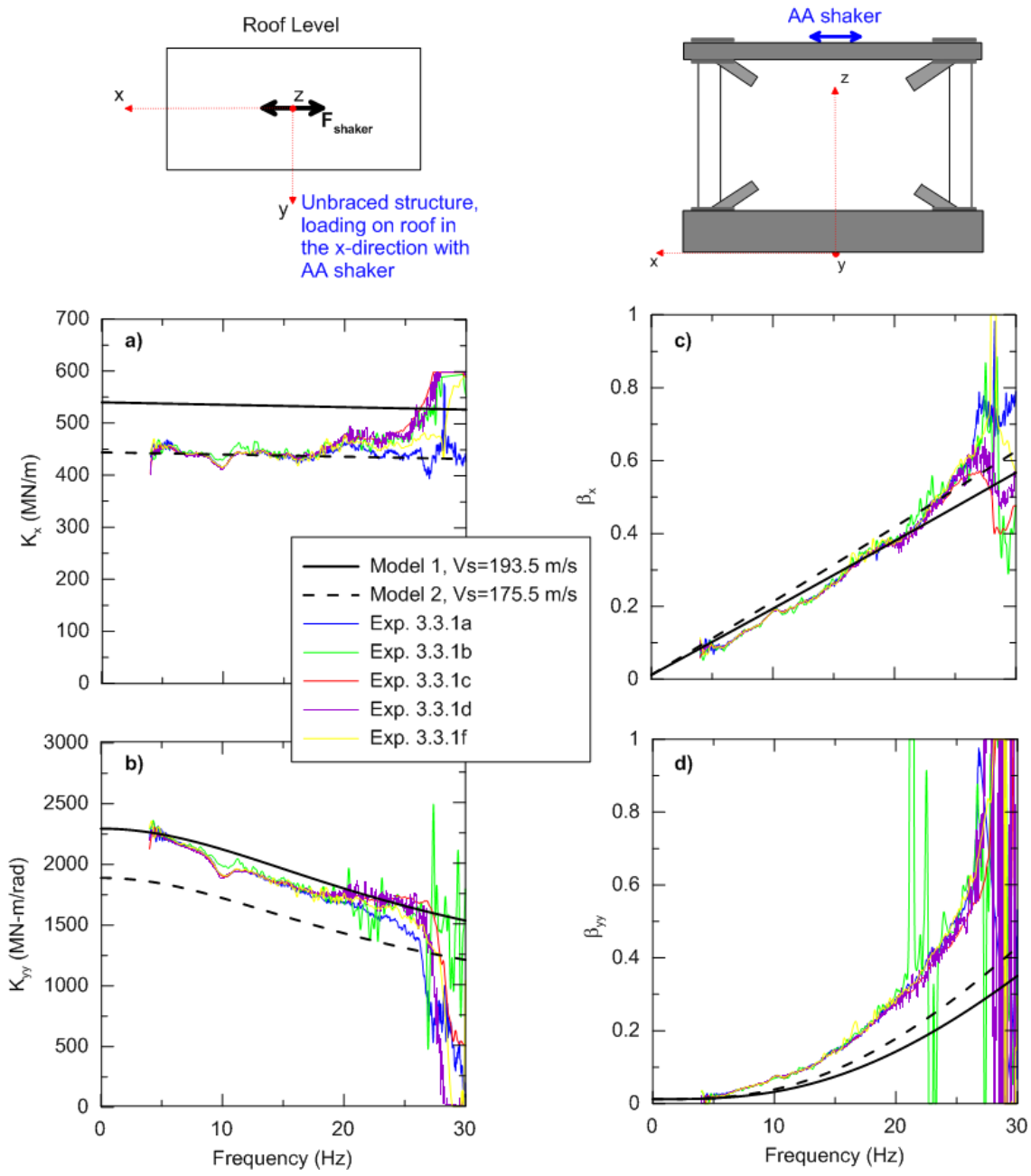

Figure 6-17 **Inverted impedance function results from analysis of Exp. 3.3.1 (Unbraced condition, Atom Ant shaker loading on the roof in the x-direction). The plots show a) the translation stiffness, b) rocking stiffness, c) translation damping ratio, and d) rocking damping ratio of the SSI system in the direction of loading.**

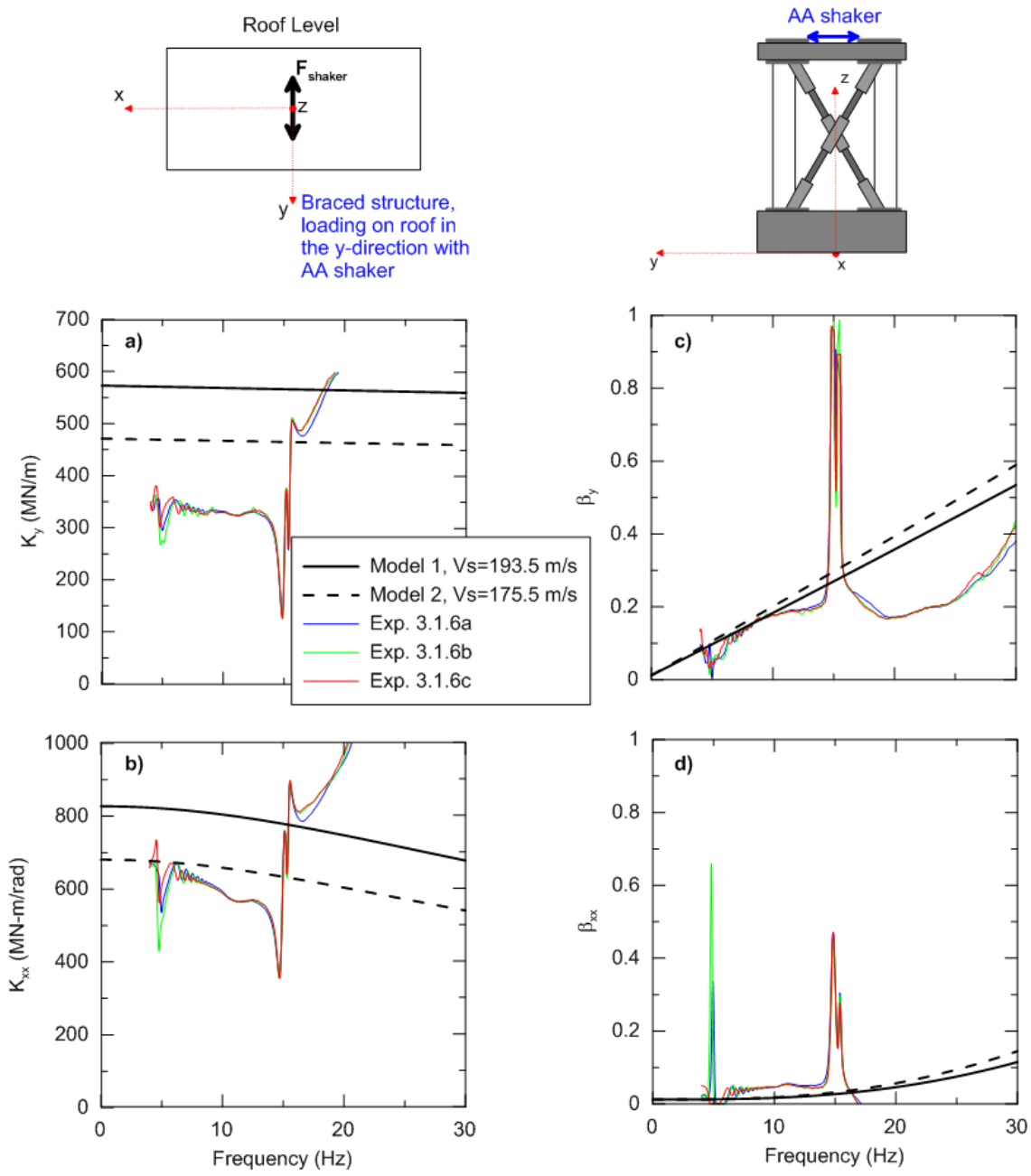

Figure 6-18 **Inverted impedance function results from analysis of Exp. 3.1.6 (Braced condition, Atom Ant shaker loading on the roof in the y-direction). The plots show a) the translation stiffness, b) rocking stiffness, c) translation damping ratio, and d) rocking damping ratio of the SSI system in the direction of loading.**

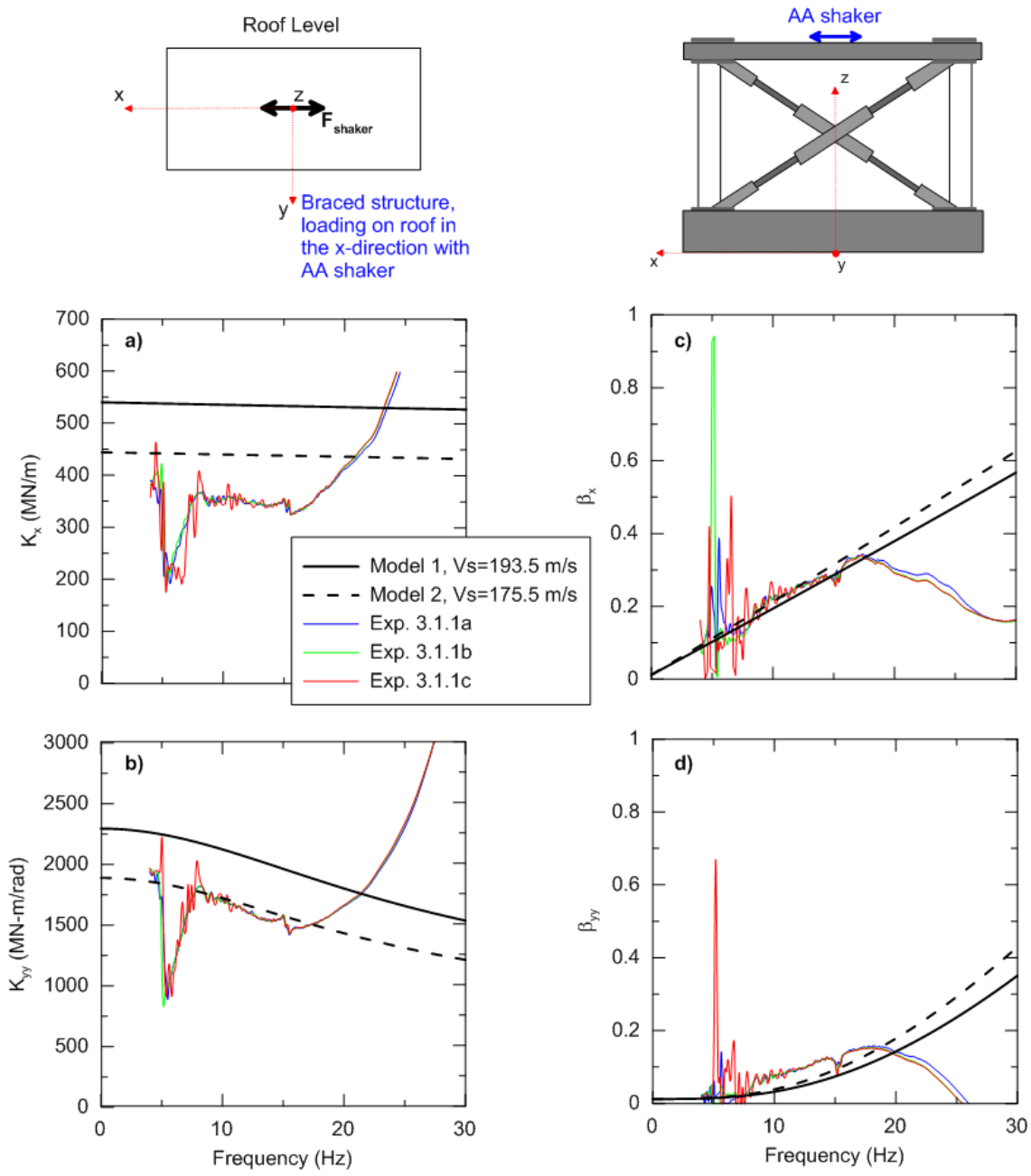

Figure 6-19 **Inverted impedance function results from analysis of Exp. 3.1.1 (Braced condition, Atom Ant shaker loading on the roof in the x-direction). The plots show a) the translation stiffness, b) rocking stiffness, c) translation damping ratio, and d) rocking damping ratio of the SSI system in the direction of loading.**

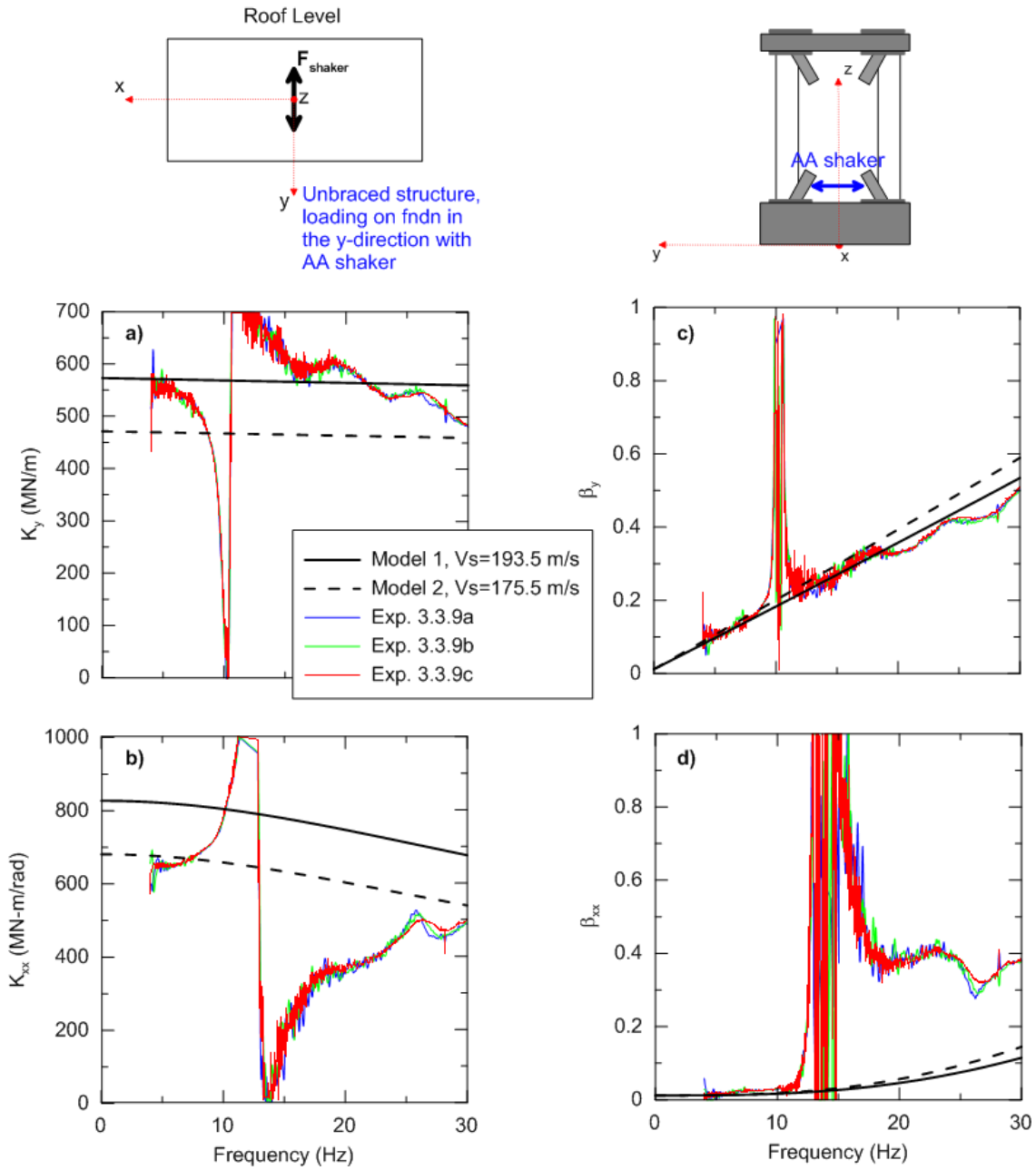

Figure 6-20 **Inverted impedance function results from analysis of Exp. 3.3.9 (Unbraced condition, Atom Ant shaker loading on the foundation in the y-direction). The plots show a) the translation stiffness, b) rocking stiffness, c) translation damping ratio, and d) rocking damping ratio of the SSI system in the direction of loading. Note: the shaker was not externally mounted to the structure.**

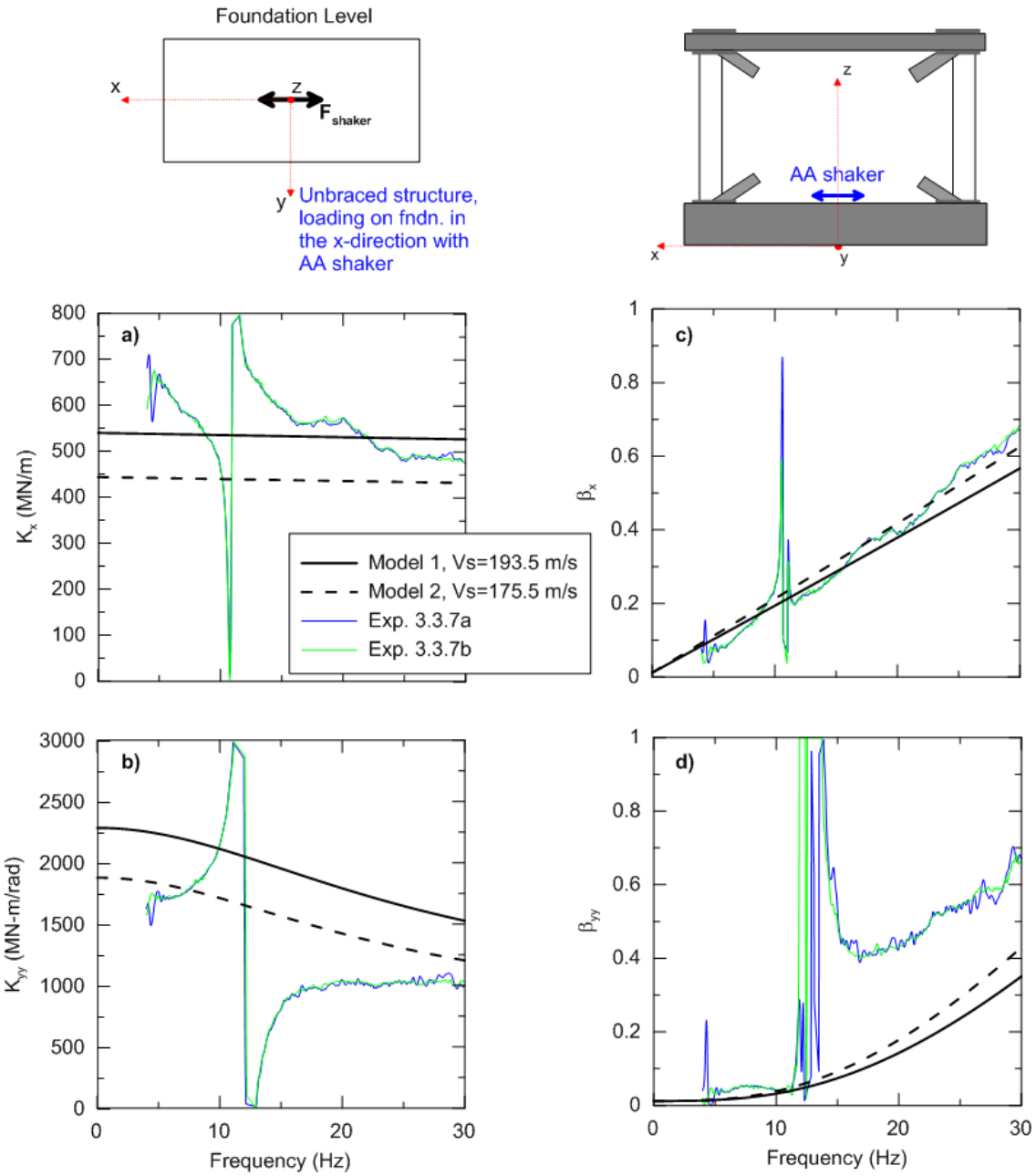

Figure 6-21 **Inverted impedance function results from analysis of Exp. 3.3.7 (Unbraced condition, Atom Ant shaker loading on the foundation in the x-direction). The plots show a) the translation stiffness, b) rocking stiffness, c) translation damping ratio, and d) rocking damping ratio of the SSI system in the direction of loading. Note: the shaker was not externally mounted to the structure.**

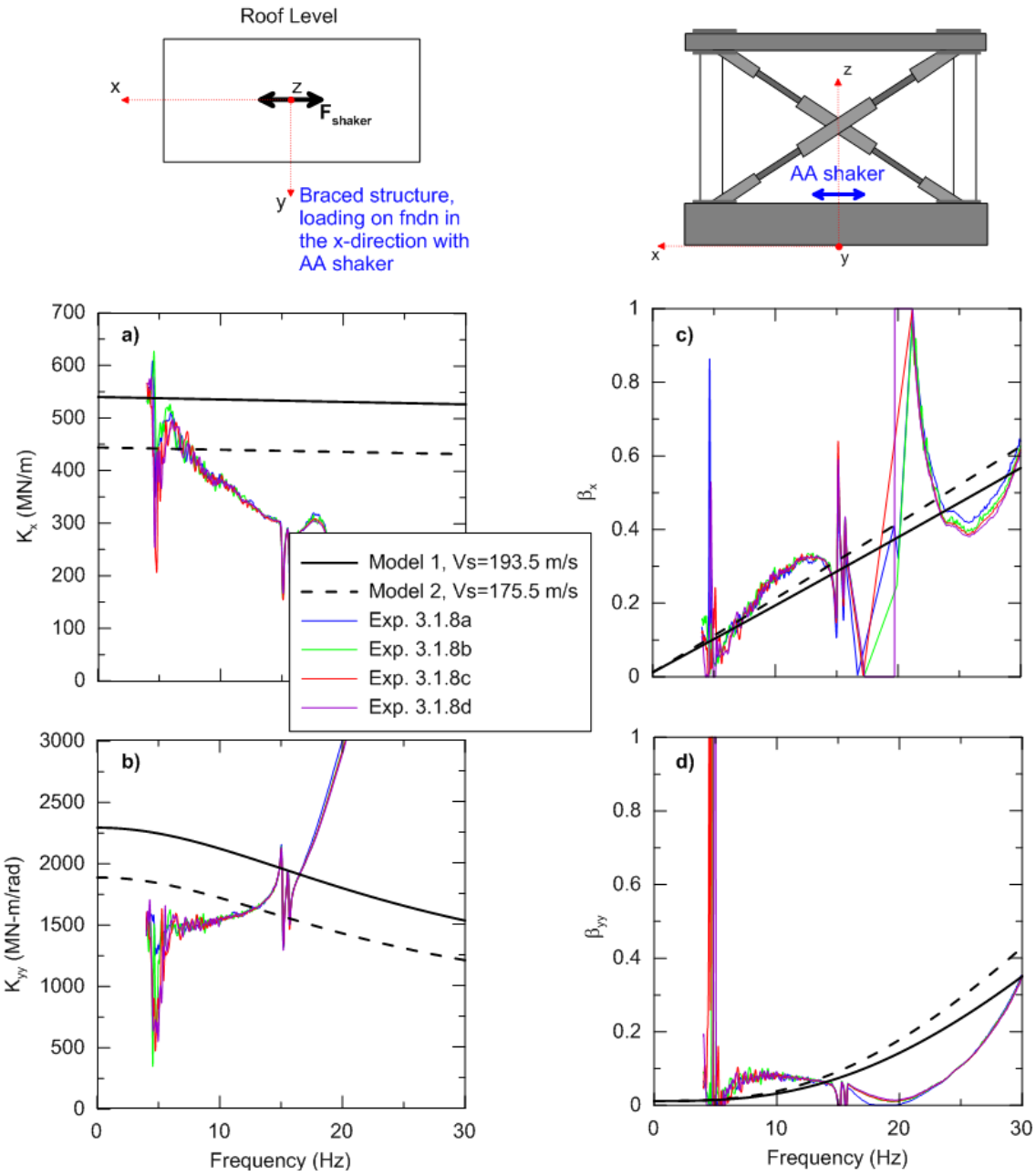

Figure 6-22 **Inverted impedance function results from analysis of Exp. 3.1.8 (Braced condition, Atom Ant shaker loading on the foundation in the x-direction). The plots show a) the translation stiffness, b) rocking stiffness, c) translation damping ratio, and d) rocking damping ratio of the SSI system in the direction of loading. Note: the shaker was not externally mounted to the structure.**

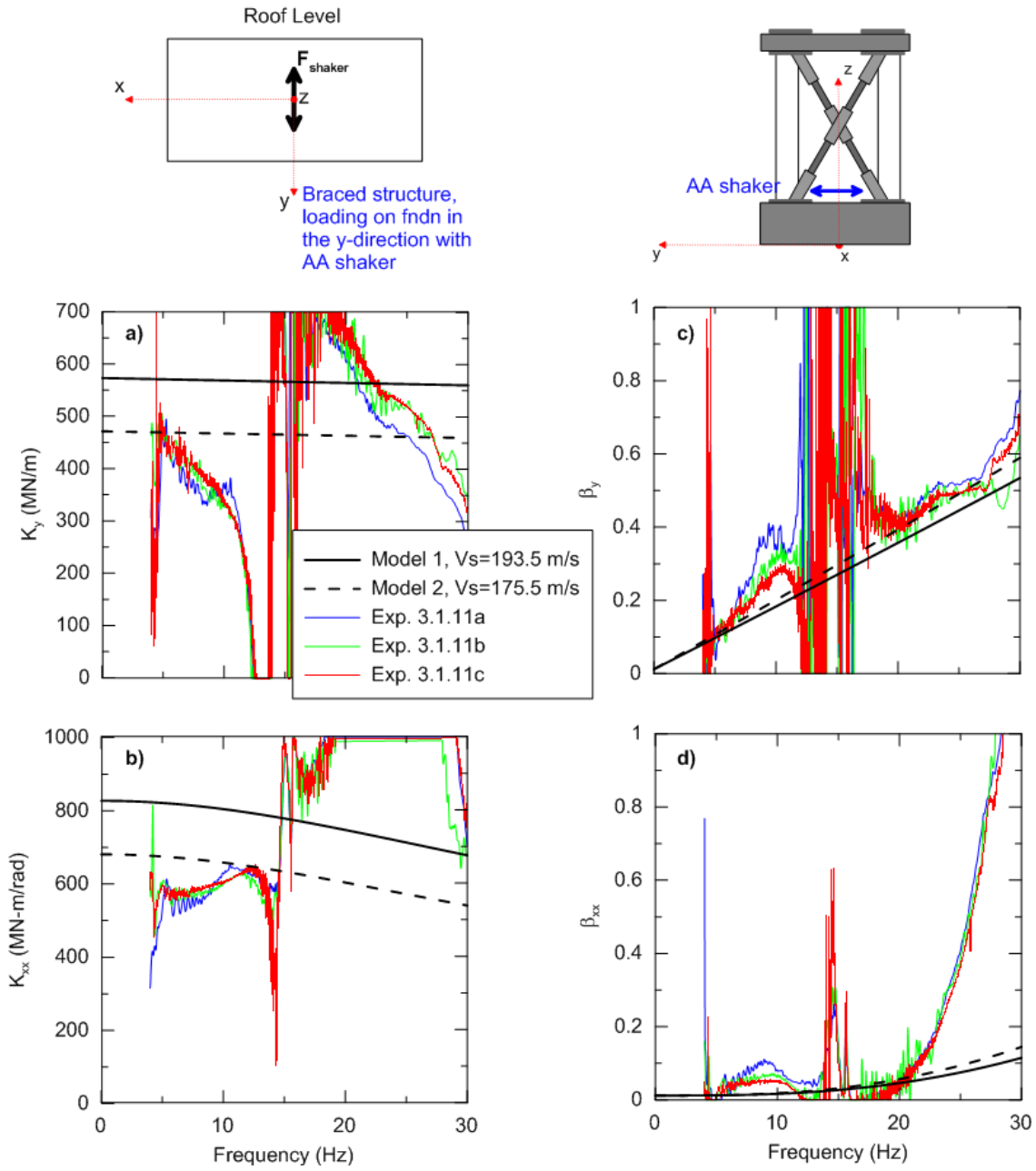

Figure 6-23 **Inverted impedance function results from analysis of Exp. 3.1.11 (Braced condition, Atom Ant shaker loading on the foundation in the y-direction). The plots show a) the translation stiffness, b) rocking stiffness, c) translation damping ratio, and d) rocking damping ratio of the SSI system in the direction of loading. Note: the shaker was not externally mounted to the structure.**

6.5.2 Large Amplitude Forced Vibration Testing

The large amplitude forced vibration testing consisted of shaking Mini-Me in both the braced and unbraced stiffness conditions. Experimental impedance functions for a) translation and b) rotation were back-calculated using the Tileylioglu et al. (2011) and Crouse et al. (2001) method (Eqs 6-15 and 6-16). The structural response acceleration histories and shaker force were used as input parameters. The shaker force was determined by methods described in Section 5.3.6.3, Eq. (5-2).

Figures 6-24 through 6-36 show the experimentally derived impedance functions for the SSI system. The experiment numbers associated with each figure can be referenced to the testing details in Chapter 5 (Tables 5-4 and 5-6). A discussion about the interpretation of the data is in Section 6.9.2. Frequency smoothing was applied using 10 passes of an 11-point hamming window based on methods described by Mikami et al. (2008). The peak shear strain (γ) at the foundation-soil contact was approximated based on the comparison of the foundation peak velocity (PGV) and soil shear wave velocity as:

$$\gamma = \frac{PGV}{V_s} \tag{6-16}$$

where V_s=193.5 m/s (Model 1 value) and PGV was derived from integration of the average recorded accelerometer response of the foundation. The foundation response was determined in the *x*-direction from channel nos. 3, 6, 9, and 12 and in the *y*-direction with channel nos. 2, 5, 8, and 11. For each frequency, we calculated the soil's shear modulus reduction (G/G_0) and damping (β_s) using Menq's model (2003) based on the estimated peak shear strain. The modulus reduction is represented by the ratio of the shear modulus

(G_0) at small strains and strain-dependent shear modulus (G) Figures 6-24 through 6-36 include plots at the bottom to represent the approximate soil strain, G/G_0 and β_s over the frequency ranges tested. The frequency-dependency of the strains is expected since the peak velocities used in Eq. (-16) for evaluation are frequency-dependent.

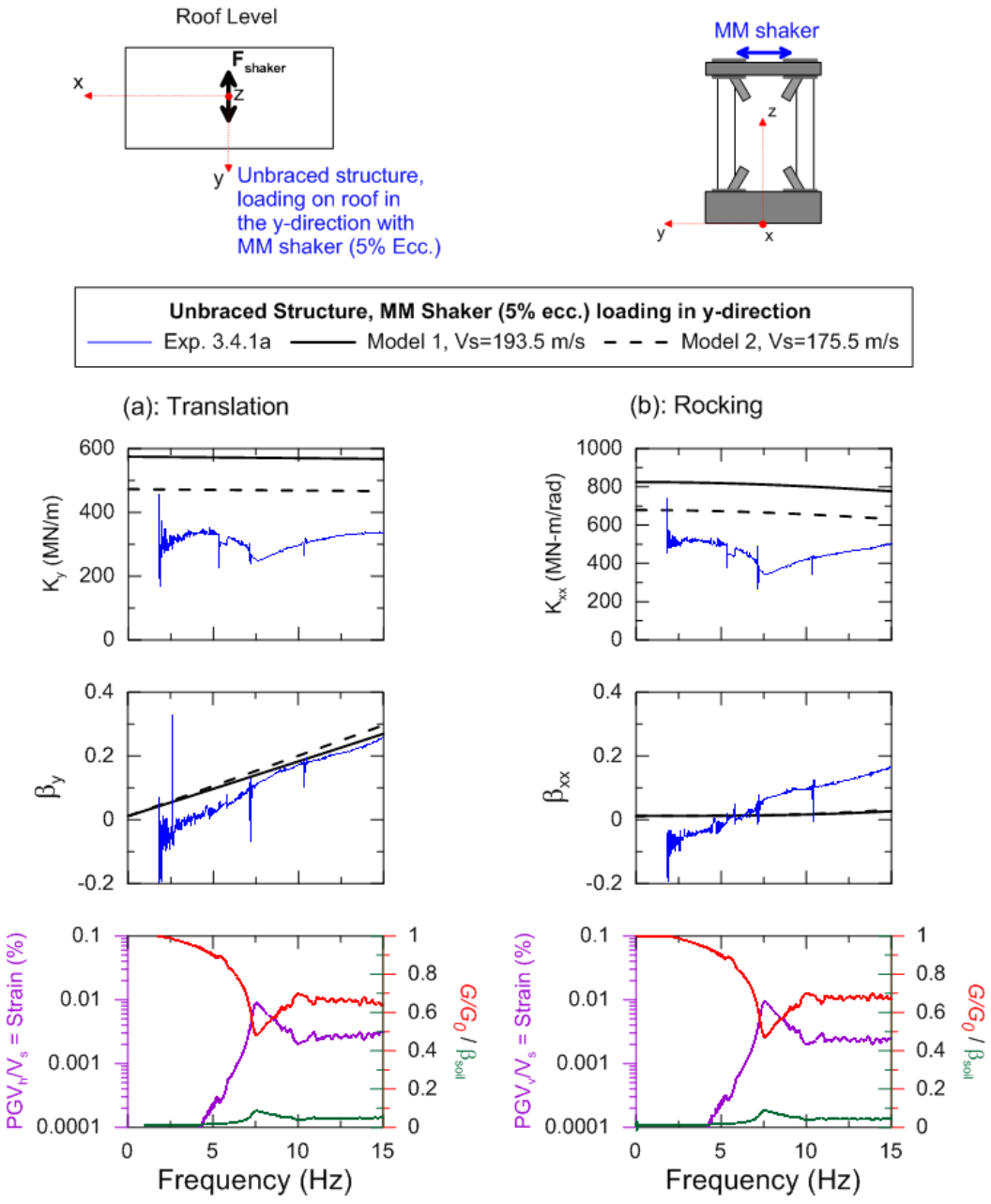

Figure 6-24 **Inverted impedance function results from analysis of Exp. 3.4.1a (Unbraced condition, Mighty Mouse shaker (5% ecc.) loading on the roof in the y-direction). The plots show impedance functions in the a) translational and b) rocking modes of vibration. The bottom plots represent the soil nonlinearity for each mode.**

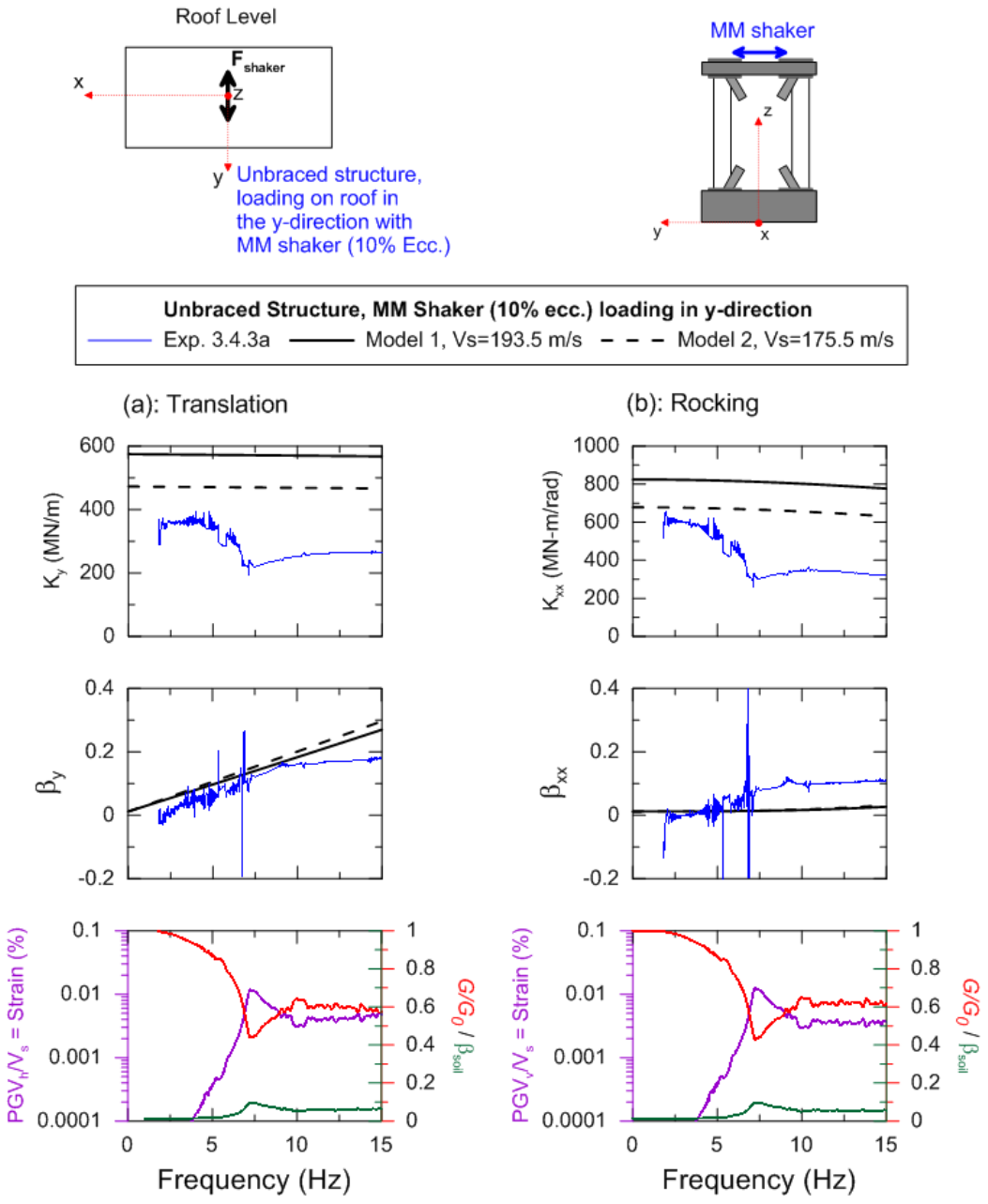

Figure 6-25 **Inverted impedance function results from analysis of Exp. 3.4.3a (Unbraced condition, Mighty Mouse shaker (10% ecc.) loading on the roof in the y-direction). The plots show impedance functions in the a) translational and b) rocking modes of vibration. The bottom plots represent the soil nonlinearity for each mode.**

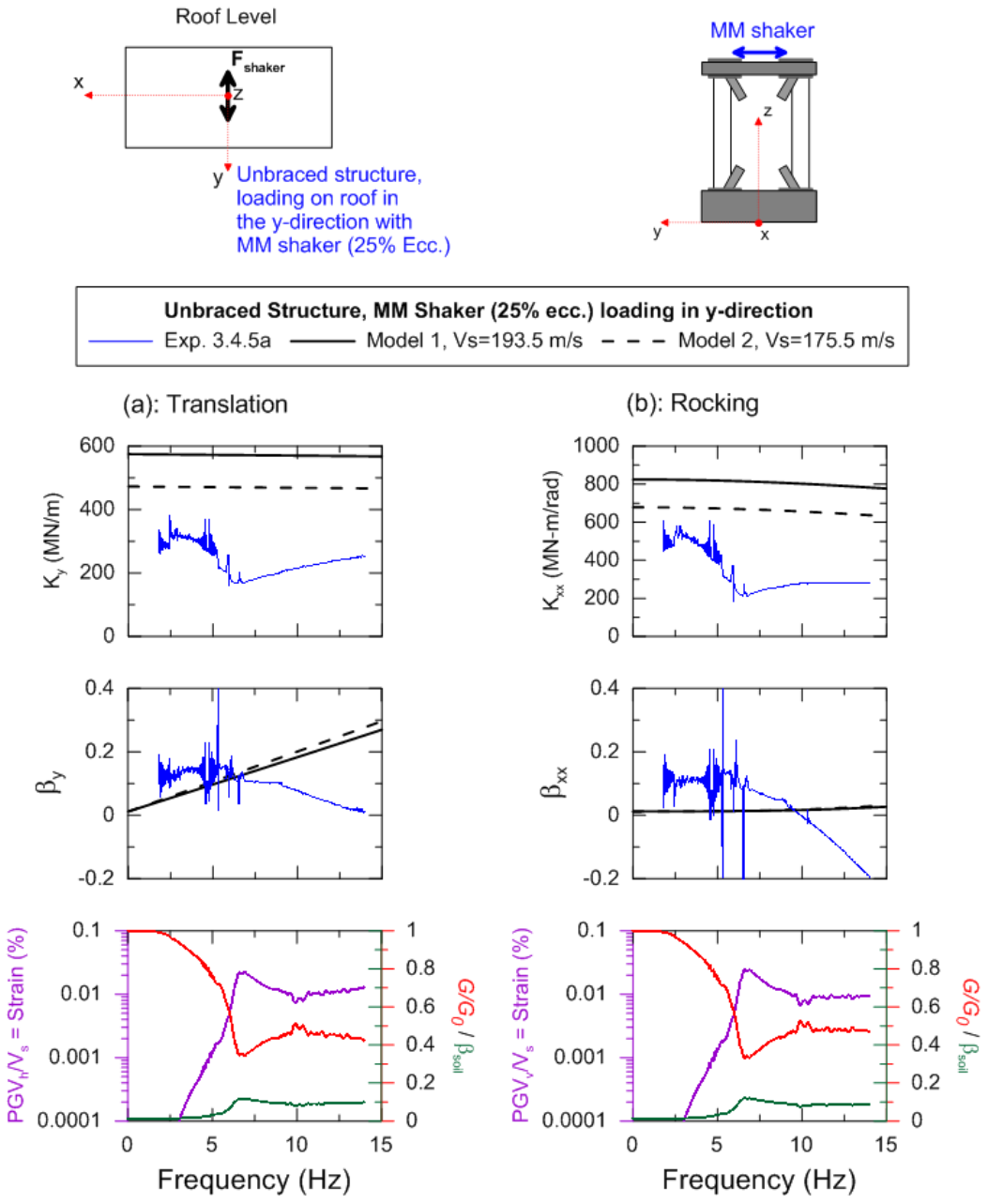

Figure 6-26 **Inverted impedance function results from analysis of Exp. 3.4.5a (Unbraced condition, Mighty Mouse shaker (25% ecc.) loading on the roof in the y-direction). The plots show impedance functions in the a) translational and b) rocking modes of vibration. The bottom plots represent the soil nonlinearity for each mode.**

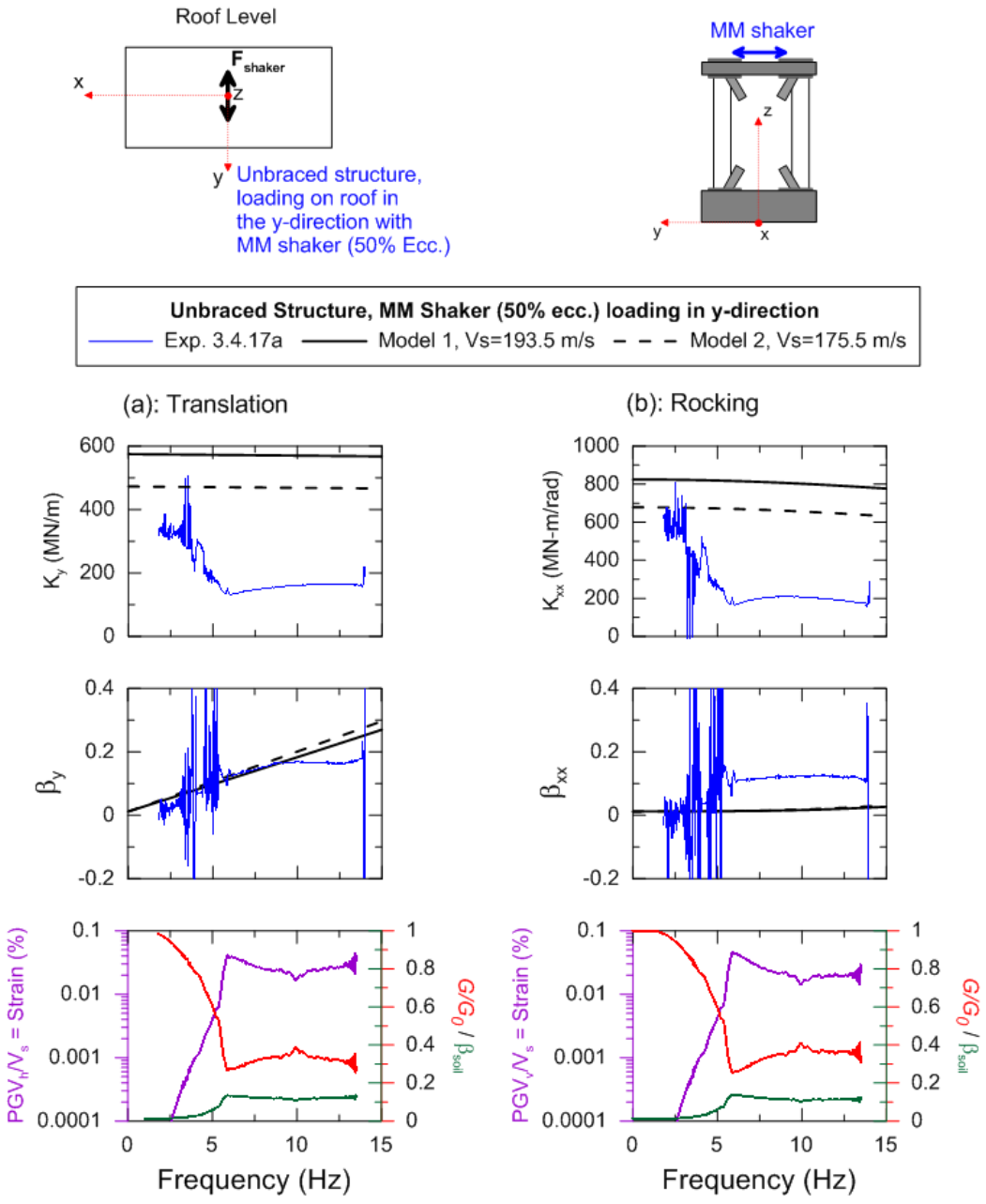

Figure 6-27 **Inverted impedance function results from analysis of Exp. 3.4.17a (Unbraced condition, Mighty Mouse shaker (50% ecc.) loading on the roof in the y-direction). The plots show impedance functions in the a) translational and b) rocking modes of vibration. The bottom plots represent the soil nonlinearity for each mode.**

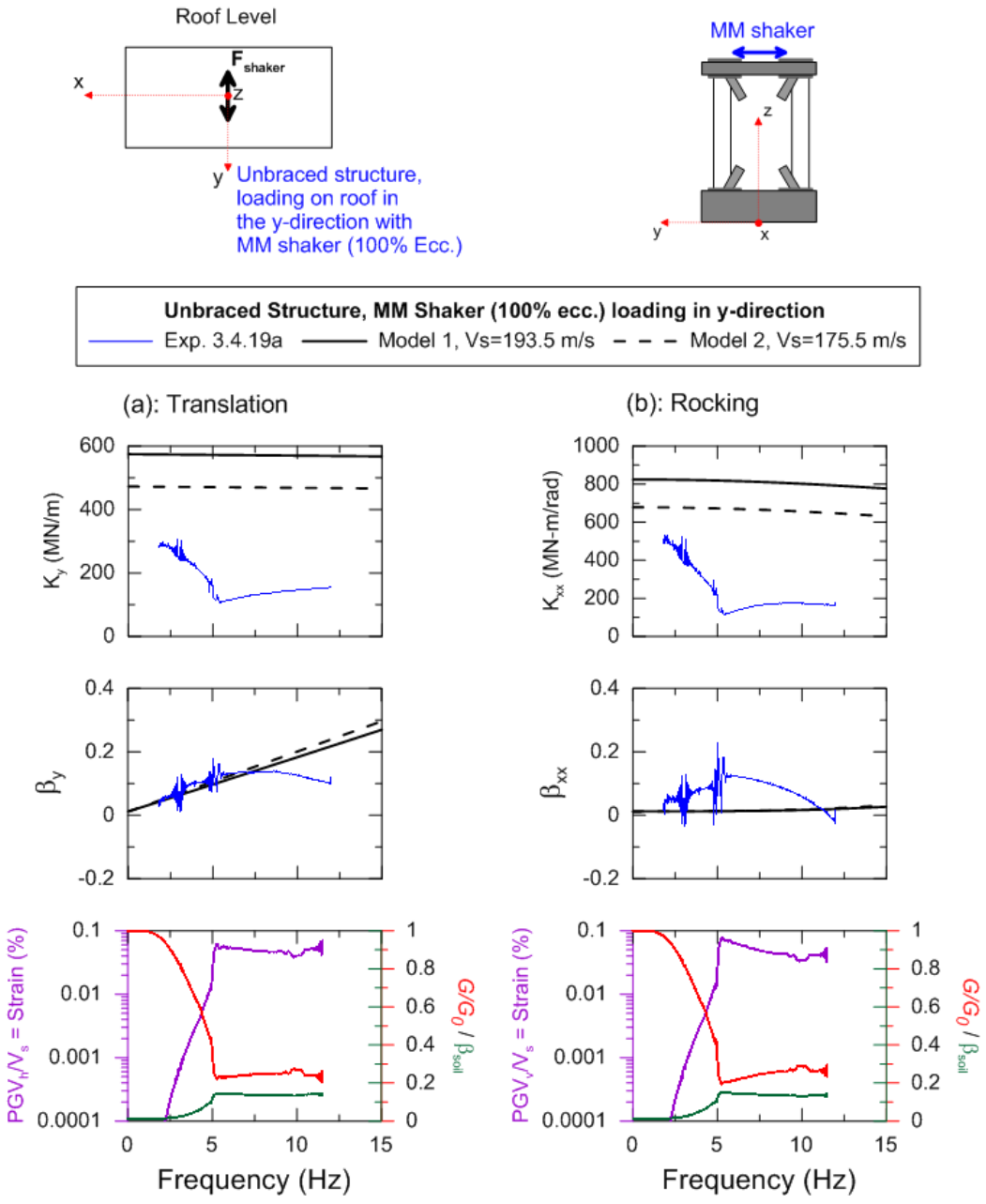

Figure 6-28 **Inverted impedance function results from analysis of Exp. 3.4.19a (Unbraced condition, Mighty Mouse shaker (100% ecc.) loading on the roof in the y-direction). The plots show impedance functions in the a) translational and b) rocking modes of vibration. The bottom plots represent the soil nonlinearity for each mode.**

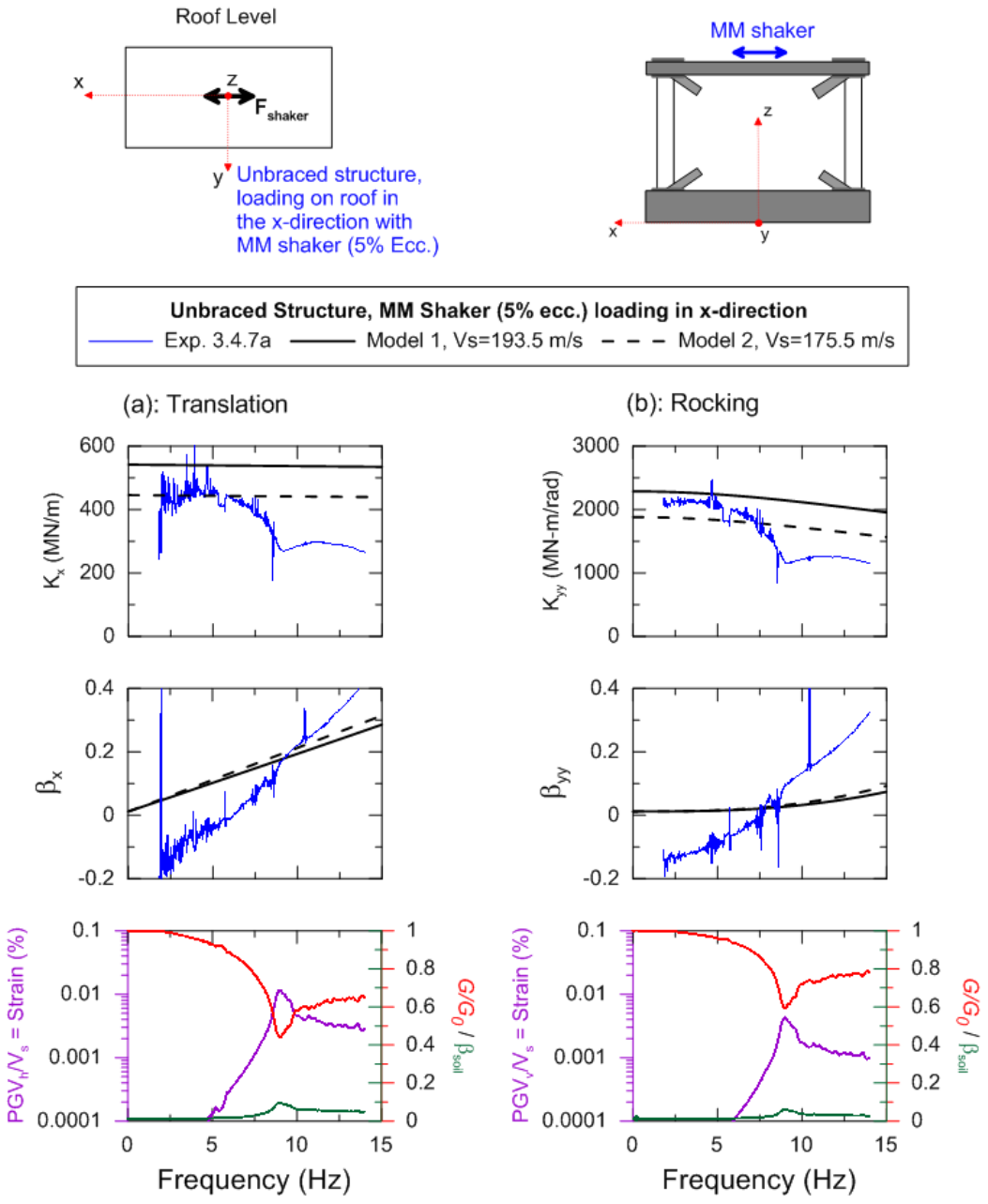

Figure 6-29 **Inverted impedance function results from analysis of Exp. 3.4.7a (Unbraced condition, Mighty Mouse shaker (5% ecc.) loading on the roof in the x-direction). The plots show impedance functions in the a) translational and b) rocking modes of vibration. The bottom plots represent the soil nonlinearity for each mode.**

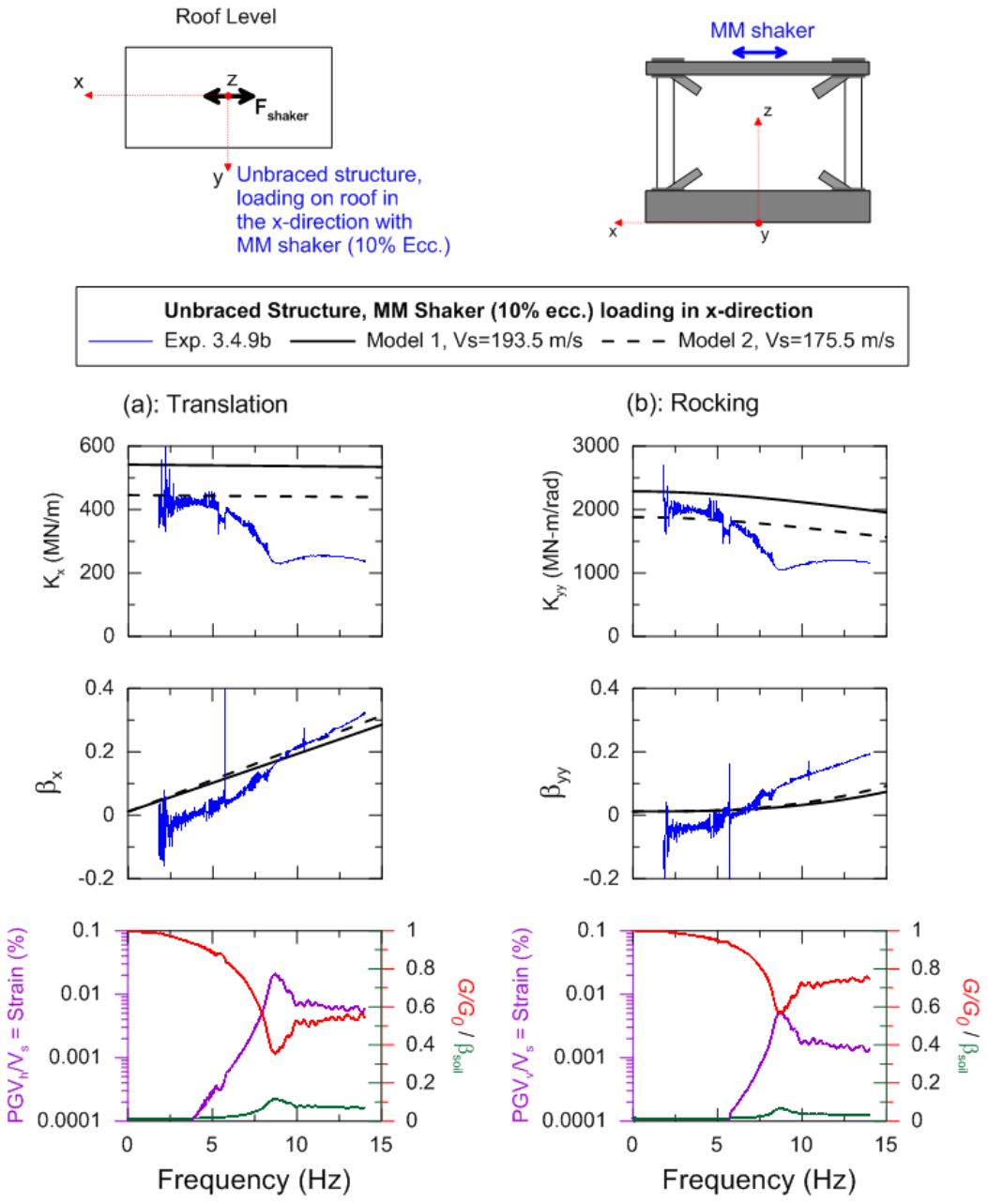

Figure 6-30 **Inverted impedance function results from analysis of Exp. 3.4.9b (Unbraced condition, Mighty Mouse shaker (10% ecc.) loading on the roof in the x-direction). The plots show impedance functions in the a) translational and b) rocking modes of vibration. The bottom plots represent the soil nonlinearity for each mode.**

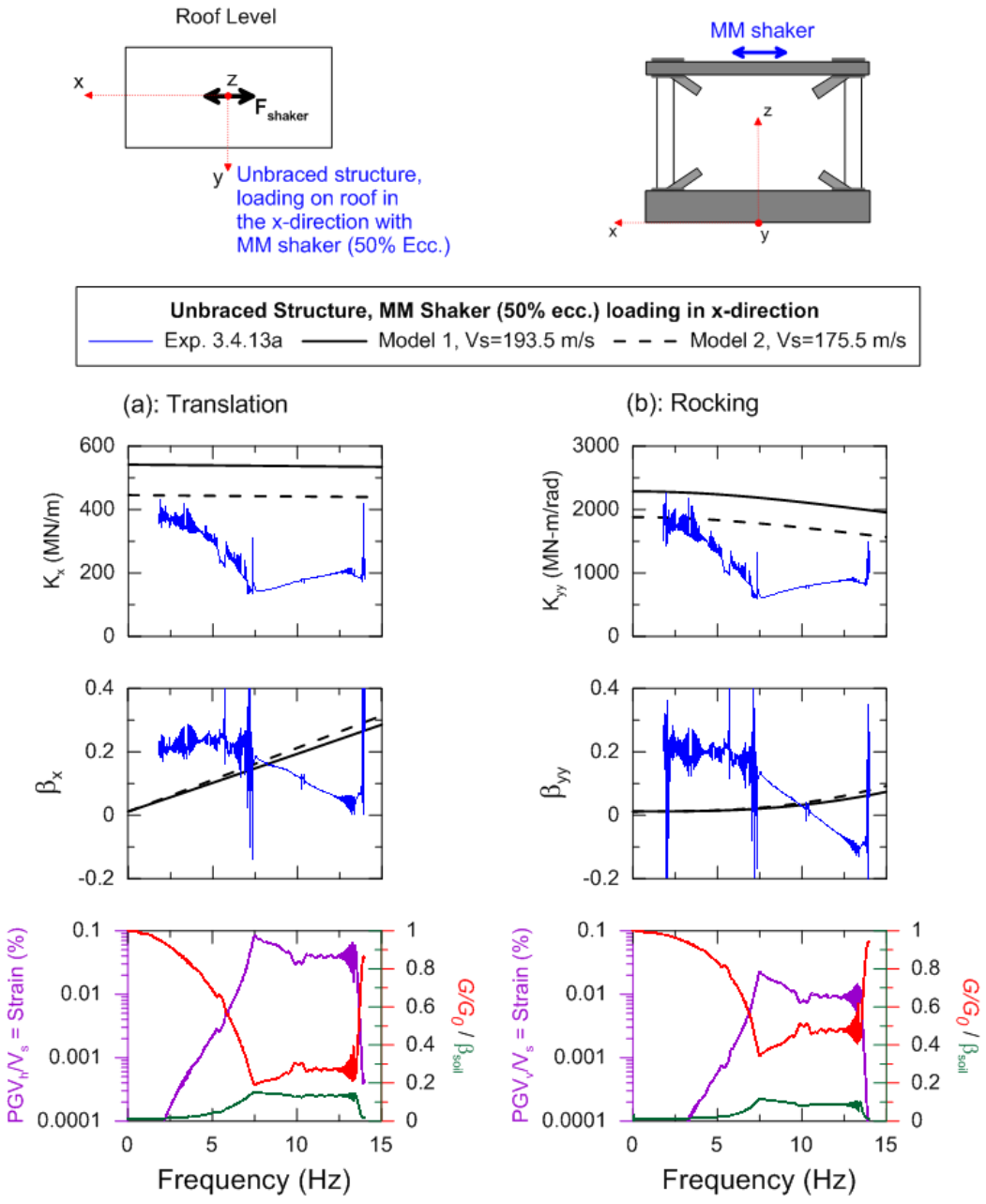

Figure 6-31 **Inverted impedance function results from analysis of Exp. 3.4.13a (Unbraced condition, Mighty Mouse shaker (50% ecc.) loading on the roof in the x-direction). The plots show impedance functions in the a) translational and b) rocking modes of vibration. The bottom plots represent the soil nonlinearity for each mode.**

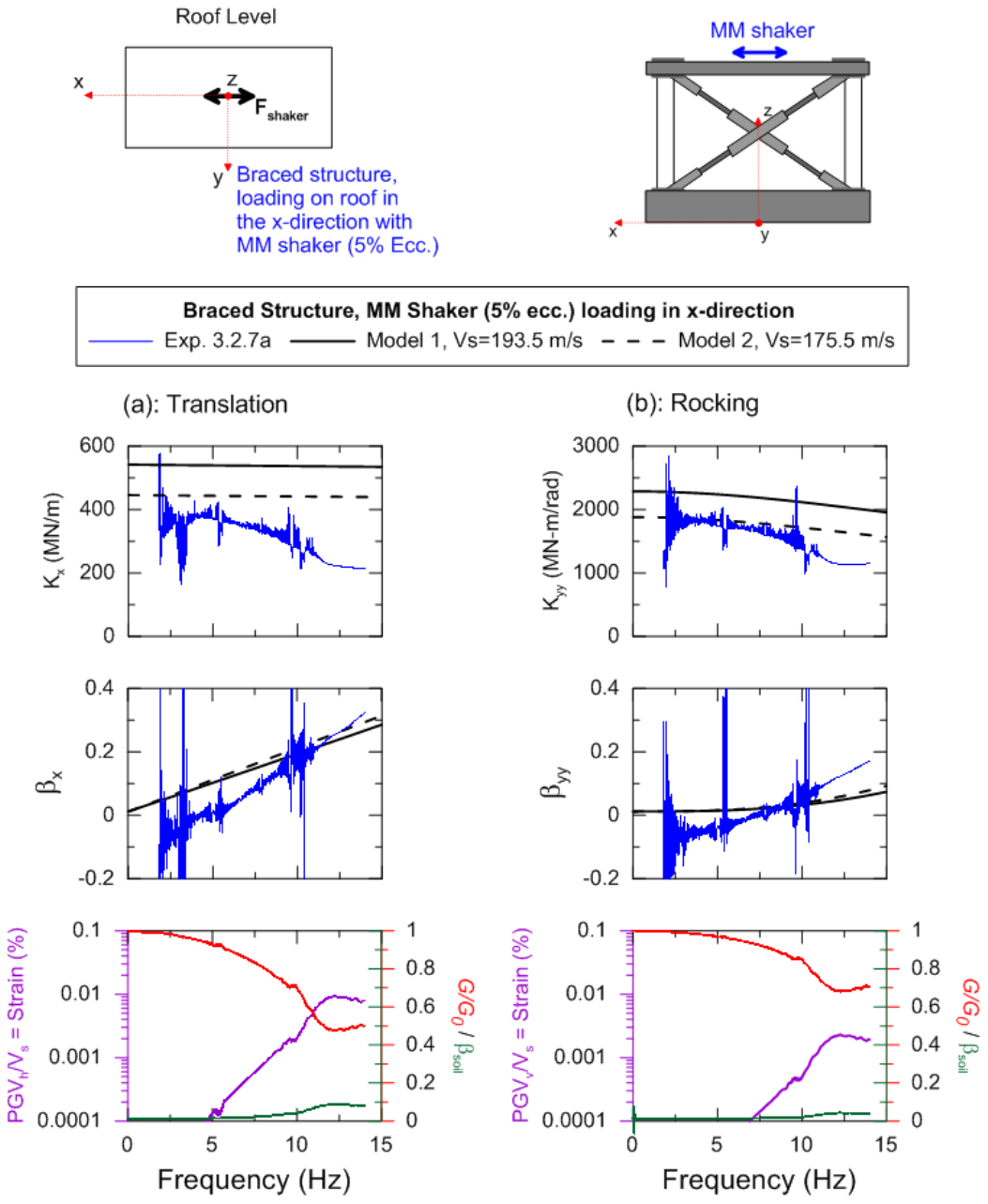

Figure 6-32 **Inverted impedance function results from analysis of Exp. 3.2.7a (Braced condition, Mighty Mouse shaker (5% ecc.) loading on the roof in the x-direction). The plots show impedance functions in the a) translational and b) rocking modes of vibration. The bottom plots represent the soil nonlinearity for each mode.**

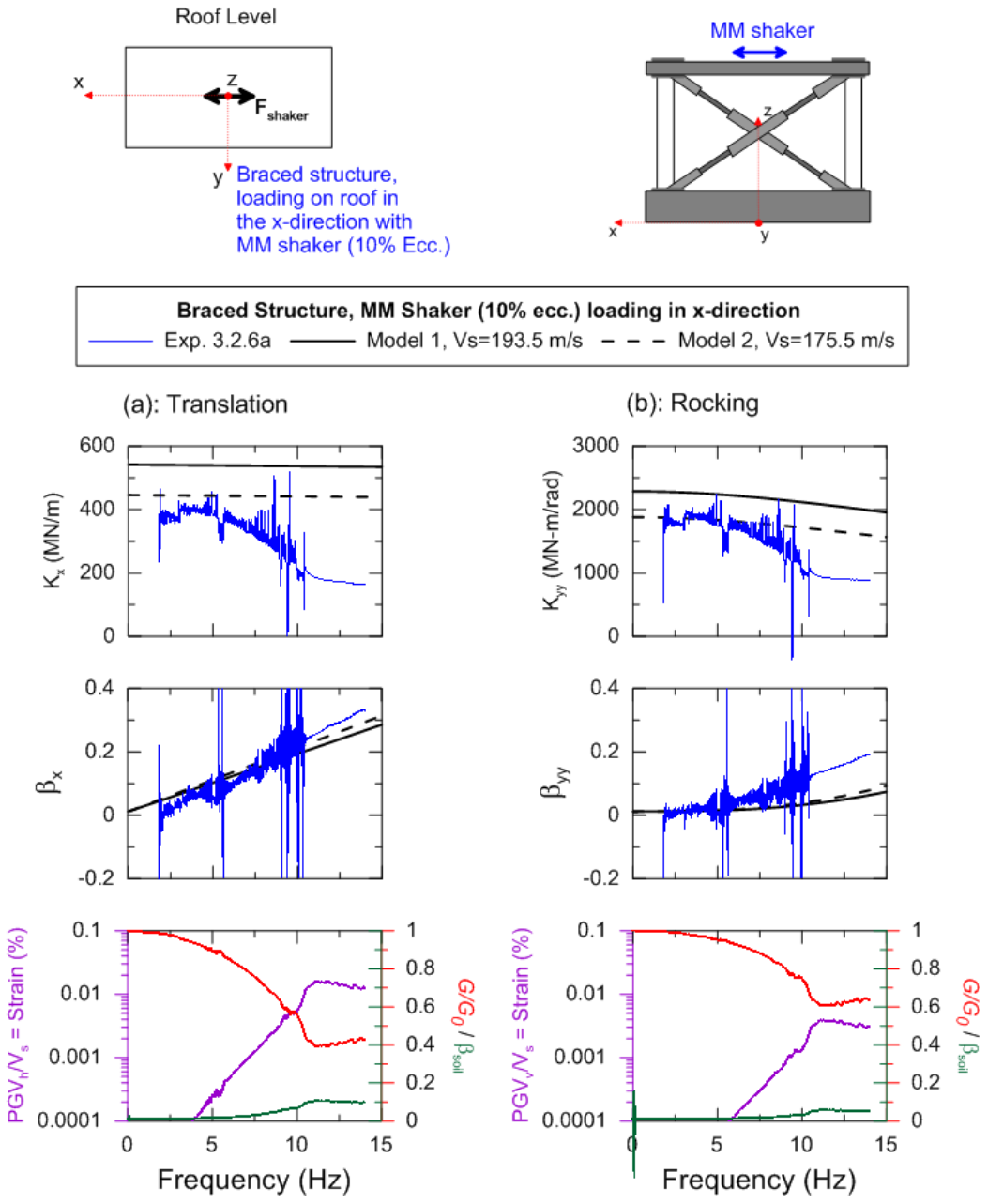

Figure 6-33 **Inverted impedance function results from analysis of Exp. 3.2.6a (Braced condition, Mighty Mouse shaker (10% ecc.) loading on the roof in the x-direction). The plots show impedance functions in the a) translational and b) rocking modes of vibration. The bottom plots represent the soil nonlinearity for each mode.**

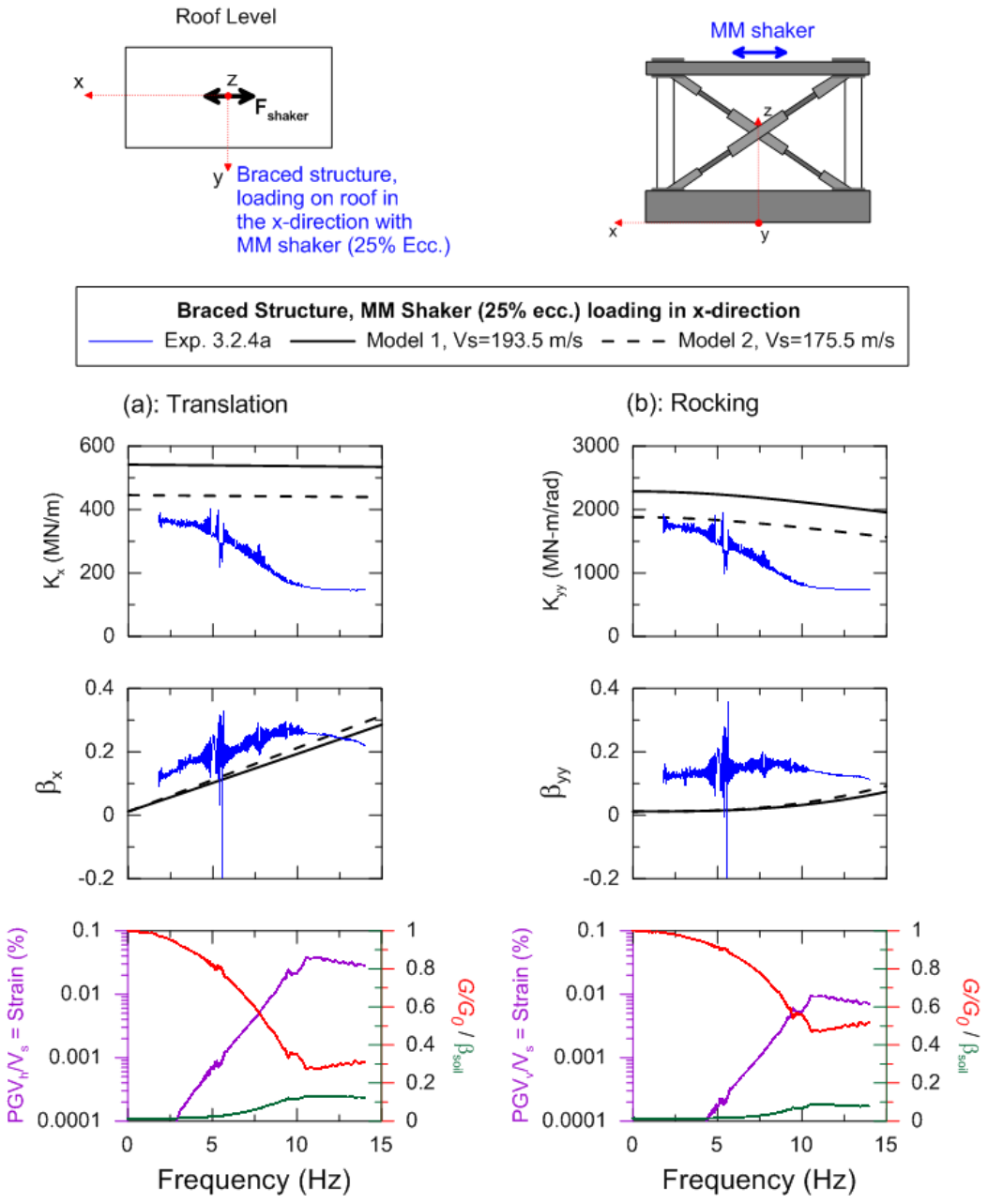

Figure 6-34 **Inverted impedance function results from analysis of Exp. 3.2.4a (Braced condition, Mighty Mouse shaker (25% ecc.) loading on the roof in the x-direction). The plots show impedance functions in the a) translational and b) rocking modes of vibration. The bottom plots represent the soil nonlinearity for each mode.**

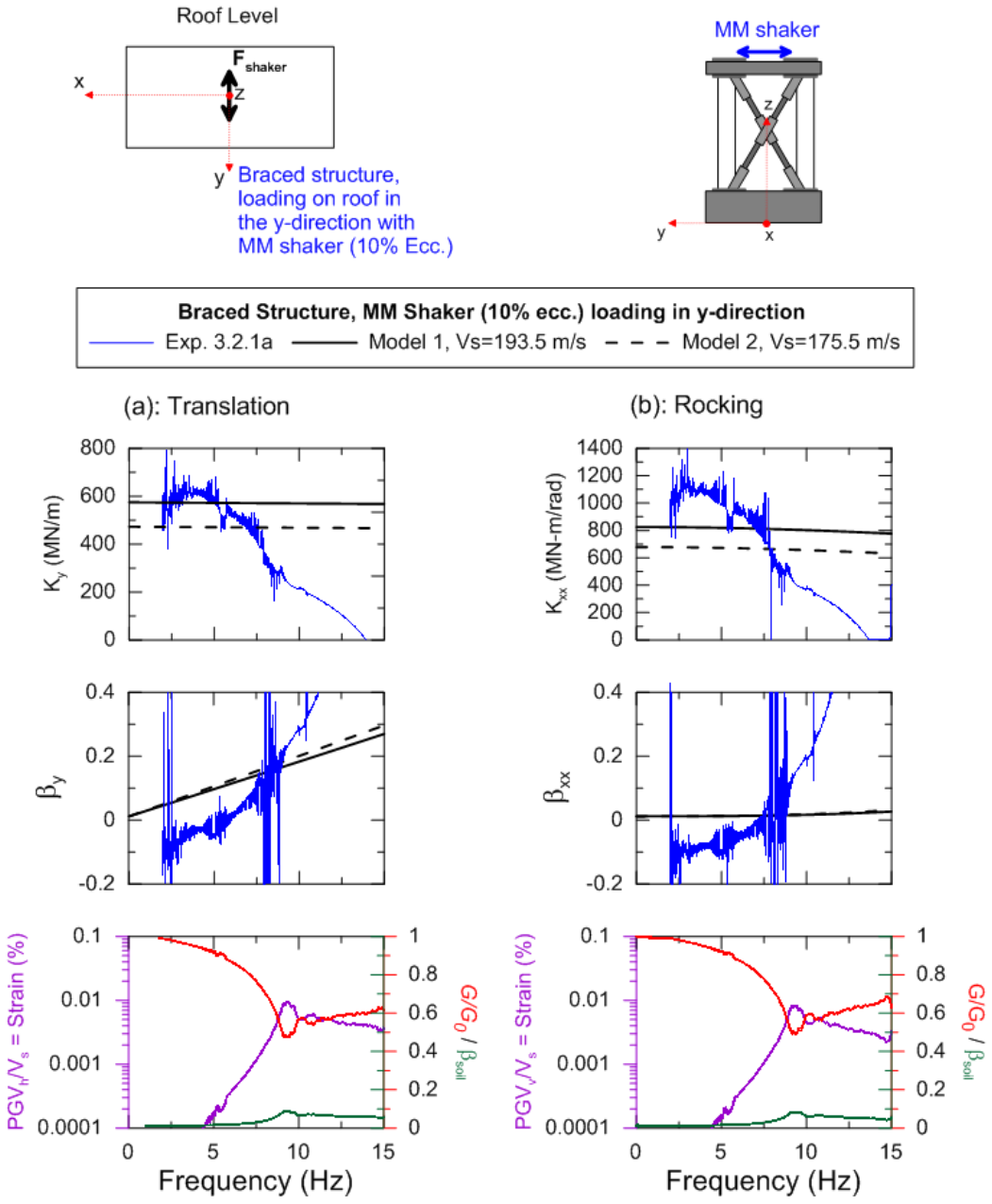

Figure 6-35 **Inverted impedance function results from analysis of Exp. 3.2.1a (Braced condition, Mighty Mouse shaker (10% ecc.) loading on the roof in the y-direction). The plots show impedance functions in the a) translational and b) rocking modes of vibration. The bottom plots represent the soil nonlinearity for each mode.**

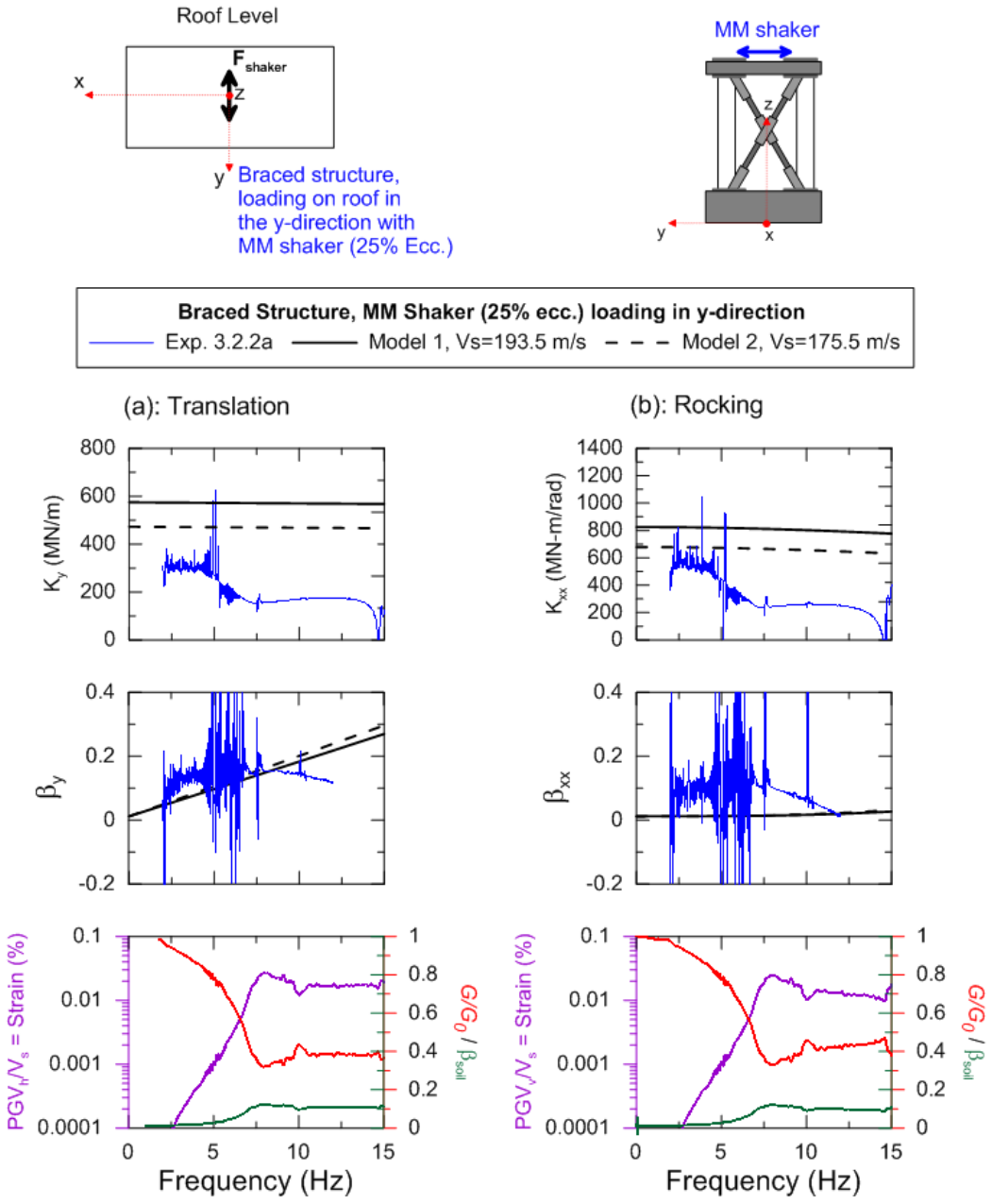

Figure 6-36 **Inverted impedance function results from analysis of Exp. 3.2.2a (Braced condition, Mighty Mouse shaker (25% ecc.) loading on the roof in the y-direction). The plots show impedance functions in the a) translational and b) rocking modes of vibration. The bottom plots represent the soil nonlinearity for each mode.**

6.6 Parametric System Identification of Forced Vibration Testing

6.6.1 System Identification Method

System identification refers to the process of computing the unknown properties of a system given an input signal entering that system and the output signal that is modified from the input as a result of system response. The 'system' in this case is various components of the SSI test structure, whereas the input and output signals are various combinations of recordings from the forced vibration testing.

In this section, I utilize system identification to estimate the modal properties of the SSI system using data generated from the forced vibration testing described in Chapter 5. The modal properties of period and damping ratio are evaluated for two cases of base fixity (fixed-base and flexible-base). Non-parametric and parametric methods can be used to perform system identification. Non-parametric methods consist of evaluating the complex-valued transmissibility function of the input-output motions of a system without matching an underlying model (e.g., Ljung, 1987, Pandit, 1991). Parametric system identification consists of evaluating the transfer function surface in the Laplace domain by fitting an underlying model (Stewart and Fenves, 1998). A parametric analysis is more quantitative in the sense that specific values of period and damping ratio are recovered, and hence are generally preferred for studies of this type.

Parametric system identification analysis begins with an iterative process to evaluate the time delay between input-output signals and the number of modes required to best capture the system response. The iterative process uses least-squared techniques to identify the model parameters that produce the smallest error between the model and

output signal. The total duration of the signal is used in this process (i.e., recursive procedures are not considered). The model generated by the least squares regressions describes a surface in the Laplace domain. That surface is referred to here as a transfer function. As described by Stewart and Fenves (1998), the horizontal plane below the surface has axes that can be interpreted in the form of frequency and damping ratio, with the peaks (i..e., "poles") of the surface defining modal properties. The intersection of the surface with a vertical plane drawn through the frequency axis is the parametric estimate of the so-called transmissibility function. That parametric estimate of the transmissibility function can be compared to the non-parametric transmissibility functions evaluated essentially as an output/input signal ratio, using procedures given in Mikami et al. (2008).

A key issue in the use of either parametric or non-parametric system identification methods is what combinations of input-output signals should be used to recover specific system properties of interest. Stewart and Fenves (1998) evaluated these motions for the case of earthquake excitation and system properties corresponding to fixed-base (representing structural flexibility and mass only), pseudo flexible-base (representing structural mass and flexibility from the structure and foundation in rocking), and flexible-base (representing structural mass and flexibility from the structure and foundation in rocking and translation). For the case of forced vibration testing, the input-output pairs for application to single degree-of-freedom structural systems have been evaluated by Tileylioglu (2008) by solving equations of motion in the Laplace domain, with the results in Table 6-2. Input-output pairs for more general application involving multi-degree of freedom structures have yet to be identified.

Table 6-2 Input-Output Pairs To Evaluate Flexible-Base and Fixed-Base Modal Parameters. (Tileylioglu, 2008)

Base Fixity	Input	Output
Flexible-Base	$\frac{F_s}{m_s}$	$\ddot{u}_f + h\ddot{\theta}_f + \ddot{u}_s$
Fixed-Base	$\frac{F_s}{m_s} - \ddot{u}_f - h\ddot{\theta}_f$	$\ddot{u}_s$

See Section 6.3 for definitions in table.

6.6.2 System Identification of Instrumented Field Test Structures

As described in Section 2.6.2, Stewart et al. (1999b) performed parametric system identification of 58 buildings shaken by earthquakes to identify fixed-based, pseudo flexibile-base, and flexible-base modal properties. The properties of greatest interest for SSI applications are the first-mode period and damping ratio for the fixed-base (T, β_i) and flexible-base ($\widetilde{T}, \beta_0$) conditions. Since the work of Stewart et al. (1999b), a number of case studies of forced vibration have become available from which these same properties can be identified. The available data comes from this study along with Tileylioglu et al. (2011) for the GVDA Dr Evil structure and Star (2011) for the Mini Me structure at the WLA site. The results of this work have been plotted and interpreted in Section 2.6.2 for use in investigating period lengthening and foundation damping models. This subsection describes the parametric system identification work that produced the modal properties from the instrumented field test structures.

Table 6-3 shows the attributes of the instrumented field test structures (i.e., data source, loading source, shaking direction, etc.), velocity reduction (V_s/V_{s0}) due to

estimated shear strain (evaluated using procedures given in Section 6.5), parametric system identified results, and relevant SSI parameters ($h/(V_sT)$, $\widetilde{T}/T$ and β_f). As shown previously in Figure 2-14, the data occupies a previously sparsely populated region of moderately high $h/(V_sT)$ = 0.14 to 0.45, and hence is a valuable addition to the database of Stewart et al. (1999b).

The data contributed by Tileylioglu et al. (2011) for the Dr Evil structure come from earthquake shaking and forced vibration testing (4 record sets). An additional 19 record sets have been derived from forced vibration testing of Mini-Me at the GVDA (this study, Chapter 5) and WLA (Star, 2011) sites. Data sets from both sites are available for braced and unbraced structural conditions. The distinction in structural stiffness is important in this case because the stiffer structure produces higher $h/(V_sT)$ and related SSI effects. As shown in Table 6-3, similar forcing of Mini-Me (Exps. 3.1.1a and 3.3.5a) showed larger results for the braced condition [$h/(V_sT)$=0.22 and $\widetilde{T}/T = 1.38$] compared to the unbraced condition [$h/(V_sT)$=0.17 and $\widetilde{T}/T = 1.31$].

Table 6-3 System Identification of Instrumented Field Test Structures

Structure & Site[a]	Data Source[b]	Structure Cond.	Direction of Shaking	Shake Source[c]	h[d] (m)	B (m)	L (m)	V_{s0} (m/s)	V_s/V_{s0}[e]	$h/(V_sT)$	β_s[e] (%)	System Identification					
												T_i (sec)	$\beta_{i,i}$ (%)	$\tilde{T}_i$ (sec)	$\beta_{0,i}$ (%)	$\tilde{T}_i/T_i$	$\beta_{f,i}$ (%)
DE @ GVDA	TEA (2011)	Unbraced	NA	EQ M_L = 4.2	4.36	2.03	2.03	198.0	1.00	0.15	1.2	0.149	0.5	0.172	1.3	1.15	0.9
	TEA (2011)	Unbraced	NA	EQ M_w = 5.4					1.00	0.15	1.2	0.149	0.9	0.172	4.1	1.15	3.4
	TEA (2011)	Unbraced	NA	LM					1.00	0.14	1.2	0.152	1.5	0.166	1.7	1.09	0.4
	TEA (2011)	Braced	NA	LM					1.00	0.28	1.2	0.078	9.3	0.101	4.6	1.29	0.0
MM @ GVDA	Exp. 3.3.1a	Unbraced	X	AA	2.87	1.07	2.13	193.5	1.00	0.17	1.2	0.089	0.9	0.101	3.1	1.13	2.4
	Exp. 3.4.9b	Unbraced	X	MME-10%					0.65	0.26	9.8	0.088	2.9	0.114	6.1	1.28	4.3
	Exp. 3.4.13a	Unbraced	X	MME-50%					0.50	0.29	13.7	0.101	2.1	0.127	7.7	1.25	6.4
	Exp. 3.4.15a	Unbraced	X	MME-100%					Error in test								
	Exp. 3.3.5a	Unbraced	Y	AA					1.00	0.17	1.2	0.087	1.7	0.114	3.4	1.31	2.4
	Exp. 3.4.3a	Unbraced	Y	MME-10%					0.73	0.23	7.0	0.088	2.3	0.141	9.1	1.61	8.2
	Exp. 3.4.17a	Unbraced	Y	MME-50%					0.57	0.27	12.1	0.096	0.4	0.169	8.8	1.76	8.7
	Exp. 3.4.19a	Unbraced	Y	MME-100%					0.54	0.26	12.9	0.104	0.0	0.185	11.1	1.78	11.1
	Exp. 3.1.1a	Braced	X	AA					1.00	0.24	1.2	0.063	8.0	0.070	7.2	1.12	0.8
	Exp. 3.2.6a	Braced	X	MME-10%					0.68	0.33	9.0	0.067	1.7	0.089	11.0	1.33	10.0
	Exp. 3.2.12a	Braced	X	MME-50%					0.49	0.45	13.9	0.067	7.2	0.109	11.8	1.63	9.1
	Exp. 3.2.14	Braced	X	MME-100%					0.45	0.31	14.9	0.106	0.0	0.119	13.5	1.12	13.5
	Exp. 3.1.6a	Braced	Y	AA					1.00	0.22	1.2	0.067	5.6	0.092	5.5	1.38	2.5
	Exp. 3.2.1a	Braced	Y	MME-10%					0.73	0.31	7.1	0.065	2.7	0.106	6.3	1.65	5.3
	Exp. 3.2.11	Braced	Y	MME-50%					0.56	0.27	12.4	0.097	5.5	0.159	9.9	1.63	7.8
	Exp. 3.2.15	Braced	Y	MME-100%					0.56	0.34	12.4	0.079	1.8	0.179	15.1	2.27	14.8
MM @ WLA	Exp. 2.1.9a	Unbraced	X	AA	2.87	1.07	2.13	106.0	1.00	0.33	2.0	0.082	1.4	0.118	9.5	1.44	8.8
	Exp. 2.1.7a	Unbraced	Y	AA					1.00	0.29	2.0	0.093	6.5	0.143	8.8	1.53	6.0
	Exp. 2.1.17a	Braced	X	AA					1.00	0.41	2.0	0.065	2.1	0.100	12.7	1.53	11.8
	Exp. 2.1.15a	Braced	Y	AA					1.00	0.39	2.0	0.069	7.8	0.125	9.1	1.81	6.7

[a]GVDA - Garner Valley Downhole Array Site; WLA - Wildlife Liquefaction Array Site; DE - Dr. Evil Structure; MM - Mini-Me Structure (See Chap. 5)

[b]TEA = Tileylioglu et al (2011); Data with "Exp" names were compiled as part of a UCLA field testing series, information can be found at https://nees.org/warehouse/project/637/ and Chapter 5.

[c]AA = Atom Ant shaker; MME-#% = Mighty Mouse shaker with #% eccentricity force; LM - Linear mass shaker, similar to AA

[d]Center of mass height of the roof slab

[e]Based on Menq (2003) model using 65% of approximated strain values (fondation velocity per soil shear wave veolicty) at flexible-base frequency, Note: $V_s/V_{s0} = (G_s/G_{s0})^{1/2}$ and WLA site approximated $\beta_s = 0.2$

The parametric studies using the measured responses of Mini-Me were performed as part of this study. Nineteen data sets were evaluated using the input-output pairs in Table 6-2 (hence, 19 values each of period lengthening and foundation damping result from these computations). The iterative process described in Section 6.6.2 to identify optimal values of time delay and number of modes was undertaken for each input-output signal pair. For consistency, typically the same best fit delay and number of modes was used for both the fixed-base and flexible-base cases. For each input-output pair, we check results by comparing the transmissibility function from parametric system identification with the corresponding non-parametric result. A small misfit between the fixed-base cases occurred because of the accuracy that was applied to the delay and number of modes. Greater precision could have been achieved by using different parameters for the fixed-base and flexible-base cases at the cost of accuracy. I felt the relative accuracy between analyses would better predict the SSI parameters ($h/(V_sT)$, $\widetilde{T}/T$ and β_f).

Figures 6-37 and 6-38 show example transmissibility functions from parametric and non-parametric system identifications procedures using data from forced vibration testing with the Atom Ant shaker at GVDA. Figure 6-37 shows the fixed-base and flexible-base transmissibility functions for forced vibration testing of Mini-Me in an unbraced condition for both a) shaking in the long (x) direction and b) shaking in the short (y) direction. The peaks occur at modal frequencies, with the first distinct peak representing first-mode response. Figure 6-38 shows similarly formatted results for Mini-Me in a braced condition. As expected, the first-mode frequency is higher with bracing,

particularly for the fixed-base condition. The fixed-base peak is also broader, indicating higher damping.

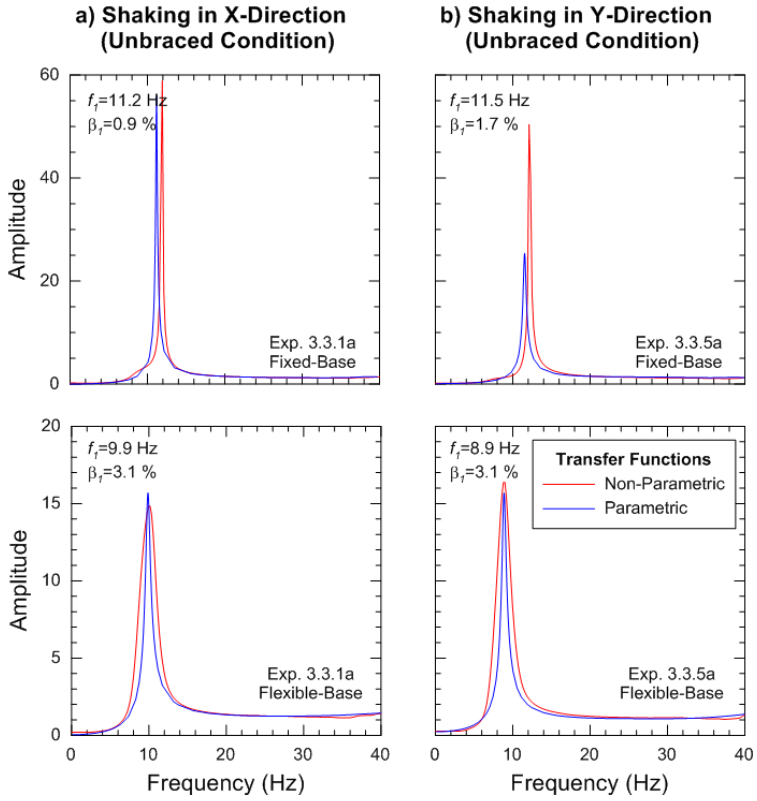

Figure 6-37 **Transmissibility functions from parametric and non-parametric system identification using response history data from forced vibration testing at GVDA with Atom Ant shaker. a) Exp. 3.3.1a (Unbraced condition, loading on the roof in the x-direction) and b) Exp. 3.3.5a (Unbraced condition, loading on the roof in the y-direction). f_1= first-mode frequency and β_1= corresponding first-mode damping.**

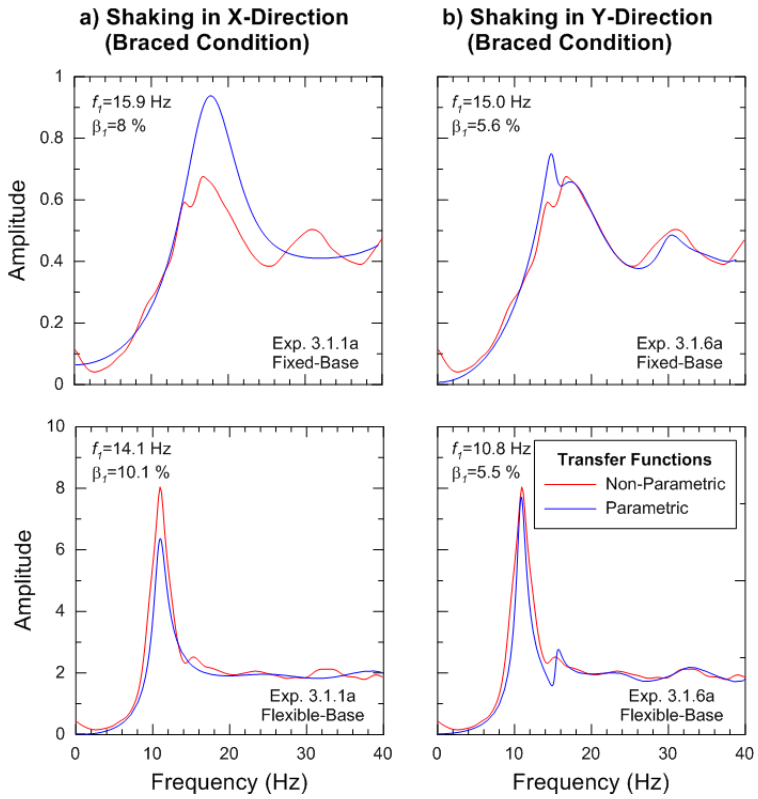

Figure 6-38 **Transmissibility functions from parametric and non-parametric system identification using response history data from forced vibration testing at GVDA with Atom Ant shaker. a) Exp. 3.1.1a (Braced condition, loading on the roof in the x-direction) and b) Exp. 3.1.6a (Braced condition, loading on the roof in the y-direction). f_1= first-mode frequency and β_1= corresponding first-mode damping.**

The period lengthening and foundation damping computed from identified first-mode parameters were compared to model predictions represented by closed-form equations in Chapter 2. Input parameters for the foundation damping models, appropriate soil shear wave include each of the variables in the wave parameter $h/(V_sT)$ along with soil hysteretic damping (β_s), soil Poisson's ratio ν, and mass ratio γ_m. The soil shear wave velocity (V_s) includes the effects of the weight of the structure and is taken as the time-

averaged value from the surface to the relevant z_p depth as described in Section 2.6.1. Peak shear strains for a given test were evaluated using procedures given in Section 6.5. Since those are peak shear strain, they are reduced to an effective strain that is 65% of the peak, and those effective strains were then used to evaluate soil hysteretic damping (β_s) and shear modulus reduction (G/G_0) values for each test using the generic models of Menq (2003), as shown in Figures 6-24 through 6-36. No modulus reduction was applied for the small linear mass shakers and the minimum β_s value was used (i.e., D_{min}). The shear modulus reduction can be equated to soil shear wave reduction as $V_s/V_{s0} = \sqrt{G/G}_0$. The modulus reduction was used for both the determination of the impedance function input G value used in the computation of period lengthening and foundation damping and in the computation of the $h/(V_sT)$ value used for plotting purposes. It should be noted the h values represent the height of the single-degree of freedom mass height which is represented at the middle of the upper concrete deck. Poisson's ratio was chosen for analyses as ν=0.35 by Tileylioglu et al. (2011), ν=0.45 for WLA and ν=0.33 for this study of GVDA. The average mass ratio (γ_m=0.15) was used for evaluation of the predicted period lengthening and foundation damping in Section 2.6.2.

6.7 Kinematic Interaction Analysis from Forced Vibration Testing at GVDA

During testing at GVDA, a preexisting non-embedded 12.2 m (40 ft) x 18.3 m (60 ft) concrete slab was instrumented to evaluate kinematic soil-structure interaction effects associated with forced vibration testing of the neighboring Mini Me structure. Recall from Chapter 3, *base slab averaging* is a kinematic effect where motions on foundations

are reduced in amplitude relative to free-field motions. This section looks to gain insight into the base-slab averaging phenomenon by investigating differences in the particle motions between the ground motions and slab foundation motions at select frequencies of excitation. Additionally, the vertical and horizontal transfer functions discussed in Chapter 3 are examined.

Figure 6-39 shows the concrete slab location compared to the test structures described in Chapter 5 and the sensor array. During selected forced vibration tests of Mini-Me with the large eccentric mass shaker (described in Section 5.2.4) in the *x* and *y* directions, a wireless data acquisition (DA) system was installed with four accelerometers: two (sensors 'B' and 'C') on the slab and two on the ground (sensor 'A' and 'D'). A fifth sensor ('E') was placed near the middle of the longitudinal (long) direction of the slab on the ground surface and attached to the previously established structural DA described in Section 5.2.5. Four experiments were performed while accelerometers were situated on the concrete slab. The details of the experiments are listed in Table 6-4.

Table 6-4 Test Experiments of Kinematic Interaciton Due to Forced Vibration Testing.

Test Experiment	Loading Direction	Loading Shaker[a]	Eccentricity[b] (%)	Mini-Me Stiffness[c]
Exp. 3.5.1, shaking perpendicular to slab	Y	MM	100	Unbraced
Exp. 3.5.2, shaking perpendicular to slab	Y	MM	100	Unbraced
Exp. 3.5.3, shaking normal to slab	X	MM	100	Unbraced
Exp. 3.5.4, shaking normal to slab	X	MM	100	Unbraced

[a] MM=Mighty Mouse loading to Mini-Me test structure.

[b] Maximum force applied from the shaker.

[c] Stiffness is adjusted by bracings (i.e., either braced or unbraced condition).

Forced vibration testing of a structure is not an ideal source for seismic waves, since test structures are expected to generate surface waves, whereas seismic excitation over the frequency range of typical interest in kinematic SSI problems is dominated more by body waves. Nonetheless, the test was undertaken to see if useful results could potentially be generated from a test configuration of this sort, which if successful is potentially of substantial value. The wireless DA was provided by NEES@UCLA and the details of the accelerometers and sampling rate are described in Section 5.2.3.

Figure 6-40a and Figure 6-40b show 3D depictions of the seismic wave particle motions for Experiment 3.5.1 while the shaker was applying force frequencies of 5 Hz and 10 Hz to the Mini-Me structure. The frequencies were determined from the synchronized Mighty Mouse shaker and Structural Response DA systems in a similar fashion as described in Section 5.3.6. All plotted scales in Figure 6-40 have been kept consistent relative to each other, with the exception of accelerometers 'A' and 'B' in Figure 6-40a that required a larger scale. The red lines in the figures represent the projection of motion in any given plane. Figure 6-40 presents the following observations of the particle motions:

- Motions of 'A' and 'B' are dominated by vertical motions
- The intensity of the vertical motion declines from north-south (i.e., A > E > D)
- The slab motions are altered from the ground surface motions. The motion alteration is well observed in the comparison of motions of 'A' and 'B' in Figure 6-38a, where the ground surface is dominated by an elliptical motion in

the *x-z* plane (normal-vertical to shaking) and the slab motion resembles the motion of the other slab accelerometer 'C,' rather than the adjacent motion of 'A'

- Due to the existence of the larger motions to the north, the wave passage is compensated by the alteration of slab motion intensity. The northern motion of the slab ('B') is slightly reduced compared to the local ground motion ('A'), while the southern motion of the slab ('C') is larger than the local ground motion ('D')

Base slab averaging is quantified by transfer functions (H_u) as discussed in Chapter 3. Figures 6-41 through 6-44 shows the observed vertical and horizontal H_u along with predicted horizontal H_u using the NIST procedure in Equation 3-1. The modeled used a V_s=266.9 m/s (875.7 ft/s) from SASW testing that was conducted between the source of excitation (the Mini-Me location) and the concrete slab (Stokoe et al., 2004). Figures 6-41 through 6-44 generally show a good match between the NIST model predictions and observed data. The results are further discussed in Section 6.9.5

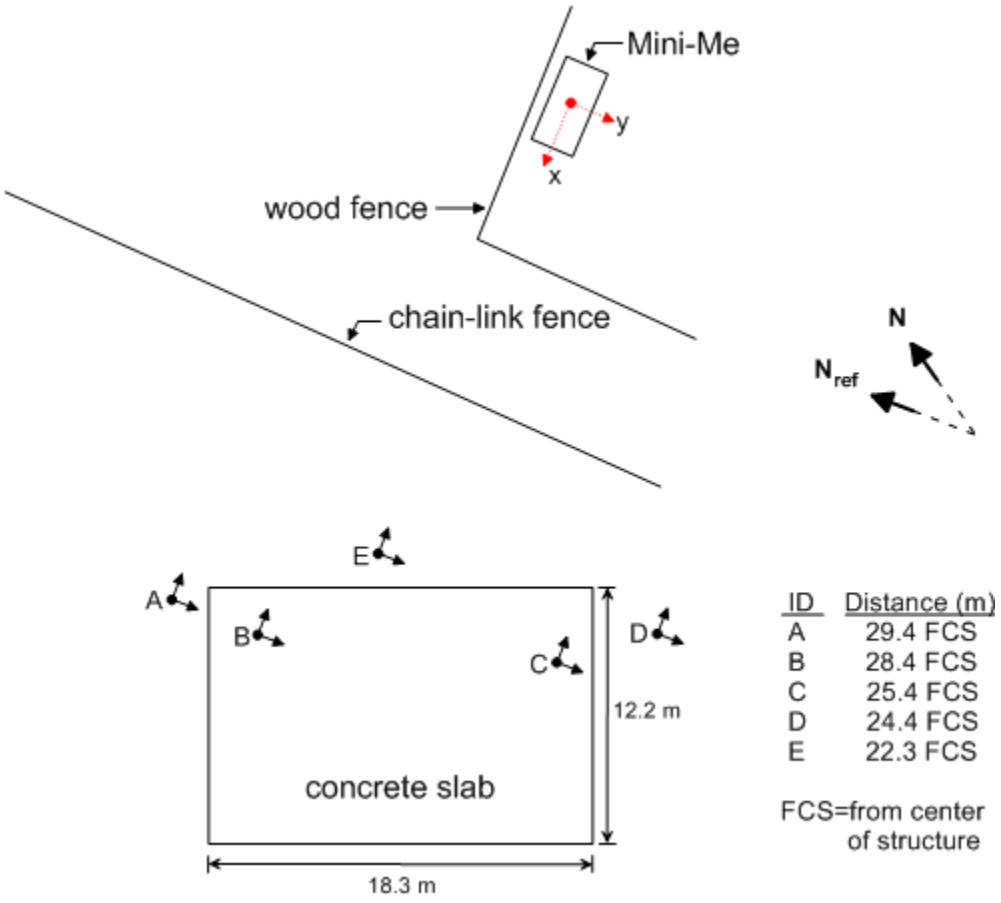

Figure 6-39 **Sketch showing the kinematic interaction test setup with an instrumented concrete slab near the location of the forced vibration testing of Mini-Me. The sensor IDs are shown along with their distance from the center of the Mini-Me test structure.**

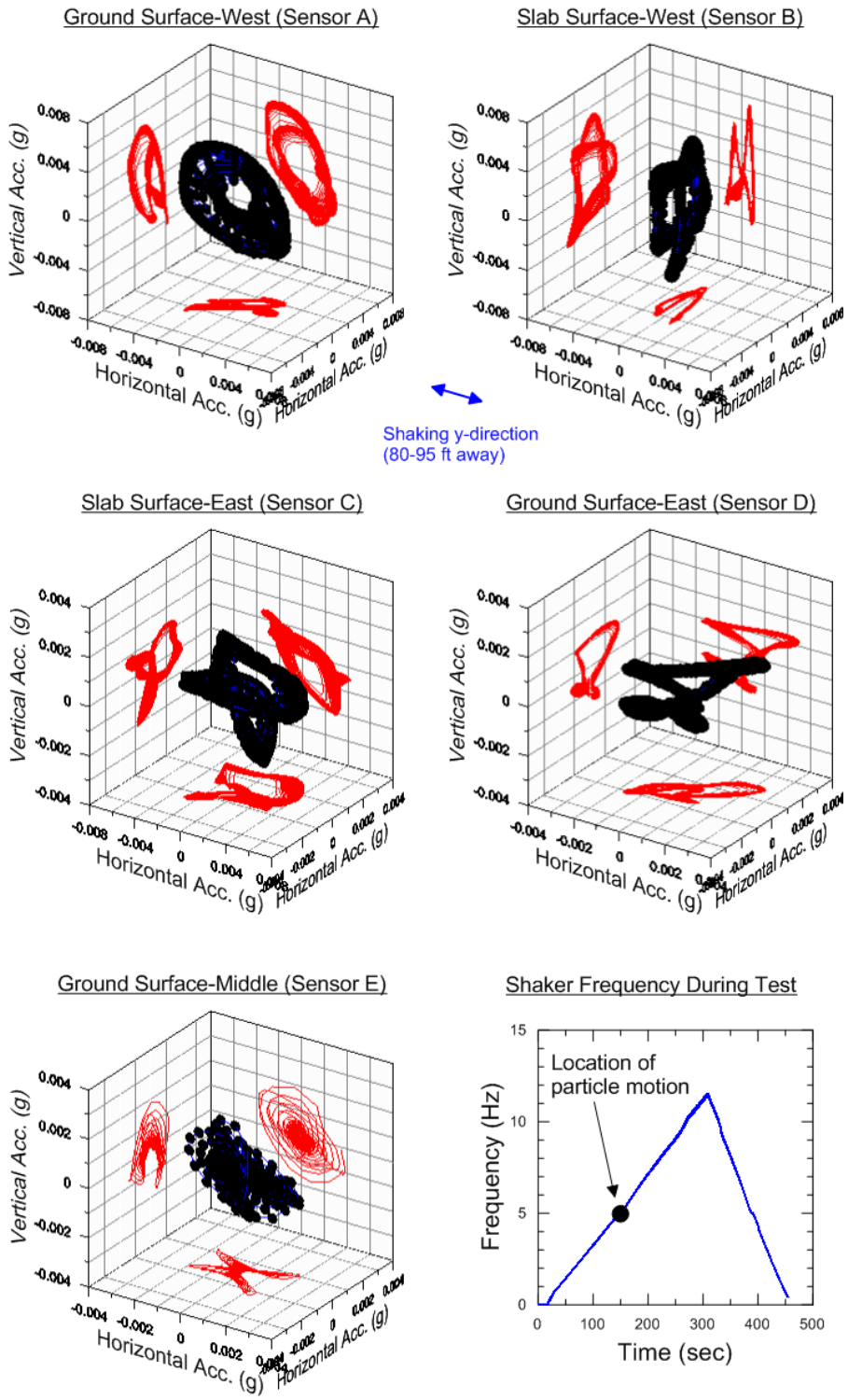

Figure 6-40a **3D depiction of particle motions at each accelerometer (A-E) at 5 Hz frequency excitation as shown in the bottom right corner (Mighty Mouse shaker frequency).**

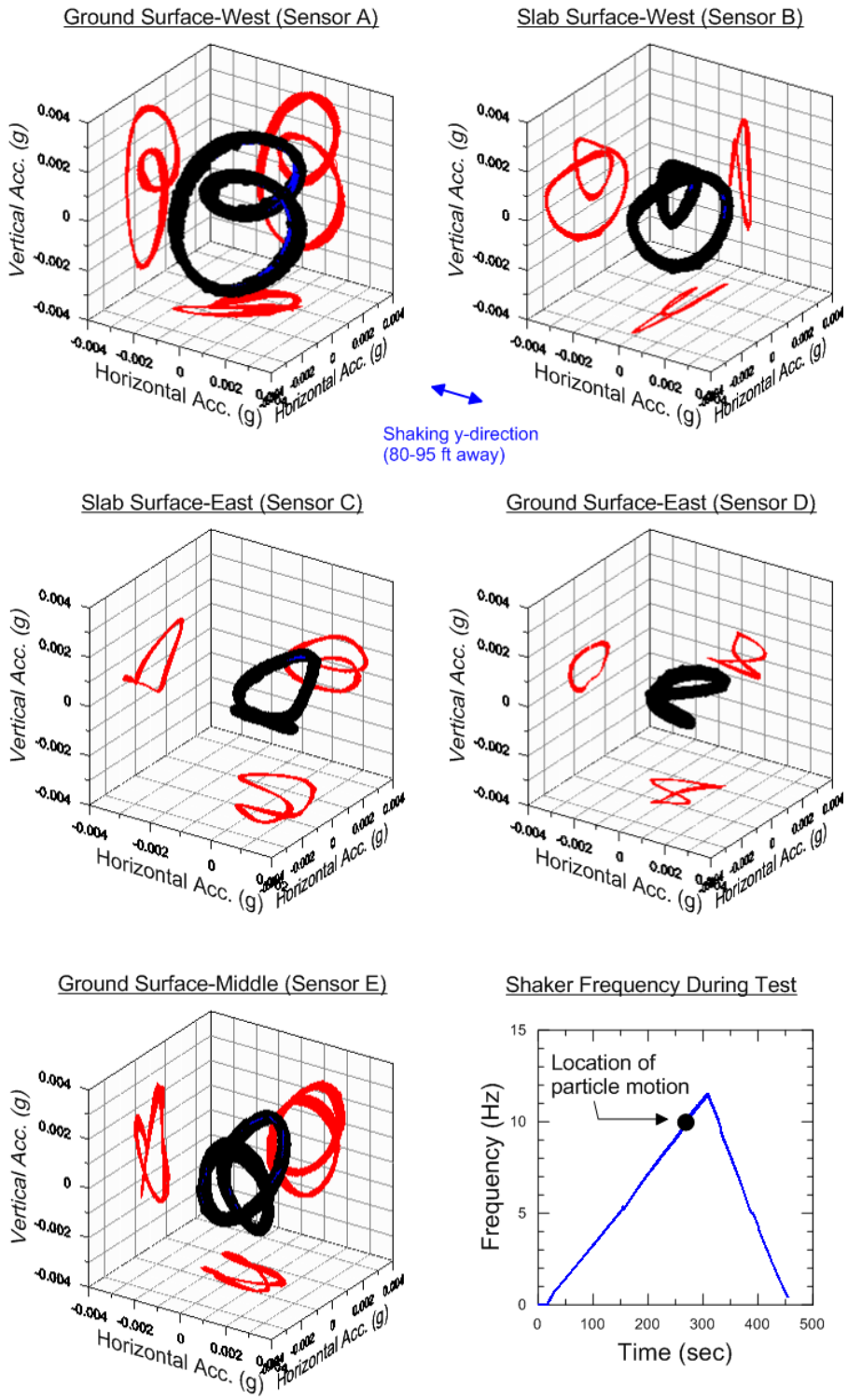

Figure 6-40b **3D depiction of particle motion at each accelerometer (A-E) at 10 Hz frequency excitation 10 Hz as shown in the bottom right corner (Mighty Mouse shaker frequency). Based on Exp. 3.5.1 data.**

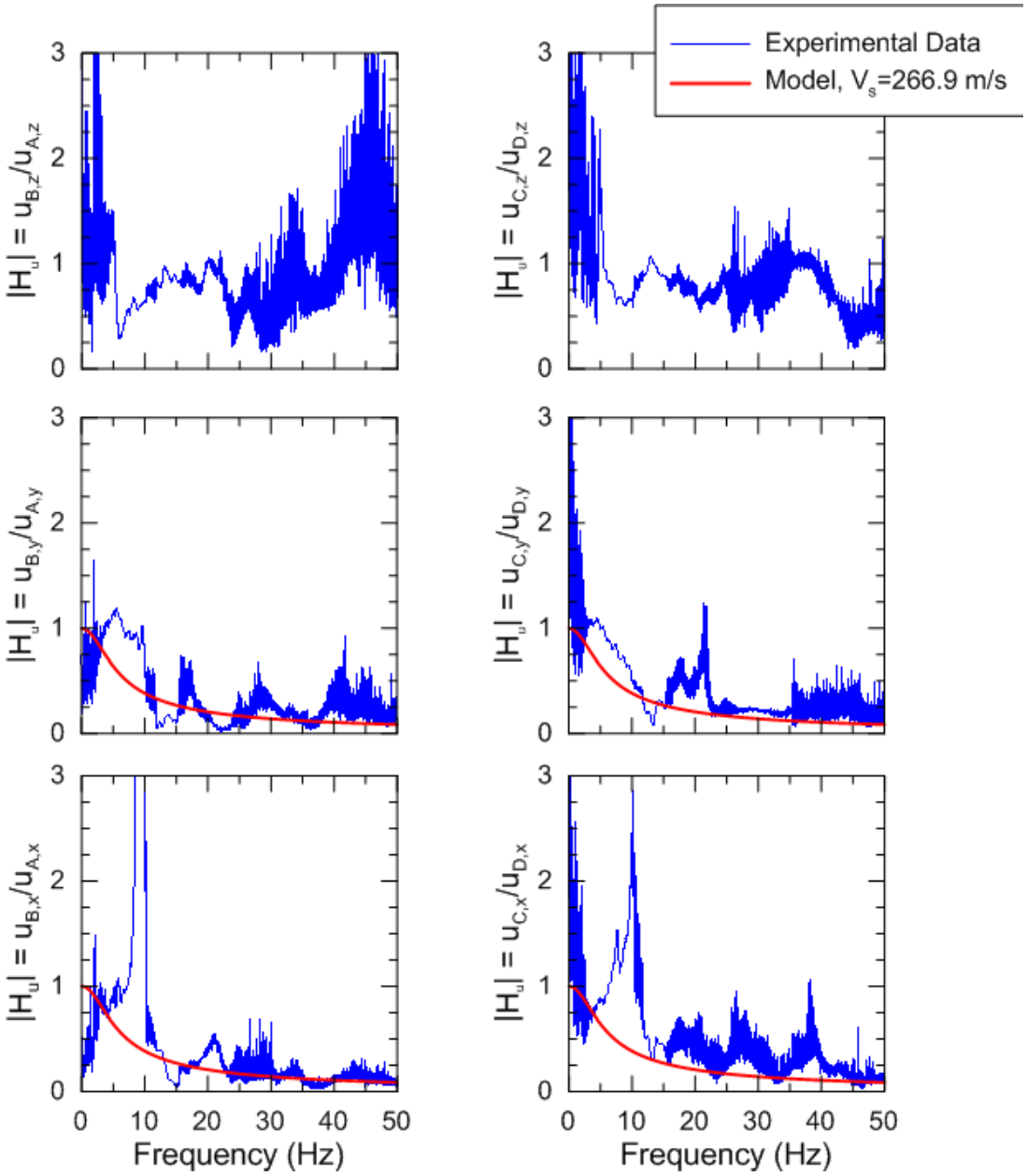

Figure 6-41 **Experimental vertical and horizontal transfer functions (H_u) shown in blue and the predicted horizontal H_u shown in red. Seismic source was from the harmonic forced vibration testing of Mini-Me structure with shaking from the Mighty Mouse shaker at 100% ecc. in the *y*-direction. Based on Exp. 3.5.1 data.**

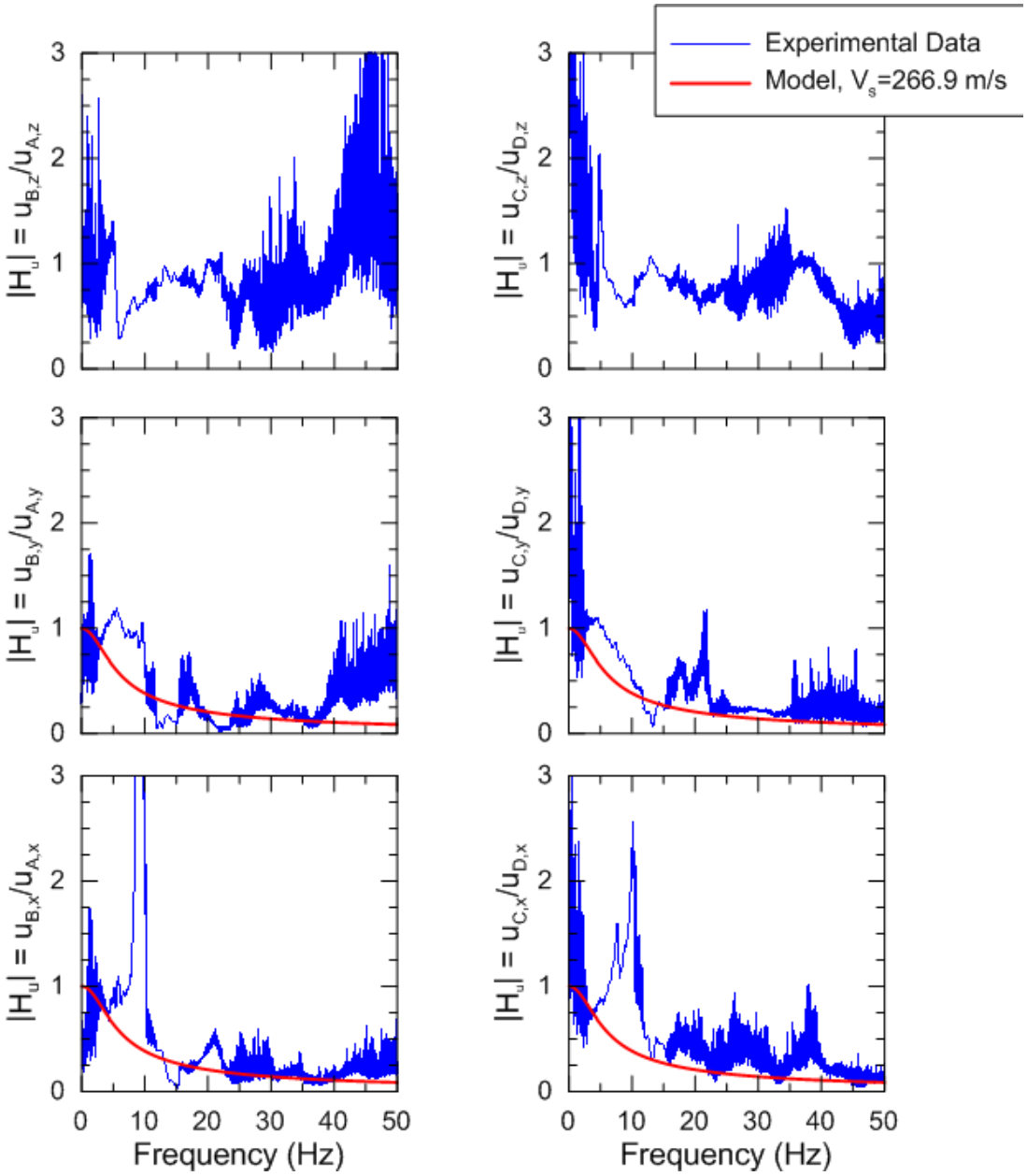

Figure 6-42 **Experimental vertical and horizontal transfer functions (H_u) shown in blue and the predicted horizontal H_u shown in red. Seismic source was from the harmonic forced vibration testing of Mini-Me structure with shaking from the Mighty Mouse shaker at 100% ecc. in the *y*-direction. Based on Exp. 3.5.2 data.**

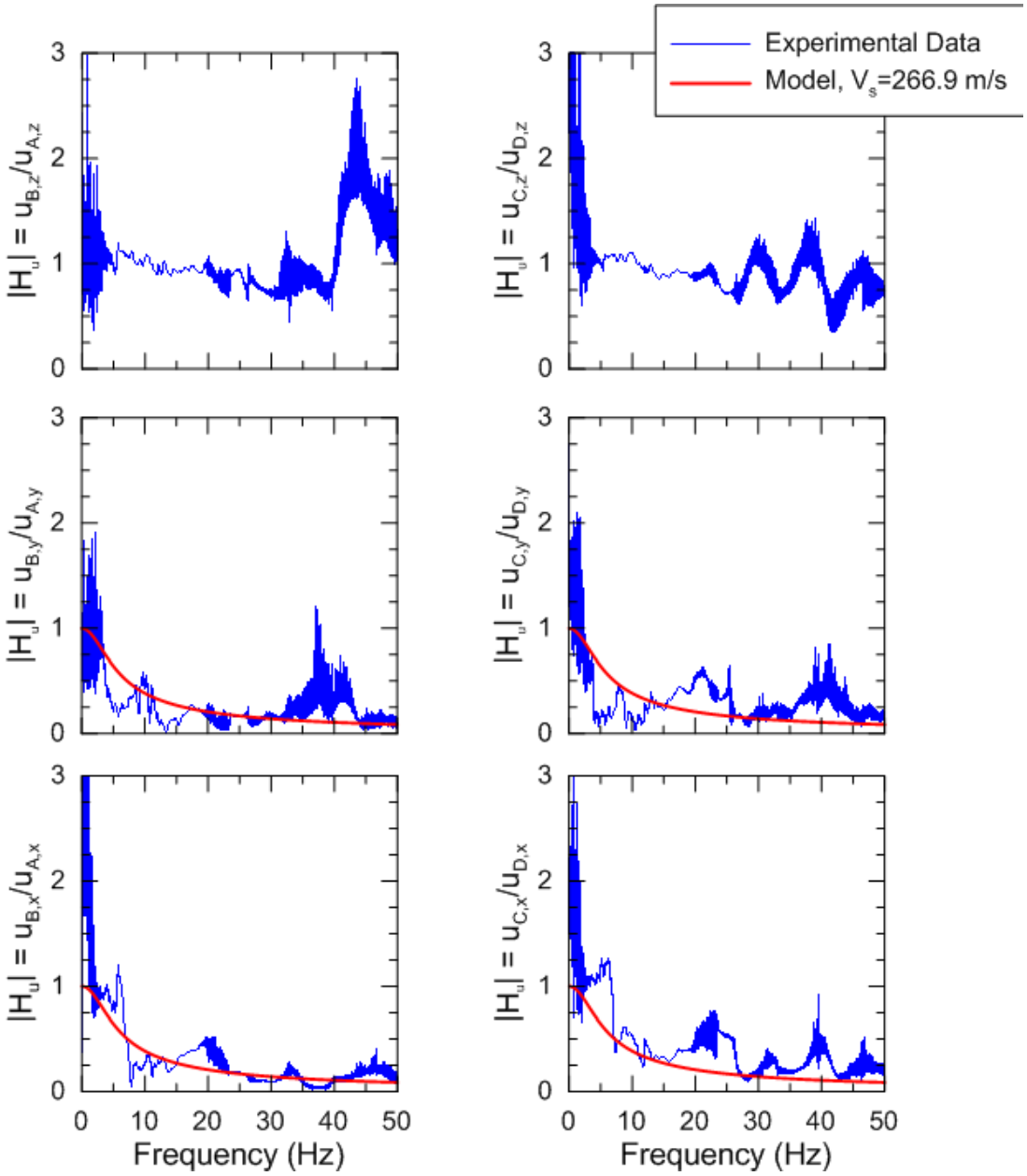

Figure 6-43 **Experimental vertical and horizontal transfer functions (H_u) shown in blue and the predicted horizontal H_u shown in red. Seismic source was from the harmonic forced vibration testing of Mini-Me structure with shaking from the Mighty Mouse shaker at 100% ecc. in the *y*-direction. Based on Exp. 3.5.3 data.**

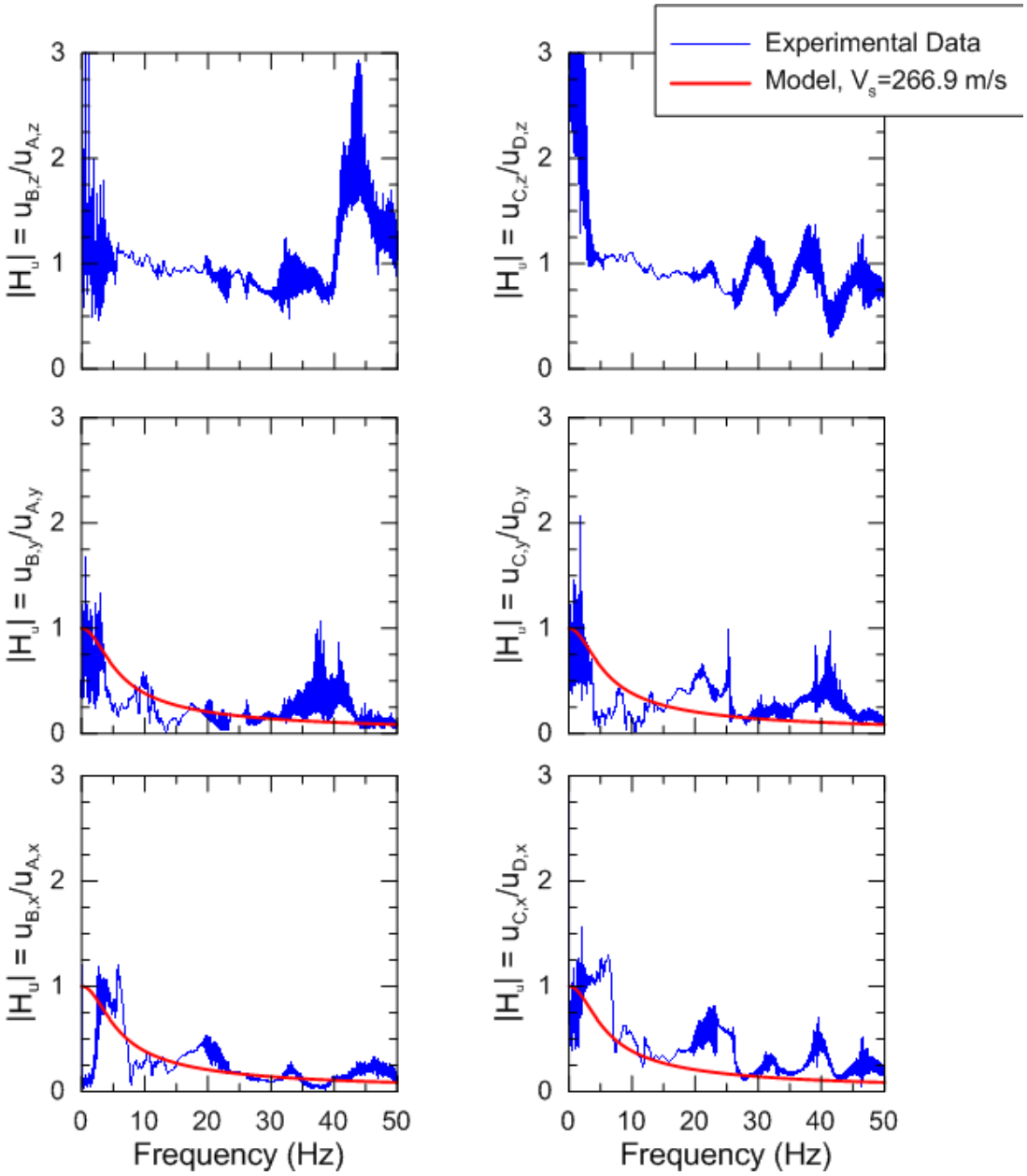

Figure 6-44 **Experimental vertical and horizontal transfer functions (H_u) shown in blue and the predicted horizontal H_u shown in red. Seismic source was from the harmonic forced vibration testing of Mini-Me structure with shaking from the Mighty Mouse shaker at 100% ecc. in the *y*-direction. Based on Exp. 3.5.4 data.**

6.8 Structure-Soil-Structure Interaction from Forced Vibration Testing

The forced vibration testing at GVDA described in Chapter 5 provides a unique opportunity for investigation of the interaction of the forced vibrations from Mini-Me to Dr. Evil through the soil medium. Luco and Contesse (1973) numerically investigated the effects of SSSI from vertical incident SH waves. They found SSSI can be important at low a_0 values (< 2) and at the fixed-base first-mode frequency of the adjacent structure. In this section, I evaluate SSSI occurring during forced vibration testing that is principally emitting surface waves. The absence of the body waves allow for a direct evaluate of the energy transmitted to Dr. Evil during testing, using transfer functions. Transfer functions and coherence are calculated as described in Section 3.4.1 with Eqs. (3-4) and (3-5). However, for these analyses the 'input' is the foundation translation of Mini-Me (u_{MM}), while the 'output' is the foundation translation of Dr. Evil (u_{DE}).

To evaluate the varying interactions from different loading forces, transfer functions were performed using the foundation response histories from the experiments outlined in Section 5.4 (Table 5-7, Figure 5-14) that represent a spectrum of loading conditions tested at GVDA. The sensor locations, foundation locations, and acceleration records for the tests analyzed (referenced as small, medium and large amplitude force tests) are shown in Section 5.4 (Figures 5-15e, 5-16e, 5-17e, respectively). All three tests had the shaker installed on the roof with the shaking applied in the *y*-direction (towards Dr. Evil). Both structures were in the unbraced condition during these tests. Accelerometers situated closest together in the direction of shaking were used for

analysis (Dr. Evil, Ch. 30 and Mini-Me, Ch. 3). Figures 6-45 through 6-47 show the transfer functions and coherence of the SSSI between the two structures at GVDA.

Figure 6-45 shows results from small amplitude force (Exp. 3.3.5a, Atom Ant Shaker), which is not expected to produce nonlinearity in the response of the foundation soils. The transfer function amplitude rises from 0.04 to about 0.1 from 6-25 Hz. A distinctive peak is observed following the first-mode frequency (Section 6.6.2, f_1 = 11.5 Hz) of Mini-Me.

Figure 6-46 shows results from medium amplitude force (Exp. 3.4.1a, Mighty Mouse 5% ecc.), which is expected to produce nonlinearity in the response of the foundation soils. Shaking for this test was limited to the frequency range of 4-18 Hz. The transfer function shows a general amplitude trend at about 0.025 with a small peak to 0.08 at 5.5 Hz.

Figure 6-47 shows results from large amplitude force (Exp. 3.4.19a, Mighty Mouse shaker full force) testing that was limited from 4-12 Hz to stay in the safe limits of operation. As discussed in Section 5.4, the loading conditions caused gapping of the foundation from rocking that was consistent with visual observations in the field. The transfer function shows a decrease for low frequencies (3-6 Hz) that drops by an order of magnitude (0.04 to 0.004) and then increases to 0.03 at 12 Hz. Figures 6-45 through 6-47 show that from small to large amplitude force testing the transfer functions decrease. The nonlinearity produced in the response of the foundation soils tend to reduce the interaction between the structures.

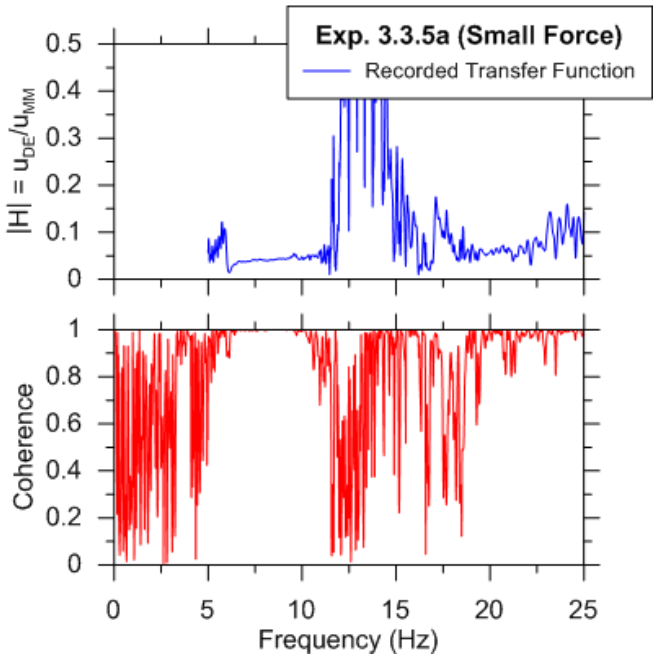

Figure 6-45 **Transfer function and coherence for Dr. Evil and Mini-Me foundations. Exp. 3.3.5a (Unbraced structure, shaking in y-direction with Atom Ant).**

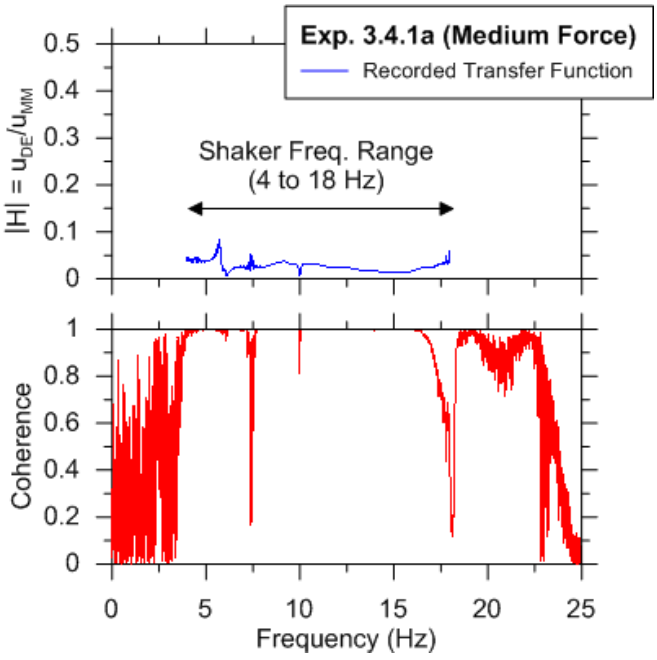

Figure 6-46 **Transfer function and coherence for Dr. Evil and Mini-Me foundations. Exp. 3.4.1a (Unbraced structure, shaking in y-direction with Mighty Mouse 5% ecc).**

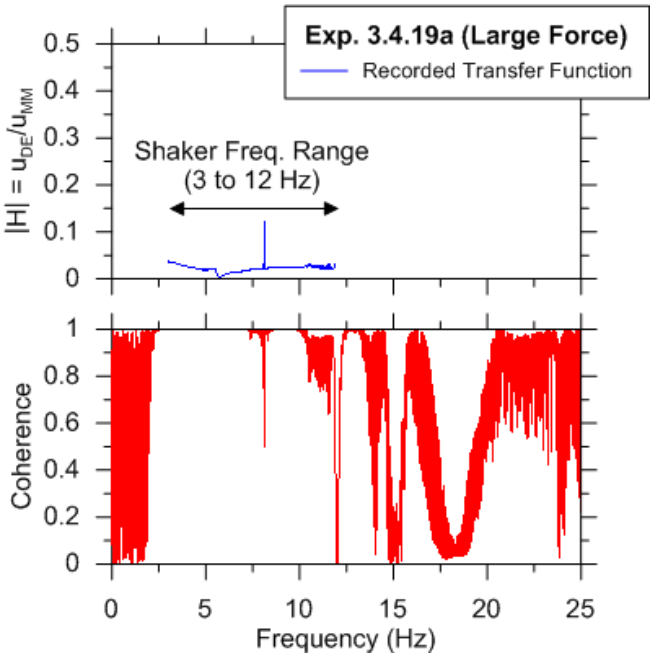

Figure 6-47 **Transfer function and coherence for Dr. Evil and Mini-Me foundations. Exp. 3.4.19a (Unbraced structure, shaking in y-direction with Mighty Mouse 100% ecc).**

6.9 Interpretation of Soil-Structure Interaction Effects from Forced Vibration Testing

6.9.1 Small Amplitude Forced Vibration Testing

Small amplitude harmonic forced vibration testing was performed to evaluate the relatively linear range of the SSI system. A relatively uniform load across the range of 4-50 Hz was applied by the linear mass shaker referred to as "Atom Ant." As shown for Experiment 3.3.5a in Figure 6-10, the response loop for translation show a frequency independent demand on the soils.

The shaker location of applied force and structure stiffness (i.e. bracing condition) introduced local complexities (i.e. near the bracing frequency). The Atom Ant shaker was

tied and secured in place during testing at the roof slab, whereas shaking applied at the foundation slab only used the weight of the shaker itself. The lack of an external mount (i.e., rope or bolts) during shaking at the foundation slab introduced noise into the data obscuring the impedance results, as shown in Figures 6-20 to 6-23. Testing in the braced condition resulted in additional noise at the resonance of the braces. As displayed in Figures 6-18 and 6-19, obvious disturbances in our ability to read the impedance function trends are seen at 15 Hz.

The experiments having the cleanest data sets at GVDA are those from the structure in an unbraced condition with forcing at the roof. The testing was absent of the bracing resonance effect and the shaker was secured in place so that no adverse (artificial) displacements would occur during the test experiment. Therefore the remainder of this section will discuss interpretations of the small amplitude forced vibration testing shown in Figures 6-16 and 6-17.

The horizontal translational stiffnesses were observed as frequency independent and stable from about 4-20 Hz. The observed translational stiffnesses are softer than predicted based on direct crosshole testing of the soil after construction (Model 1). The translational stiffnesses were closest to the predictions based on Model 2 velocities back-calculated from field data, which excludes overburden pressures from the structure. Shaking in the *y*-direction resulted in lower translational stiffnesses as compared to shaking in the *x*-direction. This contradicts the models that predict the opposite trend (*y*-direction stiffness $\geq$ *x*-direction stiffness). A 15% reduction of the overburden in-situ shear wave velocity (V_s) would be required to match the experimental translational

stiffness in the *y*-direction, while the *x*-direction is matched well by Model 2 (which is a 10% reduction). One speculation is that the reduction from the expected stiffnesses (Model 1) arises from localized shearing of the soil underlying the foundation. The dynamic interaction of the concrete-soil contact could cause disturbances to the shear stiffness of a thin layer of soil in the immediate vicinity of the foundation that are not captured by the crosshole seismic testing at 1m (3.3 ft) depth.

The rotational stiffnesses and damping ratios showed a frequency-dependency (4-20 Hz), where the rotational stiffnesses decreasesat higher frequencies. When shaking the structure in the *x*-direction, the rotational stiffness matched the expected results of Model 1, whereas shaking *y*-direction produced a rotational stiffness that was softer than expected and matched Model 2. The translational damping ratios were also relatively well captured by Model 2. The predictive models underestimated the rotational damping ratios compared to the observed results. The larger than predicted rotational damping is suspected to arise from one or a combination of the following phenomena (listed in no particular order):

1. Hyperelasticity in the underlying soils produced from the rocking mode of vibration.
2. Small compliances (flexibility) of the foundation that introduce out-of-phase radiation waves from the sides of the foundation. Such waves would be destructive resulting in more than expected radiation damping.
3. Foundation-soil contact friction.

4. A thin, soft unidentified layer under the foundation where the V_s is smaller than the surrounding material.
5. Model-based radiation damping is limited because it applies for homogeneous soil conditions in which upward and downward excitation from a rocking slab effectively cancels out at large distances (St. Venant's principal, as applied to a dynamic problem). In contrast, the actual site lacks homogeneity, so the perfect cancelation of the radiated waves does not occur, increasing radiation damping relative to model predictions.

6.9.2 Large Amplitude Forced Vibration Testing

Large force harmonic excitation is expected to produce some nonlinearity in the response of the foundation soils. The cyclic load-deformation loops were established for the translation-shear and rocking-moment (as previously shown in Figures 6-10, 6-12, and 6-14). Figures 6-48 and 6-49 show lines representing secant stiffnesses for particular loops (lines and loops for a common frequency share a like color). Figure 6-48 and Figure 6-49 show the impedance and cyclic loops from testing in the *y*-direction from the 'moderate' force Experiment 3.4.1a (max force of 7.1 kN) and 'large' force Experiment 3.4.19a (max force of 61.7 kN), respectively. The decreasing trend (3-8 Hz) and then increasing trend of the stiffnesses (8-15 Hz) of the foundation-soil system occurs for frequencies below and above, respectively, the system's resonant frequency. Those trends are illustrated by both the impedance functions and loop slopes. As a check of the impedance ordinates evaluated from frequency-domain procedures (Section 6.5), we plot in Figures 6-48 and

Figure 6-49 discrete dots representing the slopes of the secant lines at selected frequencies (the agreement is excellent).

Forced vibrations with the Mighty Mouse shaker were performed while the structure was in braced and unbraced conditions. A series of tests were performed at varying degrees of intensity conditioned in the field by the percent eccentricity of the shaker. The shaker force was proportional to the frequency and mass eccentricity. This resulted in the maximum forces near the maximum frequency of the test, with the mass situated at 100% eccentricity being the maximum force tested at GVDA. The approximated nonlinear nature of the soil below the foundation shows the same trend. The shaker force introduces a frequency-dependency into these tests.

The translational and rotational stiffnesses generally follow the trend of the approximated nonlinearity of the soils underlying the foundation. Low eccentricity (5-10 %) produce similar results as the low amplitude force testing at low frequencies (2-5 Hz). As the frequency increases, the foundation soil becomes increasingly nonlinear as indicated by lower foundation stiffnesses. As the eccentricity is increased (25-100%), the stiffness impedance functions become much lower than the low-force testing results even at low frequencies (2-5 Hz).

The structural condition (i.e. braced or unbraced) affects the overall trend of the system stiffness because of its affect on the system's resonant frequency. As frequency increases for the unbraced case (e.g. Figure 6-30), the demand increases causing a reduction in the soil stiffness until the resonant frequency is reached. Then the soil stiffness rebounds and strengthens, whereas the braced condition (e.g. Figure 6-34)

produced a gradual reduction over the frequencies tested (4-14 Hz). The resonance of the bracing is not as pronounced in the impedance functions from large shaker as previously seen in the low-force amplitude testing.

The existence of negative damping ratios of the large-force test results (e.g. Figure 6-24) indicate that the results have been compromised. It is suspected that phasing issues derived from either the Mighty Mouse data acquisition (DA) system or the synchronization of the two DA systems resulted in irrational results. Many of the damping ratios show negative results for low frequencies (2-6 Hz). The Mighty Mouse shaker force was derived by converting a recorded pulse at the time when the weights were aligned in the direction of loading. Sensitivity studies were performed to evaluate if a phase shift of the shaker pulse would produce more realistic results. It was found that improvement could be made at low frequencies, but at the cost of the accuracy of the higher frequencies. Therefore, it is suspected that some of the damping ratio results are realistic, but there are no means to classify the difference. Another possibility for the negative damping ratios at low frequencies could be the small phase difference at low frequencies and our ability in resolving through measurements of the very small numbers. If the latter is true, then at the larger frequencies where phase differences increase, the results would be considered more reliable.

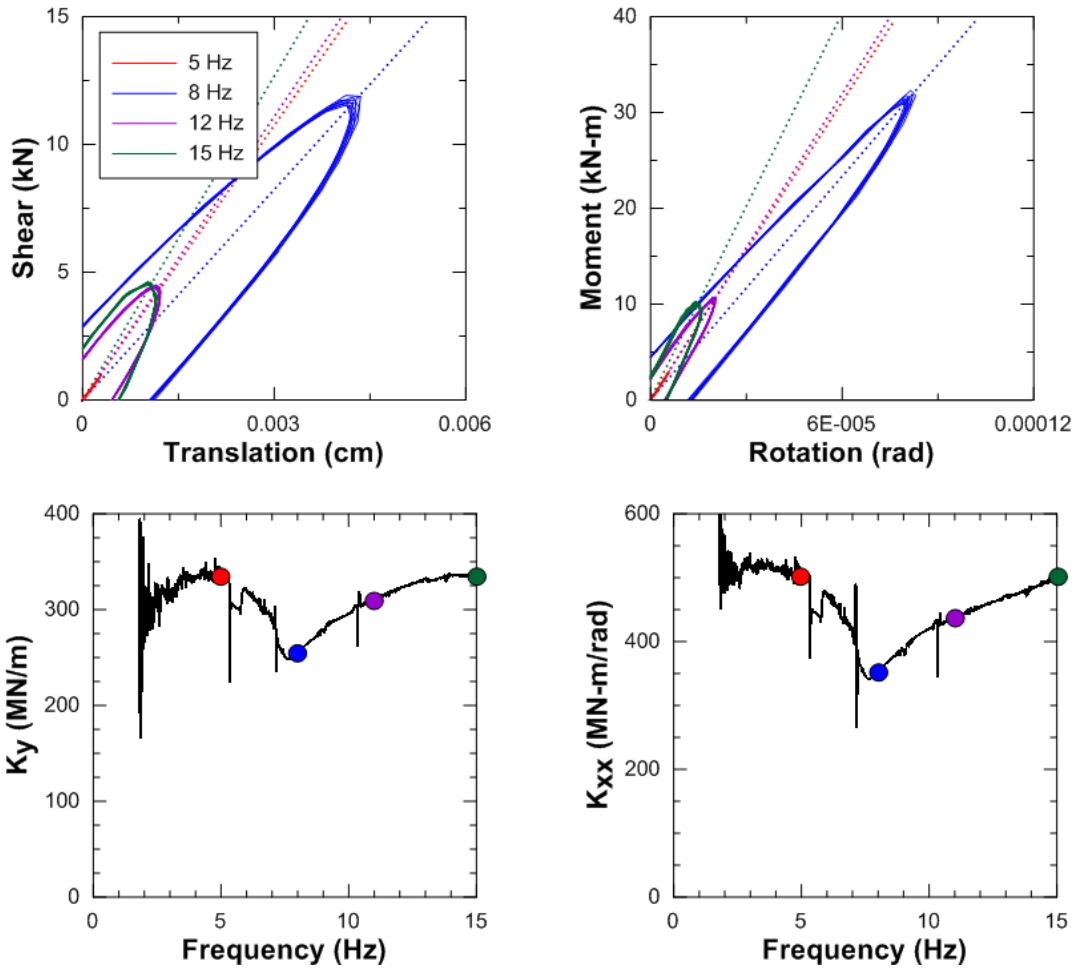

Figure 6-48 **Hysteretic response secant stiffnesses (depicted by the dotted lines) and their relationship to the load-deformation loops for the system. Exp. 3.4.1a (Unbraced structure, shaking in the y-direction with Mighty Mouse at 5% eccentricity).**

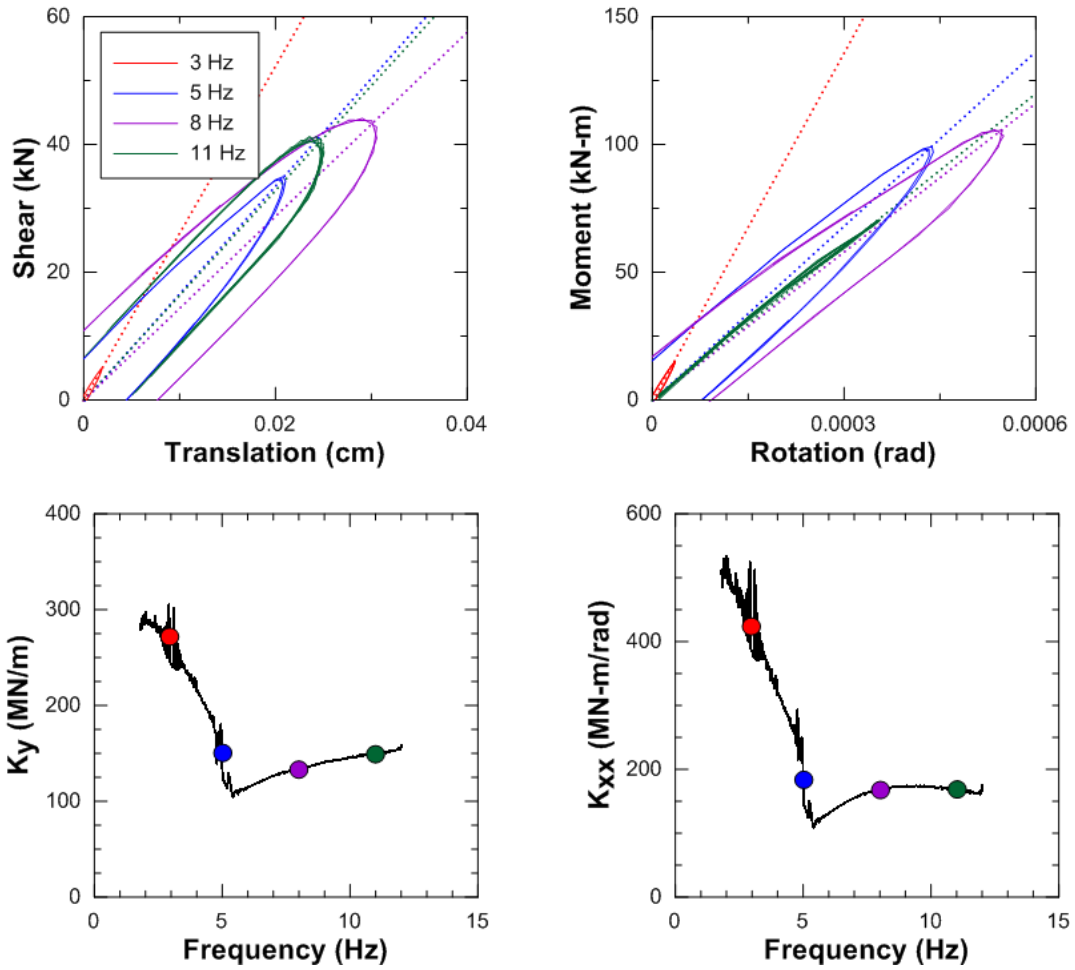

Figure 6-49 **Hysteretic response secant stiffnesses (depicted by the dotted lines) and their relationship to the load-deformation loops for the system. Exp. 3.4.19a (Unbraced structure, shaking in the y-direction with Mighty Mouse at 100% eccentricity).**

6.9.3 Small Amplitude to Large Amplitude Comparisons

Figure 6-50 shows a comparison of the normalized experimental results for the small (AA shaker), moderate (MM shaker @ 5% ecc.) and large (MM shaker @ maximum capacity) representative force cases, as shown in Table 5-8. The stiffnesses are normalized by G_0B and G_0B^3 for translation and rocking, respectively, where G_0 is the

small-strain maximum shear modulus of the soil. The model in Figure 6-50 results from the normalization of Model 1 and Model 2. The frequency axis in Hz has been replaced with dimensionless frequency a_0 (Eq. 2-7b).

The small force produced results over the broadest range of frequencies (a_0 = 0.2 – 1). As force amplitude increased, the frequency ranges narrow: a_0 = 0.1 – 0.6 for moderate forces and a_0 = 0.05 – 0.4 for large forces. The large range produced by the small force is a result of the small shaker's force being relatively consistent and not proportional to frequency. Therefore, the Atom Ant shaker could be applied to higher frequencies (up to 45-50 Hz). In contrast, the Mighty Mouse shaker force is proportional to frequency and has limiting conditions based on safety of the equipment. As loading increases, observed foundation stiffnesses decrease, indicating an increase in strain applied to the soils underlying the foundation. Based on the phasing issues discussed in Section 6.9.2, the damping results at low frequencies appear to be in error. However, it is suspected from sensitivity studies that the moderate force results are reliable for a_0 = 0.3-0.6. As forces increase to higher frequencies, the translational damping ratio matched the Models well, while the rotational damping ratio was larger than expected. The sensitivity studies involved incremental changes to the recorded angular position of the large shaker rotating masses described in Eq. (5-2). As the angular position was changed by a few degrees, resulting in an updated forcing function, the observed impedance functions improved compared to the models at lower frequencies. However this was at the cost of the observed impedance functions at higher frequencies.

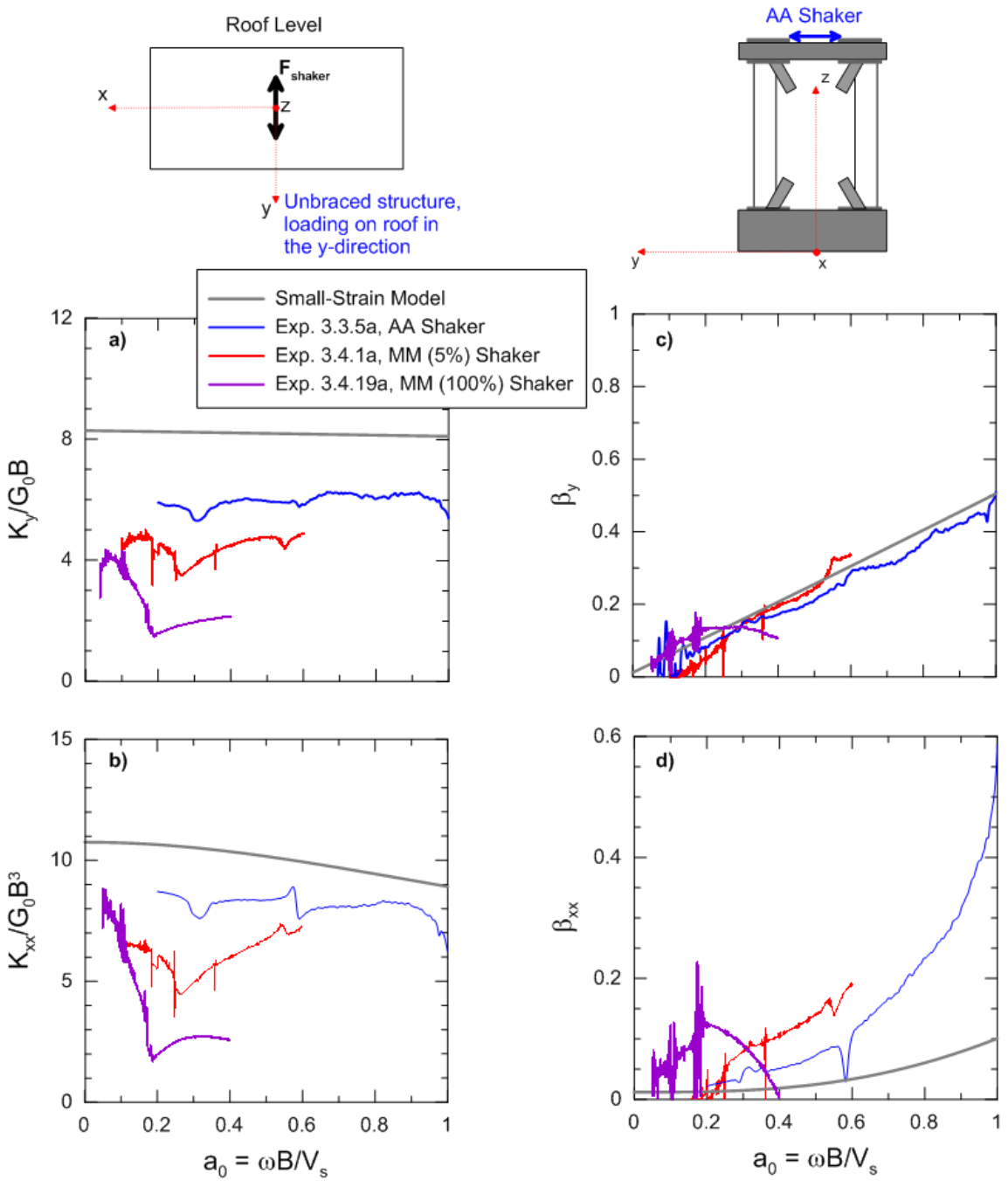

Figure 6-50 **Normalized impedance function results from analysis of the Mini-Me test structure (unbraced condition) loaded on the roof in the y-direction by various loading amplitudes. The plots show impedance functions in the a) translational and b) rocking modes of vibration. The bottom plots represent the soil nonlinearity for each mode.**

6.9.4 GVDA Results and Previous Studies

Figure 6-51 shows a comparison of the normalized stiffness and damping ratios from WLA and GVDA for shaking with Atom Ant at the roof in the *y*-direction. The stiffnesses are normalized by the site-specific G_0 and B (translation) or B^3 (rocking). Additionally all impedance functions are plotted against a_0 rather than frequency in Hz. Two models using Table 2.1 impedance functions have been plotted. To represent the different sites the models use a ν=0.45 and ν=0.33 to represent the WLA and GVDA sites, respectively. The models show a Poisson's ratio effect in which stiffness increases and damping decreases as Poisson's ratio increases. With the exception of the translational damping ratio, this Poisson's effect is also evident in the observed data. It should be noted that a prominent difference between the two testing schemes was that no external support for the shaker was used at WLA. As a result, the GVDA testing produced more stable results to higher frequencies (a_0 = 1) compared to WLA. The deviation from the expected trend of the WLA results at a_0 > 0.5 is likely due to slip of the shaker on the top slab of Mini Me.

Previous case studies performed for evaluation of impedance functions from forced vibration testing have been discussed in Section 6.2. The results of the previous studies have been visually discritized and fit with spline smoothing. The fitted curves were then normalized by their site-specific G_0 and foundation half-width (B) raised to an appropriate power (one for translation, three for rocking). Figure 6-52 shows normalized results of the impedance functions for the previous studies described in Section 6.2 with

the omission of GVDA and WLA. As represented in Table 6-1, previous studies typically had foundations with $L/B = 1$, whereas GVDA and WLA structure has $L/B = 2$. Therefore for comparative reasons Figure 6-51 shows only the recent studies of Mini-Me with $L/B = 2$, whereas Figure 6-52 shows previous studies with foundations of $L/B = 1$. This presentation allows for a direct comparison of the stiffness and damping effects investigated from forced vibration testing. For comparison a predicted model using Table 2-1 impedance functions with $L/B = 1$ is included in Figure 6-52. It should be noted that the models use a consistent ν=0.33 even though some sites are situated on soils with larger values of ν (clay sites). That would produce similar results as discussed in relation to Figure 6-51

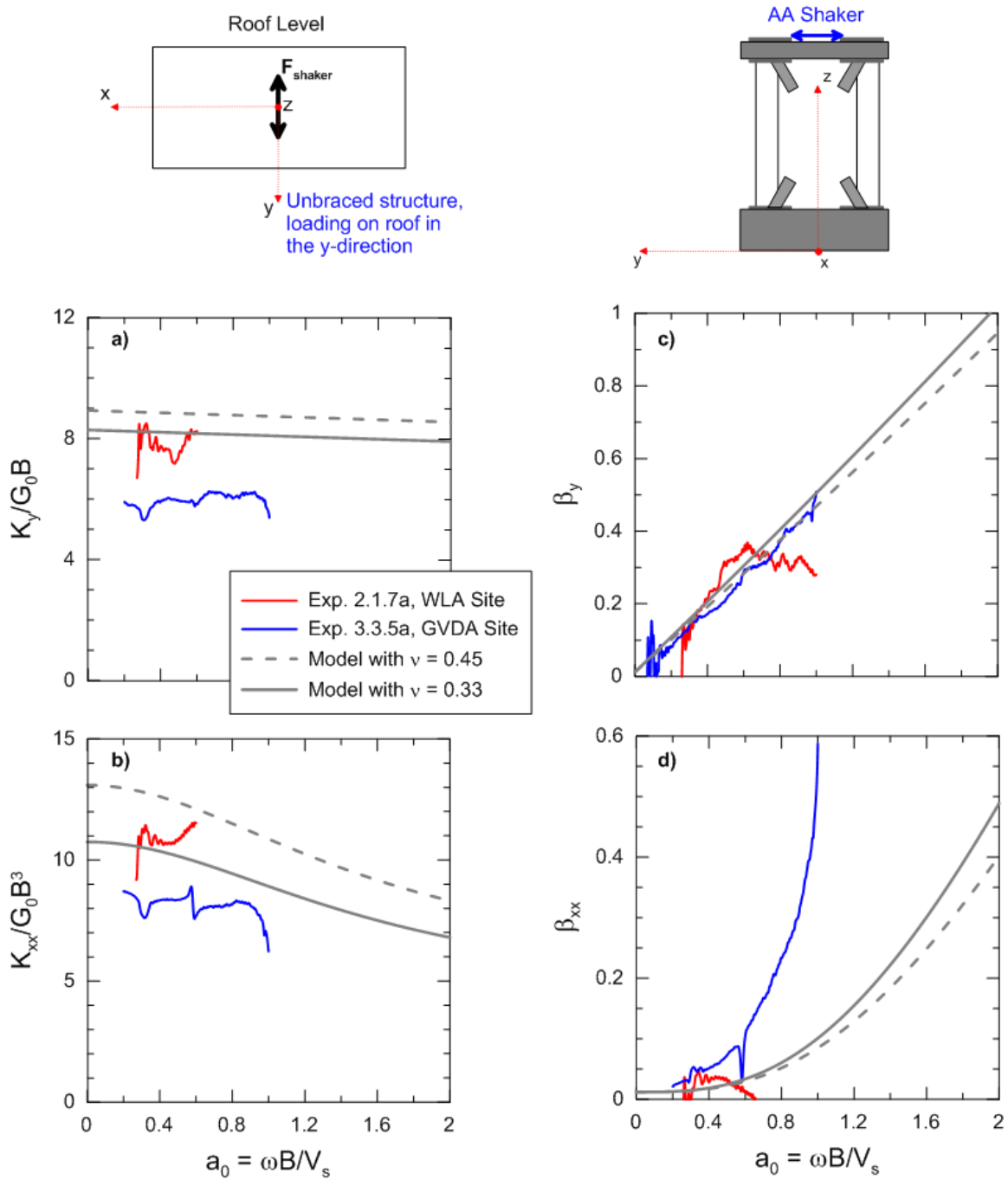

Figure 6-51 **Normalized impedance function results from analysis of the Mini-Me test structure (unbraced condition) loaded on the roof in the y-direction with Atom Ant shaker at GVDA (Exp. 3.3.5a) and WLA (Exp. 2.1.7a). The plots show the a) horizontal translational stiffness, b) rotational stiffness, c) horizontal translational damping ratio and d) rotational damping ratios. Included are modeled impedance functions based on Table 2.1 for ν = 0.33 and ν = 0.33.**

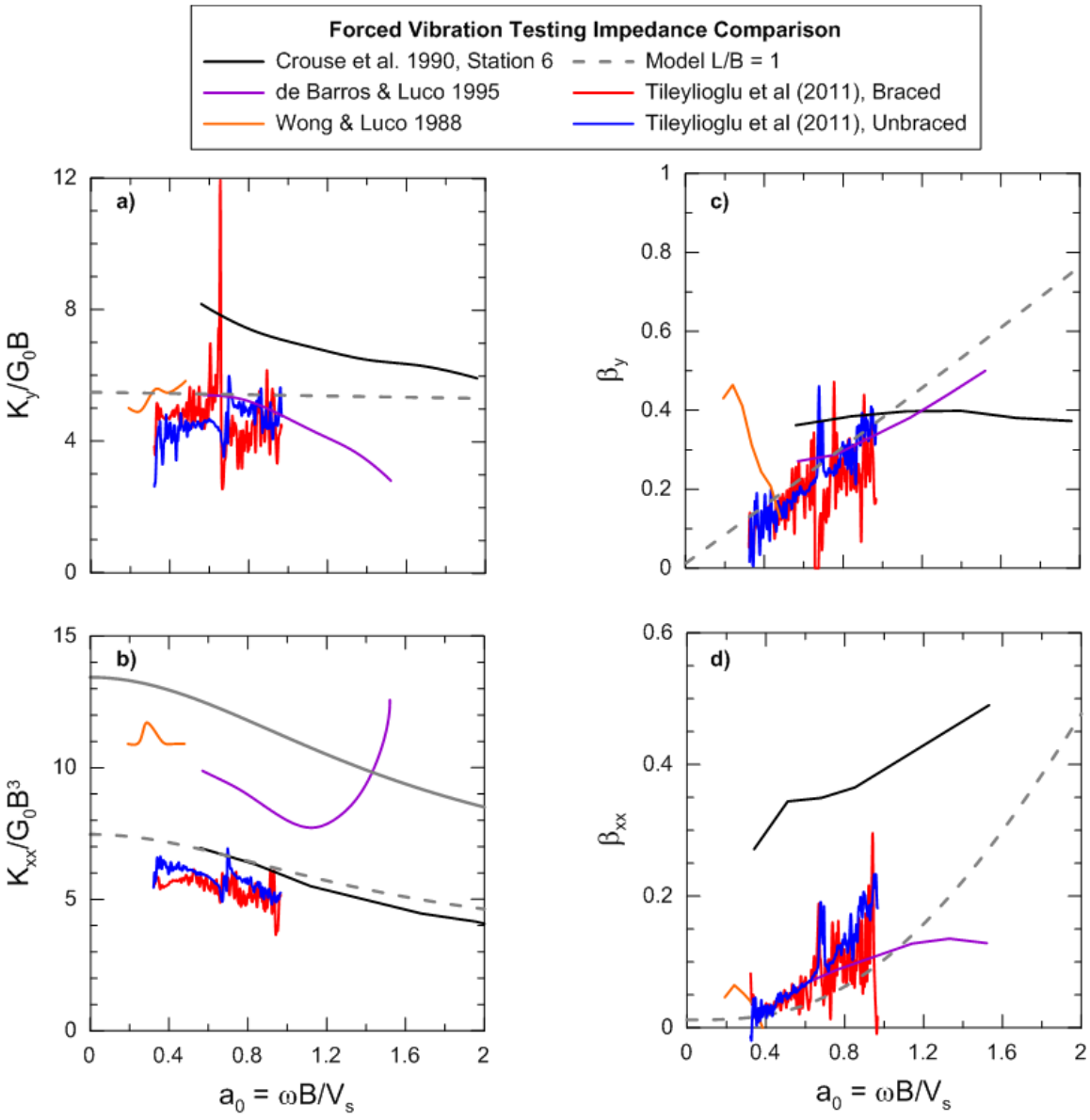

Figure 6-52 **Normalized impedance function results from previous forced vibration studies. The plots show the a) horizontal translational stiffness, b) rotational stiffness, c) horizontal translational damping ratio and d) rotational damping ratios. Included are modeled impedance functions based on Table 2.1 for *L/B*=1 using ν = 0.33 and D=0.**

6.9.5 Kinematic Interaction and Structure-Soil-Structure Interaction Interpretation

Kinematic interaction (Section 6.7) and structure-soil-structure interaction (SSSI) (Section 6.8) effects were investigated from the data accumulated from the forced vibration testing at GVDA. The forced vibrations of the structure produced principally surface waves, , whereas seismic excitation over the frequency range of typical interest in kinematic SSI problems is dominated more by body waves. Surface waves could be expected for SSSI problems, however, the SSSI problem would typically be introduced from body waves and then surface waves could be generated from both structures.

The particle motions discussed in Section 6.7 showed the phenomenon of base-slab averaging. The averaging was only slight in that the motions were not the same at both sides of the slab. General trends of the motions on the slab were similar whereas the adjacent ground surface motion was distinctly different. The vertical transfer functions were observed to be about one, while the horizontal transfer functions generally decreased with frequency. The NIST horizontal transfer function model discussed in Chapter 3, matched the experimental data well, with the exception of some peaks that were greater than the model.

Three transfer functions are evaluated to investigate the relative motions of the Mini-Me and Dr. Evil foundations from small, medium and large amplitude forced vibrations. Only the small amplitude testing (Figure 6-45) showed a distinctive response of Dr. Evil's foundation near the fixed-base first-mode frequency of Mini-Me. However as the loading and induced nonlinearity of the foundation soils increased, the interaction of the systems decreased. Particularly this can be seen by comparing the approximated

strain and shear modulus reductions for the same test (Figure 6-28). The distinctive reduction to the transfer function up to 6 Hz (Figure 6-47) correlates well to the increased strain to the foundation soils. However the transfer function shows a rebound whereas the strain rate is approximated as unchanged (no decrease) for the higher frequencies.

6.10 Conclusions

The forced vibration testing at GVDA produced data that was evaluated for SSI effects (i.e., inertial interaction and kinematic interaction). The most useful data for comparison of experimentally derived impedance functions to the predicted models was from testing performed when Mini-Me was in an unbraced condition and was excited by the small linear mass shaker (Atom Ant) at the roof. During these tests the shaker was secured in-place from movement at higher frequencies. The large eccentric mass shaker (Mighty Mouse) produced forces large enough to cause significant strains in the soils underlying the foundation to behave nonlinear. Monitoring of the concrete slab and adjacent soil during the forced vibration testing provided data for evaluation of kinematic interaction.

The modeled predictions of the impedance functions tended to overpredict the stiffnesses, while the rotational damping ratio is well underpredicted. It was found that a V_s reduction of about 10-15% from the in-situ V_s would be required to match the models to the observed data. The experimental translational stiffness was found to be stiffer in the *x*-direction compared to the *y*-direction, which is the opposite of the modeled results.

The particle motions generated adjacent and on the concrete slab showed an averaging effect. The waves generated at either side of the slab were not identical in motion or amplitude, but did exhibit different motions then the adjacent ground surface

accelerometer. The motions on the slab showed a tendency towards similar motions. Interestingly, kinematic interaction effects observed on an adjacent slab excited principally by surface waves were of a similar character to expectations from analytical models for body wave excitation from earthquakes. If verified, these results could lead to site- and foundation-specific test methods for evaluating kinematic interaction effects.

Structure-soil-structure interaction (SSSI) was briefly investigated from forced vibration testing. Transfer functions showed at small amplitude forces Dr. Evil had a small response at the fixed-base frequency of Mini-Me. The transfer functions showed that nonlinearity significantly reduces the interaction between the foundations.

7 CONCLUSIONS AND RECOMMENDATIONS

7.1 Scope of Research

The objective of this research was to evaluate the effects of soil-structure interaction (SSI) through careful interpretation of available data from instrumented buildings and recently performed forced vibration experiments on instrumented buildings and test structures. Analyses of field performance data was undertaken to provide deeper insights into SSI phenomena ranging from kinematic effects on foundation ground motions to mobilized foundation stiffness and damping across a wide range of frequencies and loading levels. These data were interpreted to evaluate strengths and limitations of engineering analysis procedures for SSI.

Following the introduction of the SSI problem, this research began by studying the contribution of foundation damping to the overall damping of a soil-foundation-structure system (Chapter 2). An initial step commonly taken to evaluate the effect of SSI on the seismic response of a particular structure is a representation through its impact on the fundamental-mode period and damping ratio (i.e., response spectra). As part of this research, two equally viable equations for foundation damping were derived and

compared to previous solutions and empirical data. Current seismic guidelines use foundation damping solutions based on rigid circular foundation types on homogenous half-space. Considering most foundations are neither circular nor situated on uniform soils, procedures were presented to consider various site-specific conditions such as rectangular footprint, embedment and non-uniform soil conditions. The two foundation damping solutions derived as part of this work along with the aforementioned procedures were then compared to empirical data.

Simple kinematic interaction models were compared to newly available Japanese data and more robust finite element modeling results (i.e. SASSI) in Chapter 3. Limited case studies are compared to modeled transfer functions; however, this work expands the data inventory to buildings not located in the California where sites were used to develop the simplified models. A subset of the Japanese buildings includes relatively stout pile foundations that were not part of the earlier California data set. This work is part of a long-term goal to re-generate the kinematic interaction models. Observations as to the comparison of the models and Japanese data transfer functions were made.

Various approaches can be used to analyze seismic response to SSI at the base of a building, including ignoring SSI effects altogether. Chapter 4 presents a study that identifies suitable instrumented buildings that have recorded earthquakes, develops complete SSI models for substructure-based analysis of seismic response (referred to as a baseline model), roughly calibrates the structural elements of the baseline model to approximately match recordings, and then removes components of the baseline model for additional analyses to evaluate the impact of those components. This process was used to

identify the critical components of an SSI model for use in response history analysis, and develop recommendations based on those results as well as prior results in the literature.

Forced vibration testing of a well-instrumented test structure was performed in Garner Valley, CA to expand the data inventory for analysis of SSI effects. Chapter 5 presents the details of the field testing and associated data files created as part of the work. In addition to monitoring of the test structure, instrumentation included monitoring of a local concrete slab and adjacent structure during the forced vibration testing. The additional monitoring was done to establish field data for evaluation of kinematic interaction and structure-soil-structure (SSSI).

The output/input forced vibration testing data was used for evaluation of inertial and kinematic interaction effects (Chapter 6). Horizontal impedance functions of the system were evaluated from the recorded data and then compared to the analytical solutions in Chapter 2. Additionally the output/input signals were analyzed using parametric system identification procedures to establish fixed-base and flexible-base first mode periods and damping ratios. The particle motions generated from the field test structure during forced vibration testing were evaluated on and adjacent a local concrete slab to investigate kinematic interaction. The particle motions were reviewed to gain insight into the slab-ground interaction. Then transfer functions were computed and compared to the simplified kinematic interaction model in Chapter 3. SSSI analysis was performed by evaluating transfer functions of the foundation motions of Mini-Me and Dr. Evil from three intensity-levels of forced vibration loading conditions.

7.2 Research Findings and Recommendations

7.2.1 Chapter 2; Foundation Damping

1. Foundation damping incorporates the combined effects of energy loss due to waves propagating away from the vibrating foundation in translational and rotational modes (radiation damping), as well as hysteretic action in the soil (material damping). Foundation damping is sensitive to the height aspect ratios (*h/r & h/B*) and foundation aspect ratio (*L/B*). Much more foundation damping is produced when translation controls (i.e. $h/B \le 2$) the SSI system as compared to rocking (i.e. $h/r \,\&\, h/B > 2$). As the foundation aspect ratio increases $(L/B > 1)$, shaking in the long direction (*x*-direction) produces higher foundation damping than does shaking in the short (*y*) direction. Rocking becomes less pronounced in the long direction, in turn causing foundation translation to dominate, which produces more foundation damping.
2. Foundation damping expressions (Eqs. 2-25 and 2-35) were derived by starting from fundamental principles of equating the properties of an equivalent fixed-base oscillator to that of a flexible-base oscillator. The derivations were performed by both matching the imaginary component and considering the full complex valued stiffness. These derivations lead to two equally viable solutions for foundation damping.
3. Procedures were presented to consider various site-specific conditions such as rectangular footprint, embedment, soil nohomogeneity and nonlinearity

conditions. As a result of these recommendations, foundation damping can be solved using closed-form solutions (Eqs. 2-25 and 2-35);

4. Empirical data was used to guide in the selection of a single solution for foundation damping. It was found that the levels of damping from Eq. (2-25) are higher than those from Eq. (2-35) for foundations of modest height aspect ratios. The lower damping from Eq. (2-35) is generally more consistent with field case histories. Eq. (2-35) appears to be the preferred formulation at the present time.

7.2.2 Chapter 3; Kinematic Soil-Structure Interaction Effects from Building and Free-Field Seismic Arrays in Japan

1. A list of well-instrumented Japanese sites has been compiled and three were evaluated for transfer functions between the foundation and free-field motions. This work adds to the inventory of case studies looking specifically at simplified kinematic interaction models. This work is limited in that it only reviewed three sites for comparison of the horizontal transfer functions and one site for rocking transfer function. However, this work does expand the data invitory to include buildings with stout piles that were not considered in the data set used to develop the models;
2. NIST-type kinematic models for horizontal transfer functions matched the finite element modeling code SASSI results well for frequencies of principal interest (up to about 10 Hz). The NIST-type model predicted kinematic base rocking well, as opposed to the SASSI model that was too low compared to the data;

3. Model-based horizontal transfer functions were too large (hence conservative) for the Sendai and Onagawa sites. The model predictions are fairly accurate relative to data at the Nagoya site, which is dominated by embedment effects;
4. For the Japanese buildings situated on piles at the ground surface, the NIST-type model tends to underpredict the ground motion reduction from kinematic interaction for frequencies larger than the structure's resonant frequency. This is a component of kinematic interaction that does not have an analytical model;
5. The NIST-type model worked well for the limited cases examined, even though the base-slab averaging model is semi-empirical and developed based on western United State sites. The models either matched the ground motion reduction or underpredicted (hence conservative).

7.2.3 Chapter 4; Assessment of Alternative SSI Modeling Strategies

1. Baseline models (MB) type models can match observed responses with modest adjustments of structural mass and damping;
2. An equivalent-linear spring and dashpot approach for SSI modeling can provide satisfactory predictions of soil-foundation-building performance;
3. Four simplified models were considered for response history analysis. Model 1 includes the above ground portion of the structure as fixed at the ground surface (excluding subterranean levels and foundation components), excited by the free-field motion (u_g). Model 2 includes the above ground and subterranean portions of the structure, but ignores the embedment soils (no soil springs) and is fixed at the base, excited by u_g. Model 3 includes subterranean levels with horizontal and

vertical soil springs, with the horizontal springs at the base are excited by u_g and the springs at higher elevations are fixed and the end with no input motion. Model 4 includes subterranean levels supported by horizontal and vertical soil springs that are fixed at their ends to a rigid "bathtub," excited by the foundation input motion (u_{FIM}) or u_g.

4. Engineering demand parameters (EDPs) such as inter-story drifts, story shear distributions, and floor accelerations were evaluated for each modeling scheme and compared to the baseline model (MB).
5. Model 2 and Model 4 (bathtub) had the best performance for the above-ground portion compared to the MB model;
6. Model 3 performed the worst compared to the above-ground portion of the MB Model and should not be used;
7. Model 1 is the next least-desirable compared to Model 3, with the level of error increasing with stiffer structures or deeply embedded structures;
8. None of the simplified modeling schemes (Models 1-4) were able to match the MB response below the ground line.

7.2.4 Chapter 5; Forced Vibration Testing of a Test Structure

1. The response histories have been processed from the unprocessed data files to convert to engineering units, convenient time formats, and to remove baseline errors. Visual inspection revealed several problems: a disconnected LVDT (Ch. 46), baseline errors of accelerations from the foundation of adjacent structure Dr. Evil, and a conversion error of three vertical foundation LVDTs (Chs. 44, 46, 47).

The artificial LVDT conversion error can be corrected by multiplying the response by a factor of 10. The data files created from the forced vibration testing at GVDA have been archived at the NEEShub (https://nees.org/warehouse/project/637);

2. The observed responses indicate no significant torsional response for the lowest shaking level, but asymmetric responses during testing with the large shaker suggest a torsional response;
3. Gapping was observed in the LVDT displacements applied by the strongest shaking, which is consistent with visual observations from the field.

7.2.5 Chapter 6; Evaluation of Soil-Structure Interaction Effects from Forced Vibration Testing

1. Impedance functions have been analyzed from the output/input responses of the Mini-Me test structure. Comparison of the results from the different loading conditions, structural condition (i.e., braced or unbraced), and shaker location revealed varying degrees of noise in the data. Local complexities were produced when testing in the braced condition due to the resonance of the braces. The large shaker was affixed to the Mini-Me structure for all tests, whereas the small shaker was externally mounted for testing on the roof, but not for testing on the foundation. As a result noise was introduced into the recorded shaker response as the shaker produced artificial translations not associated with the loading of the structure. Testing in an unbraced condition with the small shaker externally mounted on the roof produced the best reading of the impedance ordinates.

2. The data was analyzed to evaluate the stiffness and damping associated with the foundation-soil interaction, revealing linear-elastic behavior at low forcing levels characterized by smaller stiffnesses and both lower and higher damping than was predicted by classical models. Modeling to account for the overburden of the structure tended to overpredict the stiffness values. Shaking in the long direction (y-direction) resulted in lower stiffnesses as compared to shaking in the short (x) direction, which is opposite of the modeled trends. Whereas the translational damping ratio was either matched well or slightly overpredicted by the models, the rotational damping ratio was much larger than predicted;
3. The foundation soil strain (γ) was approximated for the large amplitude force vibration testing by comparing the foundation peak velocity (PGV) and soil shear wave velocity $\left(\gamma = PGV/V_s\right)$. Shear modulus reduction (G/G_0) and damping (β_s) was then evaluated using Menq's model (2003) at the corresponding strain. The strains showed a frequency-dependency. A rapid increase in demand occurs at low frequencies (0-7 Hz). At larger frequencies (7-14 Hz) the demand would either steady at large strains for eccentricity tests $\left(\geq 50\%\right)$ or slightly relax. This frequency-dependency of the strains was able to capture the observed behavior of the foundation-soil system well. Similar trends were observed in the inverted stiffness results.
4. At small frequencies (where small soil strains are expected) from testing with the large shaker, the experimental stiffness values are smaller than the results from the testing with the small shaker.

5. Negative damping ratios of the large-force test results indicate that the results have been compromised. It is suspected that the small phase difference at low frequencies and our ability in resolving through measurements of the very small numbers resulted in the negative damping ratios.
6. Kinematic interaction effects were investigated from the response data processed for the local concrete slab and adjacent ground surface. Interestingly, the kinematic interaction effects observed on the adjacent slab excited principally by surface waves were of a similar character to expectations from analytical models for body wave excitation from earthquakes. If verified, these results could lead to site- and foundation-specific test methods for evaluating kinematic interaction effects.
7. The Stewart et al. (1999b) data set from instrumented structures has been expanded to include results from forced vibration tests. The new data occupies a previously sparsely populated region of moderately high $h/(V_sT)$ = 0.14 to 0.45, and hence is a valuable addition to the previous database.
8. Structure-soil-structure interaction (SSSI) was evaluated through use of transfer functions of the foundation motions of Dr. Evil and Mini-Me. The transfer functions showed that nonlinearity significantly reduces the interaction between the foundations.

7.3 Recommendations for Future Research

The following are recommendations for future research:

1. Forced vibration testing showed a reduction of the stiffnesses as loading was increased from test to test. Forced vibration testing that is expected to cause large stress should include strain gauges in the soil to evaluate the soil's strain underneath the foundation.
2. Improve upon the current instrumentation programs, such as CSMIP and USGS, to include SSI-type sensor plans. The objective is to identify buildings that are moderately to highly susceptible to period lengthening, foundation damping and kinematic interaction. An initial evaluation of a building for the inertial interaction level of interest can be made based on $h/V_s T > 0.1$. Buildings in areas prone to high frequency content seismic events (such as east coast buildings) should be identified for kinematic interaction arrays. SSI-type sensor plans designed to capture SSI effects on buildings requires at least the horizontal accelerometers at the free-field, foundation, and roof and two vertical accelerometers on the foundation to evaluate rocking response (Stewart and Fenves, 1998).
3. Kinematic interaction models (as considered in Chapter 3) currently do not capture the reduction of ground motion at low frequencies for buildings situated on piles at the ground surface. A verified model to capture the effect of piles should be developed.

4. Kinematic interaction models should be evaluated with computer based software, such as SASSI, to validate or update the input parameters. Currently the models are based on κ_a and a_0. The κ_a term was semi-empirically derived as a function of V_s and $a_0^r = \omega r / V_s$. The implication is that both ω and r have an equal effect on kinematic interaction. It should be determined if the frequency or geometry has a greater effect to kinematics and possibly decoupled as an input parameter.

8 REFERENCES

Abrahamson, NA, 1991. Spatial variation of strong ground motion for use in soil-structure interaction analysis, *Proceedings of Fourth U.S. National Conference on Earthquake Engineering*, Vol.1, 317-326.

American Society of Civil Engineers, ASCE, 2010. Minimum Design Loads for Buildings and Other Structures, *Report ASCE/SEI 7-10*, Reston, VA.

American Society of Civil Engineers, ASCE, 2006. Seismic rehabilitation of existing buildings, *Report ASCE/SEI 41-06*, Reston, VA.

Ancheta, TD, JP Stewart, and NA Abramhamson, 2011. Engineering characterization of earthquake ground motion coherency and amplitude variability, *Proc. 4th International Symposium on Effects of Surface Geology on Seismic Motion*, IASPEI / IAEE, August 23–26, 2011, University of California, Santa Barbara.

Applied Technology Council, ATC, 1996, Seismic evaluation and retrofit of concrete buildings, *Report ATC-40,* Redwood City, CA.

Apsel, R.J. and Luco, J.E., 1987. Impedance functions for foundations embedded in a layered medium: an integral equation approach, *Earthquake Engineering and Structural Dynamics*, Vol. 15, No. 2, pp. 213-231.

Aviles, J. and Perez-Rocha, L.E., 1996. Evaluation of interaction effects on system period and the system damping due to foundation embedment and layer depth, *Soil Dyn. and Eqk.Engrg.,* 15, 11-27.

ASCE, 2013, *Seismic Evaluation and Retrofit of Existing Buildings*, ASCE/SEI 41-13, American Society of Civil Engineers, Reston, Virginia.

ASCE, 2010, *Minimum Design Loads for Buildings and Other Structures,* ASCE/SEI 7-10, American Society of Civil Engineers, Reston, Virginia.

ASCE, 2006, *Minimum Design Loads for Buildings and Other Structures,* ASCE/SEI 7-05, American Society of Civil Engineers, Reston, Virginia.

Bielak, J., 1971. Earthquake response of building-foundation systems, *Ph.D. Dissertation*, California Institute of Technology, Pasadena.

Bielak, J., 1975. Dynamic behavior of structures with embedded foundations, *J. Earthquake Engng. Struct. Dyn*, 3, 259-274.

Bielak J 1976. Modal analysis for building-soil interaction, *J. Engrg. Mech*, 102, 771-786.

Boore, D.M., and Boomer, J.J., 2005. Processing of strong-motion accelerograms: needs, options and consequences, *Soil Dyn. and Eqk.Engrg.,* 25, 93-115.

California Strong Motion Instrumentation Program (CSMIP), 2011. Accessed through website at http://www.strongmotioncenter.org

Chubu Regional Bureau office, MLIT, 2003. PS logging at Nagoya Courthouse building complex, unpublished report (in Japanese).

Chubu Regional Bureau office, MLIT, personal communication 2005. Portions of construction drawings and the soil investigation (in Japanese).

Chopra, A.K. 2011. *Dynamics of structures, theory and application sto earthquake engineering, fourth edition*, Prentice Hall, Upper Saddle River, NJ.

Chopra, A.K., and Goel, R.K., 1999. Capacity-demand-diagram methods based on inelastic design spectrum, *Earthquake Spectra*, Vol. 15, No. 4, pp. 637-656.

Crouse, C.B., Hushmand, B., Luco, J.E., and Wong, H.L., 1990, "Foundation impedance functions: Theory versus experiment," *Journal of Geotechnical Engineering*, Vol. 116, No. 3, pp. 432-449.

Darendeli, 2001. Development of a new family of normalized modulus reduction and material damping curves, *Ph.D. Dissertation*, Univ. of Texas at Austin.

De Barros, F.C.P. and Luco, J.E., 1995, "Identification of foundation impedance functions and soil properties from vibration tests of the Hualien containment model," *Soil Dynamics and Earthquake Engineering*, Vol. 14, pp. 229-248.

Fadum, R.E., 1948, "Influence values for estimating stresses in elastic foundations," *Proceedings*, 2nd International Conference on Soil Mechanics and Foundation Engineering, Rotterdam, Vol. 3, pp. 77-84.

Federal Emergency Management Agency (FEMA), 2003. *NEHRP Recommended Provisions for Seismic Regulations for New Buildings and Other Structures, FEMA 450*, Federal Emergency Management Agency, Washington, D.C.

Federal Emergency Management Agency (FEMA), 2005. *Improvement of Inelastic Seismic Analysis Procedures, FEMA 440*, Federal Emergency Management Agency, Washington,D.C.

Federal Emergency Management Agency (FEMA), 2009. *NEHRP Recommended Seismic Provisions for New Buildings and Other Structures*, Document FEMA P-750, 2009 Edition. Building Seismic Safety Council, Washington DC.

Fumal, T.E. and Tinsley, J.C., 1985. Mapping shear wave velocities of near surface geologic materials, in evaluating earthquake hazards in the Los Angeles region-an earth-science perspective, *U.S. Geol. Surv. Profess. Pap*, 1360, 101-126.

Gazetas, G., 1991. Foundation vibrations, *Foundation Engineering Handbook,* 2nd Edition, Chapter 15, H.-Y. Fang, ed., Chapman and Hall, New York, NY.

Ghiocel, DM, 2006. ACS SASSI Version 2.3 – An advanced computational software for system analysis for soil-structure interaction; User manual, *Technical Report,* Rochester, NY.

Harding, Miller, Lawson, and Associates, 1970. Foundation investigation Walnut Creek office building for Dillingham Corporation, Walnut Creek, California, *Report 3008,002.04*, San Francisco, CA.

Haselton, C.B., Leil, A.B., Deierlein, G.G., and Chou, J.H., 2011, "Seismic Collapse Safety of Reinforced Concrete Buildings: I, Assessment of Ductile Moment Frames," *Journal of Structural Engineering*, Vol. 137, pp. 481-491.

Holtz, R.D., Kovacs, W.D., and Sheahan, T.C., 2010. *An Introduction to Geotechnical Engineering*, 2nd Edition, Prentice Hall, Englewood Cliffs, NJ.

Idriss, IM, and JI Sun, 1991. User's manual for SHAKE91: A computer program for conducting equivalent linear seismic response analyses of horizontally layered soil deposits, *Center for Geotechnical Modeling,* Univ. of California, Davis.

International Building Code, IBC, 2012. *2012 International Building Code,* prepared by International Code Council (ICC), Washington, D.C.

Iguchi, M. and Luco, J.E., 1982. Vibration of flexible plate on viscoelastic medium*, J. Eng.Mech.,* 108(6), 1103-1120.

Kausel E, A Whitman, J Murray, and F Elsabee, 1978. The spring method for embedded foundations*, Nuclear Engrg. and Design*, 48, 377-392.

Kim S and JP Stewart, 2003. Kinematic soil-structure interaction from strong motion recordings, *Journal of Geotechnical and Geoenvironmental Engineering*, ASCE, 129(4), 323-335.

Kwok, A.O., Stewart, J.P., Hashash, Y.M.A., Matasovic, N., Pyke, R., Wang, Z., and Yang, Z., 2007. Use of exact solutions of wave propagation problems to guide implementation of nonlinear seismic ground response analysis procedures, *J. Geotech. & Geoenv. Engrg.*, ASCE, 133 (11), 1385-1398.

LeRoy, Crandall and Associates, 1978. Report of supplementary studies proposed retaining walls proposed Sherman Oaks Galleria, Ventura and Sepulveda Boulevards, Los Angeles, California, for Kendall International, *Report No. ADE-78044*, provided by MACTEC, Los Angeles, CA.

LeRoy, Crandall and Associates, 1982. Completion of exploration program proposed office building and parking structure, Ventura and Sepulveda Boulevards, Los Angeles, California, for McNeill Enterprises, *Report No. ADE-81384*, provided by MACTEC, Los Angeles, CA.

Lin, A.N. and Jennings, P.C., 1984, Effect of embedment on foundation-soil impedances, *J. of Engrg. Mech.*, Vol. 110, No. 7, pp. 1060-1075.

Ljung, L., 1987, *System Identification: Theory for the User*, Prentice Hall, Englewood Cliffs, NJ.

Luco, J.E. and Westmann, R.A., 1971, Dynamic response of circular footings, *J. of Engr. Mech.*, Vol. 97, No. 5, pp. 1381-1395.

Luco, J.E. and Contesse, L., 1973, Dynamic structure-soil-structure interaction, *Bulletin of Seismo. Soc. of America*, Vol. 63, No. 4, pp. 1289-1303.

Luco, J.E., 1976, Vibrations of a rigid disc on a layered viscoelastic medium, *Nuclear Engrg. and Design*, Vol. 36, pp. 325-340.

Luco, J.E., Trifunac, M.D., and Wong, H.L., 1988, Isolation of soil-structure interaction effects by fullscale forced vibration tests, *Eqk. Engrg. and Struc. Dyn.*, Vol. 16, No. 1, pp. 1-21.

Lysmer, J, M Tabatabaie-Raissi, F Tajirian, S Vahdani, and F Ostadan, 1981. SASSI – A system for analysis of soil-structure interaction, *Report No. UCB/GT/81-02*, Geotechnical Engineering, University of California, Berkeley.

Lysmer, J, F Ostadan and C Chin, 1999. SASSI2000 *Theoretical Manual*, Geotechnical Engineering Division, Civil Engineering Department, University of California, Berkeley.

Maravas, A., Mylonakis, G., and Karabalis, D.L., 2007. Dynamic characteristics of simple structures on piles and footings, *Proc. 4th Int. Con. on Eqk. Geotech. Engrg.,* Thessaloniki, Greece, June 25-28, Paper No. 1672.

Menq., F.-Y, 2003. Dynamic properties of sandy and gravelly soils, *Ph.D. Dissertation*, Univ. of Texas at Austin.

Mikami, A, JP Stewart, F Ostadan, and CB Crouse, 2006. Representation of ground motion incoherence for the analysis of kinematic soil-structure interaction, *Proc. 8th U.S. Nat. Conf. Eqk. Engrg*, April 18-22, San Francisco, CA, Paper 1071.

Mikami, A, JP Stewart, and M Kamiyama, M.., 2008. Effects of time series analysis protocols on transfer functions calculated from earthquake accelerograms, *Soil Dyn. and Eqk.Engrg.,* 28, 695-706.

Mylonakis, G., Nikolaou, S., and Gazetas, G., 2006. Footings under seismic loading: Analysis and design issues with emphasis on bridge foundations, *Soil Dyn. & Eqk. Engrg.,* 26, 824-853.

Naeim, F., Tileylioglu, S., Alimoradi, A., and Stewart, J.P., 2008. Impact of foundation modeling on the accuracy of response history analysis of a tall building, *Proc. SMIP2008 Seminar on Utilization of Strong Motion Data*, California Strong Motion Instrumentation Program, Sacramento, CA, 19-55.

Network for Earthquake Engineering Simulations hub (NEEShub), 2012. Mitigation of collapse risk in vulnerable concrete buildings, *Project NEES-2008-0637*, access online at https://nees.org/warehouse/project/637.

Network for Earthquake Engineering Simulations at University of California, Los Angelse (NEES@UCLA), 2012. Access online at http://nees.ucla.edu/equipment.html.

Network for Earthquake Engineering Simulations at University of California, Santa Barbara (NEES@UCSB), 2012. Access online at http://nees.ucsb.edu/facilities/gvda.

National Institute of Standards and Technology, NIST (2012). Soil-Structure Interaction for Building Structures, *Report NIST/GCR 12-917-21*, presented by NEHRP Consultants Joint Venture, J.P. Stewart (project director), September.

Ostadan, F, 2005. Soil-structure interaction analysis including ground motion incoherency effects, *18th International Conference on Structural Mechanics in Reactor Technology* (*SMiRT 18*), Beijing, China.

OYO Corporation, 2007. PS logging at Tokoku Institute of Technology campus in 2007, unpublished report, September 2007 (in Japanese).

Pais, A. and Kausel, E., 1988. Approximate formulas for dynamic stiffnesses of rigid foundations, *Soil Dyn. & Eqk. Engrg.,* 7 (4), 213-227.

Pak, R.Y.S., and Guzina, B.B., 1998. Vertical vibration of a circular footing on a linear-wave-velocity half-space, *Geotechnique*, 48 (2), 159-168.

Pandit, S.M., 1991. *Modal and Spectrum Analysis*. Wiley, New York

PEER, 2010. *Tall Buildings Initiative, Guidelines for Performance-Based Seismic Design of Tall Buildings*, Report No. 2010/05, Pacific Earthquake Engineering Research Center, UC Berkeley.

Powell, G.H., 2006. Static pushover methods – explanation, comparison and implementation, Modeling for Structural Analysis: *Proc. 8th U.S. National Conference on Earthquake Engineering*, San Francisco, California.

Raney Geotechnical, 1983. Foundation investigation North Main Centre, North Main St. and Principle Ave., Walnut Creek, CA, Repot 029-005, West Sacramento, CA.

Roesset, J.M., 1980. Stiffness and damping coefficients of foundations, *Proc. ASCE Geotechnical Engineering Division National Convention*, Oct. 30, 1-30.

Salgado, R., 2008. *The Engineering of Foundations*, McGraw-Hill, New York.

Scott, R., 1981, *Foundation Analysis*, Prentice Hall, Englewood Cliffs, NJ.

Star. L., 2011. Seismic vulnerability of structures: Demand characteristics and field testing to evaluate soil-structure interaction effects, *Ph.D. Dissertation*, Univ. of CA, Los Angeles.

Stewart, J.P, and Stewart, A.F, 1997. Analysis of soil-structure interaction effects on building response from earthquake strong motion recordings at 58 sites, Report UCB/EERC-97/01, University of Berkeley, CA.

Stewart, J.P. and Fenves, G.L., 1998. System identification for evaluating soil-structure interaction effects in buildings from strong motion recordings, *J. Eqk Engng. Struct. Dyn.,* 27, 869-885.

Stewart, J. P., Seed, R. B., and Fenves, G. L., 1999a. Seismic soil-structure interaction in buildings. I: Analytical aspects, *J. Geotech. Geoenviron. Engrg.* 125, 26–37.

Stewart, J.P., Fenves, G.L., and Seed, R.B., 1999b. Seismic soil-structure interaction in buildings. II: Empirical findings, *J. Geotech. Geoenviron. Engrg.* 125, 38–48.

Stewart, J.P., Kim, S., Bielak, J., Dobry, R., and Power, M., 2003, "Revisions to soil structure interaction procedures in NEHRP design provisions," *Earthquake Spectra*, Vol. 19, No. 3, pp. 677-696.

Stokoe, K.H., Graves J.C., Graves M.T., Kurtulus, A., and Menq, F.Y., 2004. Data Report: SASW measurements at the NEES Garner Valley Test Site, California., Access online at http://nees.ucsb.edu/facilities/gvda.

Tileylioglu, S., 2008. Evaluation of soil-structure interaction effects from field performance data, *Ph.D. Dissertation*, Univ. of California, Los Angeles.

Tileylioglu, S., Naeim, F., Alimoradi, A., and Stewart, J.P., 2010. Impact of foundation modeling on the accuracy of response analysis for a tall building, *Proc. 9th US National & 10th Canadian Conf. on Earthquake Engrg.,*, EERI and Canadian Assoc. for Earthquake Eng., July 25-29, 2010, Paper No. 1666.

Tileylioglu, S, JP Stewart, and RL Nigbor, 2011. Dynamic stiffness and damping of a shallow foundation from forced vibration of a field test structure, *J. Geotech. & Geoenv. Engrg.*, 137 (4), 344-353.

Tohoku Electric Power Company, 2009. Seismic analysis of Onagawa NPS#1, Siryo 2-1 report (in Japanese).

Tohoku Electric Power Company, 2009. Vibration characteristics of the ground site, Siryo 2-3 report (in Japanese).

Tohoku Electric Power Company, 2011. Accelerograms observed at Onagawa NPS during 2011 Great East Japan Earthquake, available on CD-ROM from Japan Association for Earthquake Engineering.

Veletsos, A.S. and Wei, Y.T., 1971. Lateral and rocking vibrations of footings. *J. Soil Mech. and Found. Div.,* 97**(**9), 1227-1248.

Veletsos, AS, and B. Verbic, 1973. Vibration of viscoelastic foundations, *J. Eqk. Engrg. Struct. Dyn.*, 2, 87-102.

Veletsos, A.S. and Meek, J.W., 1974. Dynamic behavior of building-foundation systems, *J. Eqk. Engrg. and Str. Dyn.*, 3, 121–138.

Veletsos, A. S., and Nair, V. V., 1975. Seismic interaction of structures on hysteretic foundations, *J. Struct. Engrg.* 101, 109–129.

Veletsos, A. S., 1977. *Dynamics of Soil-Foundation Systems*, in W.J. Hall (ed.) Structural and Geotechnical Mechanics, Prentice-Hall, Inc., Englewood Cliffs, New Jersey, pp 333-361.

Veletsos, AS and AM Prasad, 1989. Seismic interaction of structures and soils: Stochastic approach, *J. Struct. Engrg.,* 115 (4), 935–956.

Veletsos, AS, AM Prasad, and WH Wu, 1997. Transfer functions for rigid rectangular foundations, *J. Eqk. Engrg. Struct. Dyn.*, 26 (1), 5-17.

Vrettos, C., 1999. Vertical and rocking impedances for rigid rectangular foundations on soils with bounded non-homogeneity, *J. Eqk. Engrg. and Str. Dyn.,* 28, 1525-1540.

Wolf, J.P., 1985. *Dynamic Soil-Structure Interaction*, Prentice-Hall, Inc., Englewood Cliffs, New Jersey.

Yamada, S., Hyodo, M., M., Orense, R.P., Dinesh, S.V., and Hyodo, T., 2008. Strain-dependent dynamic properties of remolded sand-clay mixtures, *J. Geotech. & Geoenv. Engrg.*, 137 (4), 344-353.

Zerva, A and V Zervas, 2002. Spatial variations of seismic ground motion – an overview. *Applied Mechanics Reviews*, 55, 271-297.